UNIVERSITY OF SHEFFIELD

# An investigation of classifying the flow over rough surfaces into k- and d- type in turbulent channel flow

by

Almajd A. Alhinai

Supervisor: Dr Andrzej F. Nowakowski

A thesis submitted in partial fulfilment for the degree of PhD

in the

Faculty of Engineering

Department of Mechanical Engineering

August 2015

UNIVERSITY OF SHEFFIELD

# *Abstract*

Faculty of Engineering
Department of Mechanical Engineering

PhD

by Almajd A. Alhinai
Supervisor: Dr Andrzej F. Nowakowski

This thesis is concerned with the classification of roughness into k- and d- type in turbulent channel flow. Despite the practical importance of this type of flow, the literature review suggest that advancements in the field have been slow due to the difficulty of making accurate measurements close to the wall when using experimental methods. In recent years, numerical modelling has provided a good alternative to studying this type of flow. In this work, an Implicit Large Eddy Simulation (ILES) approach was developed to carry out numerical simulations for turbulent channel flow over rough surfaces. The application was developed based on the Finite Element Method and implemented using the Multi-Physics platform COMSOL. Verification and validation of the numerical model was carried out to asses the predictive capabilities of the model, including sensitivity analysis to quantify the uncertainty and comparison with results from literature to validate the model. In our analysis, we considered rough surfaces with square and triangular roughness elements with a constant roughness height and varying distributions of the roughness elements. The results demonstrated that the model is capable of resolving the coherent large eddy structures associated with the k- and d- type behaviours. The classification reported here is based on the coherent structures associated with the k- and d- type behaviours. Furthermore, we investigated the effects of roughness geometry on the k- and d- type behaviours. To this end, flow visualizations were used to study the interaction between the inner and outer layer of the flow. The results demonstrated that the geometry of the roughness elements has little effect on the coherent structures associated with the k- and d-type behaviours, these effects of the roughness geometry are confined to the inner region. However, the results show that the roughness geometry has a strong influence on the interaction between the inner and outer flow regions.

# *Acknowledgements*

I would like to express my deep gratitude to Dr. Andrew Nowakowski for his guidance, support and supervision throughout my PhD study. Also, I would like to thank H.M Sultan Qaboos government for funding this research and awarding me the scholarship that made this PhD possible. I would like to dedicate this work to my father Ahmed Alhinai for all his help and support and to the rest of the family for their continuous love and prayers throughout my PhD. Last but not least, a special thank you to Rebecca King for the support throughout my studies and to all my friends and colleagues at the University of Sheffield.

# Contents

# List of Figures

# List of Tables

# Abbreviations

| | |
|---|---|
| **AIAA** | American Institute of Aeronautics and Astronautics |
| **AMR** | Adaptive Mesh Refinement |
| **CFD** | Computational Fluid Mechanics |
| **DoF** | Degrees of Freedom |
| **DNS** | Direct Numerical Simulation |
| **FEM** | Finite Element Method |
| **FVM** | Finite Volume Method |
| **ILES** | Implicit Large Eddy Simulation |
| **LES** | Large Eddy Simulation |
| **RANS** | Reynolds Averaged Navier-Stokes |
| **Re** | Reynolds number |

# Symbols

| | | |
|---|---|---|
| $A$ | Additive constant eq 1.2 | |
| $C_f$ | Friction coefficient | |
| $C_p$ | Pressure coefficient | |
| $\mathbf{F}$ | Body forces/source terms | |
| $H$ | Channel half height | [m] |
| $\mathbf{I}$ | Unit tensor/vector | |
| $L$ | Channel length | [m] |
| $U^+$ | Mean velocity normalized by friction velocity | |
| $d$ | Boundary layer thickness/pipe diameter | [m] |
| $k$ | Roughness height | [m] |
| $p$ | Pressure | [Pa] |
| $t$ | Time | [s] |
| $u, v$ | Cartesian velocity components | |
| $\mathbf{u}$ | Velocity vector | [m/s] |
| $u_\tau$ | Friction velocity | [m/s] |
| $x, y$ | Cartesian coordinates | |
| $y^+$ | Non-dimensional wall distance | |

| | | |
|---|---|---|
| $\Gamma_{()}$ | Boundary condition | |
| $\Omega$ | Domain/fluid region | |
| $\delta$ | Boundary layer length scale | |
| $\kappa$ | Von Karman constant | |
| $\lambda$ | Roughness distance/solidity | $[m]$ |
| $\mu$ | Dynamic viscosity | $[Pa \cdot s]$ |
| $\nu$ | Kinematic viscosity | $[m^2/s]$ |

| | | |
|---|---|---|
| $\rho$ | Fluid density | $[Kg/m^3]$ |
| $\tau_w$ | Wall shear stress | $[Pa \cdot s]$ |
| $\zeta$ | z- component of vorticity | [1/s] |

# Chapter 1

# Introduction

## 1.1 Background

Turbulent channel flows are encountered in numerous fluid dynamic engineering applications. According to Lee et al [9] the roughness of the wall surface in turbulent channel flow is an important design parameter because it influences characteristics such as the transport of heat, mass and momentum. In terms of roughness effects, the concept of standard roughness introduced in boundary layer theory, see Schlichting [10], led to a widely accepted correlation between the roughness height and the roughness function. However, it is important to mention here that using the standard roughness approach is only an approximation. The author [10] points out that this approximation can only describe the global values of the flow, and details of the wall layer of the flow could not be described in this manner. Nevertheless, a major outcome of using the standard roughness approach, based on the Colebrook formula and combined with experiments, is known as the Moody diagram represented in figure 1.1.

Young et al. [1] explained that in fact the Moody diagram is a graphical representation of the Colebrook formula, which is an empirical fit of the pipe flow pressure drop data. This diagram presents the friction factor as a function of Reynolds number and relative roughness for round pipes. A difficulty of using the Colebrook formula is that it is implicit in the dependence on the friction factor. That is, for given conditions, it is not possible to solve for the friction factor without some sort of iterative scheme. However, with the use of modern computers such calculations are not difficult. Indeed, the most cited work in channel flow literature is the Direct Numerical Simulation (DNS) of Kim et al. [7]. In this work the authors [7] presented turbulence statistics in a fully developed channel flow at low Reynolds number. Particular attention was given to the behaviour of

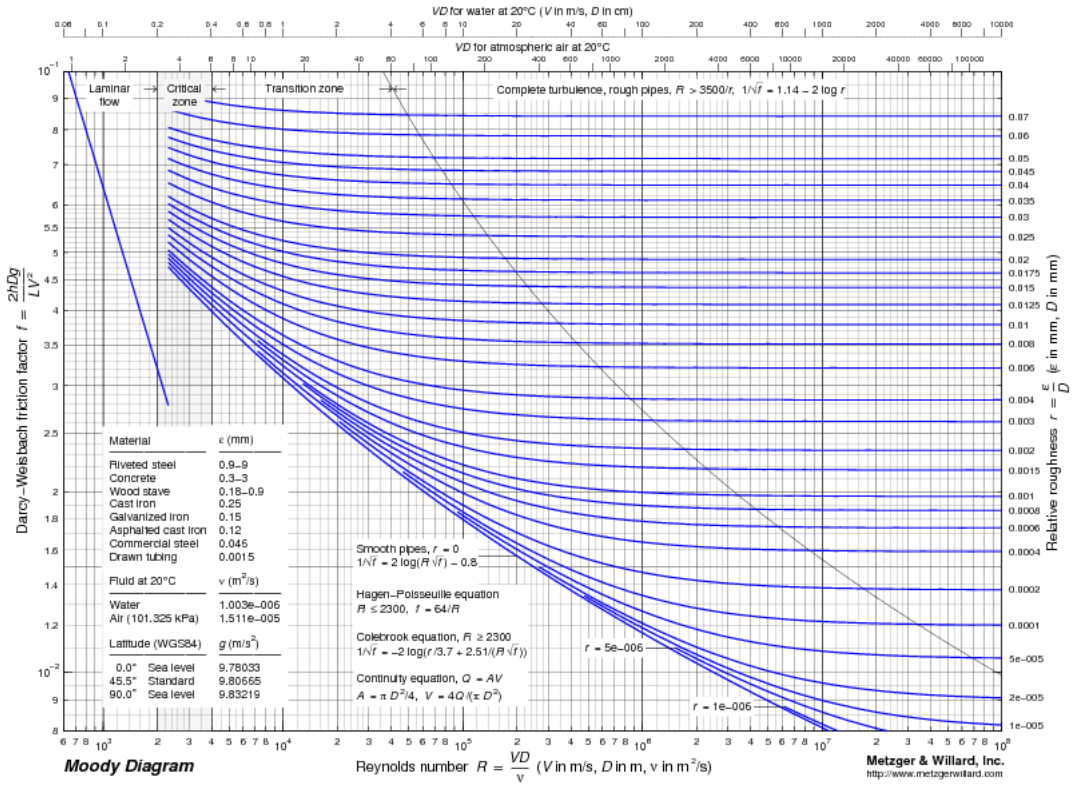


FIGURE 1.1: Moody Diagram , see Young et al. [1].

turbulence correlations near the wall. The authors also reported a number of statistical correlations which are complementary to experimental data for the first time.

Several authors (e.g Jimenez [11]) state that although the effects of surface roughness on a turbulent boundary layer has been examined in many experimental and numerical studies, knowledge of these effects remains incomplete. Piquet [12] notes that one of the reasons for the slow progress in rough wall studies is that there are intrinsic difficulties in measuring the flow near the roughness elements. Some of these difficulties are outlined by Reynolds [13] and summarized in the points below:

- An accurate prediction of friction is possible only if experimental data is available for the particular surface and flow conditions of interest;

- Some irregular surfaces have friction characteristics unlike those for sand-roughened and commercially rough surfaces widely studied. Although the mean velocity distribution is expressed in terms of the distance from the wall, the effective wall location is not readily apparent;

- The flow near the wall sometimes dominates the heat and mass transfers between the wall and the fluid. This approximation does not take into account the activity among the roughness elements and the remnants of the viscous sub-layer;

- For some roughness geometries, no single dimension of the roughness serves to define the friction characteristic or the scale of the logarithmic layer.

In recent years it became common practice to complement experiments with numerical simulations to overcome some of the issues outlined above. According to White [14], numerical analysis on a digital computer is an important method of simulating viscous flows, often with nearly exact results. He explains further that immersed body problems are currently solvable using the digital computer approach, as opposed to traditional experiments. Traditionally, numerical simulations were carried out using Direct Numerical Simulation (DNS), Large Eddy Simulation (LES) and Reynolds averaged Navier-Stokes (RANS) models. In the context of the flow over rough surfaces, we are dealing with a highly unsteady flow field. Therefore, one can rule out using RANS models to simulate this type of flow. DNS provides the most accurate means for simulating the flow over rough surfaces, however, the computational costs of such an approach are very high, even at low Reynolds number. On the other hand, LES resolves large scales of the flow field solution, allowing better fidelity than RANS methods. It also models the smallest scales of the solution, rather than resolving them as DNS does. This makes the computational cost for practical engineering systems with complex geometry or flow configuration attainable using modern digital computers.

## 1.2 The overall structures of turbulent channel flow

In turbulence literature, turbulent channel flow is generally classified as a wall-bounded flow problem. Gad-el-Hak [2] states that in wall bounded flow, a multiplicity of coherent structures have been identified mostly through visualization experiments and a number of correlation measurements. By inspecting the distribution of viscous and turbulent shear stresses in typical wall-bounded flows, the author [2] suggests the presence of three distinct regions, as shown in figure 1.2. Each region is discussed in more detail in the following subsections.

### 1.2.1 Viscous region

Near the wall, the viscous region could be subdivided into the viscous sublayer and the buffer layer. According to Gad-el-Hak [2] the turbulent shear stress is nearly zero and

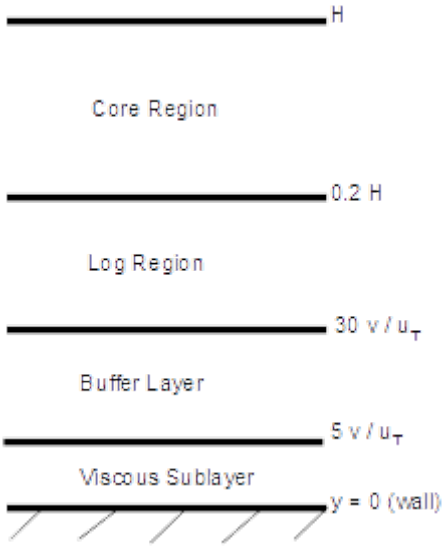


FIGURE 1.2: Sketch showing the flow regions in wall-bounded flow, adopted from Gad-el-Hak [2].

the flow is dominated mostly by the viscous stress in the viscous sublayer. This implies that the only relevant quantities for scaling are the Kinematic viscosity ($\nu$) and the friction velocity ($u_\tau$), see Jimenez [11] and Gad-el-Hak [2]. The buffer layer is where both viscous and turbulence shear stresses are important and the peak production and dissipation of turbulence kinetic energy occur [2]. Jimenez [11] explains further that this layer is home to a non-linear self-sustaining cycle, and its mechanisms involves long longitudinal streaks of high and low streamwise velocity, and shorter quasi-streamwise vortices.

### 1.2.2 Constant Reynolds stress region

In this region, the viscous stresses are negligible and the momentum flux is accomplished nearly entirely by turbulence [2]. Here, the only relevant length scale is the distance from the wall, $y$, and the appropriate velocity scale is is the square root of the nearly constant Reynolds stress, $((-\overline{uv}_{max})^{0.5})$. Thus, the mean velocity gradient may be expressed as

$$\frac{\partial \overline{U}}{\partial y} \approx \frac{(-\overline{uv}_{max})^{0.5}}{y}. \tag{1.1}$$

The well known logarithmic velocity profile follows directly from integrating equation 1.1 and using the velocity at the edge of the viscous sublayer as a boundary condition. This could be expressed as follows

$$\overline{U}^{+} = \frac{1}{\kappa} lny^{+} + A, \tag{1.2}$$

where the plus sign super-index denotes normalization by the viscous length scale ($\nu/u_\tau$), $\kappa$ is the Von Karman constant and A is an additive constant. Hence, this region is generally refereed to as the log region, as shown in Figure 1.2. Based on the observations that the total stress is approximately constant throughout the viscous and the log layers, these regions are also known as the inner layer, see [2].

### 1.2.3 Outer layer

Beyond the log-region, an outer layer is formed and is generally characterized by a diminishing turbulence shear stress [2]. For channel flow, the intermittency of turbulence and interaction with potential free stream are absent. Therefore, the core region of a channel flow differs from the outer layer of a growing boundary layer, see Schlichting [10] and Pope [6]. According to Gad-el-Hak [2] the appropriate length scale in the core region is half the channel height (H) and the mean velocity profile is characterized by the velocity defect ($U_c - \overline{U}$), where $U_c$ is the centre-line velocity at the edge of the shear layer.

## 1.3 Effects of roughness on turbulent channel flow

The best known early work into the effects of roughness are the experiments of Nikuradues, which in turn led to the Colebrook formula and the Moody diagram [10]. The results from these experiments demonstrated that the logarithmic velocity distribution, equation 1.2, could still be used in the wall layer for rough surfaces. This observation led to the concept of equivalent or effective sand roughness which is generally expressed as

$$\overline{U}^{+} = \frac{1}{\kappa} lny^{+} + A - \Delta U^{+}, \tag{1.3}$$

where the first three expressions are from the equation of the smooth wall, equation 1.2, and the last term is an offset usually called the roughness function. The concept of the effective sand roughness and its subsequent extension to the Moody diagram remain a

valuable tool in estimating the friction coefficient, based on the roughness height, for turbulent channel and pipe flows.

In a more recent research, Jimenez [11] showed that roughness affects turbulent channel flow by interfering with the operation of the buffer-layer viscous cycle discussed in the previous section 1.2.1. The main effect is to change the additive constant $A$ in equation 1.2. Also, because most of the turbulent energy is generated within the log layer, roughness may also modify the whole flow if the roughness height is not negligible with respect to the channel height [11]. In addition, subtler affects exist as well. Townsend [15] and Jimenez [11] explain that it has been known for sometime that structures with outer length scales penetrate into the buffer-layer region and suggested that those outer-layer structures grow from hairpin eddies generated near the wall. Jimenez [11] argues further that it is therefore possible that at least some rough walls may influence the whole layer by modifying the form of the hairpins, and the behaviour of the roughness layer in other cases may be directly modified by events coming from outside. Such observations highlighted the limitations of using the similarity hypothesis, a widely used concept in studying the flow over rough surfaces (see section 2.3).

More insight into the effects of roughness in turbulent channel flow was reported in the experiments of Perry et al. [3], see section 2.1. In this work the authors focused on the effects of the distribution of the roughness elements, while keeping the roughness height constant. Based on the results from these experiments, a classification of the flow over rough surfaces was proposed based on the effects that the distribution of the roughness elements has on the mean flow. Perry et al. [3] classified roughness into k- and d- type. The two types are briefly discussed in the following subsections.

### 1.3.1 k- type

This type of roughness is generally encountered when the distribution of the roughness elements is sparse. Generally, this type of behavior was observed for roughness spacing equal to approximately 3-4 times the roughness height, see Perry et al. [3] and Cui et al. [8]. A sketch of the typical flow over a k- type surface is shown in figure 1.3. The flow is generally characterized by the vortex shedding observed between the roughness elements as a result of the separation and attachment occurring in the groove between the roughness elements. It is important to note here that the effective roughness is proportional to the roughness height (k) [3]. Hence the name, k- type roughness.

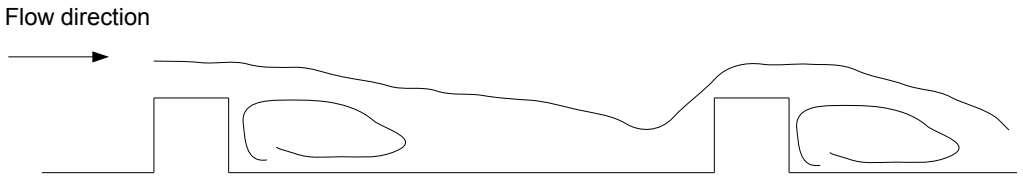


FIGURE 1.3: Sketch of the flow over a k-type rough surface, adopted from Perry et al [3].

### 1.3.2 d- type

For this type of surface, the distribution of the roughness elements is very narrow. Generally this behavior is encountered when the distance between the two elements is 0.5-2 times the roughness height. The sketch shown in figure 1.4 show a typical flow pattern for the flow over a d-type surface. According to Jimenez [11] the usual explanation for this type of behavior is that the grooves sustain stable recirculating vortices that isolate the outer flow from the roughness layer. Perry et al. [3] state that the effective roughness for this type of surface is not proportional to the roughness height but the channel half-height (H) for channel flow or the pipe diameter (d) for the flow in a pipe, hence the name d- type roughness.

## 1.4 Aim and objectives

The main aim of the research is to gain further understanding of the flow mechanics involved in a channel flow with one sided roughness, in particular the flow properties of the so called k- and d- type rough surfaces first proposed by Perry et al [3] and provide insight to some of the open research questions in the topic. The open issues considered

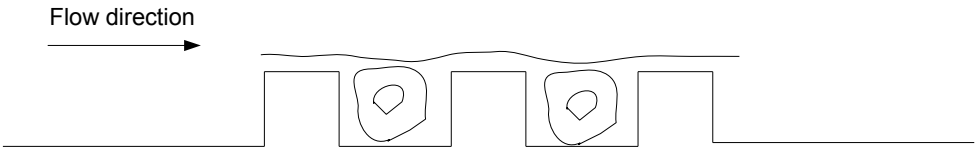


FIGURE 1.4: Sketch of the flow over a d-type rough surface, adopted from Perry et al [3].

in this work are the limitations of the vortex shedding parameter, traditionally used to classify roughness into the k- and d- type, and the effects of the roughness geometry on the interaction between the inner and outer flow regions.

The above aim is achieved through the following objectives:

- To set up verify and validate a CFD methodology for channel flow with one sided roughness and simulations of the effects of roughness geometry;
- Study the flow evolution in time by visualizing the flow field for the following parameters; velocity streamlines, friction velocity, pressure gradient, instantaneous velocity, non-dimensional wall distance $y^+$ and Falco eddies;
- Investigate the effects of the roughness geometry on the coherent structures observed in wall bounded flow using; velocity profile plots at different streamwise locations, plots for the balance of reaction forces in the channel, and the flow visualization data.

Following the achievement of the above objectives, a better understanding of the effects on channel flow would be developed which would be helpful in numerous engineering applications involving surface roughness.

## 1.5 Contribution

The contribution of this research to the topic of turbulent flow over rough surfaces are outlined in the following points:

- During the course of this research, a three-dimensional model of a channel flow with one sided roughness was developed using RANS. The results were published in a conference paper (see appendix D). The paper focused on the drag reduction properties observed in the flow over riblets. This was achieved by comparing the flow characteristics of k-, intermediate, and d- type rough surfaces arranged in the transverse and streamwise directions. This paper provided an opportunity to assess the limitations of using RANS to model this type of flow. Our results showed that RANS could provide reasonable predictive capabilities when considering d-type roughness. This is due to the steady nature of the flow between the roughness elements. However, this was not the case for k- type roughness due to the highly unsteady nature of the flow between the roughness elements. Hence, it became evident that an unsteady solver was required to model the k- type behaviour more accurately.

- Developed an application to carry out Large Eddy simulations based on the Finite Element Method (FEM) using the commercial software COMSOL; Gresho and Sani [16] argue that unlike the Finite Volume Method (FVM), the FEM has not received the same level of attention amongst CFD researchers. The authors [16] attribute this to the historical development of both FEM and FVM in CFD. During the course of this research, it became evident that CFD software based on the FVM method generally include a dedicated LES solver in addition to the traditional turbulence models. Examples include the commercial software Fluent and the open source software OpenFOAM. On the other hand, CFD software based on the FEM does not include a dedicated LES solver. Examples include COMSOL (commercial) and Elmer (open source). This could be seen as a reflection on the current state of development that supports the argument of Gresho and Sani [16]. The motivation behind using the FEM was to emphasize the similarities of the two methods and show that the FEM provide sufficient basis to carry out LES. Our focus here was on an Implicit LES, which is described in detail for the FVM by Grinstein et al [17].

- Provided a generalized verification and validation procedure that could be applied to numerous problems in CFD. A survey of the literature concerned with the verification and validation in CFD, e.g. Oberkampf and Trucnao [18], suggests that the current methods used are insufficient. Specifically the method of qualitative

graphical validation. In this work we used the concept of validation experiments introduced by Oberkampf [19] to assess the uncertainty of the results and quantify the predictive capabilities of the model.

- Given insight into the mechanics involving the interaction between the inner and outer layers and the effects of roughness geometry in turbulent channel flow. According to Gad-el-Hak [2], the interaction between the inner and outer layers remains an open research question in wall bounded flow. The ILES reported here provided an opportunity to investigate this interaction in terms of the roughness elements distribution and geometry. Here we have shown that the interaction is highly influenced by the flow separation and attachment along the rough wall. The results confirmed that the roughness geometry effects are confined to the inner layer and demonstrated that the geometry imposes different flow separation characteristics.

- Proposed the use of k- and d- type classification for engineering design applications. It is the opinion of the author that despite the limitations of the k- and d- type classification, it can still be used as a design parameter in engineering systems to control the flow. Schlichting [10] and Djenidi et al. [20] already showed that d- type roughness could be used to decrease the friction at the wall, and Cui et al. [8] showed that k- type roughness gives the best momentum and heat transfer exchange between the inner/outer layers.

## 1.6 Thesis structure

This thesis is divided into seven chapters. In this chapter we have briefly introduced the problem under investigation. We have shown that despite the advancements in the understanding of wall bounded turbulent flow in recent years, our knowledge of the effects of roughness on wall bounded flow remain incomplete. In chapter 2 we review some of the experimental and numerical work concerned with wall bounded turbulent flow over rough surfaces and discuss the universality of Townsend's similarity hypothesis, which is widely used in rough wall investigations. Chapter 3 starts by describing the theory and implementation of the Finite Element Method used to carry out the numerical simulations. This chapter also includes a description of the model and the developed application, based on the FEM software COMSOL. Chapter 4 focuses on the verification and validation aspects concerned with numerical modelling. Here, a number of procedures are described to ensure the adequacy of our numerical model and validate its predictive capabilities. Results from the numerical simulations are presented in chapter 5. The chapter starts by describing the methods used to collect the data and

then analyses certain key flow parameters. Further discussion of the results is given in chapter 6. First, the predictive capability of the ILES is discussed. Then, a discussion into the coherent structures, roughness classification and effects of roughness geometry is given. All major findings resulting from this research program are summarized and future ideas are presented in chapter 7.

# Chapter 2

# Literature review

This review is intended to present some selected contributions to the study of rough wall turbulence and the roughness classification. Textbooks on the topics of fluid mechanics and turbulent flow generally include a chapter dedicated to internal flow and a section on the effects of roughness, examples include Schlichting [10], White [14] and Young et al. [1]. The classification of roughness into k- and d- type, first proposed by Perry et al. [3], was the subject of a number of research articles, some of which are presented in this chapter. It is important to note here that this review is not an exhaustive one, but rather a selective one. The focus here is to outline the key research milestones and give a brief description of the studies used in the validation of our numerical model. A comprehensive list of literature available on the topic can be found in the review paper of Jimenez [11] or any of the other papers cited in this chapter. In the first two sections we present a brief description of experimental and numerical studies on the topic. In the final section we discuss the universality issues related to Townsend's similarity hypothesis, widely used in rough wall studies.

## 2.1 Experimental work on turbulent flow over rough walls

Perry et al [3] performed tests in a return circuit closed working section wind tunnel type for a range of Reynolds number based on the bulk velocity ($Re_b = 10^3 - 10^6$). A long flat plate was installed in the working section with a standard Prandtl tube placed near the leading edge of the plate in order to obtain a reference dynamic head. A number of two dimensional square roughness elements spaced along the plate were made removable so that an element fitted with pressure-tapped pads could be inserted into the roughness pattern. The pressure pads were made out of brass tubes soldered together and drilled at varying distances up the height of the element. A pair of corresponding tubes from

each side of the element were connected in turn to a manometer enabling the pressure difference profile across the element to be measured. The flow over the rough surfaces was investigated visually using a tufted probe, dye streaks and smoke. The wall shear stress for the boundary layer over the roughness element was evaluated by analysing the control volume around a single element. As mentioned earlier, these experiments were the first to report the classification of rough surfaces into k- and d- type.

Djenidi et al [20] conducted experiments in a closed circuit-constant head vertical water tunnel. On one of the walls, which was removable, a d- type rough surface was mounted. Like the experiment of Perry et al. [3], the d- type rough wall consisted of two dimensional elements of square cross-section. The value of Reynolds number, $Re_\theta$, based on the momentum thickness $\theta$ was about 1000. A 3-component DANTEC fibre optic LDA system was used in forward scatter mode. Only two component measurements were made (two colours, blue and violet, were used), the streamwise velocity was measured with the blue beam and the wall normal velocity was obtained using the violet beam. Enhanced Burst Spectrum Analysers (BSA) were used for processing the photo multiplier signals. The analogue outputs from the BSA were digitized into a computer and stored for subsequent data reduction and analysis. Flow visualizations were carried out using dye injection and filming with high speed video camera. A major outcome of this research is the observation that that d- type roughness occasionally ejects the fluid from the grooves between the roughness elements into the mean flow. This result was a major contradiction to the assumption that the inner and outer regions of the flow are isolated, as proposed by the similarity hypothesis.

Krogstad and Efros [21] preformed hot-wire experiments in an open return wind tunnel on two different rough surfaces, where both roughness geometries belonged to the k-type category. One test surface was made up of a woven stainless steel mesh screen and the second surface consisted of lateral rods. Mean velocities were measured using a pitot tube as well as a number of single and x-wire probes of different geometries, which also provided Reynolds stresses and triple correlations. In this experiment, measurements were made for the Reynolds number $Re_\theta = 12800$. This research addressed the limitations of Townsend's similarity hypothesis in describing the flow over a k- type rough surface for external flows.

## 2.2 Numerical methods to simulate the flow over rough walls

Leonardi et al [22] provided guidelines for modelling a two-dimensional rough wall channel flow using DNS. The flow configuration considered in this study was that of a fully

developed turbulent channel flow with square bars at the bottom wall. The numerical method solved the Navier-Stokes and continuity equations for incompressible flow in the following form:

$$\frac{\partial U_i}{\partial t} + \frac{\partial U_i U_j}{\partial x_j} = -\frac{\partial P}{\partial x_i} + \frac{1}{Re}\frac{\partial^2 U_i}{\partial x_j^2} + \Pi$$

$$\nabla \cdot U = 0$$

where $\Pi$ is the pressure gradient required to maintain a constant flow rate, $U_i$ is the component of the velocity vector in the $i$ direction and $P$ is the pressure. The Navier-Stokes equations has been discretized in an orthogonal coordinate system using the staggered central second-order finite-difference approximation. The discretized system was advanced in time using a fractional-step method with viscous terms treated implicitly and convective terms explicitly. The large sparse matrix resulting from the implicit terms was inverted by an approximate factorization technique. At each time step, the momentum equations were advanced with the pressure at the previous step, yielding an intermediate non-solenoidal velocity field. A scalar quantity $\Phi$ projects the non-solenoidal field onto a solenoidal one. A hybrid low-storage third-order Runge-Kutta scheme was used to advance the equations in time. The roughness was treated by the efficient immersed boundary technique. This approach allows the solution of flows over complex geometries without the need for computationally intensive body-fitted grids. It consists of imposing $U_i = 0$ on body surface which does not necessarily coincide with the grid. To avoid that, the geometry was described in a stepwise way, at the first grid point outside the body, the second derivatives in the Navier-Stokes equations were discretized using the distance between the velocities and the boundary of the body rather than using the mesh size. Periodic boundary conditions were applied in the streamwise and spanwise directions, with no-slip condition at the walls. The DNS of Leonardi et al [23] provided a new interpretation of d- and k- type behaviour by discussing the DNS results for six different roughness spacings at three Reynolds numbers based on the bulk velocity ($Re_b$ = 2800, 7000, 12 000). In this paper, the authors proposed an alternative view to classifying k- and d- type behaviours based on the friction and pressure drags, as opposed to the state of vortex shedding proposed by Perry et al [3].

Cui et al [8] investigated the turbulent flow in a channel with transverse rib roughness on one wall using a Large Eddy Simulation (LES) with a Dynamic sub-grid-scale model

(DSM). The three-dimensional, unsteady, incompressible, filtered continuity and Navier-Stokes equations are solved with a DSM:

$$\frac{\partial \overline{u}_i}{\partial x_i} = 0$$

$$\frac{\partial \overline{u}_i}{\partial t} + \frac{\partial}{\partial x_j}(\overline{u}_i \overline{u}_j) = -\frac{1}{\rho}\frac{\partial \overline{p}}{\partial x_i} + \nu\left(\frac{\partial^2 \overline{u}_i}{\partial x_j \partial x_j}\right) - \frac{\partial \tau_{ij}}{\partial x_j} - \frac{1}{\rho}\frac{\partial P}{\partial x}\delta_{1i}.$$

Here, $i = 1, 2$ and 3, $\overline{u}_i$ are the resolved velocity components (corresponding to $\overline{u}, \overline{v}, \overline{w}$),$\overline{u}_i = u_i - u'$ where $u'$ are sub-grid-scale (SGS) components), $x_i$ are the Cartesian coordinates (corresponding to x, y and z), $\overline{p}$ is pressure, $\nu$ is kinematic viscosity, $\frac{\partial P}{\partial x}$ is the mean pressure gradient imposed in the streamwise direction to drive the flow, $\delta_{1i}$ takes value of one only when $i = 1$, and

$$\tau_{ij} = \overline{u_i u_j} - \overline{u_i}\ \overline{u_j}$$

is the sub-grid-scale stress representing the effect of small-scale motions. Details of the solution of the governing equations using a DSM are given by Cui et al [8]. It is important to note here that a LES based on the FVM was used in this work [8], the general steps involved could be outlined as follows:

- The governing equations in general curvilinear coordinates are discretized on a non-staggered grid;
- A fractional-step method is employed and the pressure Poisson equation derived from the equation of continuity is solved with multi-grid acceleration. Here, time marching is semi-implicit with formal accuracy of second order in both space and time;
- A mean pressure gradient is imposed in the streamwise direction to drive the flow. The imposed gradient is adjusted to keep the Reynolds number based on the bulk velocity $U_b$ and half channel height constant at 10'000 for all the cases.
- Periodic boundary conditions are imposed in both streamwise and spanwise directions. No-slip boundary conditions are applied at the top and bottom channel boundaries.

In this work, the authors [8] demonstrated the predictive capability of LES in resolving the k- and d- type flow patterns and showed that reasonable predictions could be made for the resistance components (friction and pressure drags).

## 2.3 Universality issues

In recent years, universality issues related to the similarity hypothesis have come under scrutiny. The similarity hypothesis suggested by Townsend [15], when considering turbulent shear flow, can be summarized in the following three fundamental hypotheses:

- The first hypothesis is one of similarity of flow structure at all high Reynolds numbers, and it is best expressed in terms of a definite flow system whose boundary conditions can be expressed non-dimensionally in terms of a linear dimension and a velocity;
- The second hypothesis is that of self-preservation and asserts that, at any one Reynolds number, the structure at all sections of the flow at right angles of the direction of the mean flow are similar. This hypothesis, unlike that of Reynolds number similarity, depends on the notion that the flow approaches a state of moving equilibrium which is determined by the broad features of the initial conditions;
- The third hypothesis is a corollary of the second. If a flow is self-preserving through the action of a moving equilibrium, it must be expected that the final self-preserving form will not depend on the details of the boundary conditions of the flow, and that flows whose boundary conditions have similar properties of symmetry and homogeneity will have similar self-preserving flows.

Using experiments, Townsend [15] was able to provide strong evidence that supports the hypothesis of Reynolds number similarity and the inference from it that those parts of the motion that are not directly affected by viscous stresses are independent of the value of the fluid viscosity. The evidence also offers qualified support to the hypothesis of self-preservation and moving equilibrium. By applying these principles to wall bounded flow, Townsend introduced the concept that the turbulent motion close to the wall is always in a condition of dynamical similarity determined by the wall stress and viscosity. This concept is of fundamental importance in the theory of all wall flows, and its principle application is to the treatment of the mean flow problem using the universal mean velocity distribution as a starting point. According to Townsend [15], there is a great deal of experimental evidence in support of this distribution (the law of the wall).

When considering a channel flow with smooth walls, the transfer of momentum from the walls to the fluid takes place by the action of the tangential viscous stresses at the wall. If the walls are not ideally smooth there is a possibility that momentum will be transferred by the action of forces normal to the wall surface and that this transfer may depend weakly, or not at all, on the fluid viscosity. If we consider flow in a definite

channel with walls uniformly covered by roughness elements of small size compared with the width of the channel, arguments similar to Reynolds number similarity can be used to show that that there exists a constant stress layer whose motion is determined by the wall stress, the viscosity, and if geometrically similar roughness considered, the scale length of roughness.

Applying similar analysis to boundary layer flow, Townsend [15] was able to demonstrate that for both channel and boundary layer flows, most of the turbulent energy production and dissipation takes place in a thin layer close to the wall and that the shear stress may be considered constant within it. The flow in this layer is in a state of absolute energy equilibrium, and the motion is determined by the wall stress and viscosity. This inner layer is similar in both flows, however, the outer layer in the boundary layer flow is similar to wake flows. Townsend [15] explains that the turbulent motion in this region is effectively unrestricted and the process of entrainment of the undisturbed fluid outside the layer takes place by a process similar to those observed in wakes and jets. Some studies, see Amir and Castro [24], Flack et al [25] and Jimenez [11] support Townsend's wall similarity hypothesis, which suggests that it is only the inner layer of the order of roughness heights that is affected.

Other investigations, see Krogtad and Erfos [21] and Lee et al.[9], have suggested that the entire boundary layer is affected by the roughness when the roughness geometry is made up of long spanwise bars. Krogstadt and Antonia [26] suggested that the increased inner/outer layer interaction in this case may be important due to significant spanwise correlation along the roughness element, and that the length scales affecting the flow are very limited compared to surfaces made up of three dimensional elements. Lee et al.[27] and Krogstad and Erfos [21] explain that the problem has been further complicated by the observation that the effects may be different for internal and external flow.

Jimenez [11] suggested that part of the controversies observed for turbulent boundary layers may have been caused by lack of scale separation between the roughness length, $k$, and the boundary layer thickness, $\delta$. Based on simple estimates of how the roughness affects the logarithmic layer, it was suggested that for roughness elements not to act as individual obstacles submerged in a boundary layer, there should be a separation of scales between k and $\delta$ of at least $\delta/k > 40$. However, Jimenez [11] also pointed out that experimental evidence indicates that this is an optimistically low limit. The ratio suggested ensures that the roughness elements do not protrude further out than approximately halfway through the logarithmic region in a zero pressure gradient case. Furthermore, the roughness elements must be sufficiently large so that the near wall flow is no longer affected by the viscous sub-layer. With a buffer region extending out to $y^+$ $50-60$ for a smooth wall, the minimum roughness length for a fully developed rough

boundary layer ought to be $k^+ > 50$. Combined with the criterion of $\delta/k > 40$ this implies that the the Reynold's number based on the boundary layer thickness should be $\delta^+ >> 2000$, see [11].

Krogstadt and Antonia [26] studied the effect of spanwise bars on turbulent boundary layers and found significant outer layer effects. They reported that the separation of scale was $\delta/k \approx 47$, which is only slightly higher than the lower limit suggested by Jimenez [11]. In order to investigate how the flow develops and if the $\delta/k$ restriction is satisfied for the same type of surface geometry (k-type), Krogstad and Erfos [21] studied the development of the rough wall boundary layer downstream of a step change in wall condition. Based on first and second order statistics they concluded that after about $\Delta x/\delta_0 = 15$, the inner rough wall layer had grown to the outer edge of the boundary layer. Here, $\delta_0$ is the boundary layer thickness of the smooth wall boundary layer at the step. Further downstream the outer layer appeared to have the same properties as that of a fully developed smooth wall turbulent boundary layer.

Overall, our survey demonstrates that the so called d-type roughness generally adheres to Townsend's similarity hypothesis as demonstrated by Amir and Castro [24], and Jimenez [11]. However, researchers focusing on k-type roughness in external flows suggested a breakdown of this hypothesis , see Lee et al.[27] and Krogstad and Erfos [26].

# Chapter 3

# Theory and modelling

In this chapter we present the theory and modelling of fluid flow in a turbulent channel using the Finite Element Method. In section 3.1 we define the physical system of interest. Sections 3.2 and 3.3 are concerned with the theoretical aspects of modelling fluid flow. Section 3.2 outlines the theory of solving the governing equations of the fluid flow using the standard Galerkin method. This section also describes the theoretical considerations regarding the geometry of the elements used in the discretization of the fluid domain. Section 3.3 describes the theory used in boundary layer approximations including the classification of boundary layers (based on the pressure gradients they impose) and gives the theoretical solution for a boundary layer with zero pressure gradient. The model used to carry out the simulations reported in this research is described in section 3.4. Through the course of this research it became evident that this model provided sufficient basis for a LES. In section 3.5 we present the possibility of developing an Implicit LES using COMSOL. In the final section 3.6 we describe the modelling of the rough surfaces considered in this research.

## 3.1 Physical system of interest

In our analysis we define a system as a set of of physical entities that interact and are observable, where the entities can be a specified quantity of matter or a volume in space. Here, the surroundings are defined as all entities and influences that are physically or conceptually separate from the system. The system considered here is the flow in a channel with one sided roughness, see figure 3.1. Here the system is defined using the geometry, initial conditions and physical modelling parameters. The surroundings are defined using the boundary conditions and system excitation. A specification of the system and surroundings are given as follows; the geometry, shown in figure 3.1,

describes a rectangular domain with height 2H and width 8H. Previous work by Cui et al [8] demonstrated that such a domain is appropriate when considering the flow over rough surfaces. The initial conditions applied throughout are those that describe the velocity field at t=0. Here we assume that the fluid is at rest. The variables that describe the physical modelling parameters are the velocity components (u,v) , the pressure (p) and the fluid viscosity ($\mu$). Following from Jimenez [11], the system of interest here is the buffer layer. For a smooth surface this layer is home to a non-linear self-sustaining cycle, which is responsible for generating most of the turbulent energy in flows with moderate Reynolds number near the wall. The surroundings in this case are the boundary conditions described by $\Gamma_{inflow}$ and $\Gamma_{outflow}$ in figure 3.1. Later on we will sub divide these boundaries into physical and fictitious. Here the surroundings represent the limits of the flow for the smooth wall case. By introducing roughness, we arguably add excitations to the self-sustaining cycle responsible for generating the turbulent energy. Here we consider a channel with one sided roughness in order to study the extent of the roughness effects.

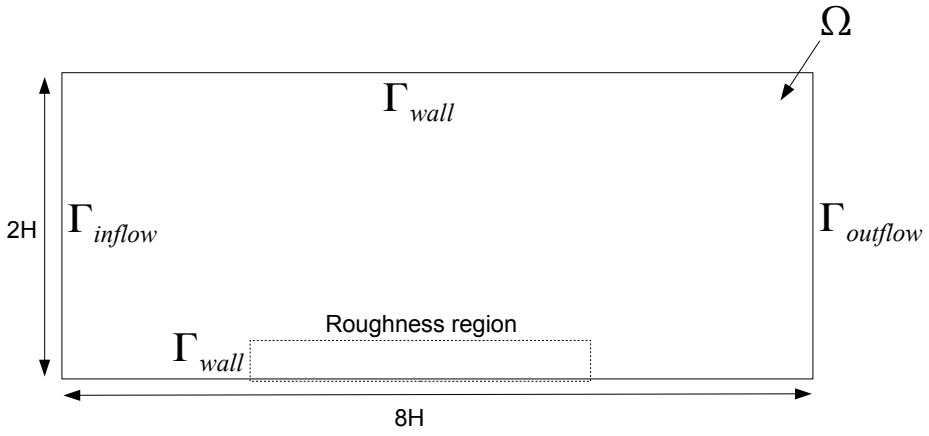


FIGURE 3.1: Sketch of channel flow domain and boundaries (H = 1m).

## 3.2 Navier-Stokes Equations and the Finite Element Method

This section will describe the theory involved with solving the Navier-Stokes equations using the FEM. First we will give a brief derivation of the governing equations in section 3.2.1 including the mathematical formulations of the problem under investigation. In section 3.2.2 we give a brief description of the general approach (Galerkin) used in the FEM to solve the governing equations, full details on the solution of the Navier-Stokes equation using the FEM are given by Cuvelier et al. [4] and Gresho et al [16]. The difficulties that arise from the discretization of the flow domian using the FEM are addressed in sections 3.2.3, 3.2.4 and 3.2.5. Finally, sections 3.2.6 and 3.2.7 will outline the general procedures used to obtain an approximate solution of the unsteady Navier-Stokes equations.

### 3.2.1 Equations of Fluid Dynamics

Here, the equations describing the dynamics of fluid flow will be introduced. We will give only a brief outline of the derivation of the equations from the basic principles of conservation of mass and momentum. For complete derivation of these equations see Landau and Lifshitz [28].

We start by mentioning that will be using the nabla notation

$$\nabla = \begin{vmatrix} \frac{\partial}{\partial x_1} \\ \vdots \\ \frac{\partial}{\partial x_n} \end{vmatrix}.$$

For a scalar function $\phi$, $\nabla\phi$ denotes grad $\phi$; for a vector $\mathbf{u}$, $\nabla \cdot \mathbf{u}$ denotes div $\mathbf{u}$; for a tensor $\underline{\underline{\sigma}}$ with components $\sigma_{ij}$ $(i, j = 1, \cdots, n)$, $\nabla \cdot \underline{\underline{\sigma}}$ denotes vector with components

$$(\nabla \cdot \underline{\underline{\sigma}})_i = \sum_{j=1}^{n} \frac{\partial}{\partial x_j} \sigma_{ij}.$$

The first principle is the conservation of mass which, according to Cuvelier et al [4], can be expressed by;

$$\frac{\partial \rho}{\partial t} + \nabla \cdot (\rho \mathbf{u}) = 0,$$

where $\rho = \rho(\mathbf{x}, t)$ is the fluid density, t the time and $\mathbf{u} = \mathbf{u}(\mathbf{x}, t)$ the velocity vector.

From the balance of momentum, see [4], we obtain

$$\rho\left(\frac{\partial \mathbf{u}}{\partial t} + (\mathbf{u}\cdot\nabla)\mathbf{u}\right) = \nabla\cdot\underline{\underline{\sigma}} + \rho\mathbf{F}, \tag{3.1}$$

where $\underline{\underline{\sigma}}$ is the stress tensor and $\mathbf{F} = \mathbf{F}(\mathbf{x}, t)$ denotes the body forces per unit mass.

Cuvelier et al [4] state that for a fluid it is convenient to regard the stress tensor $\underline{\underline{\sigma}}$ as the sum of an isotropic part ($p\underline{\underline{I}}$), having the same form of the stress tensor for a fluid at rest with a hydrostatic pressure $p$, and a remaining non-isotropic part ($\underline{\underline{D}}$), termed the deviatoric stress tensor caused entirely by the fluid motion:

$$\underline{\underline{\sigma}} = -p\underline{\underline{I}} + \underline{\underline{D}} \quad \text{with} \quad \underline{\underline{I}} \;=\; \text{unit tensor.}$$

To deduce the dependence of the deviatoric stress tensor on the local velocity gradients, it is assumed that $D_{ij}$ is a linear function of the various components of the velocity gradients and that the fluid is isotropic. Such a fluid is called a Newtonian fluid, see [4], and its constitutive relation reads:

$$\underline{\underline{D}} = 2\mu\left(\underline{\underline{e}} - \frac{1}{3}(\nabla\cdot\mathbf{u})\underline{\underline{I}}\right) \quad \text{with} \quad e_{ij} = \frac{1}{2}\left(\frac{\partial u_i}{\partial x_j} + \frac{\partial u_j}{\partial x_i}\right),$$

in which $\underline{\underline{e}}$ is the symmetrical part of the velocity gradient tensor, known as the rate of strain tensor, and $\mu$ is the fluid viscosity depending on temperature $T(\mathbf{x}, t)$. Substitution into the momentum equation 3.2 then gives for the velocity

$$\rho\left(\frac{\partial \mathbf{u}}{\partial t} + (\mathbf{u}\cdot\nabla)\mathbf{u}\right) = \rho\mathbf{F} - \nabla p + \nabla\cdot\left[2\mu(\underline{\underline{e}} - \frac{1}{3}(\nabla\cdot\mathbf{u})\underline{\underline{I}})\right].$$

These equations are known as the Navier-Stokes equations for fluid motion. Assuming the flow is incompressible and independent of temperature the Navier-Stokes equations reduce to

$$\rho\left(\frac{\partial \mathbf{u}}{\partial t} + \mathbf{u}\cdot\nabla\mathbf{u}\right) = \rho\mathbf{F} - \nabla p + \mu\nabla^2\mathbf{u}.$$

With the assumptions above, the equations of motion reduce to

$$\begin{aligned} &\nabla\cdot\mathbf{u} = 0 \\ &\rho\left(\tfrac{\partial \mathbf{u}}{\partial t} + \mathbf{u}\cdot\nabla\mathbf{u}\right) = \rho\mathbf{F} - \nabla p + \mu\nabla^2\mathbf{u}. \end{aligned}$$

To this system of partial differential equations, which according to Cuvelier et al [4] is parabolic in $\mathbf{u}$ , we add initial conditions

$$\mathbf{u}(\mathbf{x}, 0) = \mathbf{u}^0(\mathbf{x}) \ , \ \mathbf{x} \in \Omega \cup \Gamma$$

and boundary conditions of which we only consider Dirichlet and Neumann type in 2D. Cuvelier et al. [4] state that for $\mathbf{u}$ we can prescribe one or two velocity components on $\Gamma$ (Dirichlet boundary condition):

$$u_i \text{ prescribed on } \Gamma, \ t \geq 0$$

or one or two Neumann conditions which are conditions for the normal and/or tangential components of stress:

$$\sigma_n \equiv (\underline{\underline{\sigma}} \cdot \mathbf{n}) \cdot \mathbf{n} = \sum_{i,j=1}^{2} \sigma_{ij} \, n_i \, n_j = \text{normal stress},$$

$$\text{prescribed} \quad \text{on } \Gamma, \ t > 0,$$

$$\sigma_t \equiv (\underline{\underline{\sigma}} \cdot \mathbf{n}) \cdot \mathbf{t} = \sum_{i,j=1}^{2} \sigma_{ij} \, n_i \, t_j = \text{tangential stress},$$

$$\text{prescribed} \quad \text{on } \Gamma, \ t > 0,$$

where $\mathbf{n}$ is the unit normal and $\mathbf{t}$ is the unit tangent on $\Gamma$ as shown in figure 3.2.

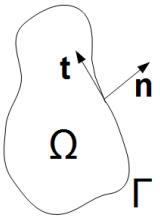


FIGURE 3.2: Fluid region $\Omega$ and boundary $\Gamma$ showing unit normal ($\mathbf{n}$) and tangential ($\mathbf{t}$) adopted from Cuvelier et al. [4].

Finally, the time dependent version of the Navier-Stokes equations for incompressible flow could be stated as follows:

Find $\mathbf{u} = \mathbf{u}(\mathbf{x}, t)$ and $p = p(\mathbf{x}, t)$, $\mathbf{x} \in \Omega \cup \Gamma$ , $t \geq 0$
such that
$\nabla \cdot \mathbf{u} = 0$
$\rho \left( \frac{\partial \mathbf{u}}{\partial t} + \mathbf{u} \cdot \nabla \mathbf{u} \right) = \rho \mathbf{F} - \nabla p + \mu \nabla^2 \mathbf{u}$
with boundary conditions for $\mathbf{u}$ on $\Gamma$ for $t > 0$ and initial
conditions for $\mathbf{u}$ in $\Omega \cup \Gamma$ at $t = 0$.

### 3.2.2 FEM General Approach

Cuvelier et al. [4] state that for a 2D flow field in a Cartesian co-ordinate system the equations of motion reduce to the momentum equation

$$\rho \frac{\partial u_i}{\partial t} - \mu \nabla^2 u_i + \rho \left( u_1 \frac{\partial u_i}{\partial x_1} + u_2 \frac{\partial u_i}{\partial x_2} \right) + \frac{\partial p}{\partial x_i} = \rho F_i, \quad i = 1, 2. \tag{3.2}$$

Together with the continuity equation

$$\frac{\partial u_1}{\partial x_1} + \frac{\partial u_2}{\partial x_2} = 0. \tag{3.3}$$

Furthermore, the authors [4] show that the non-dimensional form of equation 3.2 could be written as

$$\frac{\partial u_i}{\partial t} - \frac{1}{Re} \nabla^2 u_i + u_1 \frac{\partial u_i}{\partial x_1} + u_2 \frac{\partial u_i}{\partial x_2} + \frac{\partial p}{\partial x_i} = \rho F_i, \quad i = 1, 2. \tag{3.4}$$

To obtain a unique solution for equations 3.3 and 3.4 it is necessary to give both initial and boundary conditions. The initial conditions consist of a given velocity at the initial time $t = 0$ prescribed as follows

$$u_i(\mathbf{x}, t) = u_i^0(\mathbf{x}), i = 1, 2. \tag{3.5}$$

It is important to mention that the initial velocity field $u_i^0(\mathbf{x})$ must satisfy the incompressibility constraint (equation 3.3).

Throughout this section Dirichlet boundary conditions are assumed:

$$u_i(\mathbf{x}, t) = g_i(\mathbf{x}, t), \mathbf{x} \in \Gamma, i = 1, 2. \tag{3.6}$$

Cuvelier et al. [4] states that it is easy to verify that the pressure in this case is fixed up to an additive function of time (not space) i.e:

$$p(x,t) = p_c(x,t) + c(t).$$

In order to prescribe the function $c(t)$ we demand:

$$\int_\Omega p \; d\Omega = 0, \text{for all } t. \tag{3.7}$$

For the solution of equations 3.3 and 3.4 with the initial (equation 3.5) and boundary (equation 3.6) conditions the Galerkin method is applied. To this end equation 3.4 is multiplied by arbitrary, time dependent, test functions $v_i$ and the continuity equation 3.3 by test function $q$, see [4]. Integration over the domain results in:

$$\int_\Omega \frac{\partial u_i}{\partial t} v_i \; d\Omega + \int_\Omega \left[ -\frac{1}{Re}\nabla^2 u_i + u_1 \frac{\partial u_i}{\partial x_1} + u_2 \frac{\partial u_i}{\partial x_2} + \frac{\partial p}{\partial x_i} \right] v_i \; d\Omega = \int_\Omega f \; v_i \; d\Omega, \tag{3.8}$$

and

$$\int_\Omega q \left( \frac{\partial u_1}{\partial x_1} + \frac{\partial u_2}{\partial x_2} \right) \; d\Omega = 0 \tag{3.9}$$

Application of Gauss theorem, see [4], gives:

$$\int_\Omega \frac{\partial u_i}{\partial t} v_i \; d\Omega + \int_\Omega \left[ \frac{1}{Re}(\nabla u_i \cdot \nabla v_i) + (u_1 \frac{\partial u_i}{\partial x_1} + u_2 \frac{\partial u_i}{\partial x_2}) v_i \right] \; d\Omega - \int_\Omega p \frac{\partial v_i}{\partial x_i} \; d\Omega = \int_\Omega f_i \; v_i \; d\Omega + \int_\Gamma (\nabla \mathbf{u}_i \cdot \mathbf{n}) v_i \; d\Gamma - \int_\Gamma p \; v_i \; n_i \; d\Gamma, i = 1, 2$$

and

$$\int_\Omega q \; div \; \mathbf{u} \; d\Omega = 0.$$

According to Cuvelier et al. [4] the boundary integrals vanish due to the boundary condition:

$$u_i(\mathbf{x}) = 0, \mathbf{x} \in \Gamma. \tag{3.10}$$

For the weak formulation of the problem (equations 3.3 to 3.7)the function spaces $\mathbf{V}_0$, $\mathbf{V}_g$ and $Q$ are introduced:

- $\mathbf{V}_0$ is the space of vector functions $\mathbf{v} = (v_1, v_2)$ satisfying equation 3.10.
- $\mathbf{V}_g$ is the space of vector functions $\mathbf{v} = (v_1, v_2)$ satisfying equation 3.7.
- $Q$ is the space of functions satisfying equation 3.9.

Then the weak formulation of the problem reads:

Find $\mathbf{u}(t) \in V_g$ and $p(t) \in Q$ such that

$$\int_\Omega \frac{\partial u_i}{\partial t} v_i \, d\Omega + \int_\Omega \left[ -\frac{1}{Re}(\nabla u_i \cdot \nabla v_i) + (u_1 \frac{\partial u_i}{\partial x_1} + u_2 \frac{\partial u_i}{\partial x_2}) v_i \right] d\Omega - \int_\Omega p \frac{\partial v_i}{\partial x_i} \, d\Omega = \int_\Omega F_i \, v_i \, d\Omega, \text{ and} \tag{3.11}$$

$$\int_\Omega q \, div \, \mathbf{u} \, d\Omega = 0. \tag{3.12}$$

For all $\mathbf{v} \in \mathbf{V}_0$ and all $q \in Q$.

For the construction of the approximation of the solution, $u_1, u_2$ and $p$ are written as linear combinations of time-independent basis functions with time-dependent coefficients, see [4]:

$$u_i(\mathbf{x}, t) = u_{i0}(\mathbf{x}, t) + \sum_{j=1}^{\infty} u_{ij}(t) \, \phi_j(\mathbf{x}),$$

$$p(\mathbf{x}, t) = \sum_{j=1}^{\infty} p_j \, (t) \, \psi_j \, (\mathbf{x}),$$

with

$$u_{i0}(\mathbf{x}, t) = g_i(\mathbf{x}, t), \ \mathbf{x} \in \Gamma.$$

The basis functions $\phi_i$ are substituted for the test function $v_i$ (see equation 3.11) and the test function $q$ is replaced by $\psi_i$ (see equation 3.12). According to Cuvelier et al. [4] if we limit ourselves to approximate solutions, constructed by a finite number of basis

functions i.e:

$$\widetilde{u}_i(\mathbf{x},t) = \widetilde{u}_{i0}(\mathbf{x},t) + \sum_{j=1}^{\infty} u_{ij}(t)\ \phi_j(\mathbf{x}),$$

$$\widetilde{p}(\mathbf{x},t) = \sum_{j=1}^{\infty} p_j\ (t)\ \psi_j\ (\mathbf{x}),$$

then the following system of Galerkin equations remain:

$$\int_\Omega \frac{\partial \widetilde{u}_1}{\partial t}\phi_i\ d\Omega + \int_\Omega \left[-\frac{1}{Re}(\nabla \widetilde{u}_1 \cdot \nabla \phi_i) + (\widetilde{u}_1 \frac{\partial \widetilde{u}_1}{\partial x_1} + \widetilde{u}_2 \frac{\partial u_1}{\partial x_2})\phi_i\right]\ d\Omega - \int_\Omega \widetilde{p}\ \frac{\partial \phi_i}{\partial x_1}\ d\Omega = \int_\Omega F_1\ \phi_i\ d\Omega, i = 1, 2, \cdots, N.$$

$$\int_\Omega \frac{\partial \widetilde{u}_2}{\partial t}\phi_i\ d\Omega + \int_\Omega \left[-\frac{1}{Re}(\nabla \widetilde{u}_2 \cdot \nabla \phi_i) + (\widetilde{u}_1 \frac{\partial \widetilde{u}_2}{\partial x_1} + \widetilde{u}_2 \frac{\partial u_2}{\partial x_2})\phi_i\right]\ d\Omega - \int_\Omega \widetilde{p}\ \frac{\partial \phi_i}{\partial x_1}\ d\Omega = \int_\Omega F_2\ \phi_i\ d\Omega, i = 1, 2, \cdots, N.$$

$$\int_\Omega \psi_i \left(\frac{\partial \widetilde{u}_1}{\partial x_1} + \frac{\partial \widetilde{u}_2}{\partial x_2}\right)\ d\Omega = 0, i = 1, 2, \cdots, M.$$

In matrix-vector notation the above system could be written as:

$$\begin{aligned} M\ \dot{\mathbf{u}} + S\ \mathbf{u} + N(\mathbf{u})\ \mathbf{u} + L^T \mathbf{p} &= \mathbf{F}, \\ L\ \mathbf{u} &= 0, \end{aligned} \tag{3.13}$$

where S is the diffusion matrix, N is the convective matrix, L is the continuity matrix, $\mathbf{u}$ is the velocity vector, $\mathbf{p}$ is the pressure vector and $\mathbf{F}$ is the right hand side vector which contain all the contribution of the source term, the boundary integrals as well as the contribution of the prescribed boundary conditions. Here M is the so called mass matrix, for 2D it can be expressed as:
$\begin{bmatrix} M_1 & 0 \\ 0 & M_1 \end{bmatrix}$ where

$$M_1\ (i,j) = \int_\Omega \phi_i\ \phi_j\ d\Omega \text{ and } \dot{\mathbf{u}} = \frac{\partial \mathbf{u}}{\partial t}.$$

Note that vectors **u** and **p** depend on time. Also, the solution of the above system of equations 3.13 introduces two difficulties. Firstly, the non-linearity of the equations require some iterative procedure to reach a solution. This will be addressed in the treatment of non-linear terms sections. Secondly, the expression of the continuity equation does not contain the unknown pressure, which introduces a number of extra complications that will be discussed in the necessary conditions for the elements and admissible elements sections.

### 3.2.3 Treatment of the non-linear terms

In order to solve the system of non-linear equations 3.13, an iterative procedure is necessary, see [4]. The most common type of such procedure is based on Newton methods. Here, the Newton method was used to first linearise the the non-linear differential equations and then to discretize the resulting linear equations. Since it is the non-linear terms in the equations of motion we are interested in we consider only the convective terms. After linearisation of the convective terms the standard Galerkin method maybe applied, resulting in a system of linear equations. An important question with respect to iterative methods is how to find a good initial estimate, see [4]. In our analysis we started with a low Reynolds number, as the initial estimate and increased it gradually until the iteration process no longer converges. Such a process is generally called a continuation method, see [4].

### 3.2.4 Necessary conditions for the elements

So far we have derived the standard Galerkin method and showed that it results in a system of non-linear equations of the form given in equations 3.13. After linearisation, this system can be written as, see [4]:

$$\begin{aligned} \mathbf{SU} + \mathbf{N}(\mathbf{U}^k) - \mathbf{L}^T\mathbf{P} &= \mathbf{F}, \\ \mathbf{LU} &= 0, \end{aligned}$$

where $\mathbf{U}^k$ is the solution of the previous iteration. Cuvelier et al. [4] state that it is necessary for the velocity that the approximations over the element-sides must be continues, whereas the pressure approximations may be discontinues. However, as discussed earlier, the issue that the continuity equation ($\mathbf{LU} = 0$) does not contain the pressure unknowns remains to be resolved. The authors [4] explain that when using the FEM, we have to demand that the pressure unknowns never exceed the velocity unknowns and that this demand should be valid independently of the number of elements. This demand restricts the number of applicable elements considerably. In order to satisfy this

criterion, a generaly accepted rule is that the order of approximation of the pressure must be one lower than the order of approximation of the velocity, see [4].

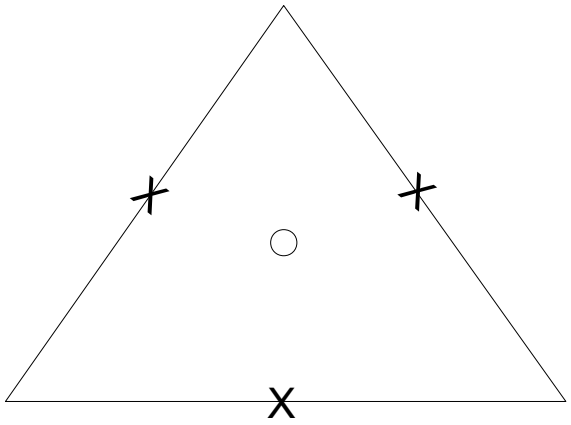

FIGURE 3.3: Example of an admissible triangular element (O=Pressure, X=Velocity), adopted from Cuvelier et al. [4].

Figure 3.3 shows an example of an admissible triangular element from [4]. In this example the velocity unknowns are positioned in the mid-points of the sides. The velocity approximation is linear but not continuous over the element boundaries. Cuvelier et al [4] state that such an element is called non-conforming, and for this reason introduces extra problems with the approximation. This will be addressed next, however, with regard to the continuity equation the element satisfies the demand that there most be more velocity unknowns than pressure unknowns.

### 3.2.5 Admissible elements

For two-dimensional applications the Taylor-Hood family of elements are characterized by the fact that the pressure is continuous across the element [4]. A typical example is a quadratic triangle, shown in figure 3.4, where the velocity is approximated by a quadratic polynomial and the pressure by a linear polynomial. The quadrilateral counterpart of this triangle is shown in figure 3.5.

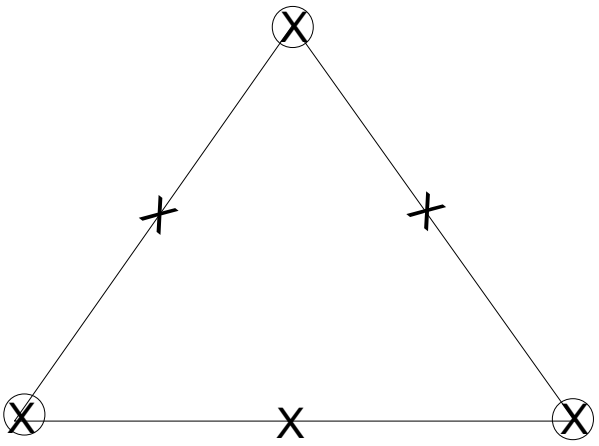

FIGURE 3.4: Taylor-Hood element, $P_2 - P_1$. [O=Pressure (Linear;3 nodal points), X=Velocity (Quadratic;6 nodal points)], adopted from Cuvelier et al. [4].

This type of elements is very suitable for the Galerkin method. The triangular and quadrilateral elements described here were used throughout this work to discretize the fluid domain.

### 3.2.6 Solution of the system of linear equations

So far, we have shown that in each step of the non-linear iteration process it is necessary to solve a system of linear equations of the shape:

$$\mathbf{Su} - \mathbf{L}^t\mathbf{p} = \mathbf{F},$$
$$\mathbf{Lu} = 0.$$

Here **Su** denotes the discretization of both the viscous terms and the linearised convective terms. Cuvelier et al [4] states that if the unknowns are numbered in the following sequence; first all velocity unknowns and then all the pressure unknowns, it is clear that the system of equations gets the shape as sketched in figure 3.6 provided an optimal nodal point numbering is applied. Unfortunately this numbering is far from optimal as the total profile is still very large, see [4]. A much smaller profile may be achieved if pressure and velocity unknowns are intermixed [4]. Figure 3.7 shows a typical example

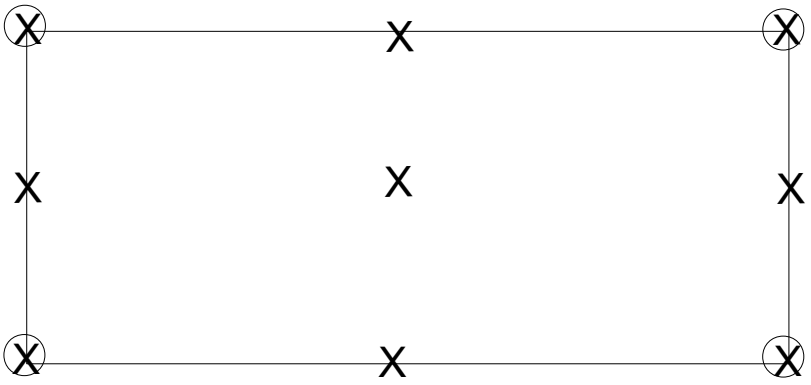

FIGURE 3.5: Taylor-Hood element, $Q_2 - Q_1$. [O=Pressure (Bi-linear;4 nodal points), X=Velocity (Bi-quadratic;9 nodal points)], adopted from Cuvelier et al. [4].

of such numbering. Component-wise renumbering of the sequence of unknowns is given by:

Degrees of freedom: $u_{11}, u_{12}, u_{13}, \cdots ; u_{21}, u_{22}, u_{23}, \cdots ; p_1, p_3, \cdots$

Nodal point-wise renumbering is given by:

Degrees of freedom: $u_{11}, u_{12}, p_1, u_{12}, u_{22}, u_{13}, u_{23}, p_3, \cdots$

According to Cuvelier et al [4], the resulting system of equations has a much smaller profile than the one for the original system of equations.

### 3.2.7 Solution of the Navier-Stokes equations using the pressure correction method

According to Cuvelier et al. [4] the absence of a time-derivative from the linearised equations 3.13 has the consequence that equations must be satisfied in every stage of the time integration. An important consequence is that, if the equations are solved in a coupled way explicit methods do not make sense [4]. With respect to the time-integration, all the classical methods may be used. Of course, the solution of the coupled equations introduces the same problems as for the steady case. As a consequence the

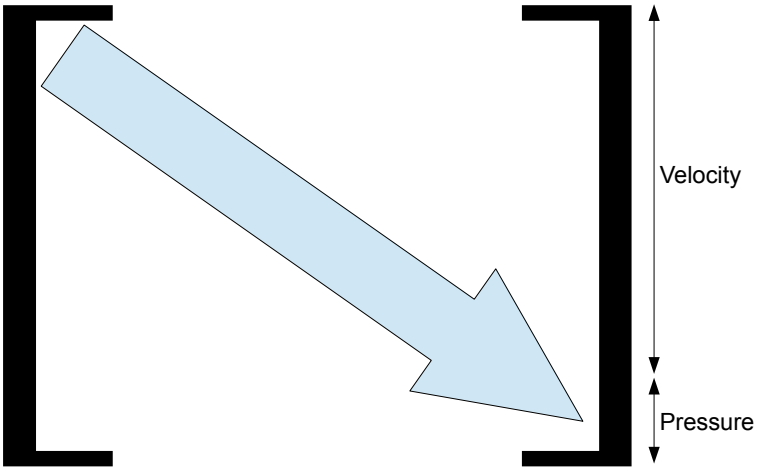


FIGURE 3.6: Profile of the large matrix used to solve the system of linear equations, adopted from Cuvelier et al. [4].

same type of solution procedure will be used. Hence it is quite usual to apply a segregated formulation in order to solve these equations. The formulation used in this work is the pressure-correction method.

Cuvelier et al. [4] states that the pressure correction method is a special method for incompressible flows, the general procedure used here, see Guermond et al. [29], could be outlined as follows:

Let $\mathbf{u}$ and $p$ be the velocity and pressure variables and $\mathbf{u}_c$ and $p_c$ the corrected velocity and pressure variables, respectively. The pressure correction algorithm solves the Navier-Stokes equations using the following steps:

1. Solve the sequence for all $\mathbf{u}$ components using the following equation:

$$\rho\frac{\partial \mathbf{u}}{\partial t} + \rho \mathrm{u}_c^n \cdot \nabla \mathbf{u}^{n+1} = -\nabla p^n + \nabla \cdot \left(\mu(\nabla \mathbf{u}^{n+1}) + (\nabla \mathbf{u}^{n+1})^T\right) + \mathbf{F},$$

   where the superscript index stands for the time step index, and $\rho\frac{\partial \mathrm{u}}{\partial t}$ is discretized using a Backward Differentiation Formula (BDF) method up to the second order where $\mathbf{u}$ values from previous time steps are replaced by $\mathbf{u}_c$ values. At the first

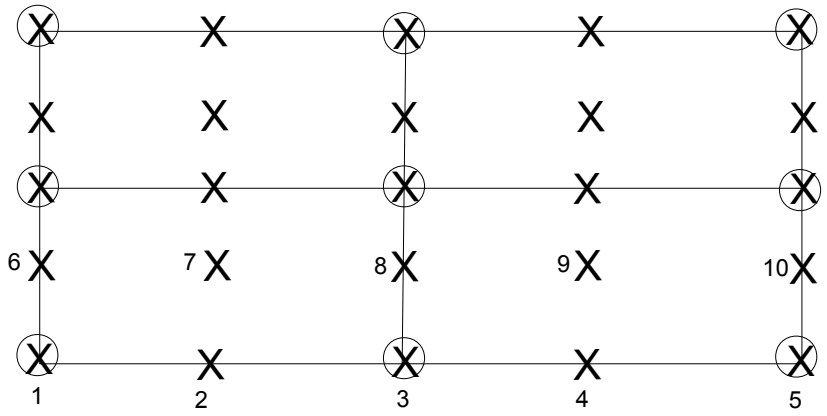


FIGURE 3.7: An example of component-wise numbering applied to a quadrilateral element, adopted from Cuvelier et al. [4].

order it is discretized it reads:

$$\frac{\mathbf{u}^{n+1} - \mathbf{u}_c}{timestep}.$$

2. Solve Poisson's equation to adjust pressure:

$$timestep\Delta(p^{n+1} - p^n) = -\nabla \cdot \rho \mathbf{u}^{n+1},$$

where $\Delta$ is the Laplace operator.

3. Update the corrected velocity:

$$\mathbf{u}_c^{n+1} = \mathbf{u}^{n+1} - \frac{timestep}{\rho}\nabla(p^{n+1} - p^n). \tag{3.14}$$

This type of method is known as a segregated method. Several variants of the original version have been developed (see Guermond et al. [29]). we note here that COMSOL uses incremental pressure-correction schemes. In the next section we will give a general description of the approach used for boundary layer approximation.

## 3.3 Boundary layer approximation

In the previous section we have described the general approach for solving the unsteady Navier-Stokes equations using the FEM. In this section we give a brief description of the theory considering the approximation of boundary layers in channel flow. Before describing the theory involving boundary layer approximations, we would like to point out that the description presented in this section is only a brief one, full details are given by Tritton [5]. Let us confine our attention to the two dimensional, steady boundary layers to illustrate the general principles involved. Here we consider the boundary layer forming on a flat wall (with the x-coordinate in the flow direction and y normal to the wall), as shown in figure 3.8. A free-stream velocity outside the the boundary layer is prescribed as a function of x.

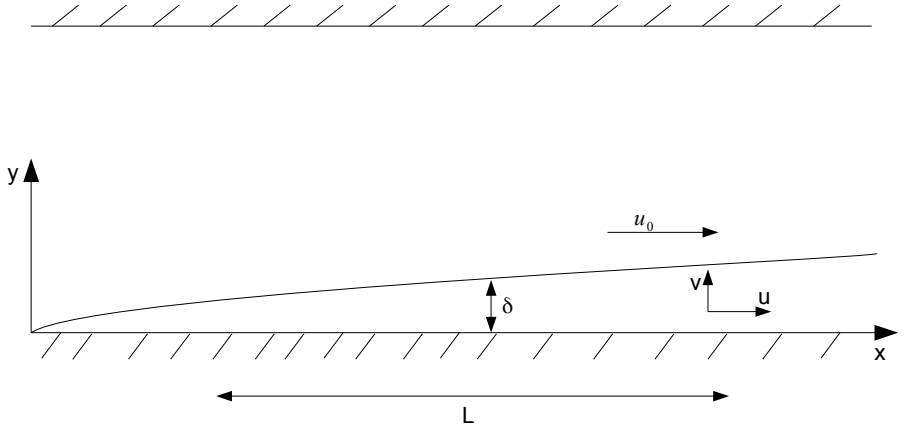


FIGURE 3.8: Sketch showing the boundary layer formation in channel flow.

We denote the free-stream velocity by $u_0$ and the pressure associated with it by $p_0$. We take the boundary layer to have a length scales $L$ and $\delta$ in the x- and y- directions. It is expected that that the velocity scales will also be different in different directions and we denote the scales of $u$ and $v$ by $U$ and $V$. Similarly, the order of magnitude of

the pressure differences across the boundary layer in the y- direction may not be the same as the order of magnitude to the imposed pressure difference outside the boundary layer; we denote the scales of the former by $\Lambda$ and the scale of the latter by $\Pi$. We now consider each of the governing equations in turn, labelling the terms with their orders of magnitude.

The continuity equation is

$$\begin{gathered}\frac{\partial u}{\partial x}+\frac{\partial v}{\partial y}=0 \\ \frac{U}{L}\ \frac{V}{\delta}\ .\end{gathered} \tag{3.15}$$

The two terms must be of the same order of magnitude; fluid entering or leaving the boundary layer at its outer edges must be associated with variations in the amount of fluid traveling downstream within the boundary layer,

$$V \sim U\delta/L; \tag{3.16}$$

Hence, the velocity component normal to the wall is small compared with the rate of downstream flow when the boundary layer is thin.

The x-component of the Navier-Stokes equation is:

$$\begin{gathered}u\frac{\partial u}{\partial x}+v\frac{\partial u}{\partial y}=-\frac{1}{\rho}\frac{\partial p}{\partial x}+\nu\frac{\partial^2 u}{\partial x^2}+\nu\frac{\partial^2 u}{\partial y^2} \\ \frac{U^2}{L}\frac{VU}{\delta}\sim\frac{U^2}{L}\quad\frac{\Pi}{\rho L}\ \frac{\nu U}{L^2}\ \frac{\nu U}{\delta^2}.\end{gathered} \tag{3.17}$$

The second expression for the order of magnitude of $v\frac{\partial u}{\partial y}$ has been written using relation 3.16. The two parts of the inertia term are comparable with one another, the smallness of $V/U$ compensating for the more rapid variation of $u$ with y than x. The two parts of the viscous term are however of different sizes when $\delta/L$ is small, and $\nu\frac{\partial^2 u}{\partial x^2}$ may be neglected.

The y-component of the Navier-Stokes equation is:

$$\begin{gathered}u\frac{\partial v}{\partial x}+v\frac{\partial v}{\partial y}=-\frac{1}{\rho}\frac{\partial p}{\partial y}+\nu\frac{\partial^2 v}{\partial x^2}+\nu\frac{\partial^2 v}{\partial y^2} \\ \frac{UV}{L}\sim\frac{U^2\delta}{L^2}\quad\frac{V^2}{\delta}\sim\frac{U^2\delta}{L^2}\quad\frac{\Lambda}{\rho\delta}\quad\frac{\nu V}{L^2}\sim\frac{\nu U\delta}{L^3}\quad\frac{\nu V}{\delta^2}\sim\frac{\nu U}{L\delta}.\end{gathered} \tag{3.18}$$

In both equations the pressure term will be of the same order of magnitude as the largest of the other terms. This gives:

$$\Pi/\rho L \sim U^2/L \sim \nu U/\delta^2 \tag{3.19}$$

$$\Lambda/\rho\delta \sim U^2\delta/L^2 \sim \nu U/L\delta \tag{3.20}$$

and so

$$\Lambda/\Pi \sim \delta^2/L^2. \tag{3.21}$$

The pressure differences across the boundary layer are much smaller than those in the x-direction. Accordingly, at any value of y the difference between $(1/\rho)\partial p/\partial x$ and $(1/\rho)dp_0/dx$ is much smaller than the significant terms in equation 3.18 and we may replace the former by the latter giving

$$u\frac{\partial u}{\partial x} + v\frac{\partial u}{\partial y} = -\frac{1}{\rho}\frac{dp_0}{dx} + \nu\frac{\partial^2 u}{\partial y^2}. \tag{3.22}$$

Outside the boundary layer there is no variation with y and

$$u_0\frac{du_0}{dx} = -\frac{1}{\rho}\frac{dp_0}{dx}, \tag{3.23}$$

a result which could also be obtained from Bernoulli's equation. Hence,

$$u\frac{\partial u}{\partial x} + v\frac{\partial u}{\partial y} = u_0\frac{du_0}{dx} + \nu\frac{\partial^2 u}{\partial y^2}. \tag{3.24}$$

This equation together with

$$\frac{\partial u}{\partial x} + \frac{\partial v}{\partial y} = 0 \tag{3.25}$$

constitute the boundary layer equations-two equations in the two variables $u$ and $v$.

### 3.3.1 Classification of boundary layers

Solutions of equations 3.24 and 3.25 requires $u_0(x)$ to be specified, both to give the the third term in 3.24 and as a boundary condition for integration with respect to y. This is why the solution of Euler's equation for the particular configuration is needed before the boundary layer can be analysed. Obviously, many different distributions of $u_0(x)$ can arise. In the next section we shall consider the simplest case of all, when $u_0$ is constant. A useful broad classification is given by the sign of $du_0/dx$ or, equivalently

through equation 3.23, the sign of $dp_0/dx$. When

$$du_0/dx > 0 \ ; \ dp_0/dx < 0 \tag{3.26}$$

(the external flow is accelerating at the pressure decreases) one talks of a boundary layer in a favorable pressure gradient. When

$$du_0/dx < 0 \ ; \ dp_0/dx > 0 \tag{3.27}$$

(the external flow is decelerating as the pressure rises) one talks of an adverse pressure gradient. One can, of course, have regions of each type of pressure gradient within a given flow. Indeed, this is usually the case for the boundary layer on an obstacle.

Boundary layers in favorable pressure gradients are relatively thin. In a region of strong enough pressure gradient the boundary layer thickness can decrease with distance downstream; the effect of the pressure gradient more than counteracts the viscous spreading process. Here we note also that instability, leading to transition to turbulence, is delayed by a favorable pressure gradient. Such a pressure gradient does not, however, introduce flow phenomena qualitatively different from those occurring in boundary layers with zero pressure gradient. The effects of an adverse pressure gradient are just the reverse of those just described. Much more significantly, however, a boundary layer in such a pressure gradient is prone to the phenomena of separation. It should be noted that the effect of separation can be to modify the solution of Euler's equation of the region outside the boundary layer. Consequently, $u_0(x)$ may differ from the form that one initially assumes.

### 3.3.2 Zero Pressure Gradient (ZPG) solution

The simplest, and in a sense most fundamental, case is the one where the pressure gradient is zero. Equivalently, $u_0$ is constant; we consider the boundary layer beneath a uniform flow. Such a boundary layer is readily observed on a thin flat plate set up parallel to the free-stream; one wall of an empty wind-tunnel or water-channel is sometimes used. The equations for this case are:

$$u\frac{\partial u}{\partial x} + v\frac{\partial u}{\partial y} = \nu\frac{\partial^2 u}{\partial y^2} \tag{3.28}$$

$$\frac{\partial u}{\partial x} + \frac{\partial v}{\partial y} = 0 \tag{3.29}$$

with boundary conditions:

$$u = v = 0 \; at \; y = 0$$
$$u \to u_0 \; as \; y \to \infty. \tag{3.30}$$

We look for a solution of the form:

$$u = u_0 g(y/\Delta) \tag{3.31}$$

where $\Delta$ is a function of x. That the solution should be of this form is an assumption. It corresponds to the velocity profile having the same shape at all values of x, although with a different scale in the y-direction, and is thus physically plausible. $\Delta$ is directly proportional to the boundary layer thickness, but it is convenient to define it slightly differently from $\delta$.

Equation 3.29 can be satisfied by introducing a stream function $\psi$ such that

$$u = \partial\psi/\partial y \; , \; v = -\partial\psi/\partial x. \tag{3.32}$$

If we take

$$\psi = u_0 \Delta f(y/\Delta) \tag{3.33}$$

then 3.32 gives 3.31 as required with

$$g = f' \tag{3.34}$$

where the prime indicates differentiation with respect to

$$\eta = y/\Delta. \tag{3.35}$$

The second of term equation 3.32 also gives

$$v = u_0(-f + yf'/\Delta)d\Delta/dx \tag{3.36}$$

and further differentiation leads to

$$\frac{\partial u}{\partial x} = -\frac{u_0 y f''}{\Delta}\frac{d\Delta}{dx} \; ; \; \frac{\partial u}{\partial y} = \frac{u_0 f''}{\Delta} \; ; \; \frac{\partial^2 u}{\partial y^2} = \frac{u_0 f'''}{\Delta^2}. \tag{3.37}$$

Substitution into equation 3.28 then gives

$$\frac{u_0^2}{\Delta}\frac{d\Delta}{dx} f f'' + \frac{\nu u_0}{\Delta^2} f''' = 0. \tag{3.38}$$

If the solution is of the assumed form this must reduce to a total differential equation in $f$ as a function of $\eta$; i.e. the total coefficients must have the same dependence on x, so that this cancels out:

$$\frac{u_0^2}{\Delta}\frac{d\Delta}{dx} \propto \frac{\nu u_0}{\Delta^2} \tag{3.39}$$

and so

$$\Delta^2 \propto \nu x/u_0 + const. \tag{3.40}$$

It is convenient to choose the constant of proportionality and the origin of x so that

$$\Delta = (\nu x/u_0)^{1/2}. \tag{3.41}$$

Equation 3.39 now becomes

$$ff'' + 2f''' = 0. \tag{3.42}$$

The boundary conditions transform to

$$\begin{aligned} f = f' = 0 \ at \ \eta = 0 \\ f' \to 1 \ as \ \eta \to \infty. \end{aligned} \tag{3.43}$$

The solution of this total differential equation has to be obtained numerically. The resulting variation of $f'$ with $\eta$, and so the velocity profile obtained numerically is compared with the theoretical profile as shown in figure 3.9. This curve is known as the Blasius profile.

It has the property that

$$f' = 0.99 \ when \ \eta = 4.99. \tag{3.44}$$

The boundary layer thickness can be defined as

$$\delta = 4.99(\nu x/u_0)^{1/2}. \tag{3.45}$$

Other ways of writing this are

$$\delta/x = 4.99 Re_x^{-1/2} \ and \ Re_\delta = 4.99 Re_x^{1/2}, \tag{3.46}$$

where $Re_x = u_0 x/\nu$ and $Re_\delta = u_0\delta/\nu$. The boundary layer thickness is small when the Reynolds number is large, as expected. This is, of course, a necessary condition

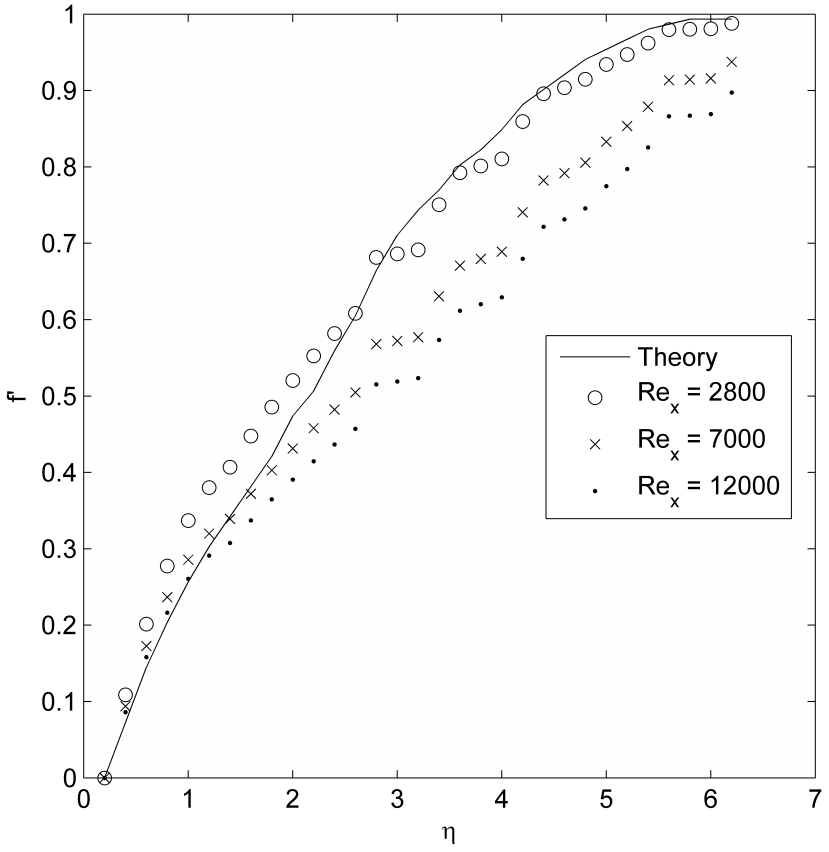


FIGURE 3.9: Theoretical Blasius profile (from Tritton [5]) compared to the numerical results obtained from the present simulations.

for the theory to apply. Also $Re_\delta$ is large when $Re_x$ is large; there is no ambiguity in talking about large Reynolds number. Figure 3.9 includes numerical results for different values of $Re_x$. The agreement with the theoretical profile is good, providing support for the various approximations and assumptions made in the course of the theory. The numerical results have been scaled to the coordinates $\eta(= y(u_0/\nu x)^{1/2})$ and $f'(= u/u_0)$.

At higher values of the Reynolds number, the Blasius profile is unstable and the boundary layer becomes turbulent. The instability depends on $Re_\delta$, which, as we can see from equation 3.46, increases with $Re_x$. Thus, any zero pressure gradient boundary layer undergoes transition if it extends far enough downstream. However, provided that the disturbance level is not too high, the range in which the Reynolds number is high enough for boundary layer formation but low enough for laminar flow is significant.

## 3.4 Model description

The model developed was based on the commercial FEM software COMSOL Multiphysics V4.3. The modelling procedure is outlined in the following steps, see [30]:

1. Geometry
2. Definition of the Partial Differential equations (PDE's);
3. Discretization;
4. Approximate solution of the PDE's;
5. Post-Processing.

### 3.4.1 Geometry and boundary conditions

The geometry and boundary conditions used to describe the channel are given in figure 3.1, where H is the half channel height and equals 1m. The channel extends a distance of 2H in the spanwise direction and 8H in the streamwise direction. The roughness region at the lower wall extends between 3H and 5H in the streamwise direction.

### 3.4.2 PDE's definition

The software solves the following form of the Navier-Stokes and continuity equations (compare with the equations of motion in section 3.2):

$$\rho\frac{\partial \mathbf{u}}{\partial t} + \rho\left(\mathbf{u}\cdot\nabla\right)\mathbf{u} = \nabla\left[-p\mathbf{I} + \mu(\nabla\mathbf{u} + (\nabla\mathbf{u})^T)\right] + \mathbf{F}, \tag{3.47}$$

$$\rho\nabla\cdot\mathbf{u} = 0 \tag{3.48}$$

The boundary conditions were implemented as follows:

- Wall (no-slip): This physical boundary was applied to the lower and upper walls. Here the following expression is used to describe the boundary; $\mathbf{u} = 0$. Details on the variables and constraints used in the prescription of this boundary condition are given in tables A.1 and A.2;

- Inlet: Here we assume a parabolic velocity at the inlet, based on the assumption that the flow is fully developed. Such a profile is obtained using the expression $u_0 = u_{in}6\ y\ (1-y)$, where $u_{in}$ is the given inlet velocity. For the unsteady case a step function was added to this expression as follows; $u_0 = u_{in}6\ y\ (1-y)step(t[1/s])$. The expression used to describe the boundary is $\mathbf{u} = -u_0\mathbf{n}$. This condition was prescribed using the variables and constraints shown in tables A.3 and A.4;

- Outlet: Here we prescribe a pressure boundary assuming parallel flow with no viscous stress. To this end we prescribe zero pressure, $p = p_0 = 0$, along with the following expression $\mu\left[\nabla\mathbf{u} + (\nabla\mathbf{u})^T\right]\cdot\mathbf{n} = 0$. The boundary condition was prescribed using the variable, constraint and weak expression given in tables A.5, A.6 and A.7;

- The fluid properties in the flow domain are prescribed using the variables in table A.8 (which includes the expressions for the stresses and the residuals), the shape functions in table A.9, and the weak expressions in table A.10.

### 3.4.3 Discretization

Once the mesh has been generated, the fluid domain is described using two dependent variables, velocity and pressure. The idea is to approximate the dependent variables with a function that you can describe with a finite number of parameters, the so-called degrees of freedom (DoF). Inserting this approximation into the weak form of the equation generates a system of equations for the degrees of freedom. Considering the problem in a two-dimensional domain, COMSOL Multiphysics forms the discretization of the PDE in the following manner, see [30]: The starting point is the weak formulation of the problem. First comes the discretization of the constraints,

- $0 = R^{(2)}$ on $\Omega$;
- $0 = R^{(1)}$ on $B$;
- $0 = R^{(0)}$ on $P$.

Starting with the constraints on the boundaries ($B$). For each mesh element in $B$ (that is, each mesh edge in $B$), consider the Lagrange points of some order k. Denote them by $x^{(1)}_{mj}$, where m is the index of the mesh element. Then the discretization of the constraint is:

$$0 = R^{(1)}\left(x_{mj}^{(1)}\right).$$

That is, the constraints must hold pointwise at the Lagrange points. The Lagrange point order k can be chosen differently for various components of the constraint vector $R^{(1)}$, and it can also vary in space. The constraints on domains $\Omega$ and points $P$ are discretized in the same way. Note that nothing needs to be done with the points $P$. One can collect all these pointwise constraints in one equation $0 = M$, where $M$ is the vector consisting of all the right-hand sides.

COMSOL Multiphysics [30] approximates the dependent variables with functions in the chosen finite element space(s). This means that the dependent variables are expressed in terms of the degrees of freedom as:

$$u_l = \sum_i U_i \phi_i^{(l)},$$

where $\phi_i^{(l)}$ are the basis functions for variable $u_l$. Let U be the vector with the degrees of freedoms $U_i$ as its components. This vector is called the solution vector because it is what you want to compute. $M$ depends only on $U$, so the constraints can be written as $0 = M(U)$.

Now consider the weak equation:

$$\begin{aligned} 0 = \int_\Omega W^{(2)} dA + \int_B W^{(1)} ds + \sum_P W^{(0)} \\ - \int_\Omega v \cdot h^{(2)T}\ \mu^{(2)} dA - \int_B v \cdot h^{(1)T}\ \mu^{(1)} ds - \sum_P v \cdot h^{(0)T}\ \mu^{(0)}, \end{aligned}$$

where $\mu^{(i)}$ are the Lagrange multipliers. To discretize it, express the dependent variables in terms of the degrees of freedom as described earlier. Similarly, approximate the test functions with the same finite elements (this is the Galerkin method):

$$v_l = \sum_i V_i \phi_i^{(l)}.$$

Because the test functions occur linearly in the integrands of the weak equation, it is enough to require that the weak equation holds when you choose the test functions as basis functions:

$$v_l = \phi_i^{(l)}.$$

When substituted into the weak equation, this gives one equation for each $i$. Now the Lagrange multipliers must be discretized. Let

$$\Lambda_{mj}^{(d)} = \mu^{(d)}(x_{mj}^{(d)})w_{mj}^{(d)},$$

where $x_{mj}^{(d)}$ are the Lagrange points defined earlier, and $w_{mj}^{(d)}$ are certain weights. The term

$$\int_B v \cdot h^{(1)T} \ \mu^{(1)} ds,$$

is approximated as a sum over all mesh elements in $B$. The contribution from mesh element number $m$ to this sum is approximated with the Riemann sum

$$\sum_j \phi_i(x_{mj}^{(1)}) \cdot h^{(1)T}(x_{mj}^{(1)})\mu^{(1)}(x_{mj}^{(1)})(w_{mj}^{(1)}) = \sum_j \phi_i(x_{mj}^{(1)}) \cdot h^{(1)T}(x_{mj}^{(1)})\Lambda_{mj}^{(1)},$$

where $w_{mj}^{(1)}$ is the length (or integral of $ds$) over the appropriate part of the mesh element. The integral over $\Omega$ and the sum over $P$ is approximated similarly.

This means that one can write the discretization of the weak equation as;

$$0 = L - N_F\Lambda,$$

where $L$ is a vector whose $i-$th component is

$$\int_\Omega W^{(2)} dA + \int_B W^{(1)} ds + \sum_P W^{(0)},$$

evaluated for $v_l = \phi_i^{(l)}$. $\Lambda$ is the vector containing all the discretized Lagrange multipliers $\Lambda_{mj}^{(d)}$. $N_F$ is a matrix whose $i-$th row is a concatenation of the vectors

$$\phi_i(x_{mj}^{(d)}) h^{(d)} (x_{mj}^{(d)})^T.$$

For problems using ideal constraints, $N_F$ is equal to the constraint Jacobian matrix $N$, which is defined as:

$$N = -\frac{\partial M}{\partial U}.$$

To sum up, the descretization of the stationary problem is:

$$\begin{aligned} 0 &= L(U) - N_F(U)\Lambda, \\ 0 &= M(U). \end{aligned}$$

The objective is to solve this system for the solution vector $U$ and the Lagrange multiplier vector $\Lambda$. $L$ is called the residual vector, $M$ is the constraint residual and $N_F$ is the constraint force Jacobian matrix.

The integrals occurring in the components of the residual vector $L$ are computed approximately using a *quadrature formula* [30]. Such a formula computes the integral over a mesh element by taking a weighted sum of the integrand evaluated in a finite number of points in the mesh element. The order of a quadrature formula on a triangular element is the maximum number $k$ such that it exactly integrates all polynomials of degree $k$. For a quadrilateral element, a formula of order $k$ integrates exactly all products $p(\xi_1)q(\xi_2)$, where $p$ and $q$ are polynomials of degree $k$ in the first and second local coordinates respectively. Thus, the accuracy of the quadrature increases with the order. On the other hand, the number of evaluation points also increases with the order. As a rule of thumb, you can take the order to be twice the order of the shape function for the finite element being used.

The discretization of a time-dependent problem is similar to the stationary problem;

$$\begin{aligned} 0 &= L\left(U, \dot{U}, \ddot{U}, t\right) - N_F\left(U, t\right)\Lambda, \\ 0 &= M\left(U, t\right), \end{aligned}$$

where $U$ and $\Lambda$ now depend on time $t$.

Consider a linearised stationary problem. The linearisation 'point' $u_0$ corresponds to a solution vector $U_0$. The discretization of the linearised problem is

$$\begin{aligned} K(U_0)(U - U_0) + N_F(U_0)\Lambda &= L(U_0), \\ N(U_0)(U - U_0) &= M(U_0), \end{aligned}$$

where $K$ is called the stiffness matrix and $L(U_0)$ is the load vector. For problems given in general or weak form, $K$ is the Jacobian of $L$:

$$K = -\frac{\partial L}{\partial U}.$$

The entries in the stiffness matrix are computed in a similar way to the load vector, namely by integrating certain expressions numerically. This computation is called the *assembling* of the stiffness matrix [30].

If the original problem is linear, then its discretization can be written as

$$\begin{aligned} KU + N_F\Lambda &= L(0), \\ NU &= M(0). \end{aligned}$$

Similarly, for a time-dependent model the linearisation involves the *damping matrix*

$$D = -\frac{\partial L}{\partial \dot{U}},$$

and the *mass matrix*

$$E = -\frac{\partial L}{\partial \ddot{U}}.$$

### 3.4.4 Solver

The discrete system of equations is solved using a non-linear solver. The non-linear solver uses an affine invariant form of the damped Newton method as described by Deuflhard [31]. One can write the discrete form of the equations as $f(U) = 0$, where

$f(U)$ is the residual vector and $U$ is the solution vector. Starting with the initial guess $U_0$, the software forms the linearised model using $U_0$ as the linearisation point. It solves the discretized form of the linearised model $f(U_0)\delta U = -f(U_0)$ for the Newton step $\delta U$ using the selected linear system solver ( $f(U_0)$ is the Jacobian matrix). It then computes the new iteration $U_1 = U_0 + \lambda\delta U$, where $\lambda(0 \leq \lambda \leq 1)$ is the damping factor. Next, the modified Newton correction estimates the error $E$ for the new iteration $U_1$ by solving $f(U_0)E = -f(U)$. If the relative error in the previous iteration is still high, the code reduces the damping factor $\lambda$ and recomputes $U_1$. The algorithm repeats the damping factor reduction until the relative error is less than in the previous iteration, or until the damping factor underflows the minimum damping factor. When it has taken a successful step $U_1$ the algorithm proceeds with the next Newton iteration.

The non-linear iterations terminate when the following convergence criterion is satisfied: Let $U$ be the current approximation to the true solution vector, and let $E$ be the estimated error in this vector. The software stops the iterations when the relative tolerance exceeds the relative error computed as the weighted Euclidean norm:

$$err = \left[\frac{1}{N}\sum_{i=1}^{N}(|E_i|/W_i)^2\right]^{1/2}. \tag{3.49}$$

Here $N$ is the number of degrees of freedom (DOF's) and $W_i = max\,(|U_i|, S_i)$, where $S_i$ is a scale factor that the solver determines based on the scaling method. Here we considered automatic scaling where $S_i$ is the average of $|U_j|$ for all DOF's $j$ having the same name as DOF's $i$ times a factor equal to $10^{-5}$ for a highly non-linear problem, or 0.1 otherwise.

The solution procedure is outlined in the following steps:

1. Step 1: Grid generation;
2. Step 2: Compute Initial solution using $(P_1 + P_1)$ discretization and Adaptive Mesh Refinement (AMR);
3. Step 3: Use the final grid from step 2 to compute the final solution using $(P_2 + P_1)$ discretization;

### 3.4.5 Adaptive Mesh Refinement (AMR)

According to Anderson [32] an adaptive mesh is a grid network that automatically clusters grid points in regions of high flow-field gradients; it uses the solution of the flow-field properties to locate the grid points. The author [32] states that an adaptive

mesh can be visualized as one which evolves in steps of time in conjunction with a time-dependent solution of the governing flow-field equations, which computes the flow-field variables in steps of time. Anderson [32] explains that during the course of the solution, the grid points in the physical plane move in order to adapt to regions of large flow-field gradients as these gradients evolve with time. Hence, the actual grid points in the physical plane are constantly in motion during the solution of the flow-field and become stationary only when the flow solution approaches a steady state [32]. An example of mesh refinement used in our analysis is shown in figure 3.11.

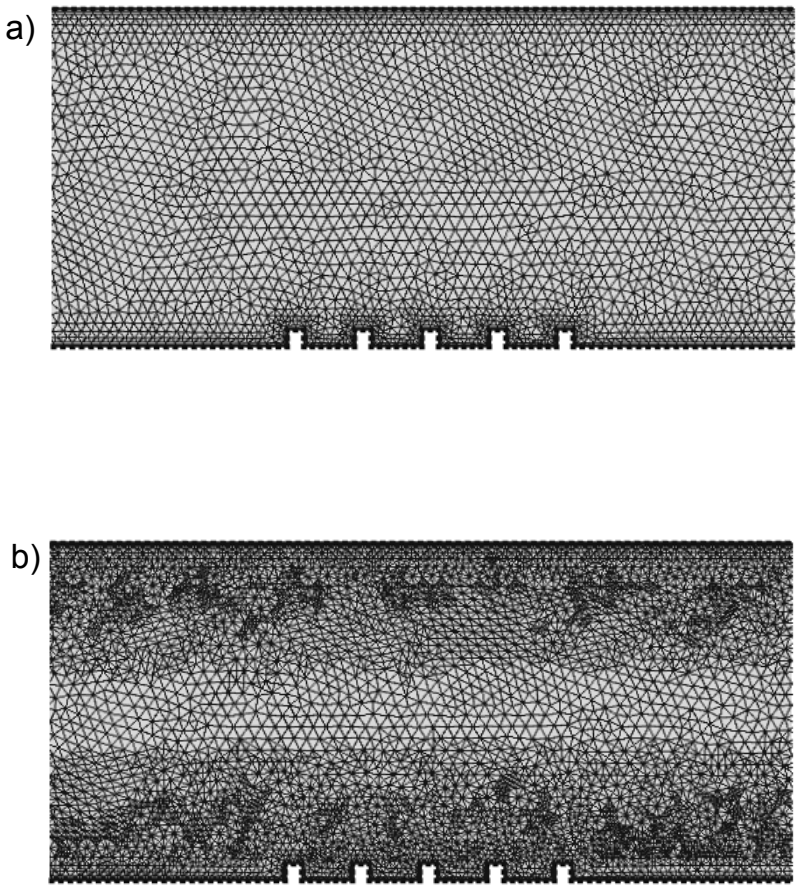


FIGURE 3.10: An example of Adaptive Mesh Refinement (AMR); a) no AMR (8304 elements); b) AMR (20159 elements).

The following general steps were followed to adaptively refine the mesh, see Zienkiewicz et al. [33]:

1. Find the solution using an initial coarse mesh;
2. Select a suitable representative scalar variable and calculate the local and maximum and minimum curvatures and directions of these at all nodes. Here the velocity gradient components $(\frac{\partial u}{\partial x}, \frac{\partial u}{\partial y})$ were used as the representative scalar variable, the reason being that we are interested in the vortical structures;
3. Calculate the new element sizes at all nodes from the maximum and minimum curvature;
4. Calculate the stretching ratio from the ratio of calculated maximum to minimum element sizes. If this is very high, limit by a maximum allowable value;
5. Re-mesh the whole domain based on the new element size, stretching ratio and the direction of stretching.

To use the above procedure, an efficient unstructured mesh generator is essential. Here we use the advancing front technique operating on the background mesh principles to carry out the simulations. The information from the previous solution in the form of local mesh sizes, stretching ratios and stretching directions are stored in the previous mesh and this mesh is used as a background mesh for the new one.

## 3.5 The possibility of ILES

LES incorporates a form of turbulence modelling applicable when the large scale flows of interest are time dependent, thus introducing common statistical models into the formulation. An alternative approach to LES involves the use of CFD algorithms, such as upwind scheme, which introduces intrinsic sub-grid turbulence models implicitly into the computed flow. This scheme is called Implicit LES (ILES), see Pope [6], and is very useful in practical flow computations because it does not need any explicit turbulence models. Unlike explicit turbulence models, ILES requires a relatively small amount of mesh system than DNS and can reproduce transition automatically from laminar flow to turbulent flow as well as DNS.

In this approach, the flow is governed by the equations 3.47 and 3.48. We know that by increasing the flows Re the numerical computations become unstable due to an insufficient viscous diffusion and growing non-linear effect. Therefore, we usually need a stabilization technique such as upwind scheme to damp out high wave number non-linear disturbance which is generated by the non-linear convective term. In order to solve these equations, the laminar flow interface of COMSOL is utilized. In addition, a number of stabilization techniques were utilized, see table A.10. Here we utilized streamline diffusion stabilization for which COMSOL uses the Galerkin Least Squares (GLS) method. Moreover, we used crosswind diffusion which tries to smear out the boundary layer so that it becomes just wide enough to be resolved by the mesh. To obtain a sharper solution and remove the oscillations of the solution, the mesh needs to refined locally at the boundary layers. Here we have to use a denser mesh near the walls where the boundary layer develops in order to satisfy the no slip condition, as shown in figure 3.11. Given that we do not violate the inherent molecular viscosity effect when using numerical stabilization techniques, it can be expected to realize ILES of the flow field in principle. It is important to mention here that the model presented in this chapter is concerned with the ILES of two-dimensional turbulence. The validity of ILES for three-dimensional turbulence has been validated in the work of Grinstein et al [17]. However, little attention has been made to the two-dimensional case, see Kent et al. [34]. An assessment of ILES for two-dimensional flow is given by Kent et al. [34], where the authors developed ILES schemes based on the FVM and assessed them in terms of weather and climate modelling.

Pope [6] states that the advantages of the ILES approach are that (for a given grid size) as much as possible of the turbulent flow is represented explicitly by the LES velocity field, and that energy is removed only where and when it is necessary to do so. It is argued that the detail of how energy is removed is unimportant, just so long as there is a mechanism to remove the energy from the smallest removed scales without

contaminating the larger scale. A further advantage is that the time and effort required to develop and test a residual stress model, used in explicit LES, are eliminated.

The primary disadvantage is that the modelling and the numerics are inseparably coupled. This implies that for a given flow, the simulation results depend both on the numerical method and on the grid used. It is not possible to refine the grid to obtain a grid-independent solution (short of performing DNS). Another disadvantage is that there is no representation or estimation of the subgrid-scale motions that can be used for defiltering or in models for other subgrid-scale processes.

## 3.6 Roughness modelling

The flow configuration considered here is a fully developed channel flow with square (see figure 3.11) and triangular (see figure 3.12) roughness elements at the bottom wall and a smooth upper wall. This configuration (one rough and one smooth) is chosen to remove the symmetry effect when both surfaces are identical and allows a comparison between between the smooth and rough walls, see Leonardi et al. [22].Several values of w/k have been investigated, with k = 0.1 H. The values for w/k considered are shown in figure 3.13 for square roughness. Identical distributions were used for the triangular roughness was used (not shown).

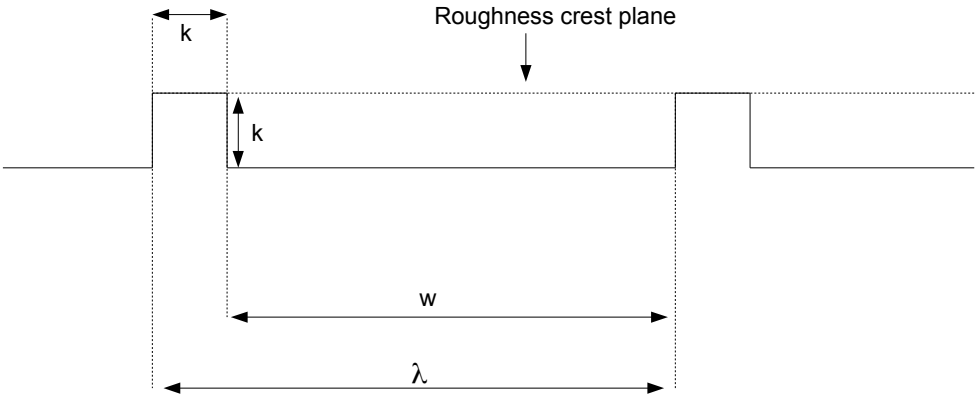


FIGURE 3.11: Sketch of the geometry of the rough surface (square).

The triangular elements have been considered for the same pitch to height ratio. Note that w is not constant, so it is more appropriate to use $\lambda$ to denote the distance between the elements. Here, the cavity is slightly larger than the square cavity. The angle at the base of the triangle is 60 degrees instead of 90 degrees for the square cavity. Circular roughness elements were also considered in the course of this research. However, during the verification process it became evident that such a geometry required a significantly denser mesh to meet the convergence criteria presented in the next chapter.

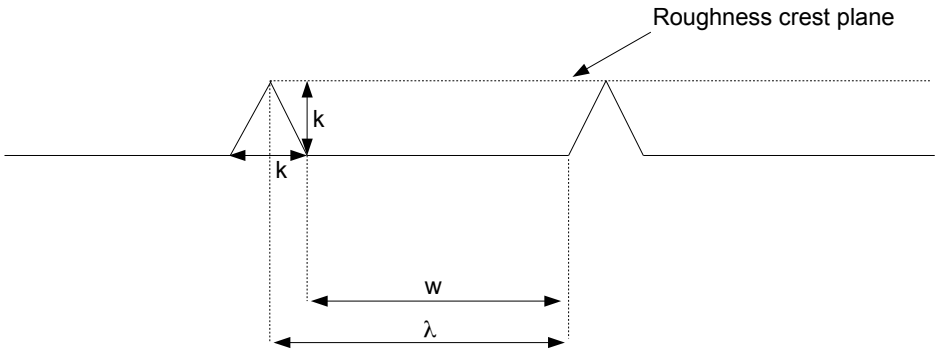


FIGURE 3.12: Sketch of the geometry of the rough surface (triangle).

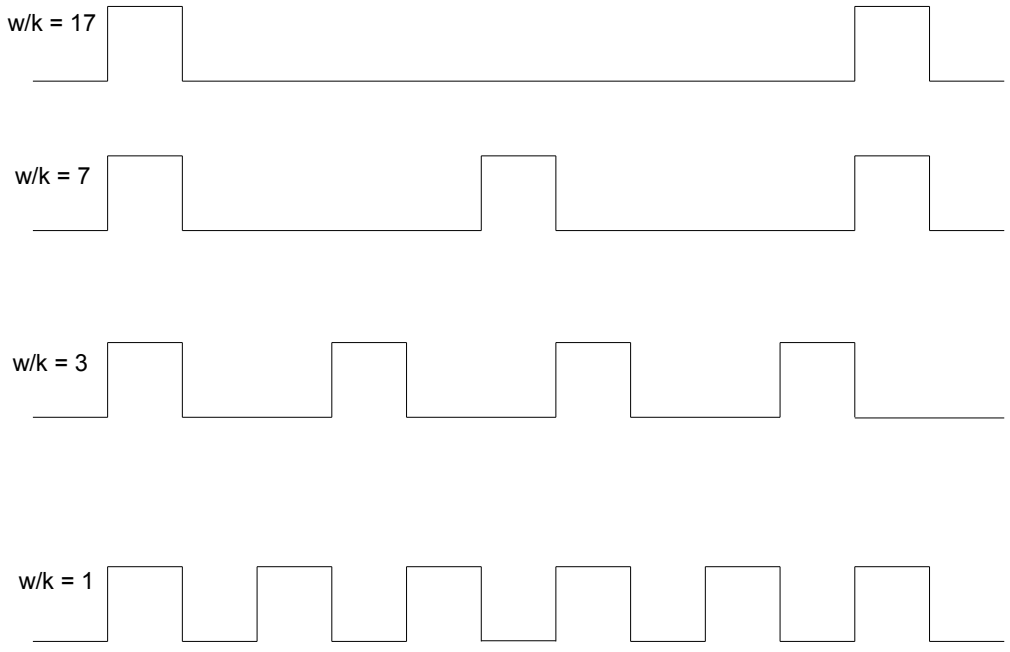


FIGURE 3.13: Sketch of the distribution of roughness elements.

# Chapter 4

# Verification and validation

In scientific computing, verification and validation are the primary means to asses accuracy and reliability in computational simulations. In a paper titled 'Verification and Validation in Computational Fluid Mechanics' Oberkampf and Trucano [18] state that "The field of CFD, in general, proceeded along a path that is largely independent of validation." The authors argue that the present method of qualitative 'graphical validation' i.e., comparison of computational results and experimental data on a graph, is inadequate. To this end, a number of verification and validation procedures were adopted from Oberkampf and Roy [19] to asses the simulations predictive capabilities. Figure 4.1 outlines the general procedure adopted and the general aspects considered at

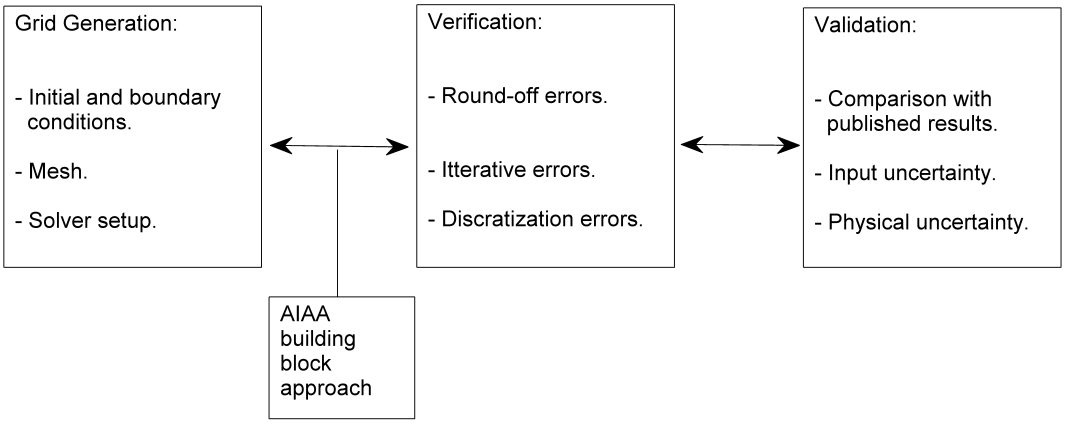


FIGURE 4.1: Outline of the verification and validation procedures.

each stage. Here the grid generation procedures were presented in the previous chapter. Section 4.1 will give a brief description of the AIAA building block approach and its implementation to the problem under consideration. In section 4.2 we present the procedures (convergence test, Richardson extrapolation and Grid Convergence Index) used in the verification process to quantify the various numerical errors. Finally, in section

4.3 the concept of 'validation experiments' given by Oberkampf and Roy [19] is used to conduct sensitivity analysis to quantify the uncertainty of the results obtained from the simulations before comparing them with results found in literature.

## 4.1 AIAA building block approach

The AIAA (American Institute of Aeronautics and Astronautics) building block approach divides a complex engineering system of interest into an arbitrary number of progressively simpler tiers. The general approach is to divide the system into three tiers; usually referred to as sub system, benchmark and unit. The strategy of the tiered approach encourages assessment of the model at multiple levels of complexity and physics coupling. In our analysis, the complete system of interest is the flow over a rough surface. The complete system was subdivided into two sub systems; the core flow and the flow near the wall, as shown in Figure 4.2. The sub systems are further divided into a combination of benchmark cases and unit problems, combining these two tiers is justified due to the basic nature of the model. In this lower tier the core flow, which is part of the system surroundings, is assumed to have a fully developed flow characteristics. On the other hand, the near wall flow is the sub system of interest in our analysis. The benchmark cases and unit problems shown in figure 4.2 reflect the phenomena under consideration. Starting with the simplest case, flow over a smooth surface, model verification and validation were carried out before introducing roughness. Once the simple case had been validated, different roughness geometries and distributions were considered to find a model with the best predictive capability.

## 4.2 Verification

According to Oberkampf and Roy [19], solution verification addresses the question whether a given simulation of a mathematical model is sufficiently accurate for its intended use. It includes not only the accuracy of the simulation for the case of interest, but also the accuracy of the inputs to the model and any post-processing of the model results. Quantifying the numerical accuracy of scientific computing simulations is important for two primary reasons:

- As part of the quantification of the total uncertainty in simulation prediction;
- For establishing the numerical accuracy of the simulation for model validation.

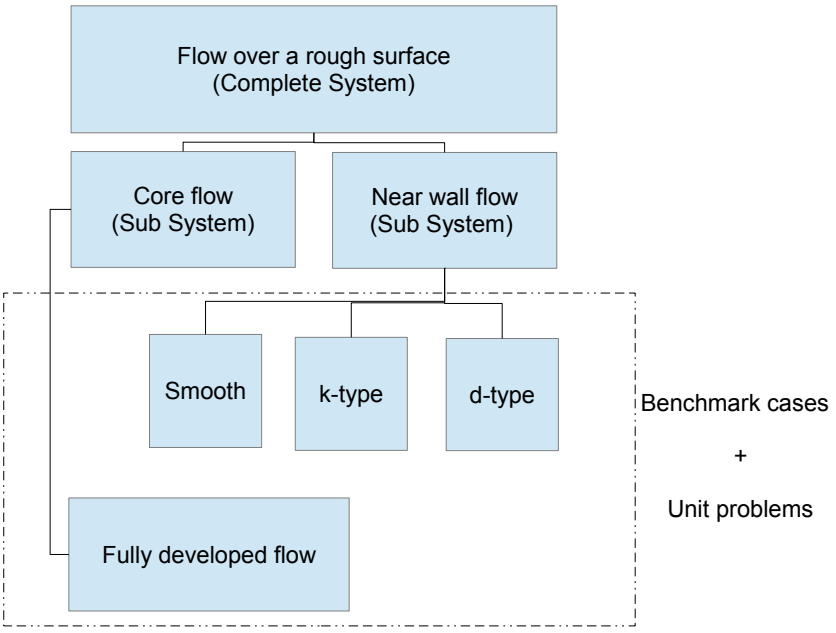


FIGURE 4.2: Outline of the AIAA building block approach.

Solution verification begins after the mathematical model has been embodied in a verified code, the initial and boundary conditions have been specified, and any other auxiliary relations have been determined. It includes the running of the code in a mesh, or a series of meshes, possibly to a specified iterative convergence tolerance. Solution verification ends after all post-processing of the simulation results are completed to provide the final simulation predictions. Therefore, the following aspects of solution verification were considered:

- Verification of input data; and
- numerical error estimation.

### 4.2.1 Verification of input data

Here, input data is defined as any information required for running the simulation. Common forms of input data include:

- Input files describing models, sub-models and numerical algorithms;
- domain grids;

- boundary and initial conditions;
- information on material properties;
- data used for sub-models; and
- CAD surface geometry information.

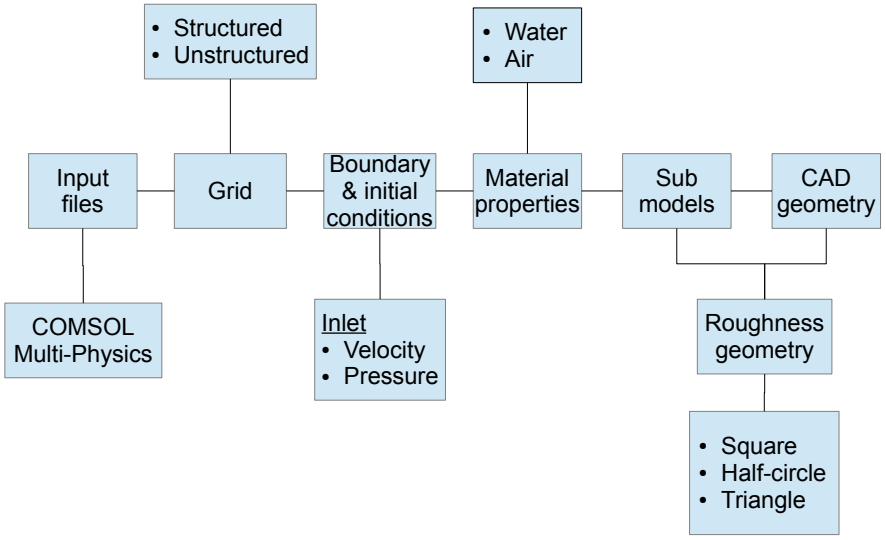


FIGURE 4.3: Outline of the aspects considered in the input data verification process

The general aspects considered in the verification process are illustrated in figure 4.3. In our analysis, verification of the input files was not necessary as the model was developed based on a well established FEM algorithm. Further details about the implementation of the FEM are given by Brookes and Hughes [35] and a comprehensive study into the error estimations of the FEM is given by Stewart and Hughes [36]. The verification of grid, material properties, sub-models and CAD geometry was carried out using a convergence test adopted from Trott and Gobbert [37]. The convergence test procedure can be summarized as follows:

- **Problem statement:** Assess the quality of Finite Element Method (FEM) solution quantitatively for all Lagrange elements with polynomial degrees $1 \leq P \leq 3$ available in COMSOL;

- **Approach:** Use guidance from the priori error estimate
  $\|u - u_h\|_{L^2(\Omega)} \leq Ch^q$ , as $h \to 0$
  with a constant $C$ independent of $h$ and the convergence order $q > 0$. Here, $h$ is the maximum side of the elements triangulation (mesh spacing);

- **Goal:** Confirm that solutions on a sequence of meshes, that are uniformly refined, behaves as predicted by the error estimates;

- **FEM theory for Lagrange elements:** For linear Lagrange elements ($P = 1$), the optimal convergence order is $q = P + 1 = 2$ in $\|u - u_h\|_{L^2(\Omega)} \leq Ch^q = Ch^2$. For Lagrange FEM with polynomial degree $p = 1, 2, 3$ we expect $q = P + 1$ in $\|u - u_h\|_{L^2(\Omega)} \leq Ch^q = Ch^{P+1}$.

The convergence test results for an unstructured domain grid are given in table 4.1, where $r$ is the refinement level, $Err^2$ is the error obtained from equation 3.49, $Err$ is the square root value of $Err^2$, $R_r$ is the ratio of $Err$ between two refinements and $Q_r = log_2 R_r$. The results show the minimum grid requirement to obtain a convergent solution. For the cases we considered a grid with a minimum number of 2878 elements (N) and 2nd order discretization (P2+P1) was required. Running the same test on a structured grid (results not shown here) required a higher computational effort to achieve convergence without any improvements in accuracy. Therefore, the unstructured grid was used throughout our analysis.

| P1+P1 | | | | | | | | |
|---|---|---|---|---|---|---|---|---|
| r | N | DoF | $Err^2$ | Err | $R_r$ | $Q_r$ | $U_c$ | $C_f$ |
| 0 | 550 | 1337 | 0.00054 | 0.0232379001 | NA | NA | 0.01283 | 4.24E-004 |
| 1 | 916 | 1824 | 0.00079 | 0.0281069386 | 1.2095300587 | 0.274446623 | 0.01308 | 4.95E-004 |
| 2 | 1486 | 2814 | 0.00022 | 0.014832397 | 0.5277130022 | -0.9221745648 | 0.01399 | 5.13E-004 |
| 3 | 2878 | 5175 | 0.00065 | 0.0254950976 | 1.7188791274 | 0.7814680972 | 0.01472 | 5.74E-004 |
| 4 | 4488 | 7836 | 0.0007 | 0.0264575131 | 1.0377490433 | 0.053457602 | 0.01488 | 5.92E-004 |
| 5 | 8146 | 13593 | 0.00031 | 0.0176068169 | 0.6654751256 | -0.5875433533 | 0.01497 | 5.82E-004 |
| 6 | 19166 | 31650 | 0.00021 | 0.0144913767 | 0.8230548918 | -0.2809394438 | 0.01498 | 5.98E-004 |
| | | | | | | | | |
| P2+P1 | | | | | | | | |
| 0 | 550 | 3241 | 1.50E-012 | 1.22474487139159E-006 | NA | NA | 0.015 | 6.00E-004 |
| 1 | 916 | 5238 | 1.30E-012 | 1.14017542509914E-006 | 0.9309493363 | -0.1032254387 | 0.015 | 6.00E-004 |
| 2 | 1486 | 8140 | 5.00E-012 | 2.23606797749979E-006 | 1.9611613514 | 0.9717082358 | 0.015 | 6.00E-004 |
| 3 | 2878 | 15091 | 5.20E-010 | 2.28035085019828E-005 | 10.1980390272 | 3.3502198591 | 0.015 | 6.00E-004 |
| 4 | 4488 | 22954 | 2.00E-010 | 1.4142135623731E-005 | 0.6201736729 | -0.6892558116 | 0.015 | 6.00E-004 |
| 5 | 8146 | 40089 | 3.00E-010 | 1.73205080756888E-005 | 1.2247448714 | 0.2924812504 | 0.015 | 6.00E-004 |
| 6 | 19166 | 93544 | 6.00E-010 | 2.44948974278318E-005 | 1.4142135624 | 0.5 | 0.015 | 6.00E-004 |
| | | | | | | | | |
| P3+P2 | | | | | | | | |
| 0 | 550 | 7745 | 2.70E-010 | 1.6431676725155E-005 | NA | NA | 0.015 | 6.00E-004 |
| 1 | 916 | 12559 | 1.20E-009 | 0.000034641 | 2.1081851068 | 1.0760015467 | 0.015 | 6.00E-004 |
| 2 | 1486 | 19581 | 2.60E-009 | 5.09901951359278E-005 | 1.4719601444 | 0.5577386087 | 0.015 | 6.00E-004 |
| 3 | 2878 | 36433 | 3.60E-009 | 0.00006 | 1.1766968108 | 0.2347426417 | 0.015 | 6.00E-004 |
| 4 | 4488 | 55527 | 6.30E-009 | 7.93725393319377E-005 | 1.3228756555 | 0.403677461 | 0.015 | 6.00E-004 |
| 5 | 8146 | 97269 | 5.60E-009 | 7.48331477354788E-005 | 0.9428090416 | -0.0849625007 | 0.015 | 6.00E-004 |
| 6 | 19166 | 227181 | 1.60E-008 | 0.0001264911 | 1.6903085095 | 0.7572865864 | 0.015 | 6.00E-004 |

TABLE 4.1: Convergence test results for a plane channel: Minimum grid requirements are N = 2878 with 15091 DoF and 2nd order discretization (P2+P1.)

The convergence test was also used to verify the choice of boundary and initial conditions. Previous work using LES, see Cui et al [8], suggest that a pressure boundary at the inlet

would provide an appropriate boundary condition. However, in our analysis, obtaining a convergent solution using this boundary condition was difficult. Therefore, a velocity boundary condition with a parabolic profile was used throughout as the inlet boundary condition. In order to ensure minimum errors from information on material properties we limited the input data to the fluid density and dynamic viscosity, instead of using the default properties form the material library provided by the software.

We expected the sub-model used to simulate the flow near the wall would be a major source of inaccuracy, especially when considering the flow over a rough surface. This inaccuracy will be further investigated in the numerical error estimation procedure. Errors arising from the CAD surface geometry information were minimized by considering simple geometries. Arguably, the half circle is the most complex geometry considered here. For this geometry, it was necessary to verify that the mesh density was sufficient to give a reasonable approximation for a half circle geometry. Results of the convergence test for the various roughness elements geometries for a k- type distribution are given in table 4.2. The results show that circular roughness elements does not meet our convergence criteria, therefore this roughness geometry was not considered in our analysis.

### 4.2.2 Numerical errors

Numerical errors occur in every scientific computing simulation, and this needs to be estimated in order to build confidence in the mathematical accuracy of the solution. Oberkampf and Roy [19] give the following types of numerical errors;

1. Round off error;
2. iterative error; and
3. discretization error.

The approach used for assessing the effects of round off errors on the simulation was to run the simulation with the desired precision, then re-run the simulation with higher precision and compare the solutions. Note that the same mesh/time-step should be employed for both cases, and when iterative methods are used then both simulations should be iteratively converged to within machine precision. Results for the estimation of round-off errors are given in table 4.3. The results show that the default tolerance 0.001 has a round-off error of approximately $10^{-2}$ and decreasing the tolerance improves the accuracy at the cost of higher computational effort. To overcome the trade-off between

| Square(w/k = 17) | | | | |
|---|---|---|---|---|
| P1+P1 | | | | |
| N | $Err^2$ | Err | $R_r$ | $Q_r$ |
| 5139 | 0.000635486 | 0.0252088477 | NA | NA |
| 12677 | 3.61E-005 | 0.0060054475 | 0.2382277687 | 0.274446623 |
| 30897 | 1.03E-005 | 0.0032026395 | 0.5332890716 | -0.9070103309 |
| P2+P1 | | | | |
| N | $Err^2$ | Err | $R_r$ | $Q_r$ |
| 5193 | 0.000457103 | 0.0213799673 | NA | NA |
| 14368 | 5.52E-006 | 0.0023491914 | 0.1098781547 | -3.1860235077 |
| 35700 | 1.06E-006 | 0.0010314553 | 0.4390682277 | -1.1874829545 |
| | | | | |
| Circle(w/k=17) | | | | |
| P1+P1 | | | | |
| N | $Err^2$ | Err | $R_r$ | $Q_r$ |
| 5528 | 0.00014822 | 0.0121745636 | NA | NA |
| 13438 | 2.42E-005 | 0.0049190751 | 0.4040452914 | -1.3074110742 |
| 31294 | 9.58E-006 | 0.003094382 | 0.6290576852 | -0.6687357751 |
| P2+P1 | | | | |
| N | $Err^2$ | Err | $R_r$ | $Q_r$ |
| 5528 | 3.65E-005 | 0.0060406126 | | |
| 14261 | 3.72E-006 | 0.0019299585 | 0.319497159 | -1.6461249923 |
| 33931 | 9.68E-007 | 0.0009838496 | 0.5097775715 | -0.972060194 |
| | | | | |
| Triangle(w/k=17) | | | | |
| P1+P1 | | | | |
| N | $Err^2$ | Err | $R_r$ | $Q_r$ |
| 5245 | 0.000352715 | 0.0187807082 | NA | NA |
| 13076 | 3.12E-005 | 0.0055898479 | 0.2976377613 | -1.748370522 |
| 31405 | 9.31E-006 | 0.0030505672 | 0.5457334784 | -0.8737315453 |
| P2+P1 | | | | |
| N | $Err^2$ | Err | $R_r$ | $Q_r$ |
| 5245 | 0.000215969 | 0.0146958838 | NA | NA |
| 14410 | 4.43E-006 | 0.0021055854 | 0.1432772238 | -2.8031188062 |
| 35198 | 9.29E-007 | 0.0009638319 | 0.4577500975 | -1.1273679016 |

TABLE 4.2: Convergence test results for the different roughness geometries with k-type distribution.

| Plane | | |
|---|---|---|
| Tolerance | $Err^2$ | Err |
| 0.001 | 1.30E-004 | 0.0114017543 |
| 0.0001 | 2.40E-006 | 0.0015491933 |
| 0.00001 | 2.40E-006 | 0.0015491933 |
| 0.000001 | 1.50E-007 | 0.0003872983 |
| 0.00000001 | 9.50E-009 | 9.7467E-005 |

TABLE 4.3: Round-off error estimation for the plane channel.

computational effort and accuracy the default tolerance was decreased by an order of magnitude (0.0001) and used throughout.

In practical scientific computing problems, it may difficult to apply iterative error estimations. Oberkampf and Roy [19] explain that most scientific codes monitor iterative convergence by examining the norms of the iterative residuals. The authors explain that, since the iterative residual norm have been shown to follow closely with the actual iterative errors for many problems, a small number of computations should be sufficient to determine how the iterative errors in the results scale with the iterative residuals for the cases of interest. The results in table 4.4 show that iterative error for the different surfaces considered here is between $10^{-4} - 10^{-7}$.

| | Residual(u) | Residual(v) | Residual(p) |
|---|---|---|---|
| Plane | -8.59366e-6 | 4.43079e-6 | -4.57947e-7 |
| d-type | -3.17572e-5 | -4.9997e-5 | -5.83345e-6 |
| k-type | -5.02957e-5 | -6.06775e-4 | 7.19508e-6 |

TABLE 4.4: iterative error estimation

Discretization errors were estimated using the the Richardson extrapolation and the Grid convergence Index (GCI). A Detailed description of both methods could be found in Oberkampf and Roy [19]. Here we present the general principles used in these methods. The results for the convergence ratio, observed order of accuracy and the GCI are given in table 4.5 for a plane channel flow. The convergence ratio (R) shows that oscillatory convergence has been achieved. The apparent order of discretization matches the formal order, which meets the criterion given for the observed order of accuracy. The relative error and GCI show that the discretization errors are below 1%.

| N | $u_c$(FEM) | $u_c$(Theory) |
|---|---|---|
| 550 | 0.01283 | 0.015 |
| 916 | 0.01308 | 0.015 |
| 1486 | 0.01399 | 0.015 |
| | | |
| | | |
| R(Convergence Ratio) | | |
| -0.9170836312 | | |
| | | |
| r21 | e32 | e21 |
| 1.6654545455 | 0.00091 | 0.00025 |
| P(Apparent Order) | | |
| 2.5328142096 | | |
| | | |
| Approximate Relative Error | | |
| 1.0066555807 | | |
| | | |
| GCI | | |
| 0.0001183712 | | |

TABLE 4.5: Verification data for a plane channel using the minimum grid requirements

## 4.3 Validation

Oberkampf and Roy [19] outline the following three aspects when considering model validation:

1. Quantification of the accuracy of the computational model results by comparing the computed system response quantities (SRQs) of interest with experimentally measured SRQs;
2. Use of computational model to make predictions, in the sense of interpolation or extrapolation of the model, for conditions corresponding to the model's domain of intended use;
3. Determination of whether the estimated accuracy of the computational model results satisfies the accuracy requirements specified for the SRQs of interest.

The first aspect deals with assessing the accuracy of the results from the model by comparison with available experimental data. Here we also considered data from DNS and LES. The assessment could be conducted for the actual system of interest or any related system. In our analysis, we considered the centre-line velocity $u_c$ and the skin friction coefficient as our SRQs. The second aspect deals with the model's predictive capability. It is important to mention here that aspect 2 does not deal with aspects of adequacy or accuracy on the prediction, but focuses on the SRQs of interest for the applications conditions of interest. The third aspect deals with (a) the comparison of the estimated model relative to the accuracy requirements of the model for the domains of the model's intended for use, and (b) the decision of inadequacy of the model over the domain of models's intended use.

Oberkampf and Roy [19] argue that there are two viewpoints in the interpretation of validation in terms of the three aspects listed above. One interpretation is called the encompassing view of validation, where all aspects are addressed. The second is the restricted view of validation, which considers each aspect of validation separately. In our analysis, the encompassing view was adopted due to the relative simplicity of the problem under investigation. The validation process starts with a number of validation experiments, shown in table 4.6, where the results are then analysed to quantify the uncertainty and compare the results with published data. Here, uncertainty was investigated in terms of the input parameters, outlined in the verification section, and physical uncertainty is concerned with validating the assumption that the flow is fully developed.

| **System Input** | **System of Interest** | **Validation Experiments** |
|---|---|---|
| Channel geometry (H, L) | H=2 | L= 5,6,7,8,9 [m]. |
| Initial conditions (u, v) | u=0 | v= $1 \cdot e^{-4}, 1 \cdot e^{-5}, 1 \cdot e^{-6}, 1 \cdot e^{-7} [m/s]$. |
| Fluid properties ($\rho, \mu$) | $\rho = 1000$ | $\mu = 0.1, 1 \cdot e^{-2}, 1 \cdot e^{-3}, 1 \cdot e^{-4}, 1 \cdot e^{-5} [Pa \cdot s]$. |
| No-slip ($\tau_w$) | SRQ | calculate $C_f$. |
| Time step($\Delta t$) | suitable time step | $\Delta t = 200, 20, 2, 0.2 [s]$ |
| **Surroundings Input** | | |
| Inlet velocity ($u_{in}$) | $u_{in} = parabolic$ | $u_{in} = 0.01, 0.025, 0.05, 0.075, 0.1 [m/s]$. |
| Outlet pressure ($p_0$) | $p_0 = 0$ | Fixed [Pa]. |

TABLE 4.6: List of validation experiments used to quantify input uncertainty.

### 4.3.1 Input uncertainty

Input uncertainty for the different parameters considered, see table 4.6, was quantified using sensitivity analysis. The data from the unsteady simulations were collected using point-probes at certain locations in the domain, see chapter 5. Here, we present the results for one parameter, the channel length (L), to illustrate the quantification procedure. Using the mean and the standard deviation (std), given in table 4.7, the uncertainty of the data obtained for $u_c$ was below 1%. This suggests that the results of the SRQ are relatively insensitive to the range of L considered here. A graphical representation of the uncertainty is given in figure 4.4 using a histogram plot along with the probability density function (PDF).

| $u_c$ | L=5 | L=6 | L=7 | L=8 | L=9 |
|---|---|---|---|---|---|
| N=10 | | | | | |
| mean | 0.1494 | 0.1494 | 0.1495 | 0.1496 | 0.1494 |
| std | 2.72E-004 | 2.28E-004 | 2.58E-004 | 2.91E-004 | 2.25E-004 |
| | | | | | |
| N=30 | | | | | |
| mean | 0.1494 | 0.1494 | 0.1495 | 0.1495 | 0.1495 |
| std | 2.10E-004 | 2.21E-004 | 1.87E-004 | 2.37E-004 | 1.85E-004 |
| | | | | | |
| N=100 | | | | | |
| mean | 0.1494 | 0.1494 | 0.1495 | 0.1495 | 0.1495 |
| std | 1.99E-004 | 1.87E-004 | 1.72E-004 | 2.24E-004 | 1.72E-004 |

TABLE 4.7: Results from the sensitivity analysis for parameter L (Theoretical $u_c$ = 0.15 [m/s]).

Similar analysis were conducted for all the parameters outlined in table 4.6, following these analysis it was evident that the dynamic viscosity parameter (used to control the flow Reynold's number) has the largest influence on the accuracy. The results shown in table 4.8 demonstrate that by increasing Reynolds number the errors become larger

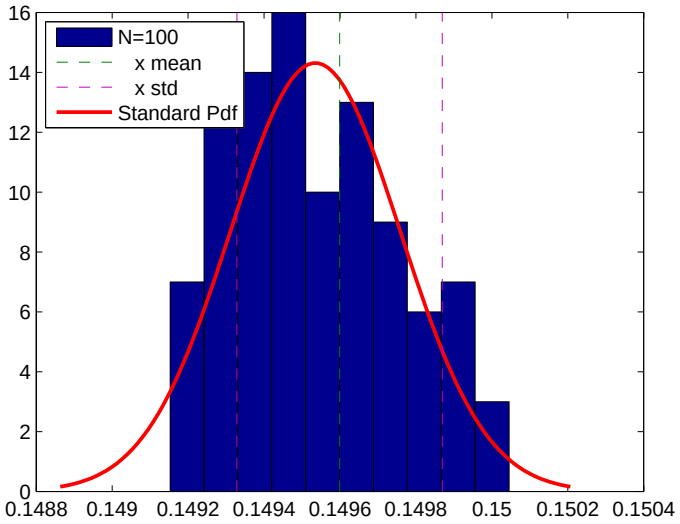


FIGURE 4.4: Histogram including PDF for the results obtained for $u_c$ using the Parameter L=8[m].

and the accuracy becomes lower. However, for the range of Reynolds number considered here (150-15000) the model demonstrated reasonable predictive capabilities.

| $\mu[Pa \cdot s]$ | $Re_b$ | $C_f$ | $C_f$[38] | Error % | Accuracy % |
|---|---|---|---|---|---|
| 1 | 150 | 0.085 | 0.08 | 5.8823529412 | ±1.88 |
| 0.5 | 300 | 0.0389 | 0.04 | 2.75 | ±5.48 |
| 0.2 | 750 | 0.0143 | 0.016 | 10.625 | ±10.2 |
| 0.1 | 1500 | 0.00687 | 0.008 | 14.125 | ±14.5 |
| 0.01 | 15000 | 0.00542 | 0.0073325044 | 26.0825534983 | ±18.8 |

TABLE 4.8: Results for the Errors and uncertainty estimation for parameter $\mu$.

### 4.3.2 Physical uncertainty

Physical uncertainty was investigated using a validation study to confirm the assumption that the flow is fully developed. Patel and Head [38] define the following criteria that describe the characteristics of a fully developed flow:

- The skin friction coefficient is related to the Reynolds number by an established law;
- The velocity distribution in the wall region follows the well known law of the wall;
- There is no intermittency present.

Here we consider the flow in a plane channel with Re range 300-3000. The results for Re against $C_f$ are shown in 4.5. The results show that profile for $C_f$ obtained by our model closely follows the empirical relation reported by Patel and Head [38].

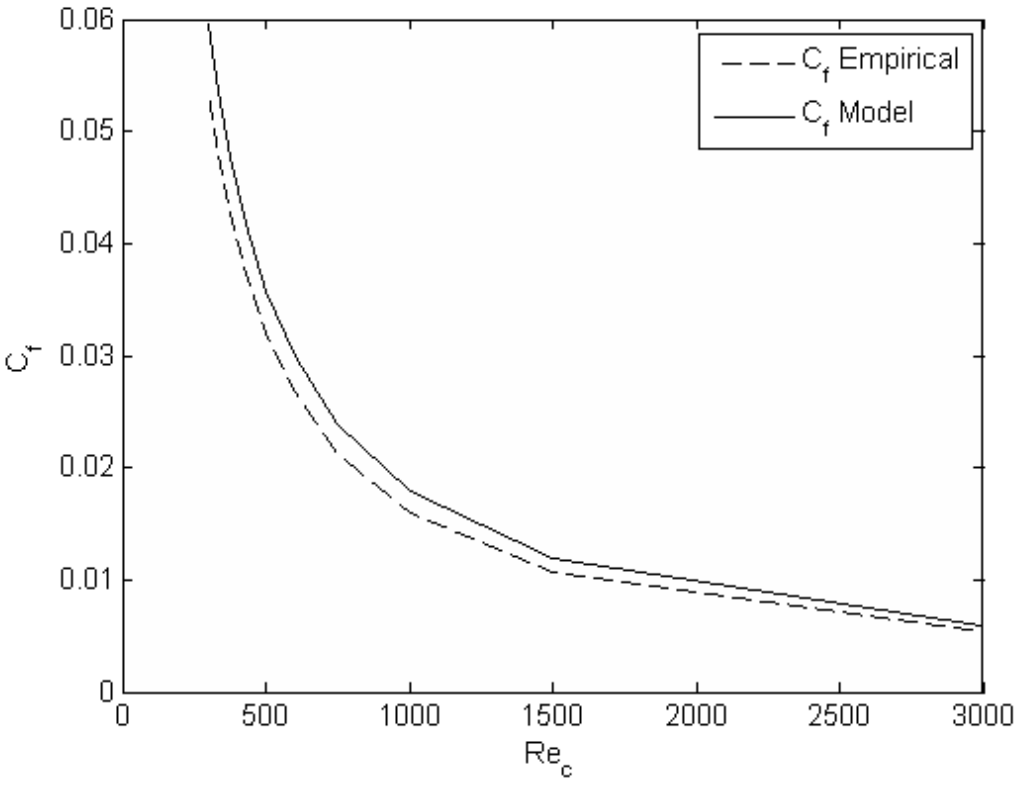


FIGURE 4.5: Comparison of the empirical and numerical $C_f$ for different Re.

The velocity distribution in the wall region was obtained by collecting data from 10 measurement points which are located at mid-channel and extend from the wall to the channel centre in the y-direction. Data for the streamwise velocity (u) was collected at different time-steps. In order to obtain the velocity distribution near the wall, the data from the measurement points were averaged and plotted in log-format, see figure 4.6. The results confirm that the velocity distribution follows the law of the wall.

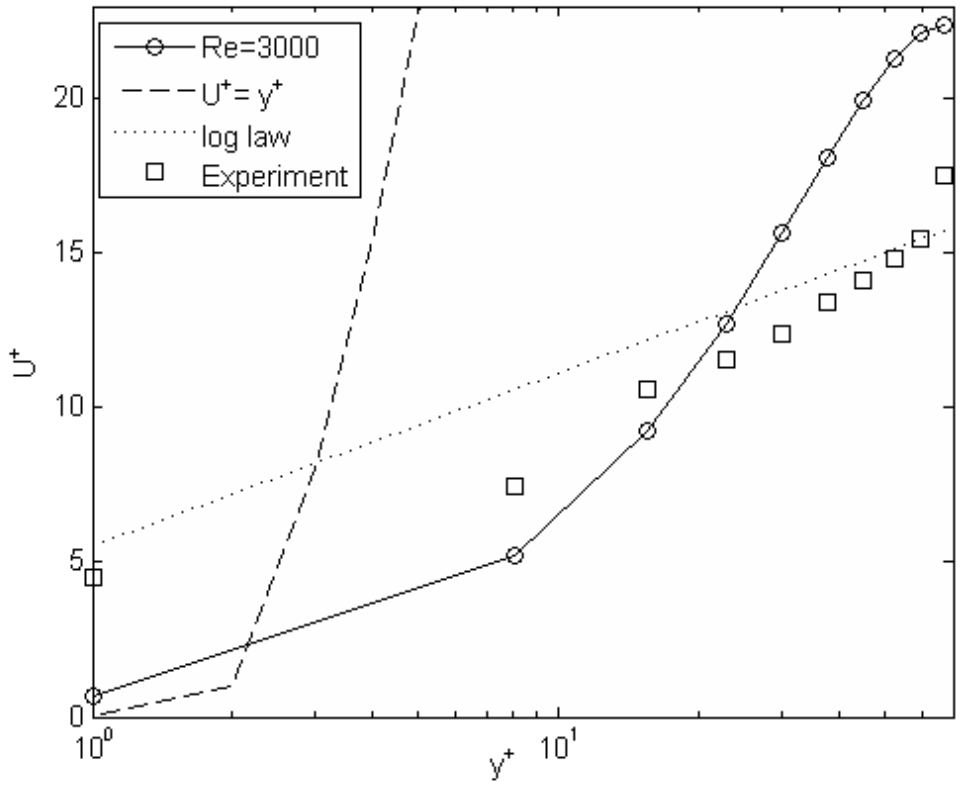


FIGURE 4.6: Comparison of the velocity distribution ($U^+$) in log-format using theory (law of the wall), experiment ([6]) and present simulation.

Comparison with the experimental data reported in Pope [6] is given in table 4.9. The results show that the model over-predicts the value of $U^+$ compared with the experimental values. The maximum error was observed at the overlap region and the lowest accuracy was at the viscous sublayer.

| Location | $y^+$ | $U^+$ [6] | $U^+$[Model] | Error % | Accuracy% |
|---|---|---|---|---|---|
| Viscous sublayer | 5 | 4.52599 | 5.2234 | 13.3516483516 | ±0.1 |
| Buffer layer | 30 | 13.3945 | 15.6854046841 | 14.6053272469 | ±0.006 |
| Overlap region | 50 | 14.8012 | 19.9743981134 | 25.8991439144 | ±0.03 |
| Outer layer | 70 | 17.4924 | 22.1187152984 | 20.9158408884 | ±0.024 |

TABLE 4.9: comparison of the simulation results for $U^+$ with experiments from Pope [6]

Previous research by Patel and Head [38] had shown that channel flow has an intermittent character in a certain region of Reynolds numbers close to the critical Reynolds number. By this we mean that the flow is occasionally laminar and occasionally turbulent. This intermittent behaviour plays an important role in the laminar-turbulent transition, which Schlichting [10] classifies as a stability problem. Such a problem is beyond the scope of this work. Here, the fully developed condition was imposed by prescribing a parabolic velocity profile at the inlet.

### 4.3.3 Dependence on Reynolds number

Further validation of our model was carried out by studying the dependence of certain flow variables on Re. The objective of this study was to validate the results by comparing them with the observations reported by Leonardi et al [23]. Here the effects of Reynolds number on the wall shear stress and the pressure were investigated using line integration to validate that the dependence of these variables decreases with increasing Reynolds number. The friction and pressure drag were calculated using line integration along the distance between two consecutive elements ($\lambda$). The frictional drag ($\overline{C}_f$) and the pressure drag ($\overline{P}_d$) were calculated as the integrals of the wall shear stress and pressure distributions along the wall as follows:

$$\overline{C}_f = \lambda^{-1} \int_0^{\lambda} \langle C_f \rangle \, \vec{s} \cdot \vec{x} \; ds \tag{4.1}$$

and

$$\overline{P}_d = \lambda^{-1} \int_0^{\lambda} \langle P \rangle \, \vec{s} \cdot \vec{x} \; ds, \tag{4.2}$$

where $s$ is a coordinate that follows the wall contour, $\vec{n}$ is a unit vector normal to the wall, and $\vec{x}$ is the unit vector along $x$, angular brackets denote averaging with respect to y and t. Figure 4.7 shows the dependence of frictional and pressure drags on the Reynolds number ($Re_b$). The results confirm that $\overline{C_f}$ decreases as Reynolds number increases and $\overline{P_d}$ is independent of Reynolds number for all flow configurations considered. The same observation was made using DNS by Leonardi et al [23].

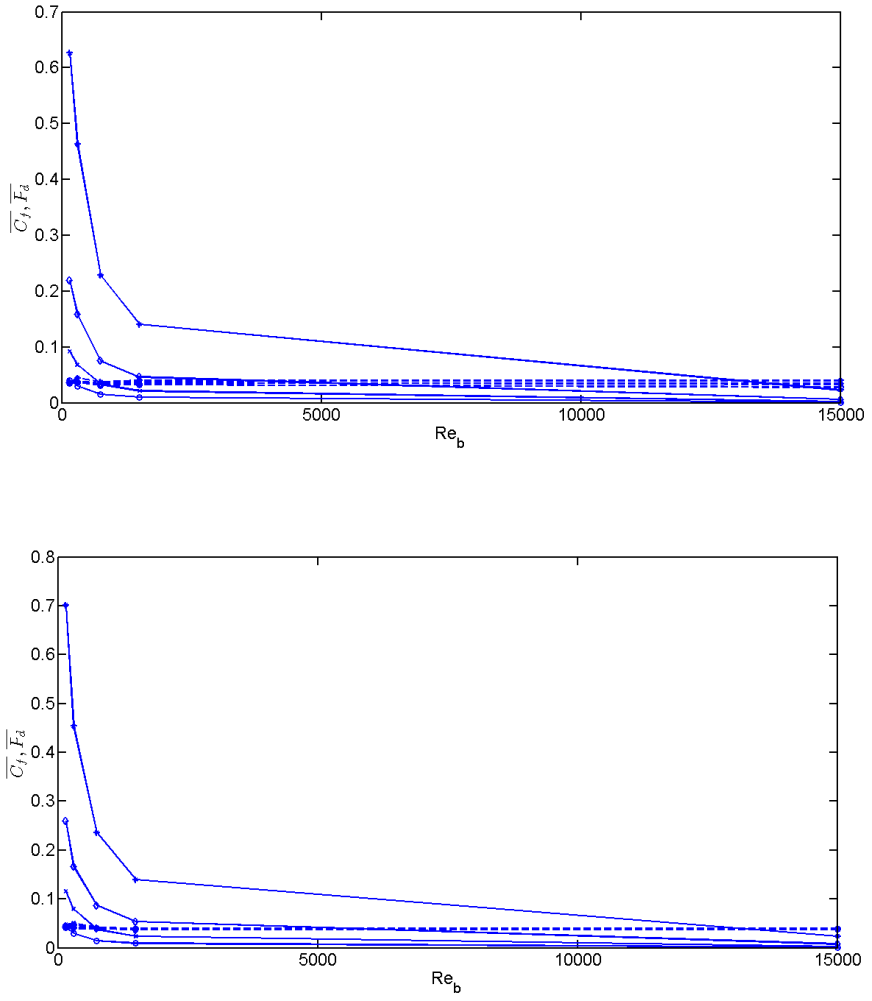


FIGURE 4.7: Dependence on Re for square (top) and triangular (bottom) roughness: symbols = $w/k$ ($w/k = 1 = (\circ), w/k = 3 = (\times), w/k = 7(\diamond)$ and $w/k = 17 = (*)$); solid lines = $\overline{C}_f$ and dashed lines = $\overline{P}_d$.

# Chapter 5

# Analysis and results

In this chapter we present the analysis and results from the numerical simulations. Section 5.1 outlines the methods used to collect data. Section 5.2 is concerned with the statistical properties of the flow. Here the velocity time-history data was used to plot the autocorrelation, two-point correlation and the energy spectrum to give insight into the statistical properties of the flow. In addition, the energy spectrum plots were used to validate the claim that the model described in chapter 3 is capable of resolving the large eddy structures, i.e. ILES. In section 5.3 we present visualizations of the evolution of the flow field in time. We start be showing the mean velocity vectors and streamlines, including a comparison with the LES of Cui et al. [8]. Then, we consider the evolution of the streamlines in time for the different surfaces considered here and demonstrate how the roughness geometry influences the ejection motion observed in the groove between the roughness elements. In section 5.4 we present a detailed investigation into the effects of surface roughness on the flow using velocity profile plots at different x-locations and wall shear stress and pressure plots. The resistance components presented in this section are used to identify the flow separation and attachment locations along the roughened wall. Finally, section 5.5 presents the results for the visualization of the instantaneous velocity flow fields.

## 5.1 Data collection

### 5.1.1 Point data

The data was collected by inserting point measurement probes at certain locations in the flow domain. The sketch shown in Figure 5.1 illustrates the locations of the data points. The points are distributed as follows:

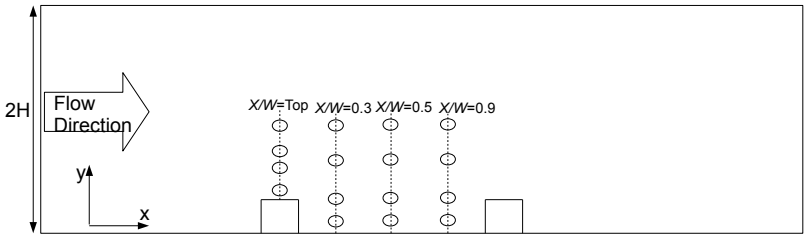


FIGURE 5.1: Sketch of an example of the locations of points and line probes used to collect and plot the data.

- In the streamwise direction, the first point is located at the top of the roughness element followed by three points at the groove between the elements. For these points, the distance x is measured from the back face of the upstream element and normalized by the spacing between the elements (w). Hence, x/w = 0.5 is at the centre of the cavity between the roughness elements;
- In the spanwise direction, the distance y is measured from the wall and normalized by half the channel height (H). The distribution considered here (y/H = 0.015, 0.34, 0.67, 0.1) corresponds to where we expect the different regions of the flow described by the law of the wall (i.e. viscous region, buffer layer, log/overlap region and outer/core region).

A similar approach was used to collect the data from the various surfaces considered here. The data points where placed along a single roughness length ($\lambda$) in the middle of the roughness region. Point data was used to collect the results of the velocity time history which in turn was used to calculate the one- and two- point correlations used to validate the statistical properties of the results. They was also used to calculate the energy spectrum, which is useful in examining the resolved and modelled motions. In addition, point data was also used to plot the wall shear stress and the pressure distributions along $\lambda$ for the various surface considered here.

### 5.1.2 Line data

In COMSOL, line data plots gives the measurements along a predefined line inserted at certain locations in the flow domain. Line data was used to plot the velocity profile at

different x-locations, see appendix C.2, that correspond the the different x/w distribution shown in figure 5.1 and extend up to H in the spanwise direction. Line data plots were also used to plot the balance between the reaction forces in the lower and upper walls (see appendix C.5). Here the lines extend along the upper walls in the streamwise direction.

### 5.1.3 Visualization

Flow visualizations were obtained using COMSOL's built-in post-processing tools. Here two types of visualizations were utilized; streamlines and contour maps. Section 5.3 and appendix C gives the velocity streamlines for the different flow configurations. The contour plots were obtained for the following flow variables; streamwise velocity ($u$), spanwise velocity ($v$), friction velocity ($u_\tau$), pressure gradient ($p_x$) and the non-dimensional parameter $y^+$. The flow visualizations are given in appendix C

## 5.2 Velocity and energy spectrum

### 5.2.1 Velocity time-history and autocorrelation

The velocity time history was collected using point plots for the different surfaces at the locations shown in figure 5.1. Here we present the data for a plane channel in order to validate the statistical properties of the data obtained from the simulation. It is expected that as the flow evolves in time, the velocity components will eventually reach a steady state regardless of the spanwise location. This was indeed the case as shown in figure 5.2. The theoretical limits for the streamwise velocity, shown in figure 5.2, were adopted from Pope [6]. For the location close to the wall ($y/H = 0.015$) we expect the velocity to be within 10 % of the bulk velocity. In the channel centre ($y/H = 1$) we expect the centre-line velocity to be $u_c = \frac{3}{2}u_b$. For the spanwise velocity, the limits presented in figure 5.3 follows from the assumption that the magnitude of $v$ is orders of magnitude smaller than $u$. Therefore, one could expect that $v$ will eventually reach zero as the flow becomes fully developed. However, we expect that this assumption would not hold at the channel centre where the core flow is located as shown in figure 5.3.

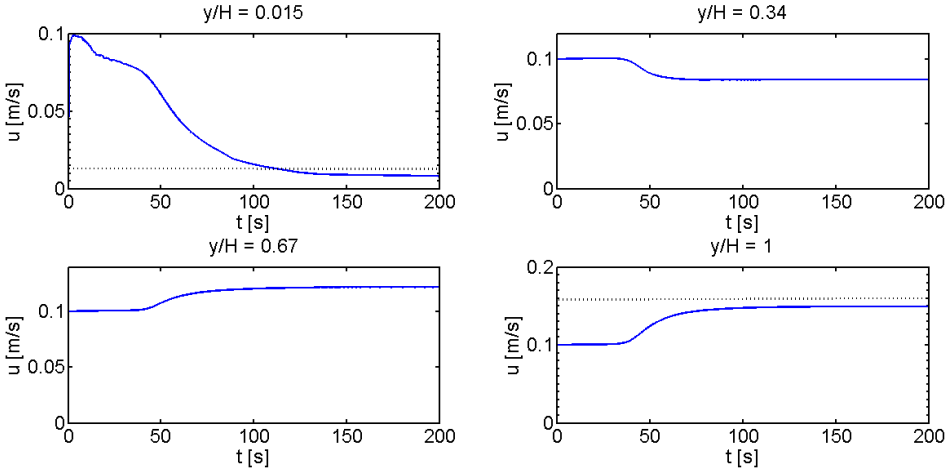


FIGURE 5.2: Streamwise velocity (u) time history for a plane channel; solid line (measurements), dashed line (theory).

The time history data was used to calculate the autocorrelation of the velocity to investigate the statistical properties of the flow. Autocorrelation is a 'two-point correlation' in time, i.e. the correlation of fluctuation with a separation in time. If $u'$ is the fluctuation, the autocorrelation reads

$$B_{11}(t^A, \widehat{t}) = \overline{u'(t^A)u'(t^A + \widehat{t})}, \tag{5.1}$$

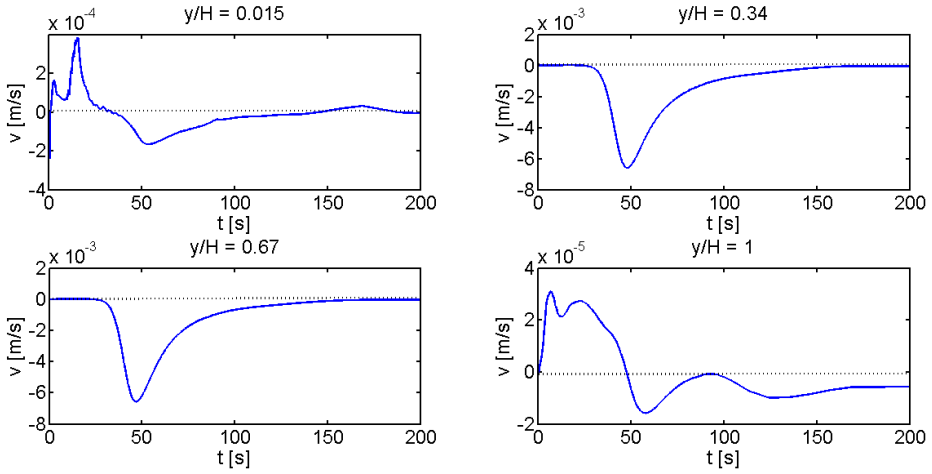


FIGURE 5.3: Spanwise velocity (v) time history for a plane channel; solid line (measurements), dashed line (theory).

where $\widehat{t} = t^C - t^A$, is the time separation between time A and C. If the mean flow is steady, the 'time direction' is homogeneous and $B_{11}$ is independent of $t^A$. In this case the autocorrelation depends only on the time separation $(\widehat{t})$ i.e.

$$B_{11}(\widehat{t}) = \overline{u'(t)u'(t+\widehat{t})}, \tag{5.2}$$

where the right hand side is time averaged over t. The normalized autocorrelation reads

$$B_{11}^{norm}(\widehat{t}) = \frac{1}{u_{RMS}^2}\overline{u'(t)u'(t+\widehat{t})}. \tag{5.3}$$

Based on the definitions given here, a Matlab script (see appendix B) was written to plot the autocorrelation for $u$ and $v$ and compare them with the DNS of Pope [6] as shown in figure 5.4. The results show that autocorrelations obtained using ILES follow the same general trends observed for a typical autocorrelation plot. The deviation from the DNS profile for a separation (s) below 1 was expected due to the limitation of ILES.

The autocorrelation plots were also useful in investigating the time scale of the large eddies. A rapid drop from 1 to 0 indicates a short time time scale, where slower drop indicates a larger time scale. For streamwise velocity, the shortest time scale was observed at the channel centre (y/H = 1). As we move closer to the wall, the eddy time scale becomes larger. Similar observations were made from the spanwise velocity, however, the longest time scale was observed in the buffer region (y/H = 0.34).

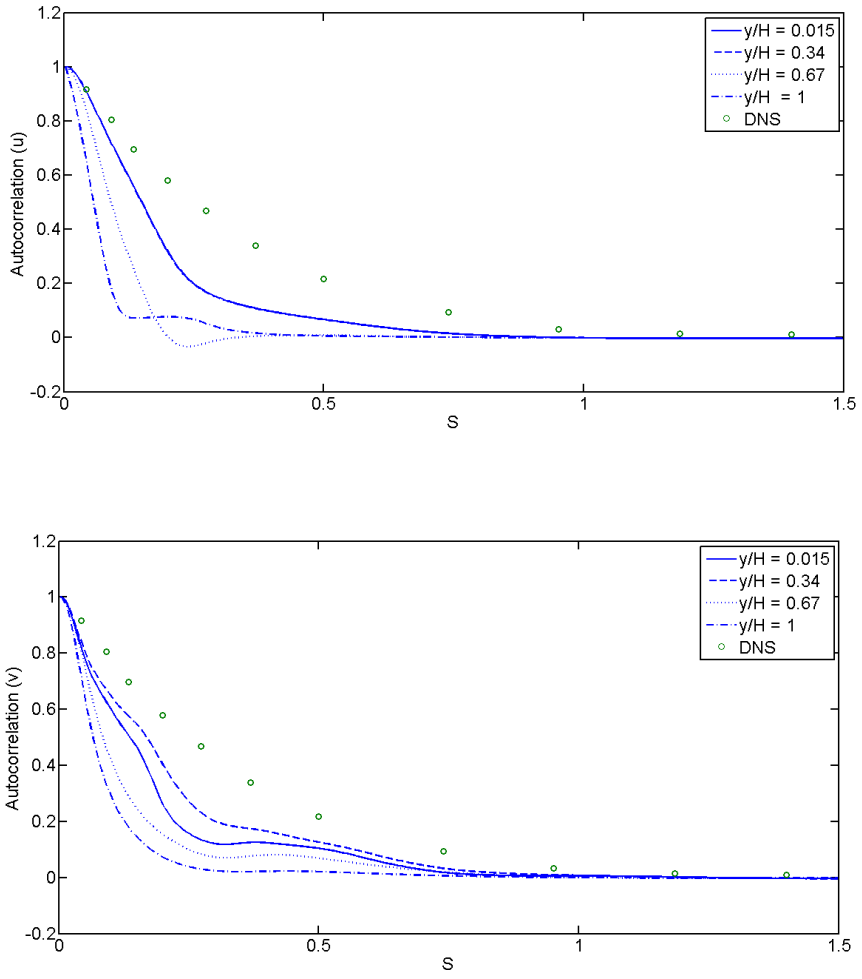


FIGURE 5.4: One point velocity-time correlation plots compared with the DNS of Pope [6]: Top (u velocity), Bottom (v velocity).

### 5.2.2 Two-point correlation

Two point correlations are useful when describing some characteristics of the turbulence. We start by picking two points along the $y$ axis, say $y^A$ and $y^C$, and sample the fluctuating velocity in the $y$ direction. We can then form the correlation of $u^{'}$ at these points as

$$B_{11}(y^A, y^C) = \overline{u'(y^A)u'(y^C)}, \tag{5.4}$$

often expressed as

$$B_{11}(y^A, \widehat{y}) = \overline{(u'(y^A)u'(y^A + \widehat{y})}, \tag{5.5}$$

where $\widehat{y} = y^C - y^A$ is the separation distance between point A and C.

It is obvious that if we move point A and C closer to each other $B_{11}$ increases; when the points are moved so close that they merge, then $B_{11} = \overline{u'^2(y^A)}$. If on the other hand we move point C further and further away from point A, then $B_{11}$ will go to zero.

It is convenient to normalize $B_{11}$ so that it varies between -1 and +1. The normalized two-point correlation reads:

$$B_{11}^{norm}(y^A, \widehat{y}) = \frac{1}{u_{RMS}(y^A)u_{RMS}(y^A + \widehat{y})} \overline{u'(y^A)u'(y^A + \widehat{y})}, \tag{5.6}$$

where the subscript RMS denotes root-mean-square, which for $u^{'}$ is defined as

$$u_{RMS} = \left(\overline{u'^2}\right)^{1/2} \tag{5.7}$$

A Matlab script was written to calculate the two-point correlations (see appendix B) and the profiles for u and v were compared with the DNS of Kim et al. [7], as shown in figure 5.5. The profiles obtained using ILES follow the same general trend of the DNS. As with the autocorrelation, deviations from the DNS profile are expected due to the limitations of the ILES.

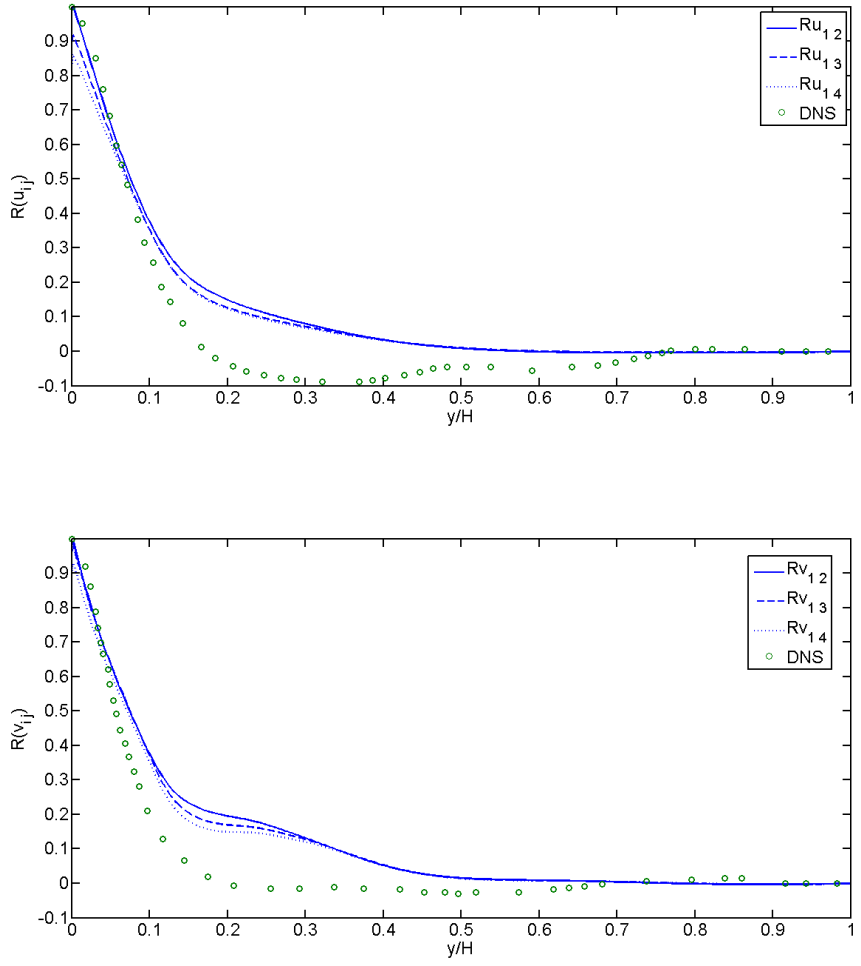


FIGURE 5.5: Two-point correlation velocity plots compared with the DNS of Kim et al. [7]: Top (u velocity), Bottom (v velocity)

### 5.2.3 Energy spectrum

One way to verify that the model resolves the turbulence properly, i.e. comparable to LES, is to look at the spectra of the resolved turbulence. One can analyze the time history of a variable, here its velocity, at a point and do a Fast Fourier Transform (FFT) of that single to get the Fourier coefficient $a_i$ and then plot $a_i^2$. Then you get the frequency spectrum, i.e. how much energy resides in each frequency. The Matlab code (given in appendix B) does a FFT of the fluctuating velocity,$u^{'}$, ($u =< u > +u^{'}$) and plots $a_i^2$. In a well resolved LES we want to have the cut-off in the inertial sub-range where the kinetic energy decays as the wave number (or frequencies) up to the power of -5/3. Therefore we want the resolved turbulence to have a behaviour like this for high frequencies. As shown in figure 5.6 this is indeed the case.

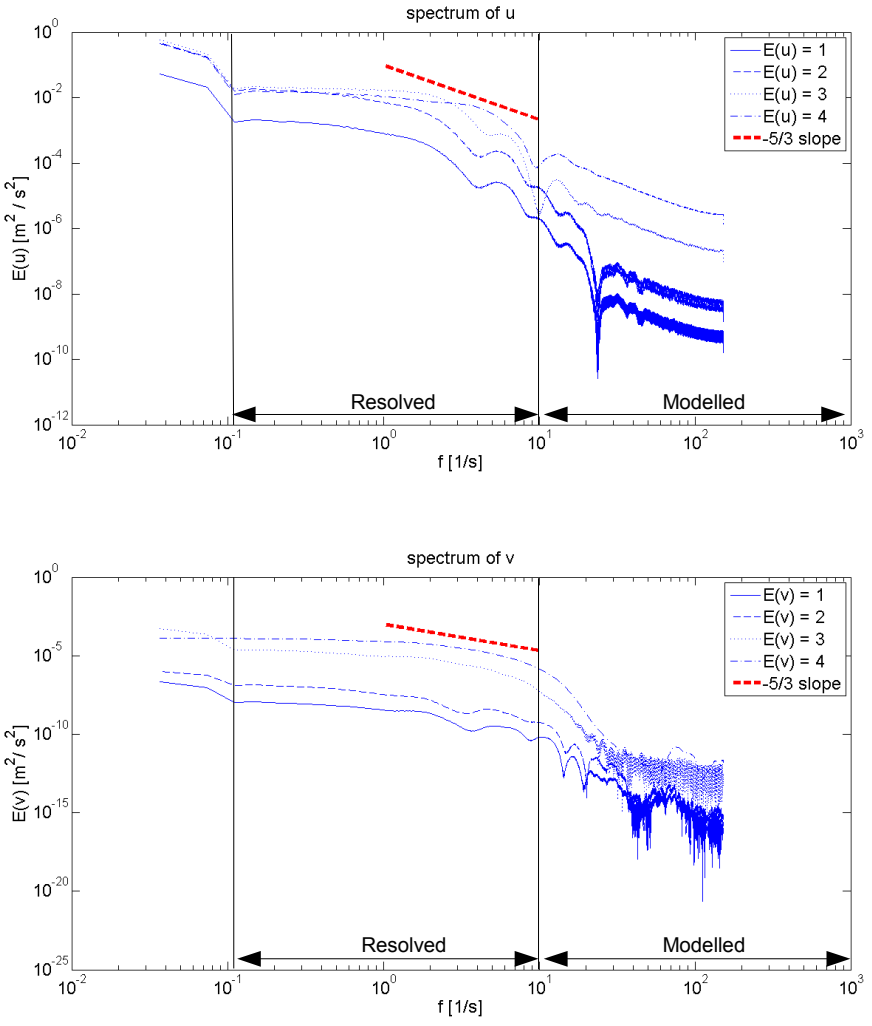


FIGURE 5.6: Energy spectrum at different y- locations showing the resolved and modelled motions: Top (u velocity), Bottom (v velocity).

## 5.3 Flow Evolution

### 5.3.1 Mean velocity vectors and streamlines

The mean velocity vectors at different locations in the channel were used to investigate the velocity profile at different streamwise locations for the different rough surfaces. Figure 5.7 shows that for $w/k = 1$ the velocity profiles appear similar regardless of streamwise location, i.e. it exhibits a d-type behavior. The results, shown in figure 5.7 a), resemble the velocity profile in a flat channel with reduced height of $H - k$, similar findings were reported by [8]. Cui et al. [8] explains that the roughness layer has little impact on the core flow except that the roughness elements block the mass flow within the roughness layer, displacing the flow up by a distance of the roughness height. The velocity magnitude in the cavities between the roughness elements is small.

For $w/k = 3$, see figure 5.7 b), and $w/k = 7$, not shown, the roughness disturbs the mean flow to a greater extent. Here, the results show that the velocity profiles at different location differ significantly. Cui et al [8] explains that the flow responds to expansion and contraction of the passage with deceleration and acceleration. Separation zones behind the ribs are longer than for d-type roughness where they are necessarily of length $w$ [8]. For $w/k = 17$ the roughness exhibits a k- type behavior. This was demonstrated by the dependence of the velocity on the distribution on the streamwise location. Furthermore, separation, reattachment, and further detachment occur in the grooves between the roughness elements. The results clearly show the effectiveness of k-type roughness in augmenting the momentum exchange between the roughness layer and the outer flow.

Streamlines for three roughness distributions are displayed in figure 5.8 and compared with the streamlines from the LES of Cui et al. [8]. For d-type roughness, see figure 5.8 a), the streamlines beyond the roughness height are nearly parallel and a vortex fills the cavity between the roughness elements. This vortex has similar properties to those encountered in the Lid-Driven cavity problem, see [8]. For intermediate roughness, see figure 5.8 b), a vortex of the same size as the groove ($w$) is formed between the roughness elements. This vortex prevents the outer flow from reattaching to the channel floor within the groove, and a smaller vortex with opposite circulation is found in the lower corner behind the roughness element [8]. Streamlines above the cavity are still nearly parallel except near the top of the roughness element.

Streamlines for k-type roughness, see figure 5.8 c), reveal a number of separation zones associated with the roughness geometry. For the square elements a small separation zone is formed on the top of the element as the sharp front edge of the square block deflects the flow from the previous groove. A large separation region is downstream of the

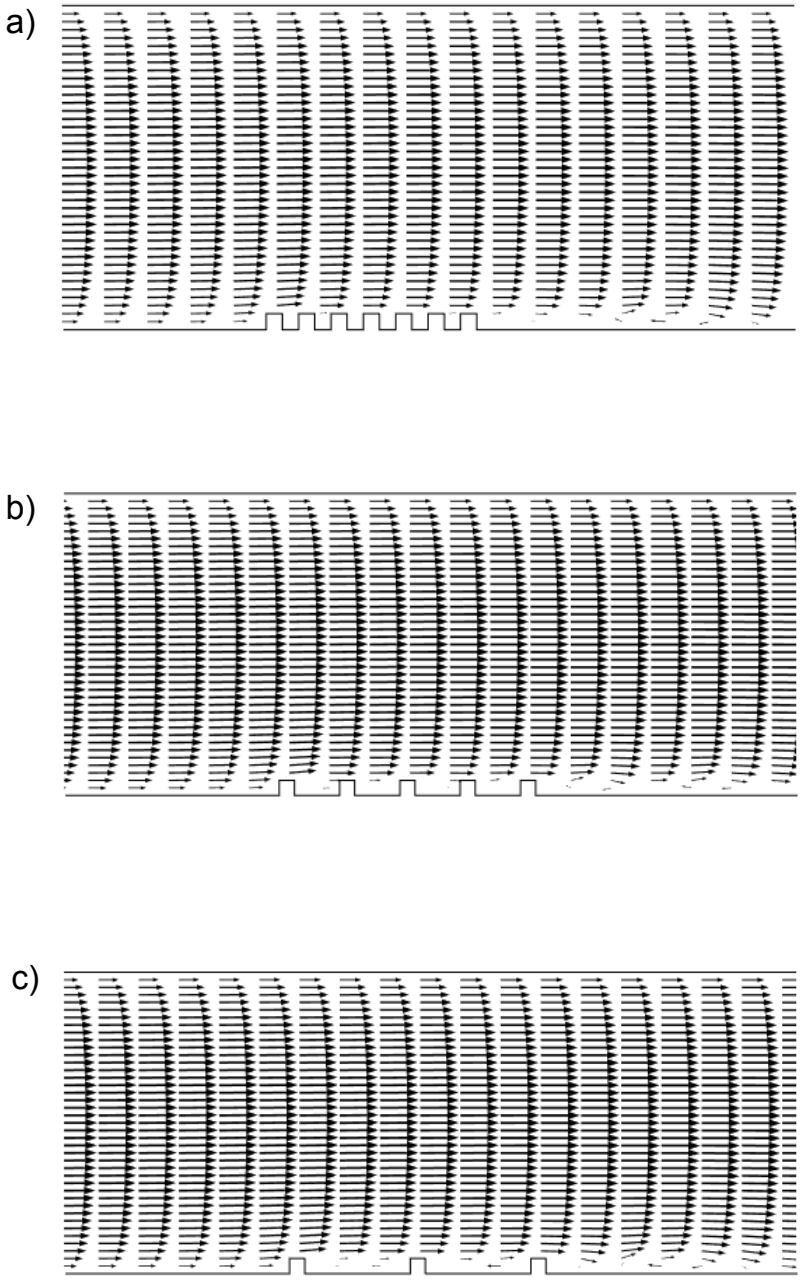


FIGURE 5.7: Mean velocity vectors at different locations in the channel: a) d-type; b) intermediate; c) k-type.

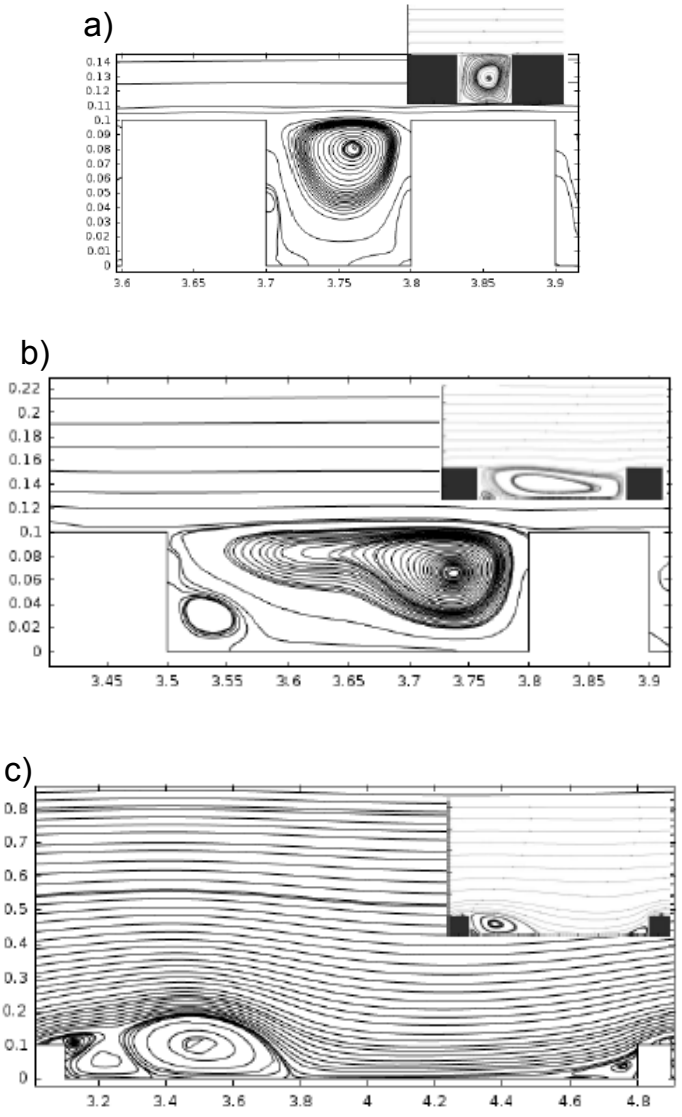


FIGURE 5.8: Mean streamlines for a) d-type, b) intermediate, and c) k-type compared with Cui et al [8] (inset).

square block accompanied by a a small vortex at the lower corner behind the roughness element. The flow reattaches to the channel floor and detaches again, forming a vortex upstream of the next roughness element. Interestingly, the reattachment point is about four times the roughness height [8]. Though streamlines far away from the roughness element are nearly parallel, in the lower half of the channel they undulate in response to the roughness geometry.

### 5.3.2 Evolution of velocity streamlines in time

The evolution of the velocity streamlines in time for the various surfaces considered here are given in appendix C.1. The results show the velocity streamlines at different time steps. The streamline plots were useful in visualizing the recirculating motion formed between the roughness elements close to the wall. The streamlines for the d-type surfaces ($w/k = 1$) show that the recirculation between the grooves reaches a quasi-steady state as the flow evolves over time. The ejection of fluid from the grooves onto the mean flow, reported by Djenidi et al [20], was also observed here. The results demonstrate that the roughness geometry has a strong influence on the direction of this ejection motion. Figure 5.9 shows that the ejected fluid is projected at angle that follows the surface contours. For square roughness, the fluid is ejected upwards following the 90 degree sharp corners that make up the square elements. For triangular roughness, the fluid is ejected upwards at a 60 degree angle. This suggests that square roughness will eject the bulk of the fluid from the grooves directly onto the mean flow. On the other hand, triangular roughness ejects the bulk of the fluid onto the next groove. The result is that triangular roughness elements produce a more stable recirculation in the grooves compared to the square elements.

For intermediate roughness ($w/k = 3$ and $w/k = 7$) the streamlines suggest a combination of d- and k- type behaviours. Our results show that for $w/k = 3$ d- type behaviour dominates the flow, where for $w/k = 7$ k- type behaviour is dominant. The velocity streamlines for $w/k = 3$ show that two recirculation regions are formed in the grooves at $t = 10s$, where the recirculation spans the entire groove. As the flow evolves in time, the flow is accelerated and the recirculation regions feed into each other and overshoot into the next groove. Eventually, the flow reaches a quasi-steady state similar to the one observed for the d- type surface. For $w/k = 7$, two recirculation regions are formed within the grooves, however, their size does not span the entire groove. Once the flow has reached the quasi-steady state, unstable recirculation that spans the entire groove is formed. The recirculation is somewhat similar to the one observed over the $w/k = 3$, however, the recirculation here is stretched due to the increase in distance between the elements, hence why the recirculation becomes unstable.

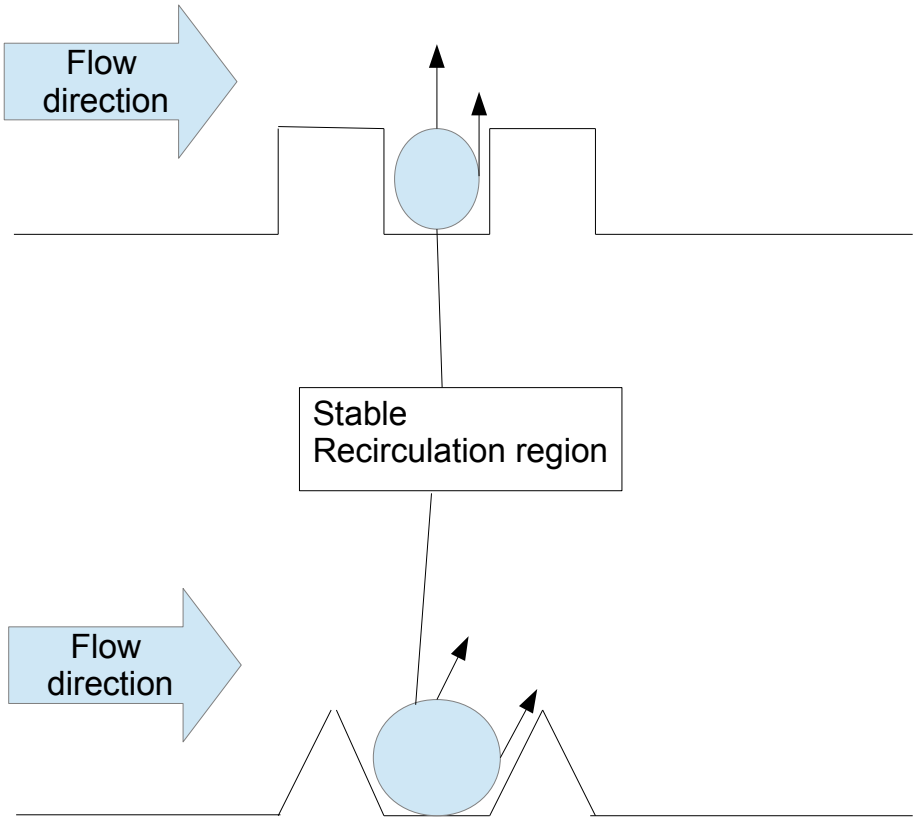


FIGURE 5.9: Illustration of the fluid ejection observed over d-type roughness for square and triangular roughness.

Results for the k-type roughness ($w/k = 17$) show that a recirculation zone behind the roughness element is formed at $t = 10s$. The recirculation regions extends a distance of approximately four times the roughness height downstream from the roughness element. As the flow evolves, the recirculation region moves downstream until it eventually reaches the second roughness element downstream and the fluid is ejected into the mean flow. Figure 5.10 shows that the roughness geometry influences the direction of the fluid ejection. The results demonstrate that for square roughness the recirculation is stretched to span the entire groove at the final time step. On the other hand, a second recirculation region is formed at the front side of the trailing element for triangular roughness.

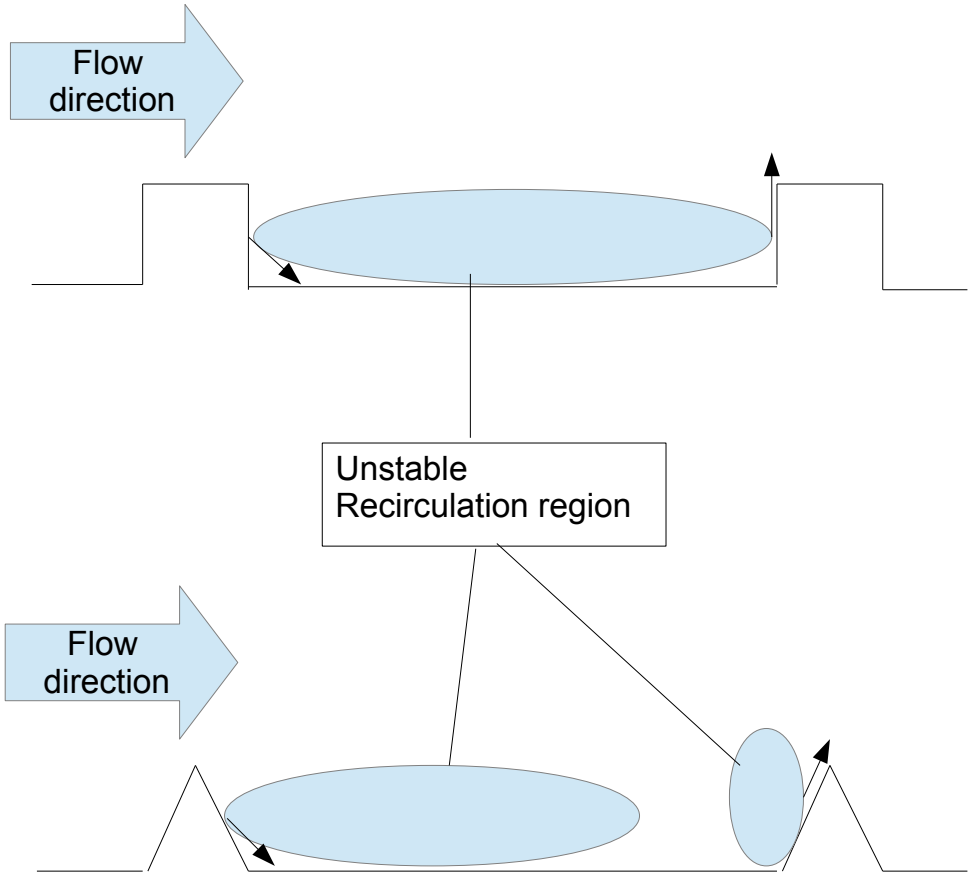


FIGURE 5.10: Illustration of the fluid ejection observed over k-type roughness for square and triangular roughness.

## 5.4 Effects of surface roughness

### 5.4.1 Velocity profile at different x-locations

The velocity profiles at different x-locations were used to further investigate the effects of roughness and the roughness geometry on the mean flow. The velocity profile plots within a single roughness distance ($\lambda$) are given in appendix C.2. The velocity profiles were obtained using line plots in the locations outlined in figure 5.1 and the values of u and v were normalized by the bulk velocity ($u_b$). The profiles presented here are for the Reynolds number $1.5 \times 10^4$.

The results show that even though the flow field changes dramatically over the rough wall, the streamwise velocity profiles are not affected beyond some distance (given in table 5.1) from the bottom wall. This observation was made for both roughness geometries considered here. The results for the spanwise velocity profiles are strongly affected by the x-location and the roughness geometry. Based on these observations, we could divide the flow over a rough surface into two regions; an inner region where the flow depends on the roughness geometry, and an outer one where it is essentially independent of the roughness geometry. An estimation of the extent of these layers could be made using the velocity profile plots, as shown in figure 5.11 for square roughness and figure 5.12 for triangular roughness. Here we only consider the d-type surface for illustration. The estimated locations of the inner/outer region overlap are given in table 5.1. Cui et al. [8] states that the beginning of the outer layer is strongly related to the roughness geometry and Reynolds number.

| Surface | $v_{max}$ | $v_{min}$ | Inner/outer location [y/H] |
|---|---|---|---|
| w/k = 1 (s) | 0.015 | -0.02 | 0.2 |
| w/k = 1 (t) | 0.013 | -0.006 | 0.15 |
| w/k = 3 (s) | 0.01 | -0.012 | 0.2 |
| w/k = 3 (t) | 0.012 | -0.012 | 0.25 |
| w/k = 7 (s) | 0.012 | -0.01 | 0.25 |
| w/k = 7 (t) | 0.01 | -0.008 | 0.31 |
| w/k = 17 (s) | 0.045 | -0.025 | 0.5 |
| w/k = 17 (t) | 0.085 | -0.01 | 0.4 |

TABLE 5.1: Results for the magnitude of spanwise velocity and inner/outer regions overlap location

The streamwise velocity profiles were extensively analysed in the work of Cui et al [8]. Therefore, we focus our analysis here to the results obtained for the spanwise velocity. The spanwise velocity was useful in further investigating the ejection and sweeping motions observed in the flow over rough walls. The results in table 5.1 show the

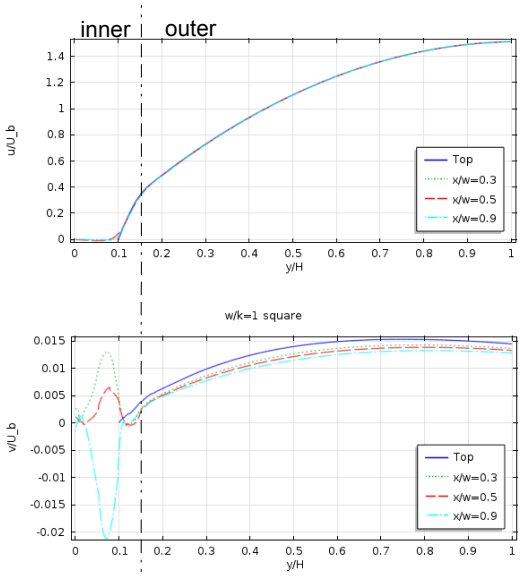


FIGURE 5.11: Velocity profiles used to estimate the overlap location of the inner/outer regions for square d- type roughness.

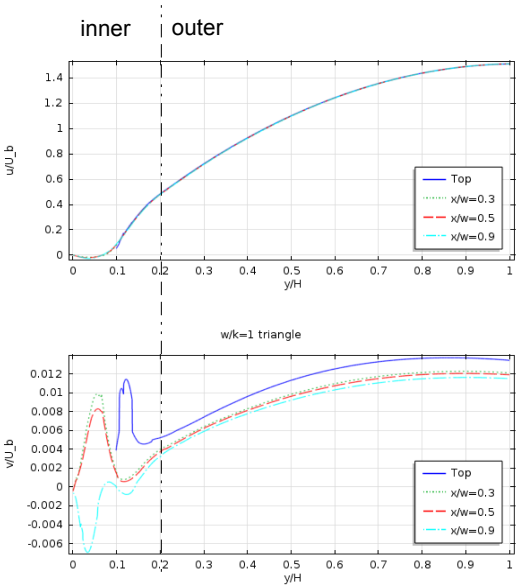


FIGURE 5.12: Velocity profiles used to estimate the overlap location of the inner/outer regions for triangular d- type roughness

magnitude of the ejection ($v_{max}$) and sweep ($v_{min}$) for the different surfaces considered here. The results show that for d- type roughness (w/k = 1) the square roughness has a higher magnitudes of ejection and sweep compared to the triangular roughness. For k-type roughness, however, triangular roughness has a higher magnitude for ejection and square roughness has a higher magnitude for sweep. Overall, it could be argued that the effects of the spanwise velocity are minimal compared to the streamwise velocity. However, the results shown here demonstrate that the spanwise velocity profiles are important in determining the locations and magnitude of the ejection and sweep motions generally observed in the flow over rough surfaces. We have shown here that when combining the two profiles, it is possible to estimate the location where the inner region ends and the outer region begins.

### 5.4.2 Wall shear stress and pressure

Figure 5.13 shows the wall shear stress distribution between successive roughness elements. The friction coefficient, $C_f$, is defined as:

$$C_f = \frac{\tau_w}{0.5\rho U_b^2}, \tag{5.8}$$

where the wall shear stress,$\tau_w$, is calculated from the slope of the velocity at the wall.

Measurements were taken at six locations in the x -direction at the wall. The first three points are located at the front side, top, and back side of the roughness elements. In the cavity, three measurement points were located at x/w = 0.3, 0.5 and 0.9. The results show that for both square and triangular roughness the friction coefficient at the front and back sides of the roughness element is zero. Strong positive friction coefficient was observed in the roughness region, the general trend observed for both surfaces is the increase of $C_f$ along the the front side to the top and a decrease along the top to the backside. However, the maximum value is $C_f$ varies with the different roughness geometry. For square roughness, the magnitude of $C_f$ is lowest for w/k =1 and increases with the increase in w/k. However, for the triangular roughness the results show that starting with w/k =1, $C_f$ decreases for w/k =3 and 7 but reaches the maximum value for w/k=17. At the cavity, both d-type surfaces, w/k = 1, show a uniform distribution of $C_f$ with a small negative value at the centre, x/w = 0.5. These results suggests that for d-type roughness the cavity is filled with separated flow where $C_f$ is negative on the cavity floor. The reversed flow is weak, and the magnitude of $C_f$ is small compared to the intermediate and k-type roughness. The k-type behaviour, which is generally associated with the sign reversals of $C_f$ in the cavity (see Cui et al. [8]), was observed for w/k = 7 over the square roughness, and w/k=3 for the triangular roughness.

Figure 5.14 displays the pressure distribution between two consecutive roughness elements. The pressure coefficient,$C_p$, is defined as:

$$C_p = \frac{\Delta p}{0.5\rho U_b^2} \tag{5.9}$$

For the square roughness elements, the pressure distribution varies with the surface. For w/k= 3 and 7 the pressure coefficient is non-zero at the front side, suggesting an adverse pressure gradient. At the top w/k=3 $C_p$ is zero but for w/k=7 the pressure coefficient remains positive and reaches zero at the back side. For w/k=1 and 17 an adverse pressure

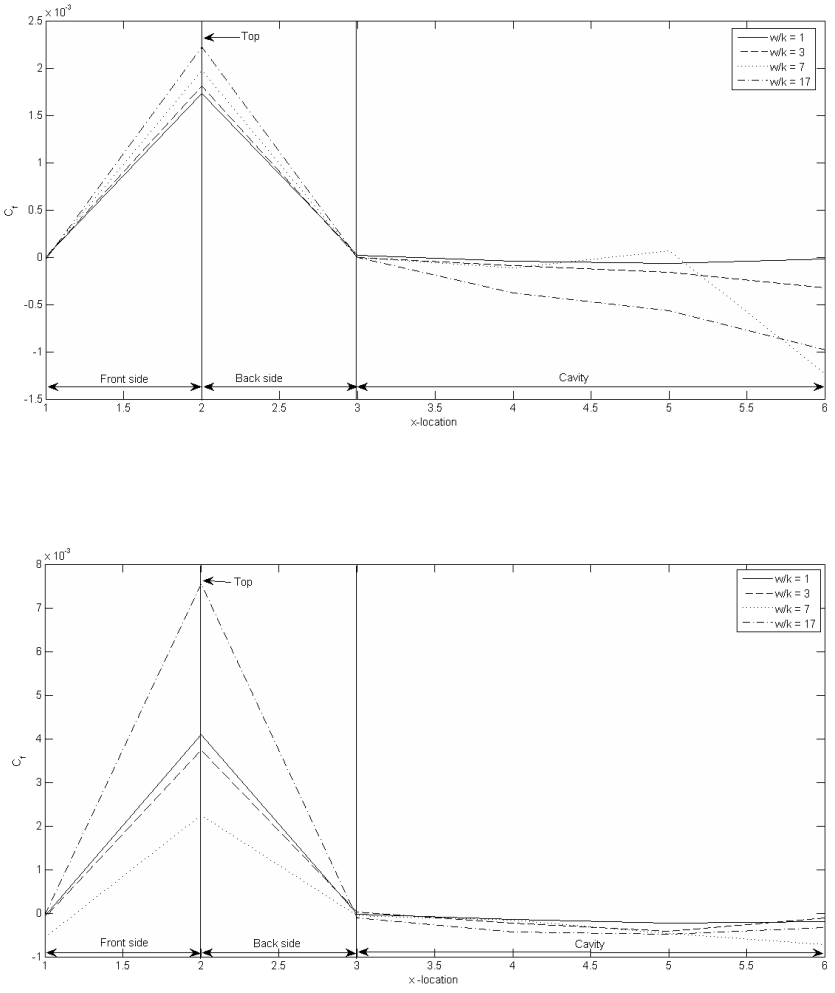


FIGURE 5.13: Wall shear stress distribution along one roughness length ($\lambda$): Top (square), Bottom (triangle).

gradient is observed at the front side and a favourable pressure gradient on the back side. This trend was also observed for all the surfaces with triangular roughness. At the cavity, the pressure coefficient is very small for all surfaces considered compared with rough region. However, for square roughness with w/k = 7 and 17 a small favourable pressure gradient was observed at x/w=0.9.

In order to visualize the friction layer formed, the wall shear stress measurements were used to plot a contour map of the friction velocity defined as

$$u_\tau = \sqrt{\frac{\tau_w}{\rho}}. \tag{5.10}$$

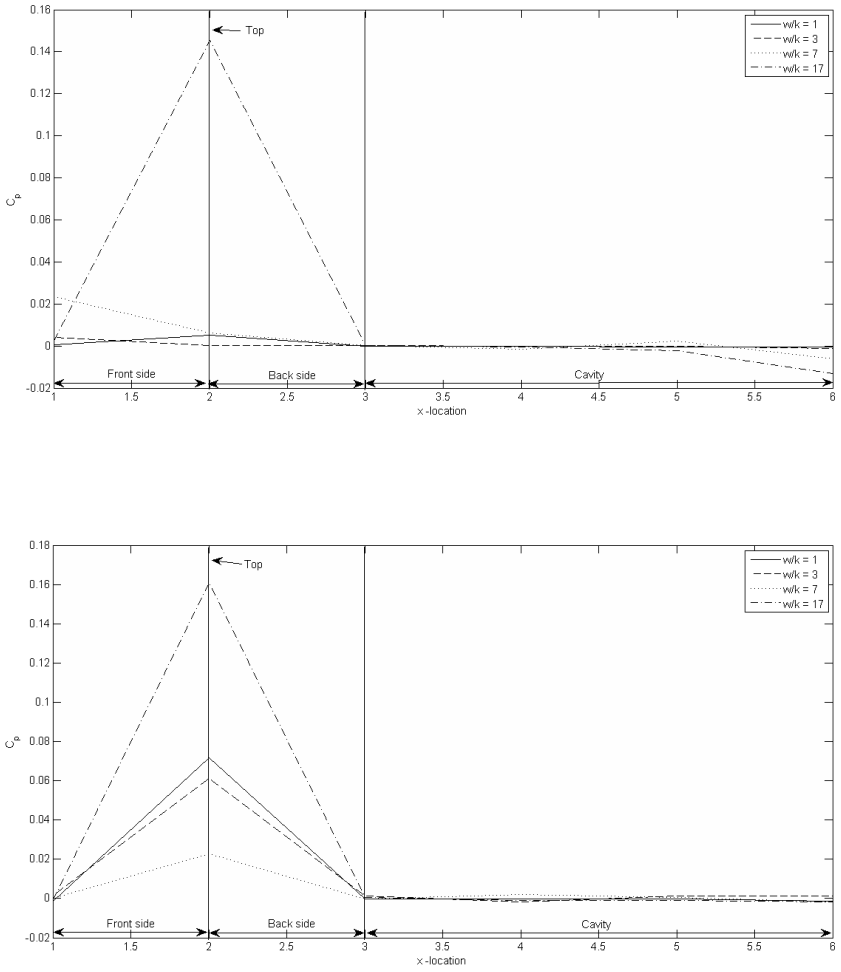


FIGURE 5.14: Pressure distribution along one roughness length ($\lambda$): Top (square), Bottom (triangle)

The flow evolution results, given in appendix C.3 and figure 5.15, show that the shape of the roughness element has a strong influence on the interaction between the inner and outer layers. For square roughness, the maximum friction velocity is located close to the roughness crest plane for w/k=1 and 3, mainly at the leading edge of the roughness element. There is limited interaction between the inner and outer layers. For w/k=7 and 17 the separation between the elements is large enough to expose the friction layer to the mean flow, resulting in a strong interaction between the inner and outer layers. Details of this friction layer are slightly different for the triangular elements, as shown in figure 5.15. Here a localised maximum was observed at the peak of the roughness elements. Due to the shape of the roughness element the flow is decelerated as it approaches the top from the front side and accelerated as it moves from the top along the backside.

Here the interaction between the inner and outer layer does not take place along the entire crest plane, a recirculation zone is formed at the peak of the roughness element which interacts with the mean flow. Similar to the square roughness, for w/k=1 and 3 a relatively stable friction layer is formed above the crest plane resulting in a limited interaction between the inner and outer layers and increasing the separation distance between the roughness elements. This has the same effect of exposing the friction layer to the mean flow.

A visualization of the evolution of the pressure gradients in the flow were also considered. The results given in appendix C.4 and figure 5.16 demonstrated that the roughness geometry has little effect on the overall characteristics of the pressure gradients. However, it was observed the roughness geometry has a direct effect on the magnitude of the pressure gradients. For d-type roughness, an adverse pressure gradient is formed at the leading roughness element and the front side of the subsequent roughness elements. For the square roughness, the magnitude of the pressure gradient is larger because of the sharp corners present in the square geometry. The results show that replacing square elements with triangular ones will reduce the pressure gradient by around 23 %.

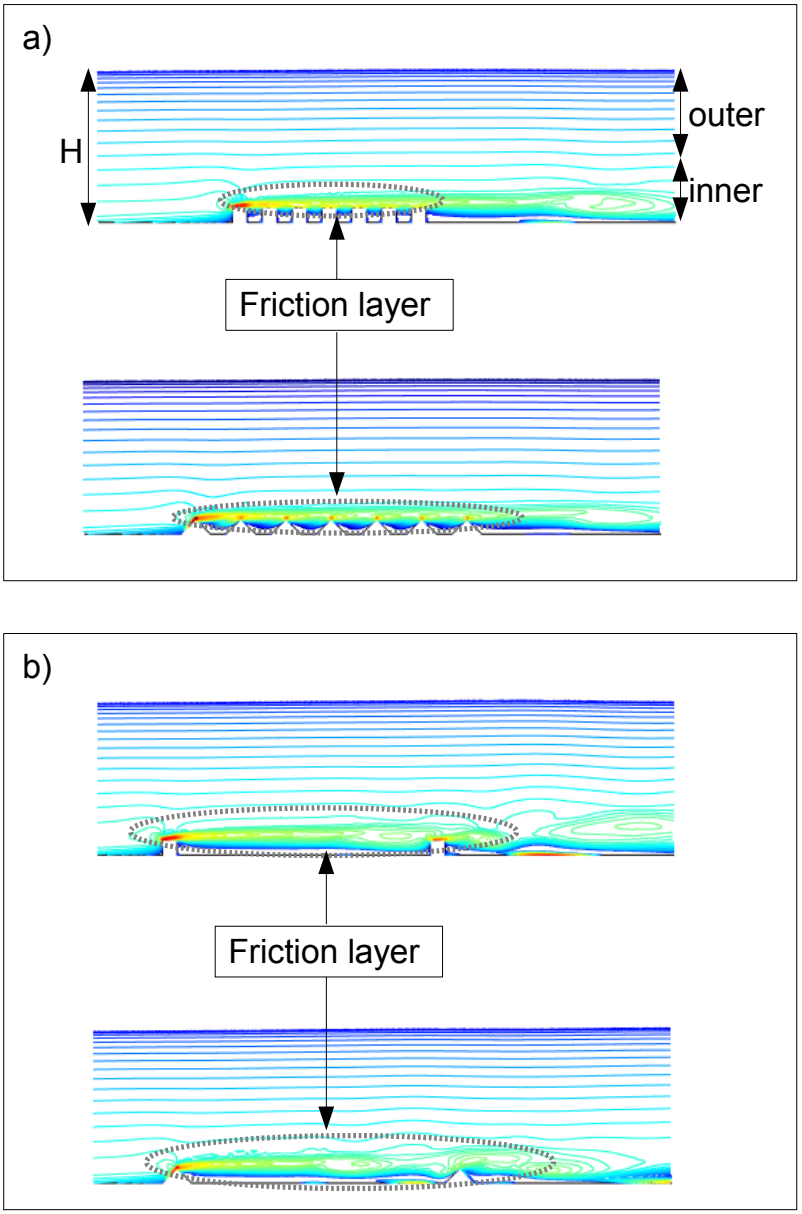


FIGURE 5.15: Visualization of the friction layer using the contour map of the friction velocity ($u_\tau = \sqrt{\tau_w/\rho}$).

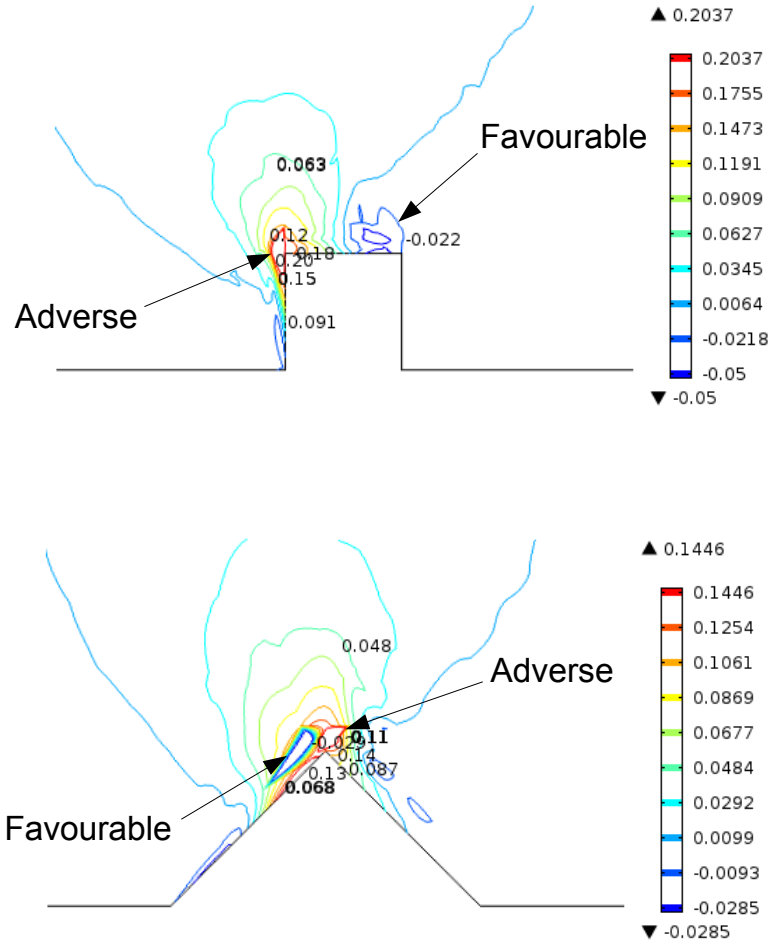


FIGURE 5.16: Visualization of the pressure gradient $p_x$ normalized by $(0.5\rho u_b^2)$.

### 5.4.3 Resistance components

The resistance components were plotted along the lower wall in the streamwise direction using the reaction force operator *reacf ()* in COMSOL. The reaction force operator evaluates the reaction force at each node point where a constraint is applied. This operator is useful when calculating integrals of reaction forces. Here the reaction force in the streamwise *reacf(u)* and spanwise *reacf(v)* were used to investigate the separation and reattachment along the rough wall. The separation condition used to analyse the data in appendix C.5 is based on the arguments of Tritton [5]. Starting with the equation for the rate of change of vorticity

$$\frac{D\omega}{Dt} = \omega \cdot \nabla u + \nu \nabla^2 \omega \tag{5.11}$$

and considering a steady two-dimensional flow for simplicity is sufficient to illustrate the principles involved, although the details of three-dimensional and unsteady flow are considerably more complicated. The restriction to two-dimensional flow is simplifying because it involves vorticity; since only one component of the vorticity is non-zero, we can discuss it as a scalar. Furthermore, the term $\omega \cdot \nabla u = 0$ in the vorticity equation above; the argument is not complicated by the processes contained in this term. Only advection $(u \cdot \nabla \omega)$ and viscous diffusion $(\nu \nabla^2 \omega)$ of vorticity are involved.

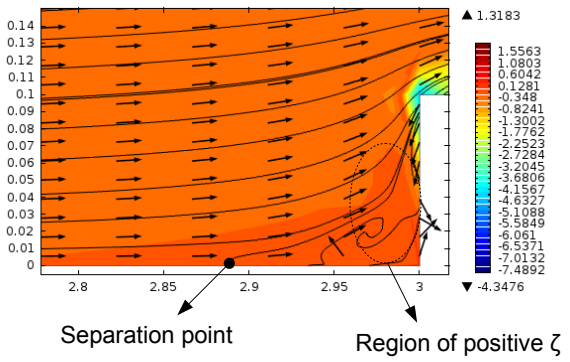


FIGURE 5.17: An illustration of the separation point and positive $\zeta$ region for square roughness using velocity streamlines and vectors superimposed on the vorticity contour plot

We take the coordinates as usual, x- the streamwise and y- the spanwise directions. The non-zero vorticity is thus the z-component($\zeta$) governed by the equation

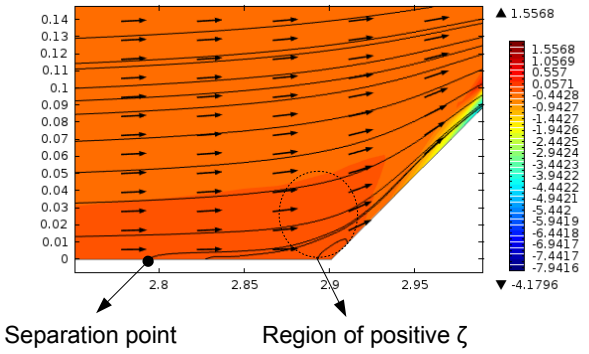


FIGURE 5.18: An illustration of the separation point and positive $\zeta$ region for triangular roughness using velocity streamlines and vectors superimposed on the vorticity contour plot

$$u \cdot \nabla \zeta = \nu \nabla^2 \zeta. \tag{5.12}$$

By definition,

$$\zeta = \frac{\partial v}{\partial x} - \frac{\partial u}{\partial y} \tag{5.13}$$

and consequently

$$\frac{\partial \zeta}{\partial y} = \frac{\partial^2 v}{\partial x \partial y} - \frac{\partial^2 u}{\partial y^2}. \tag{5.14}$$

At the wall, $y = 0$, one has $u = 0$ and $v = 0$ for all x, giving

$$(\partial v / \partial x)_{y=0} = 0. \tag{5.15}$$

Additionally the continuity equation

$$\frac{\partial u}{\partial x} + \frac{\partial v}{\partial y} = 0 \tag{5.16}$$

implies that

$$(\partial v/\partial y)_{y=0} = 0 \tag{5.17}$$

and thus

$$(\partial^2 v/\partial x \partial y)_{y=0} = 0. \tag{5.18}$$

Hence, at the wall

$$\zeta = -\partial u/\partial u \tag{5.19}$$

and

$$\frac{\partial \zeta}{\partial y} = -\frac{\partial^2 u}{\partial y^2}. \tag{5.20}$$

Tritton [5] explains that the location of separation could be identified by observing the sign change of vorticity, $(\partial u/\partial y)_{y=0}$ from equation 5.19. Therefore, separation involves the existence of a region in which the vorticity has the opposite sign of that associated with the flow as a whole. The key to understanding when separation may occur is to understand how this reversed vorticity is introduced into the flow. Note that the mean flow is in the positive x-direction and the distance from the wall is $y^+$ and $\zeta$ is negative in the oncoming flow. Hence, the region of reversed vorticity is one of positive $\zeta$, as illustrated in figure 5.23 for square roughness and figure 5.24 for triangular roughness.

Consider now how the x-component of the Navier-Stokes equations

$$u\frac{\partial u}{\partial x} + v\frac{\partial u}{\partial y} = \frac{1}{\rho}\frac{\partial p}{\partial x} + \nu\frac{\partial^2 u}{\partial x^2} + \nu\frac{\partial^2 u}{\partial y^2} \tag{5.21}$$

simplifies close to the boundary. From considerations similar to those above about the boundary conditions this becomes

$$-\frac{1}{\rho}\frac{\partial p}{\partial x} + \nu\frac{\partial^2 u}{\partial y^2} = 0 \tag{5.22}$$

at $y = 0$. Equation then gives

$$\frac{1}{\rho}\frac{\partial p}{\partial x} + \nu\frac{\partial \zeta}{\partial y} = 0 \tag{5.23}$$

at $y = 0$. The pressure gradient along the wall and the vorticity gradient normal to the wall are thus related.

It should be noted that equation 5.23 is not a general relationship but one that applies specifically at the wall as a result of the boundary conditions. The action of viscosity on vorticity is essentially one of diffusion down the vorticity gradient. The sign of the vorticity gradient at the wall thus determines the sign of the vorticity being introduced into the flow at the wall. Introduction of positive $\zeta$ into a flow predominantly negative $\zeta$ thus requires a region on the wall over which $\partial\zeta/\partial y$ is negative. Equation 5.23 tells us that this corresponds to their being a region with

$$\partial p/\partial x > 0. \tag{5.24}$$

The flow before the separation has been taken to be in the positive x-direction and relation 5.24 therefore means that the pressure must be rising in the flow direction i.e. adverse. Relation 5.24 is necessary but not sufficient condition for separation. Whether diffusion of positive vorticity into the flow produces a region of positive vorticity depends on whether this diffusion more than counter balances diffusion from the regions of negative vorticity i.e. on the whole vorticity balance of equation 5.12. The important point is that without this diffusion, there is no mechanism for a region of positive vorticity to arise. According to Tritton [5], attachment could be viewed as the opposite of separation.

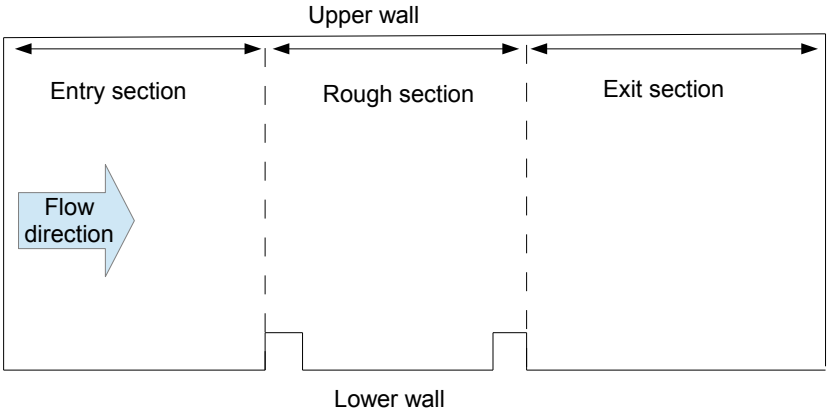


FIGURE 5.19: Sketch showing the flow sections.

Based on the separation condition described here and the flow sections illustrated in figure 5.19, the reaction forces from the upper and lower were plotted to investigate the separation and attachment locations along the lower wall in the channel. Figure 5.20 shows an example of how the reaction force plots were used to determine the locations of

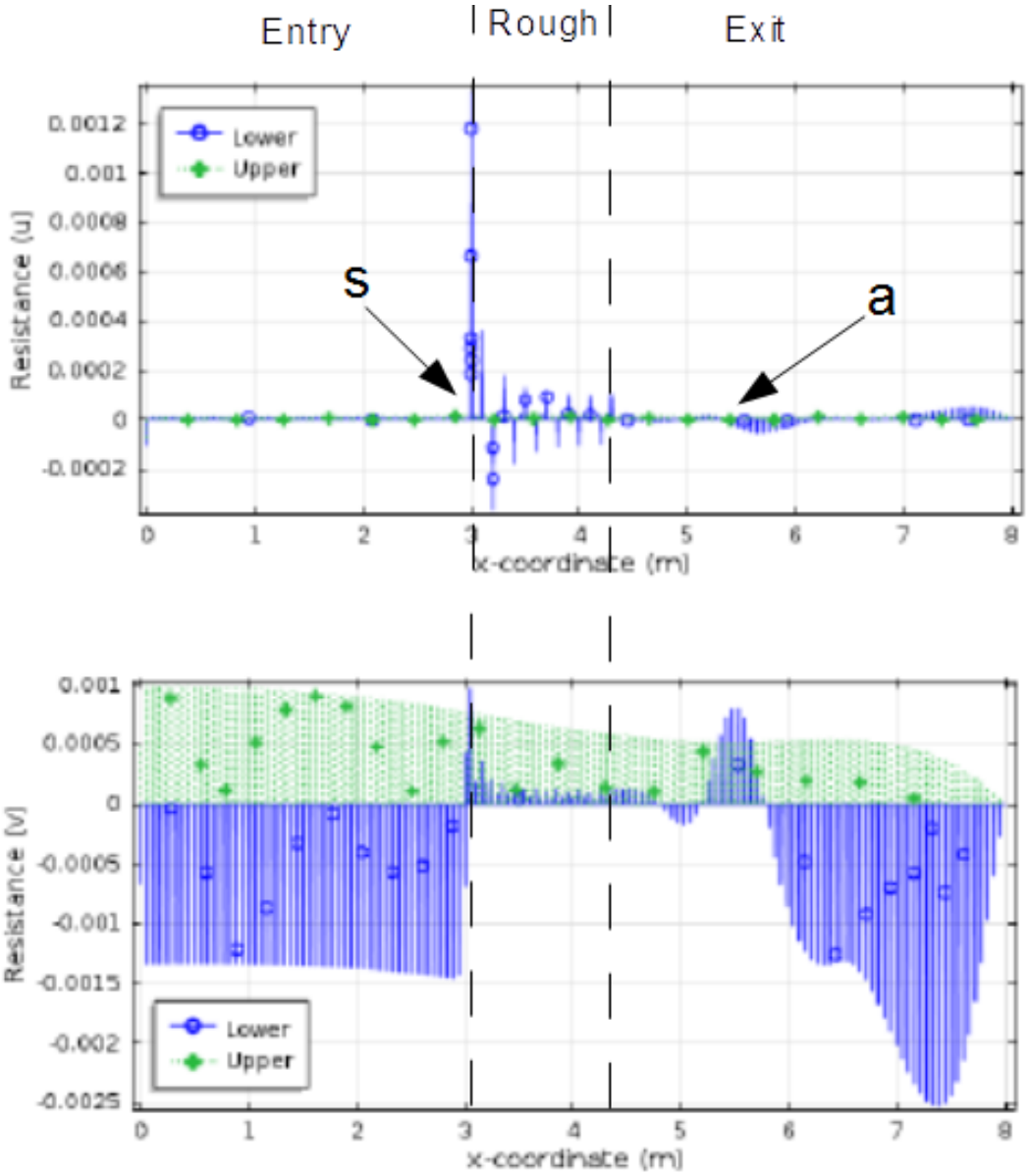


FIGURE 5.20: An example showing how the separation and attachment were determined from the reaction force plots: S= separation, a= attachment.

separation and attachment for a d- type surface with square roughness. It is important to note here that separation is a complex phenomena. Based on the data obtained here, the separation observed over a rough surface could be classified as follows:

1. Primary separation: This is indicated by a sign reversal of both reaction forces which correspond to the flow lifting up from the wall and generally observed to be steady;

2. Secondary separation: indicated by a sign reversal of one of the reaction forces. This type of separation appears downstream of the primary separation, and generally correspond to the separated flow attempting to reattach at the wall and is

observed to be highly unsteady.

A sketch of the flow showing the separation and attachment locations for k- and d- type surfaces is given in figure 5.21. The results demonstrate that the flow over the d-type roughness is generally separated along the rough section of the flow and reattaches at the exit section close to the trailing roughness element. In the case of k- type roughness, the flow separates close to the leading roughness element and reattaches and then separates again at the groove between the roughness elements. Similar observations were made using LES by Cui et al [8].

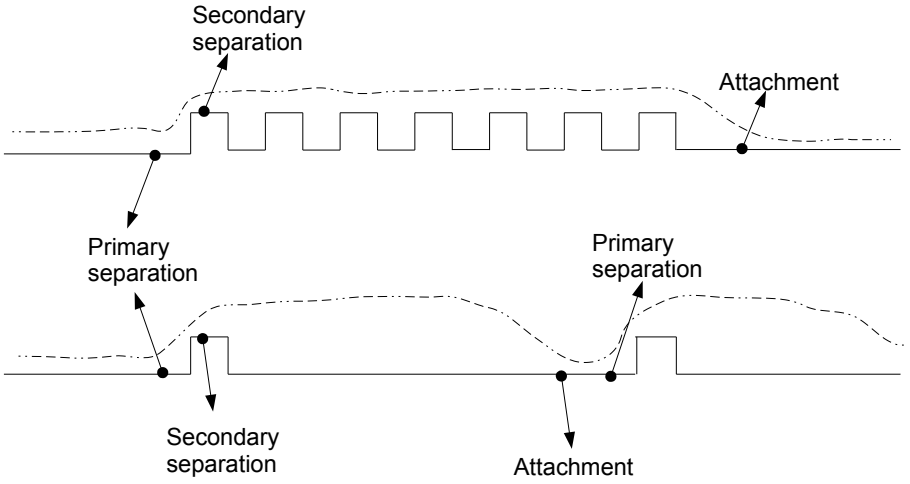


FIGURE 5.21: Sketch illustrating the locations of separation and attachment observed over k- and d- type rough surfaces.

The effects of the roughness geometry on the separation and attachment are illustrated in figure 5.22. The results demonstrated that the roughness geometry affects the location of primary separation close to the leading roughness element. For square roughness, the primary separation is located slightly upstream of the lower corner of the roughness element. Secondary separation and attachment takes place at the top of roughness element. The primary separation for the triangular roughness is located closer to the corner of the leading element. Secondary separation occurs at the front side of the roughness geometry and attachment at the occurs at the backside.

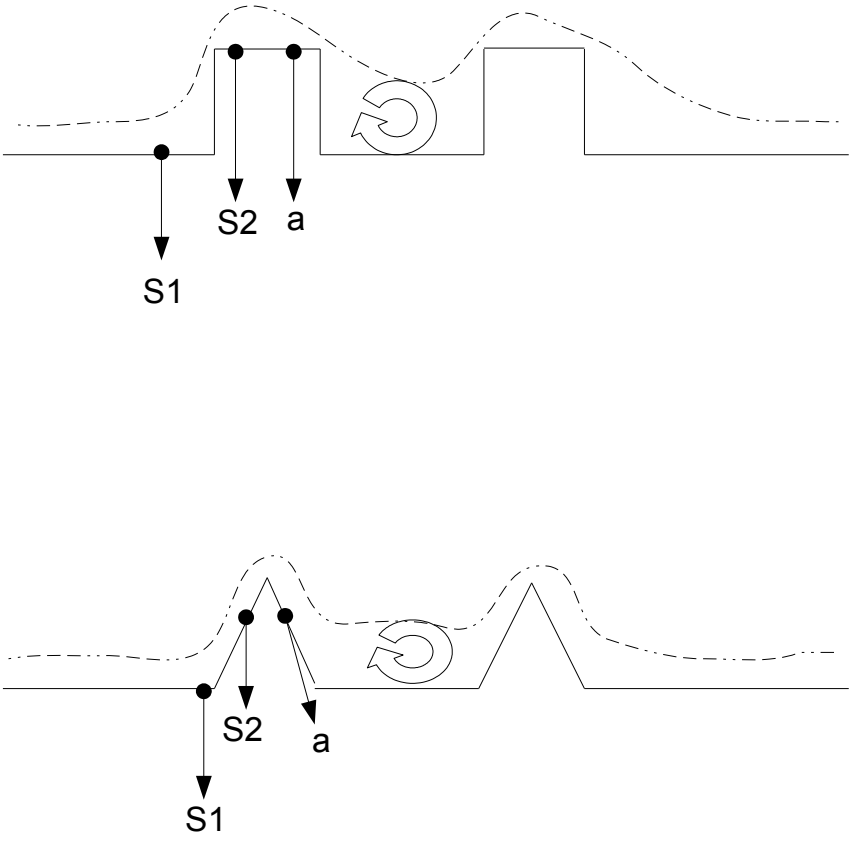


FIGURE 5.22: Sketch illustrating the effects of roughness geometry on the separation and attachment: S1 = primary separation, S2= secondary separation, a= attachment.

## 5.5 Instantaneous velocity fields

The following definitions were used in analysing the instantaneous velocity fields obtained using contour maps of the streamwise (u) and spanwise (v) velocities normalized by the bulk velocity ($u_b$), given in appendix C.6. It is possible to the classify the flow in a channel on the basis of many criteria, here we focus on the criteria based on the variation of the depth of certain flow regions ($y$) in time ($t$) and space ($x$). To this end we consider two criterion based on time and space as follows:

- If time is the criterion, then the flow may be classified as either steady; which implies that the depth of the flow region does not change with time ($\partial y/\partial t = 0$) or unsteady; which implies that the depth does change with time ($\partial y/\partial t \neq 0$);
- Similarly, if space is used as the criterion, then the flow may be classified as uniform, if the depth does not vary with distance ($\partial y/\partial x = 0$) or non-uniform, if the depth does vary with distance ($\partial y/\partial x \neq 0$).

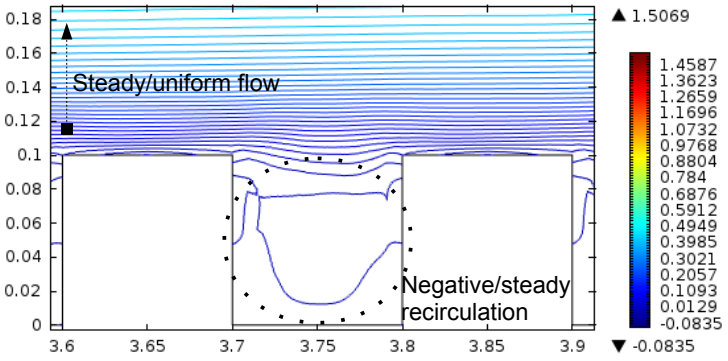


FIGURE 5.23: Visualization of the steady recirculation region using $u$ velocity contour plot for d- type roughness.

The velocity fields for the square and triangular roughness were very similar. Therefore, we only present the results for square roughness here. The results show that for d-type roughness, see figure 5.23, a stable/steady negative recirculation forms in the cavity between the roughness elements and the flow over the roughness crest plane is relatively steady and uniform. The spanwise velocity contour plot (figure 5.24) shows that in the cavity two regions of sweeping and ejection motion are formed within the cavity. The

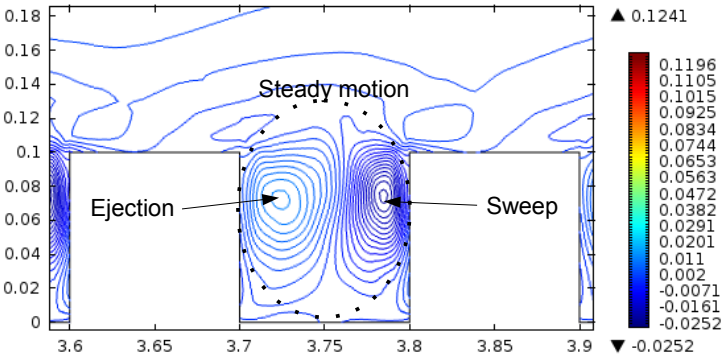


FIGURE 5.24: Visualization of the steady motion using $v$ velocity contour plot for d-type roughness.

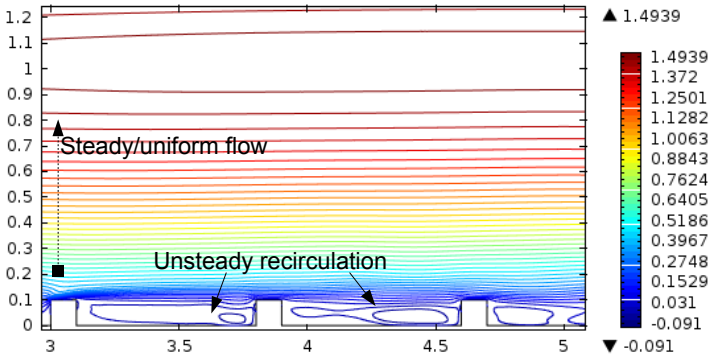


FIGURE 5.25: Visualization of the unsteady recirculation region using $u$ velocity contour plot for k- type roughness.

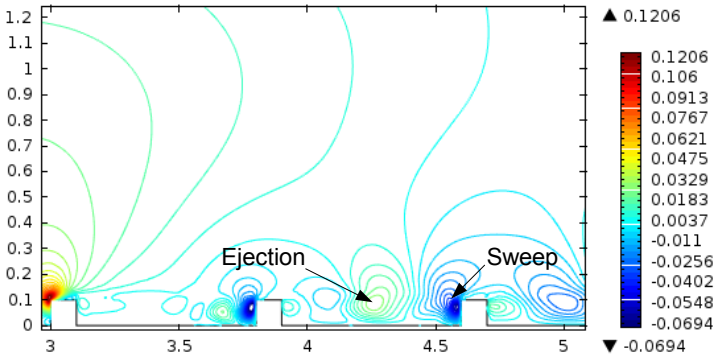


FIGURE 5.26: Visualization of the unsteady ejection and sweep motions using $v$ velocity contour plot for k- type roughness.

results demonstrate that the motion within the cavity is relatively steady despite the strong interaction with the mean flow. For k-type roughness, the streamwsise velocity plots show that the recirculation between the roughness elements is highly unsteady, see figure 5.25. However, after two roughness heights in the spanwise direction the flow is relatively steady and uniform. The spanwise velocity plots shows a steady sweeping motion and unsteady ejection, see figure 5.26. Further investigation into the sweeping and ejection motions will be discussed in the next chapter.

# Chapter 6

# Discussion

## 6.1 Predictive capabilities of the ILES model

The validation results in chapter 4 show that the results given for the base model (plane channel) demonstrate reasonably good predictive capabilities. The results for $C_f$, given in table 4.8, show an error below 30 % when compared to the experimental results of Patel and Head [38]. Similar observations were made for $U^+$, shown in table 4.9, compared to the experimental results reported in Pope [6]. It is important to note here that the results obtained for $C_f$ had a much higher uncertainty compared to $U^+$. This observation demonstrates the models limitations in accurately predicting $C_f$. However, this was expected as accurate measurements of the wall shear stress are difficult to obtain without resorting to a full LES or DNS. The Re dependence study further validated the models predictive capability by showing that the friction drag dependence on Reynolds number decreases with the increase of the flow's Reynolds number, as shown in figure 4.7.

The results for the autocorrelation (see figure 5.4) and two-point correlation (see figure 5.5) plots showed reasonable capability for predicting the statistical properties of the flow. The energy spectrum plots, given in figure 5.6, shows the resolved and modelled motions. This graph demonstrates the model's capability in resolving the large scale motions, which one would expect from any LES. The comparison of the streamlines obtained from the current model and the LES of Cui et al. [8] (see figure 5.8) give further confirmation that the model is capable of resolving these large scale motions with reasonable accuracy.

It is important to mention here that the ILES described here is for two-dimensional turbulence. Following from Kent et al. [34] the qualitative difference between three- and two- dimensional turbulence could be outlined as follows:

- For three-dimensional incompressible turbulence in neutral stratification, energy is an important conservable quantity; on average, energy cascades downscale from the large scales to the small scales.
- In contrast, two-dimensional incompressible flow has a material invariant, the (absolute) vorticity, implying an infinite family of conserved moments of vorticity. Here, the energy is transferred upscale and it is the enstrophy that cascades down scale.

The authors explain further that the upscale transfer of energy might make ILES less suitable for modelling two-dimensional turbulence; ILES tends to be less accurate for three-dimensional turbulence in situations with significant upscale energy transfer, such as near walls. On the other hand, the energy spectrum is much steeper in two-dimensional turbulence than in three-dimensional turbulence, suggesting a stronger slaving of small scales to large, which could make two-dimensional turbulence amenable to the ILES approach.

Overall, the results demonstrate the models capabilities in predicting the qualitative data of the flow. An accurate prediction of the quantitative data was difficult due to the models limitations to two-dimensional turbulence. Improving the predictive capabilities of the quantitative data will require implementing an explicit scheme to model the flow near the wall.

## 6.2 Coherent structures

According to Gad El Hak [2], despite the extensive research work into coherent structures in turbulent flow, no generally accepted definition of what is meant by coherent motion has emerged. The author [2] provides two different views, the first is general and the second more restrictive:

- A coherent motion is defined as a region of the flow over which at least one fundamental flow variable exhibits significant correlation with itself or another variable over a range of space/or time that is significantly larger than the smallest local scales of the flow;
- The restrictive definition states that a coherent structure is a connected turbulent fluid mass with instantaneously correlated vorticity over its spatial extent.

In general, the challenge here is to identify a coherent structure well hidden in an area of random background when such a structure is present either in a visual impression of the flow or in an instantaneous velocity or pressure data plots.

In wall bounded flow, the turbulence production process is dominated by the three kinds of quasi-periodic eddies, see Gad El Hak [2]; the larger outer structures, the intermediate Falco eddies and the near wall eddies. Typical flow regimes associated with wall bounded flow are shown in figures 6.1 and 6.2 for d- and k- type surfaces. The figures include the contour plots of the non-dimensional parameter $y^+$. The illustrations show that, using the contour plots, we were able to identify the different flow regimes that are observed in a typical wall bounded flow and visualize the coherent structures formed within them. The results given in appendix C.7 show the evolution of these coherent structures in time.

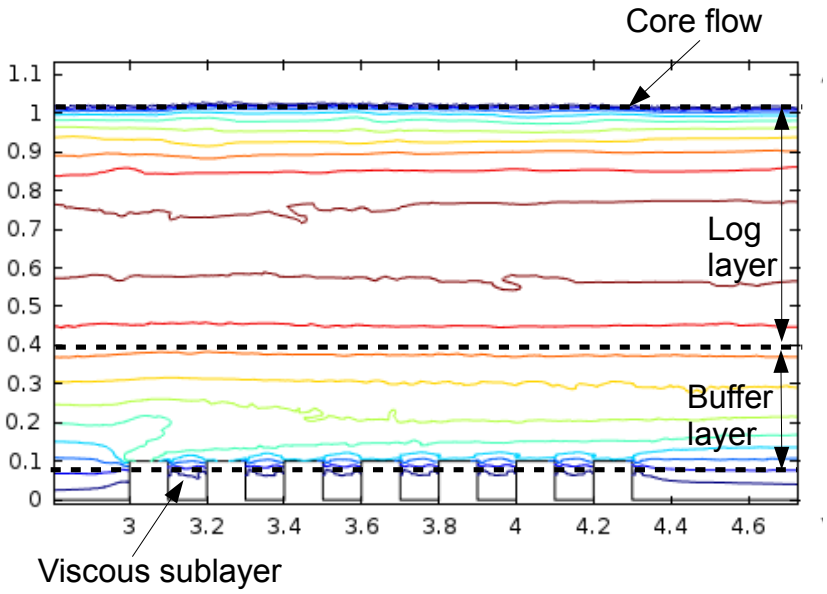


FIGURE 6.1: Visualization of the flow regimes for a d- type surface using $y^+$.

Figure 6.1 shows that for d- type roughness, the limit of the viscous sublayer coincides with the the roughness crest plane and the flow in the log-law region is relatively stable. On the other hand, k- type roughness shifts the extent of the viscous sublayer slightly below the roughness crest plane. The result is a much active buffer layer, compared to d- type, as illustrated by the turbulent spots observed in the log-law region, as shown in figure 6.2.

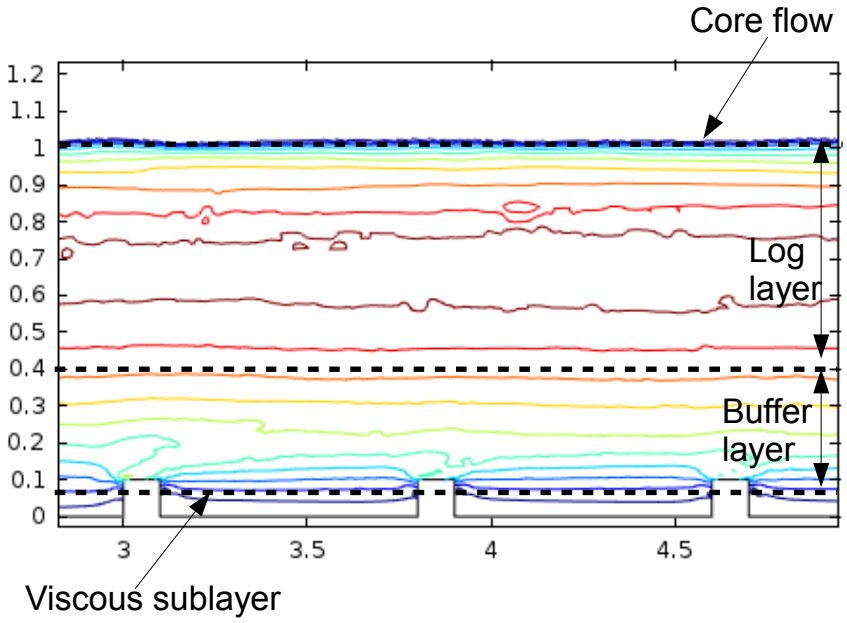


FIGURE 6.2: Visualization of the flow regimes for a k- type surface using $y^+$.

### 6.2.1 Outer structures

Visualization experiments reported in Gad El Hak [2] show large three dimensional bulges that scale with the boundary layer thickness and extend across the entire boundary layer. These eddies control the dynamics of the boundary layer in the outer region such as entrainment, turbulence production and so forth. The large eddies are characterized by a sharp interface and a highly contorted surface that exhibits a significant amount of folding. They appear randomly (quasi-periodically) in space and time and seem to be, at least for moderate Reynolds number, the residue of the transitional Emonons spots, see Gad El Hak [2]. Visualization of the flow field close to the channel centre confirmed that our model is capable of predicting the characteristics outlined by Gad El Hak [2] for the outer structures , as shown in figure 6.3.

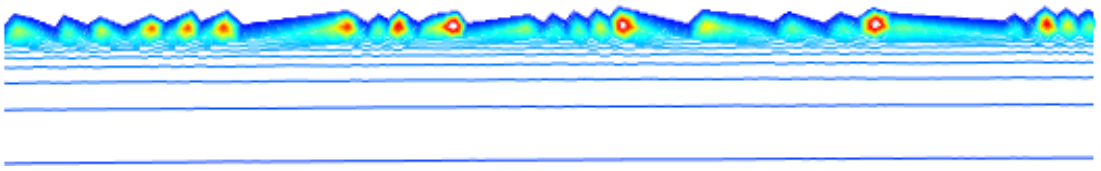

FIGURE 6.3: Visualization of the outer structures close to the channel centre.

### 6.2.2 Intermediate eddies

Intermediate eddies, also known as Falco eddies, are also highly coherent and three dimensional. They are named typical eddies because they appear in wakes, jets, boundary layers and other flow types, see Gad El Hak[2]. The characteristic scales are obtained from the magnitude of the mean vorticity in the region and its viscous diffusion away from the wall. This viscous time scale, $t_\nu$, is given by the inverse of the mean wall vorticity

$$t_\nu = \left[\frac{\partial \overline{U}}{\partial y}\right]_w^{-1} \tag{6.1}$$

and the viscous length scale, $l_\nu$, is determined by the characteristic distance by which the spanwise vorticity is diffused away from the wall. This is given by

$$l_\nu = \sqrt{\nu t_\nu}. \tag{6.2}$$

Based on the visualization experiments in a wind tunnel reported in [2], the Falco eddies appear to be an important link between the large structures and the near wall events. From these experiments, fingerprints of typical Falco eddies were identified as pockets. Further research by Splarat [39] confirmed that pockets are the signature of local wall-ward motions, evidenced by spanwise divergence of streamlines, above regions of high wall pressure. Low pressure regions, on the other hand, occur along lines of converging streamlines associated with outward motion. These motions are the sweep and the ejection events , respectively. Visualizations of the Falco eddies are given in appendix C.8 (using equation 6.2) and details of the ejection and sweeping motions were obtained from the visualization of the instantaneous spanwise velocity fields, as shown in figures 5.24 and 5.26.

### 6.2.3 Near-wall eddies

The third kind of eddies exist in the wall region, where the Reynolds stresses is produced in an intermittent fashion. Half of the total production of turbulence kinetic energy takes place near the wall in the first 5 % of the boundary layer at moderate Reynolds number, and the dominant sequence of intense organized motions there are collectively termed the bursting phenomenon, see Gad El Hak [2]. To focus the discussion on the bursting process and its possible relationship to other organized motions we refer to the schematic in figure 6.4.

Qualitatively, the process begins with elongated, counter rotating, streamwise vortices. The counter rotating vortices exist in a strong shear and induce low- and high- speed regions between them . It was observed, see Gad El Hak [2], that the low speed regions grow downstream, lift up, and develop (instantaneous) inflectional u(y) profiles. At approximately the same time, the interface between the low- and high- speed fluid begins to oscillate, signalling the onset of secondary instabilities. The low speed regions lift up away from the wall as the oscillation amplitude increases, and then the flow rapidly breaks up into a completely chaotic motion. The streak oscillation commences at $y^+ \approx 10$ ,for a plane channel, and the abrupt break up takes place in the buffer, although the ejected fluid reaches all the way to the logarithmic region. Because the breakup process occurs on a very short time scale it is called a burst. Virtually all of the kinetic energy in the near-wall region occurs during these bursts.

It was reported, see Gad El Hak [2], that the ejection phase of the bursting process is followed by large scale motion of upstream fluid that emanates from the outer region and cleanses (sweeps) the wall region of the previously ejected fluid. The sweep phase is, of course, required by the continuity equation and appears to scale with the outer

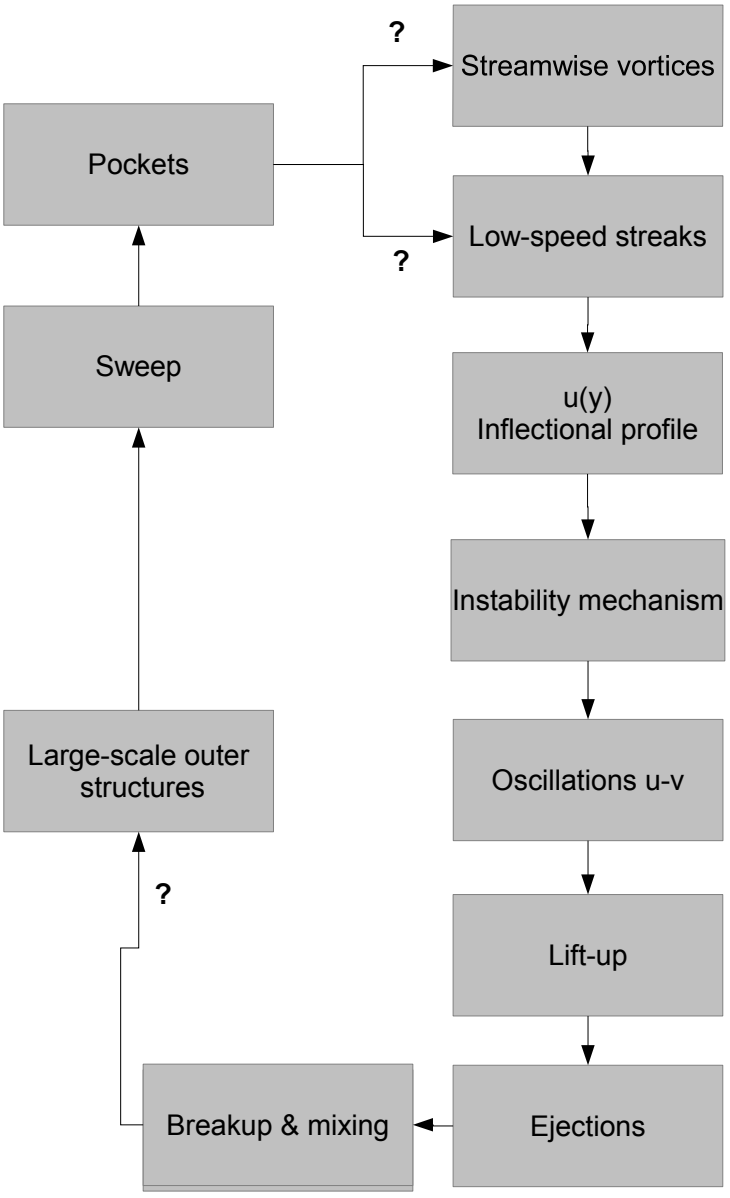


FIGURE 6.4: Simplified sequence of the bursting process. The arrows indicate the sequential events, and the '?' indicates less supporting evidence [adopted from Gad el Hak [2]

flow variables. The sweep event seem to stabilize the bursting site, in effect preparing it for a new cycle. Similar observations were made from the visualizations of the velocity streamlines (appendix C.1 and Instantaneous velocity plots (appendix C.6).

## 6.3 Roughness classification

Based on the results reported here, roughness can be classified based on the elements distribution (w/k) as follows:

- For $w/k \leq 1$ roughness exhibits a d- type behaviour;
- For $3 \geq w/k \leq 7$ roughness exhibits both k- and d- type behaviours;
- For $w/k \geq 7$ roughness exhibits k- type behaviour.

A graphical representation is presented in figure 6.5 that includes design applications for each type. The results confirm that the early classification of roughness proposed by Perry et al. [3] based on the state of vortex shedding is an over simplification. Using the friction and pressure contributions to drag, as proposed by Leonardi et al. [23], is a more comprehensive approach but requires a highly accurate numerical model. Here we propose a classification based on the coherent eddy structures associated with the different rough surfaces considered. Starting with d-type (w/k=1), the flow alternates between no slip at the top of the roughness element and slip at the cavity. In this case the cavity if filled with a steady recirculation region similar to the one observed in the lid-cavity problem. As the distribution between the elements increases ($w/k > 1$) this recirculation region is stretched and the recirculation becomes unsteady resulting in a strong interaction between the inner and outer layers of the flow. For distributions between w/k =3 and w/k = 7 the flow exhibits both k- and d- type characteristics. For distributions larger than w/k = 7 the recirculating flow between the roughness elements separates at the cavity floor and reattaches close to the roughness element downstream. This results in the vortex shedding observed in the flow over k- type rough surfaces. The graphical illustration given in figure 6.5 also shows design applications associated with k- and d- type roughness that were reported in the literature concerned with the flow over rough walls, see Djenidi et al [20], Cui et al [8] and Jimenez [11].

## 6.4 Effects of roughness geometry

Visualizations of the friction velocity (figure 5.15) and the pressure gradients (figure 5.16) show how the roughness geometry affects the roughness (inner) layer. An investigation

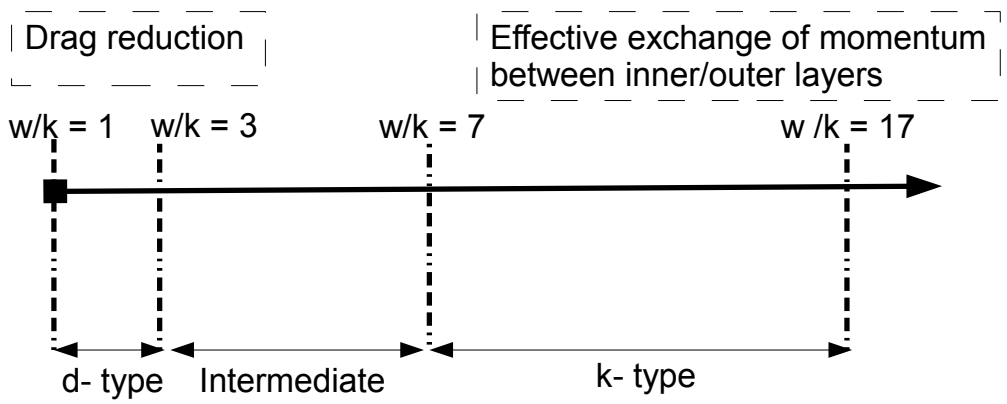


FIGURE 6.5: Illustration of the roughness classification based on the distribution of the roughness elements

into the resistance components demonstrated the different characteristics imposed by the roughness geometry on the state of flow separation and attachment, as shown figure 5.22. Comparison of the flow $Re_b$, given it table 6.1, show that the overall increase in $Re_b$ is relatively small compared to the smooth case. This confirms that the roughness geometry has little effect on the mean flow for the entire range of Re considered here. However,

| Plane | w/k = 1 | | w/k=3 | | w/k=7 | | w/k=17 | |
|---|---|---|---|---|---|---|---|---|
| $\mathrm{Re}_b$ | $\mathrm{Re}_b(s)$ | $\mathrm{Re}_b(t)$ | $\mathrm{Re}_b(s)$ | $\mathrm{Re}_b(t)$ | $\mathrm{Re}_b(s)$ | $\mathrm{Re}_b(t)$ | $\mathrm{Re}_b(s)$ | $\mathrm{Re}_b(t)$ |
| 150 | 153 | 153 | 153 | 152 | 152 | 151 | 151 | 151 |
| 300 | 305 | 305 | 305 | 304 | 304 | 303 | 303 | 302 |
| 750 | 761 | 760 | 761 | 759 | 759 | 757 | 757 | 755 |
| 1500 | 1520 | 1518 | 1520 | 1517 | 1518 | 1514 | 1514 | 1512 |
| 15000 | 15218 | 15176 | 15159 | 15138 | 15144 | 15214 | 15192 | 15158 |

TABLE 6.1: Comparison of Reynolds number based on the bulk velocity $Re_b$ for the plane and roughened channels: (s = square, t = triangular).

as we discussed in section 5.4, the effects of the roughness geometry are confined to the inner layer of the flow. We have identified some of these effects by plotting the resistance components along the wall to identify the separation and attachment locations, as shown in figure 5.20. Visualizations of the pressure gradients revealed that the roughness

geometry has a major influence on the location of the adverse and favourable pressure gradients along the rough wall, as shown in 5.16.

# Chapter 7

# Conclusion

All of the major objectives of this research work have been satisfied. It has been demonstrated that the FEM used by COMSOL is capable of conducting an Implicit Large Eddy Simulation (ILES) for two-dimensional turbulent channel flow with one sided roughness up to Reynolds number of order $10^4$. This was a major outcome of this research as COMSOL does not include a dedicated LES solver.

An investigation into the pressure and friction drags to the total stress, proposed by Leonardi et al. [23], demonstrated a better approach to classifying roughness, as opposed to the vortex shedding approach reported by Perry et al. [3]. However, the approach proposed by Leonardi et al. [23] requires highly accurate measurements of the stresses near wall, which is currently feasible only through DNS.

Results from the velocity profiles show that the flow over rough surfaces could be divided into two regions; an inner (viscous and buffer regimes) and outer regions (logarithmic and outer regimes). The velocity plots along different x- locations in the roughened channel show that the roughness geometry effects are generally confined to the inner layer. The results shown here suggest that the roughness geometry has a major influence on the interaction between the inner and the outer layers. According to Gad el Hak [2], the interaction between the inner and outer layers remains an open research issue in the identification of coherent structures in wall bounded flow.

Further investigation into the effects of roughness geometry and distribution was carried out by plotting the reaction forces along the rough wall. These plots were useful in identifying the separation and attachment locations along the rough walls. Here we have classified separation into primary and secondary. The results demonstrate that regardless of the elements geometry, a primary separation point is formed at the leading

roughness elements. It was observed that the secondary separation points differ with the roughness geometry and distribution.

Visualization of the coherent structures associated with k- and d- type behaviour demonstrated the predictive capabilities of the numerical model described here. Based on these coherent structures, a roughness classification including design applications was given in figure 6.5. This classification, albeit a limited one, is useful in design applications involving rough surfaces.

Future work will focus on further developing the ILES approach reported here. In this work we have demonstrated it's capability to simulate the effects of roughness in wall bounded flows. The analysis reported here could be extended to investigate the k- and d- type behaviour in turbulent boundary layers. Recent research (see Krogstad [21]) had suggested that despite the similarities between channel and boundary layer flows, the roughness effects are different for each type of flow. Building on the research of Kent et al [34] we propose an investigation into the effects of k- and d- type roughness on turbulent boundary layers.

# Appendix A

# Data used to prescribe the boundary conditions

| Variable | Expression | Description | Selection |
|---|---|---|---|
| $u_{bndx}$ | 0 | Velocity at boundary, x. | Upper and lower walls |
| $u_{bndy}$ | 0 | Velocity at boundary, y. | Upper and lower walls |
| $u_{bndz}$ | 0 | Velocity at boundary, z. | Upper and lower walls |

Table A.1: Variables used to prescribe the no-slip condition

| Constraint | Constraint force | Shape function | Selection |
|---|---|---|---|
| -u+$u_{bndx}$ | test(-u+$u_{bndx}$) | Lagrange (quadratic) | Upper and lower walls |
| -v+$u_{bndy}$ | test(-v+$u_{bndy}$) | Lagrange (quadratic) | Upper and lower walls |
| 0 | 0 | —- | Upper and lower walls |

Table A.2: Constraints used to prescribe the no-slip condition

| Variable | Expression | Description | Selection |
|---|---|---|---|
| $u_0$ | $u_{in}6y(1-y)step$ | Normal inflow velocity | Inlet boundary |
| $u_{bndx}$ | -nojac(nx) $u_0$ | Velocity at boundary,x. | Inlet boundary |
| $u_{bndy}$ | -nojac(ny) $u_0$ | Velocity at boundary,y. | Inlet boundary |
| $u_{bndz}$ | -nojac(nz) $u_0$ | Velocity at boundary,z. | Inlet boundary |

Table A.3: Variables used to prescribe the inlet condition

| Constraint | Constraint force | Shape function | Selection |
|---|---|---|---|
| -u+$u_{bndx}$ | test(-u+$u_{bndx}$) | Lagrange (quadratic) | Upper and lower walls |
| -v+$u_{bndy}$ | test(-v+$u_{bndy}$) | Lagrange (quadratic) | Upper and lower walls |
| 0 | 0 | —- | Upper and lower walls |

Table A.4: Constraints used to prescribe the inlet condition

| Variable | Expression | Description | Selection |
|---|---|---|---|
| $p_0$ | 0 | Pressure | Outlet boundary |

TABLE A.5: Variables used to prescribe the outlet condition

| Constraint | Constraint force | Shape function | Selection |
|---|---|---|---|
| -p + $p_0$ | test(-p + $p_0$) | Lagrange (linear) | Outlet boundary |

TABLE A.6: Constraints used to prescribe the outlet condition

| Weak expression | Integration frame | Selection |
|---|---|---|
| p (-nx test(u) – ny test(v)) | Material | Outlet boundary |

TABLE A.7: Weak expressions used to prescribe the outlet condition

| Variable | Description | Expression | Units | Selection |
|---|---|---|---|---|
| $\rho$ | Density | 1000 | $Kg/m^3$ | Domain |
| $\mu$ | Dynamic viscosity | 1 - 0.001 | $Pa \cdot S$ | Domain |
| div$\vec{u}$ | Divergence of velocity | $\frac{\partial u}{\partial x} + \frac{\partial v}{\partial y}$ | $1/s$ | Domain |
| $\gamma$ | Shear rate | $\sqrt{0.5(4\,\frac{\partial u}{\partial x}^2) + 2(\frac{\partial u}{\partial y} + \frac{\partial v}{\partial x})^2 + 4\,\frac{\partial v}{\partial y}^2 + C}$ | $1/s$ | Domain |
| $\|u\|$ | Velocity magnitude | $\sqrt{u^2 + v^2}$ | $m/s$ | Domain |
| $\omega_z$ | Vorticity component | $\frac{\partial v}{\partial x} - \frac{\partial u}{\partial y}$ | $1/s$ | Domain |
| $Re^c$ | Cell Reynolds number | $\frac{0.25\ \rho\ \sqrt{u^2+v^2}\ h}{\mu}$ | 1 | Domain |
| $T_x$ | Total stress, x | $2\ \mu\ \frac{\partial u}{\partial x}\ nx + \mu\ (\frac{\partial u}{\partial y} + \frac{\partial v}{\partial x})\ ny - p\ nx$ | $N/m^2$ | Boundaries |
| $T_y$ | Total stress, y | $\mu\ (\frac{\partial v}{\partial x} + \frac{\partial u}{\partial y})\ nx + 2\ \mu\ \frac{\partial v}{\partial y}\ ny - p\ ny$ | $N/m^2$ | Boundaries |
| $T_z$ | Total stress, z | $-p\ nz$ | $N/m^2$ | Boundaries |
| $V_x$ | Viscous stress, x | $\mu\ (2\ \frac{\partial u}{\partial x}\ nx + (\frac{\partial u}{\partial y} + \frac{\partial v}{\partial x})\ ny)$ | $N/m^2$ | Boundaries |
| $V_y$ | Viscous stress, y | $\mu\ ((\frac{\partial v}{\partial x} + \frac{\partial u}{\partial y})\ nx + 2\ \frac{\partial v}{\partial y}\ ny)$ | $N/m^2$ | Boundaries |
| $V_z$ | Viscous stress, z | 0 | $N/m^2$ | Boundaries |
| $V_{xx}$ | Viscous stress tensor,xx | $2\ \mu\ \frac{\partial u}{\partial x}$ | $N/m^2$ | Domain |
| $V_{xy}$ | Viscous stress tensor xy | $\mu\ (\frac{\partial u}{\partial y} + \frac{\partial v}{\partial x})$ | $N/m^2$ | Domain |
| $V_{yy}$ | Viscous stress tensor yy | $2\ \mu\ \frac{\partial v}{\partial y}$ | $N/m^2$ | Domain |
| $V_{test(xx)}$ | Viscous stress test tensor, xx | $2\ \mu\ test(\frac{\partial u}{\partial x})$ | $N/m^2$ | Domain |
| $V_{test(xy)}$ | Viscous stress test tensor xy | $\mu\ (test(\frac{\partial u}{\partial y}) + test(\frac{\partial v}{\partial x}))$ | $N/m^2$ | Domain |
| $V_{test(yy)}$ | Viscous stress test tensor yy | $2\ \mu\ test(\frac{\partial v}{\partial y})$ | $N/m^2$ | Domain |
| $Res_u$ | Residual, u | $\frac{\partial p}{\partial x} + \rho\ u + \frac{\partial u}{\partial x} + \rho\ v\ \frac{\partial u}{\partial y} - (\frac{d}{dx}(2\ \frac{\partial u}{\partial x}) + \frac{d}{dy}(\frac{\partial u}{\partial y} + \frac{\partial v}{\partial x}))\ \mu$ | $N/m^3$ | Domain |
| $Res_v$ | Residual, v | $\rho\ u\ \frac{\partial v}{\partial x} + \frac{\partial p}{\partial y} + \rho\ v\ \frac{\partial v}{\partial y} - (\frac{d}{dx}(\frac{\partial v}{\partial x} + \frac{\partial u}{\partial y}) + \frac{d}{dy}(2\ \frac{\partial v}{\partial y}))\ \mu$ | $N/m^3$ | Domain |
| $Res_p$ | Residual, p | $\rho\ div\vec{u}$ | $Kg/(m^3 \cdot s)$ | Domain |

TABLE A.8: List of variables used to prescribe the fluid properties in the flow domain

| Name | Shape Function | Unit | Description |
|---|---|---|---|
| u | Lagrange (quadratic) | m/s | Velocity component, x |
| v | Lagrange (quadratic) | m/s | Velocity component, y |
| p | Lagrange (linear) | Pa | Pressure |

TABLE A.9: List of shape functions used to prescribe the fluid properties in the flow domain

| Weak Expression | Integration Frame | Selection |
|---|---|---|
| $(p - V_{xx})\ test(\frac{\partial u}{\partial x}) - V_{xy}\ test(\frac{\partial u}{\partial y}) - V_{yx}\ test(\frac{\partial v}{\partial x}) + (p - V_{yy})\ test(\frac{\partial v}{\partial y})$ | Material | Domain |
| $-\rho\ (\frac{\partial u}{\partial x}\ u + \frac{\partial u}{\partial y}\ v)\ test(u) - \rho(\frac{\partial v}{\partial x}\ u + \frac{\partial v}{\partial y}\ v)\ test(v)$ | Material | Domain |
| $-\rho\ div\vec{u}\ test(p)$ | Material | Domain |
| crosswind | Material | Domain |
| streamline | Material | Domain |

TABLE A.10: List of weak expressions used to prescribe the fluid properties in the flow domain

# Appendix B

# List of Matlab scripts

## B.1 One- and two- point velocity correlation and energy spectrum

```
close all
clear all

%load data
load u_4point.dat

u1=u_4point(:,2);
u2=u_4point(:,3);
u3=u_4point(:,4);
u4=u_4point(:,5);

% time step=0.1
dt=0.003;
n=length(u1);
% compute time array
t=dt:dt:n*dt;

%%%%%%%%%%%%%%%% plotting section %%%%%%%%%%%%%%%%%%%%%%%%%%%%
% plot u time-history
plot(t,u1)
hold
plot(t,u2,'r--')
plot(t,u3,'G--')
plot(t,u4,'--')
xlabel('t')
ylabel('u')
handle=gca
set(handle,'fontsi',[20])
print u_time.ps -deps



%Plot and calculate one-point corellation data
imax=500;
two_uu_1_mat=autocorr(u1,imax);
two_uu_2_mat=autocorr(u2,imax);
two_uu_3_mat=autocorr(u3,imax);
two_uu_4_mat=autocorr(u4,imax);
figure
plot(t(1:imax),two_uu_1_mat(1:imax),'-')
hold
plot(t(1:imax),two_uu_2_mat(1:imax),'r--')
plot(t(1:imax),two_uu_3_mat(1:imax),'g:')
plot(t(1:imax),two_uu_4_mat(1:imax),'k-.')

handle=gca
set(handle,'fontsi',[20])
%Calculate integral time scale
dt=t(1);
int_T_1=trapz(two_uu_1_mat)*dt
int_T_2=trapz(two_uu_2_mat)*dt
int_T_3=trapz(two_uu_3_mat)*dt
int_T_4=trapz(two_uu_4_mat)*dt
```

```
%Plot and calculate two-point corellation data
Ru1u2= xcorr(two_uu_1_mat,two_uu_2_mat,'coeff');
Ru1u3= xcorr(two_uu_1_mat,two_uu_3_mat,'coeff');
Ru1u4= xcorr(two_uu_1_mat,two_uu_4_mat,'coeff');
Ru2u3= xcorr(two_uu_2_mat,two_uu_3_mat,'coeff');
Ru2u4= xcorr(two_uu_2_mat,two_uu_4_mat,'coeff');
Ru3u4= xcorr(two_uu_3_mat,two_uu_4_mat,'coeff');
figure
plot(Ru1u2)
hold
plot(Ru1u3,'--')
plot(Ru1u4,':')
plot(Ru2u3,'k--')
plot(Ru2u4,'k:')
plot(Ru3u4,'r:')
%Calculate integral length scale
int_S_1=trapz(Ru1u2)*dt
int_S_2=trapz(Ru1u3)*dt
int_S_3=trapz(Ru1u4)*dt
int_S_4=trapz(Ru2u3)*dt
int_S_5=trapz(Ru2u4)*dt
int_S_6=trapz(Ru3u4)*dt

%Calculate and plot the energy spectrum%


umean1=mean(u1);
umean2=mean(u2);
umean3=mean(u3);
umean4=mean(u4);

% subtract the mean
u1=u1-umean1;
u2=u2-umean2;
u3=u3-umean3;
u4=u4-umean4;
% number of points in the fft
nmax=4546;

% compute RMS
n=length(u3);
urms=0;
for i=1:n
   urms=urms+u3(i)^2/n;
end
urms=urms^0.5;

% time step (gives the right freq. on the x-axis)
dt=0.0033;
dt=0.0033;
[px,f]=pwelch(u1,nmax,[],[],1/dt);
[px1,f1]=pwelch(u2,nmax,[],[],1/dt);
[px2,f2]=pwelch(u3,nmax,[],[],1/dt);
[px3,f3]=pwelch(u4,nmax,[],[],1/dt);
plot(f,px)
```

```
hold
plot(f1,px1,'--')
plot(f2,px2,':')
plot(f3,px3,'-.')

% add line with -5/3 slope
x=[1 10];
ynoll=0.1;
y(1)=ynoll;
y(2)=y(1)*(x(2)/x(1))^(-5/3);
plot(x,y,'r--','linew',4)



title('spectrum of u','fontsize',20)
xlabel('f','fontsize',20)
ylabel('E(u)','fontsize',20)
handle=gca;
set(handle,'yscale','log','xscale','log')
set(handle,'fontsi',[20])
print u_spectum.ps -deps
%
```

# Appendix C

# Data sets

## C.1 Velocity streamlines

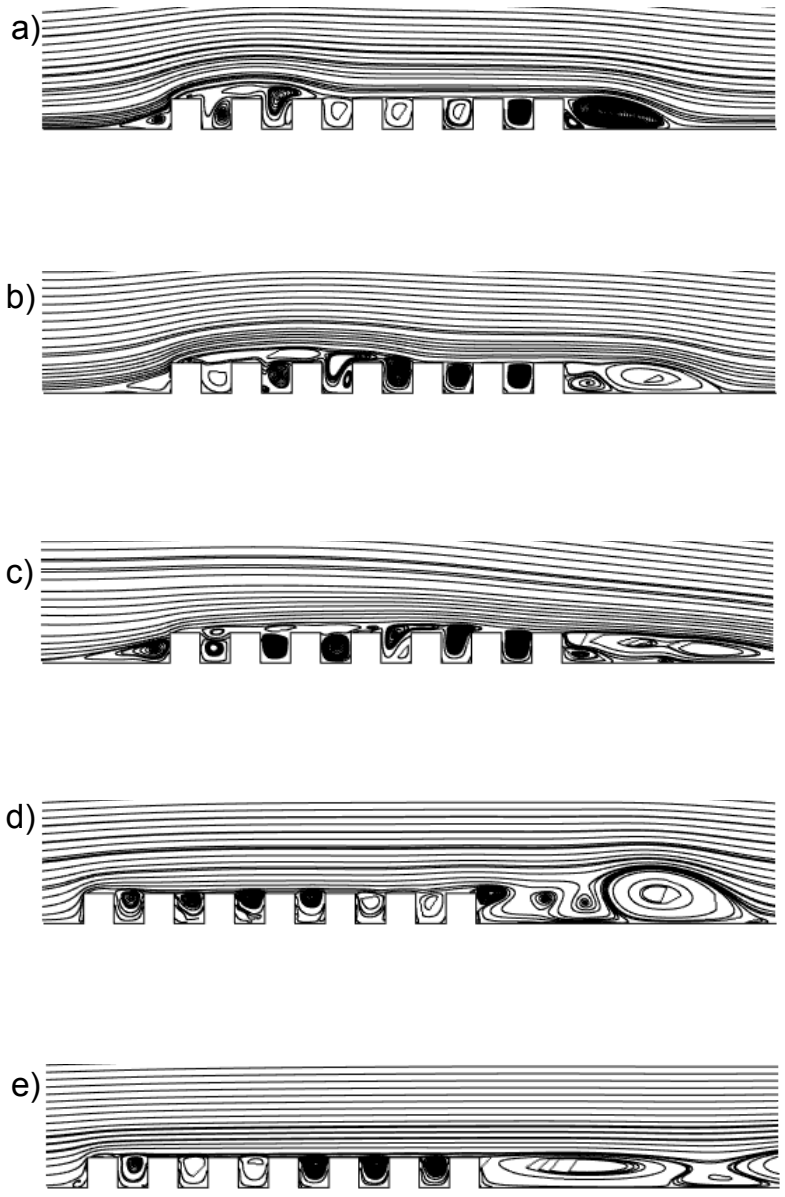


FIGURE C.1: Evolution of velocity streamlines for $w/k = 1$ (square): a) t=10.43 s, b) t= 20.1 s, c) t=40.51, d) t=83.48 s, e) t=200 s.

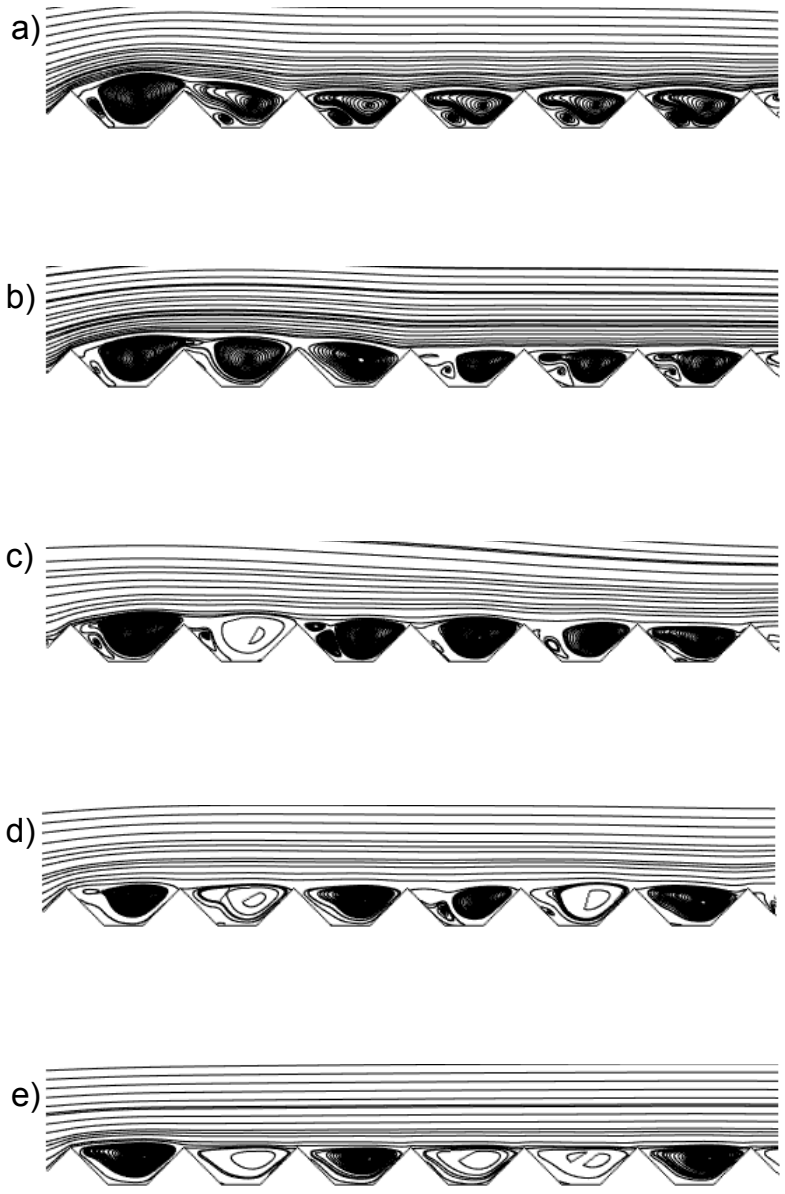


FIGURE C.2: Evolution of velocity streamlines for $w/k = 1$ (triangle): a) t=10.32 s, b) t= 20.67 s, c) t=40.14, d) t=80.07 s, e) t=200 s.

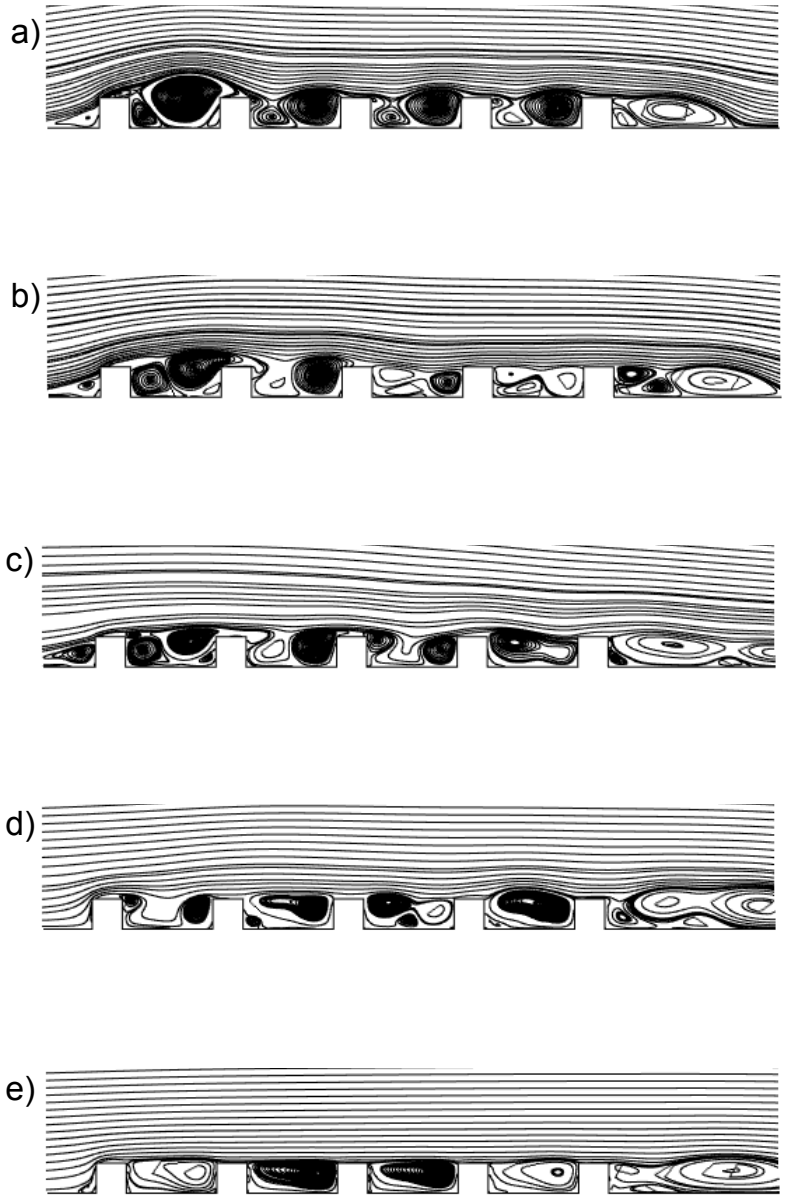


FIGURE C.3: Evolution of velocity streamlines for $w/k = 3$ (square): a) t=10.36 s, b) t= 20.39 s, c) t=40.82, d) t=80.58 s, e) t=200 s.

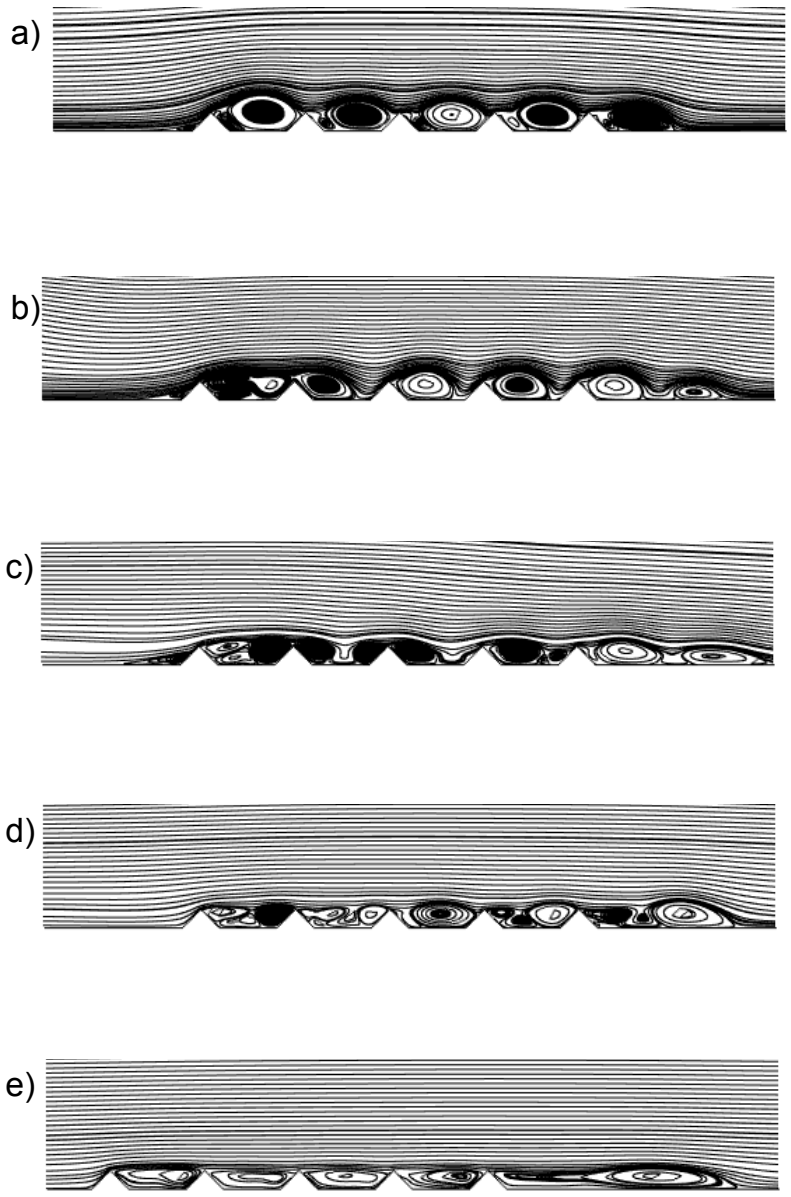


FIGURE C.4: Evolution of velocity streamlines for $w/k = 3$ (triangle): a) t=10.18 s, b) t= 20.33 s, c) t=40.65, d) t=80.59 s, e) t=200 s.

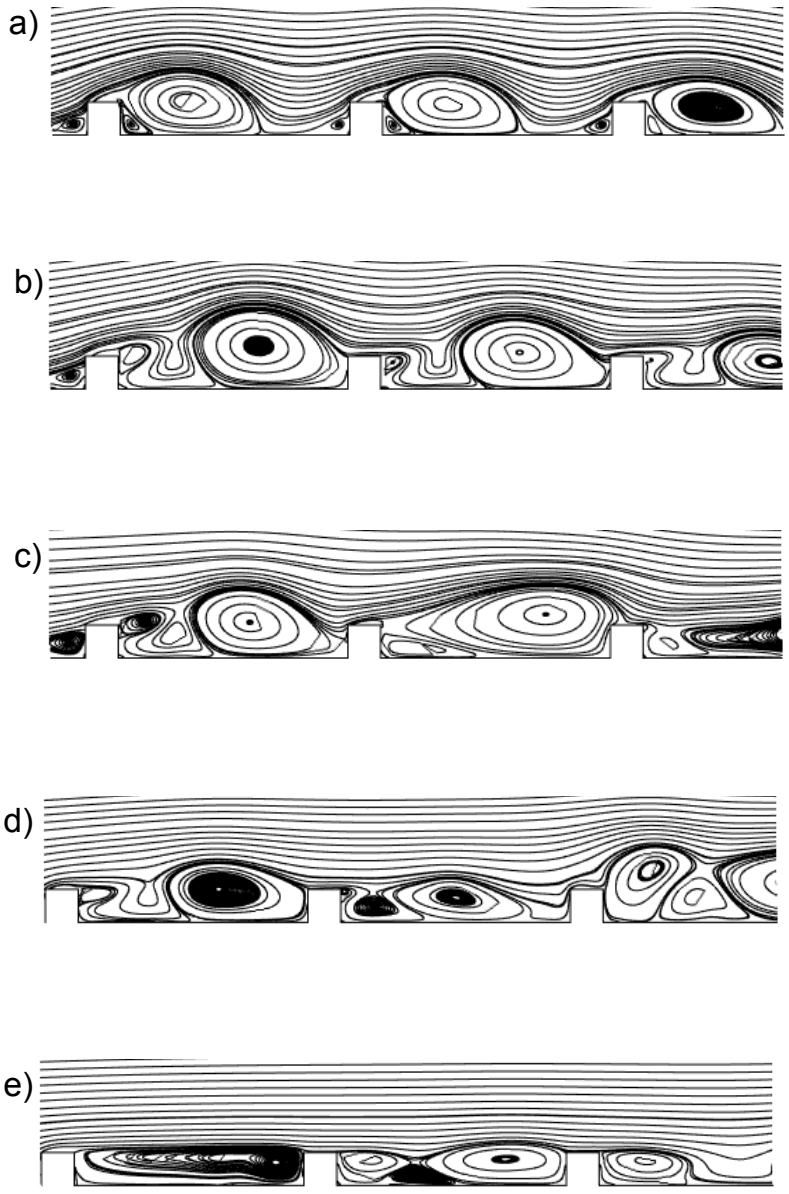


FIGURE C.5: Evolution of velocity streamlines for $w/k = 7$ (square): a) t=10.61 s, b) t= 20.04 s, c) t=40.23, d) t=81 s, e) t=200 s.

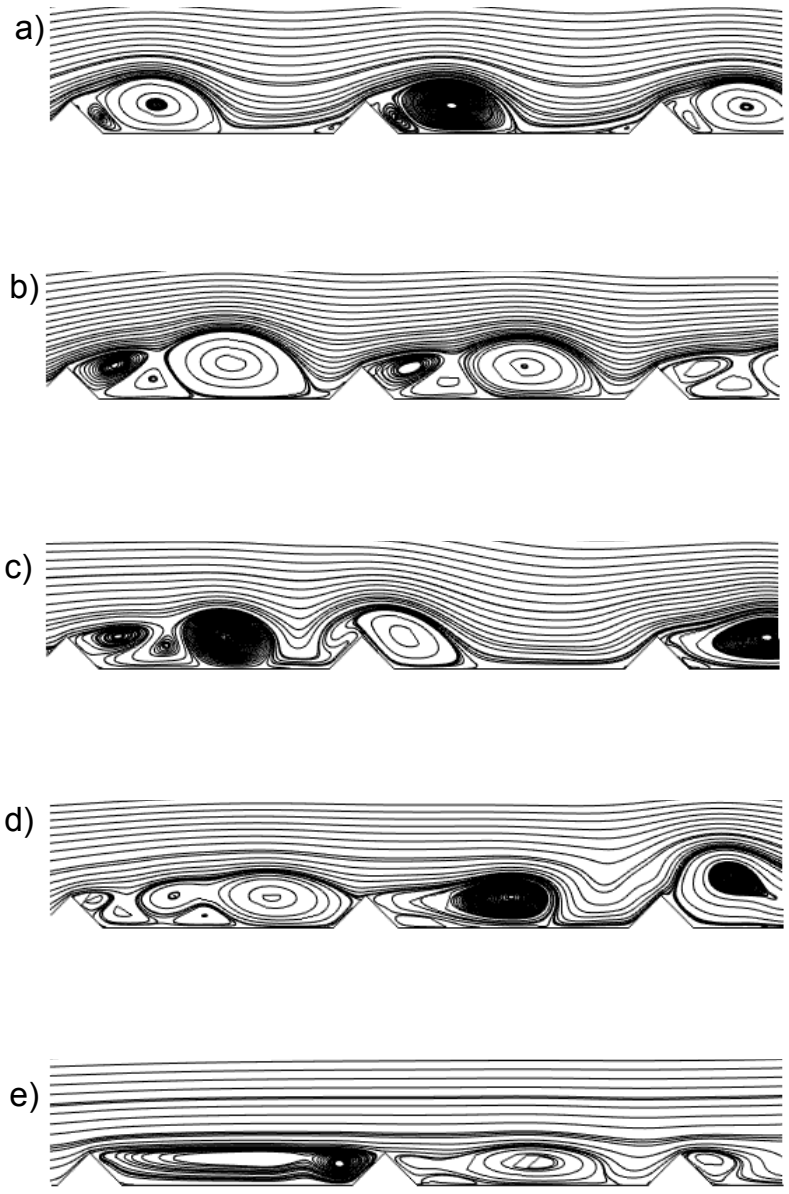


FIGURE C.6: Evolution of velocity streamlines for $w/k = 7$ (triangle): a) t=10.43 s, b) t= 20.58 s, c) t= 40.2, d) t=80.13 s, e) t=200 s.

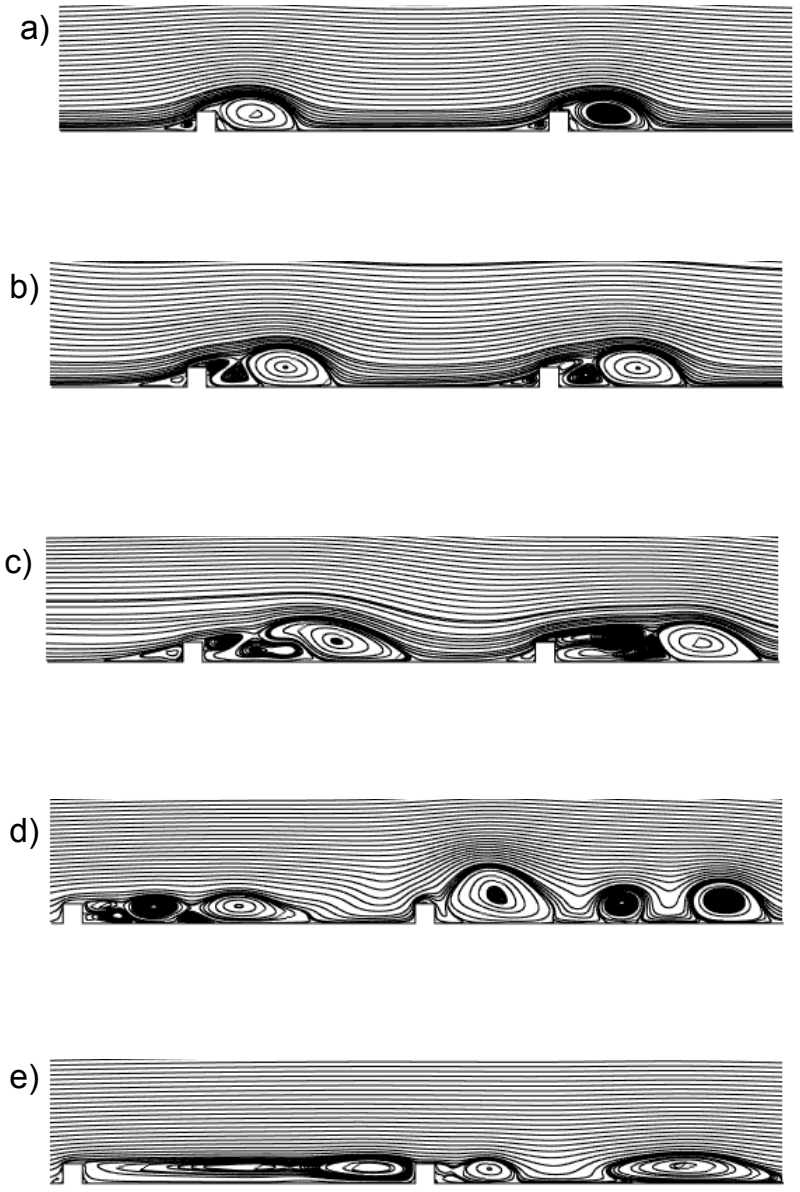


FIGURE C.7: Evolution of velocity streamlines for $w/k = 17$ (square): a) t=10.3 s, b) t= 20.61 s, c) t= 41.21, d) t=81.21 s, e) t=200 s.

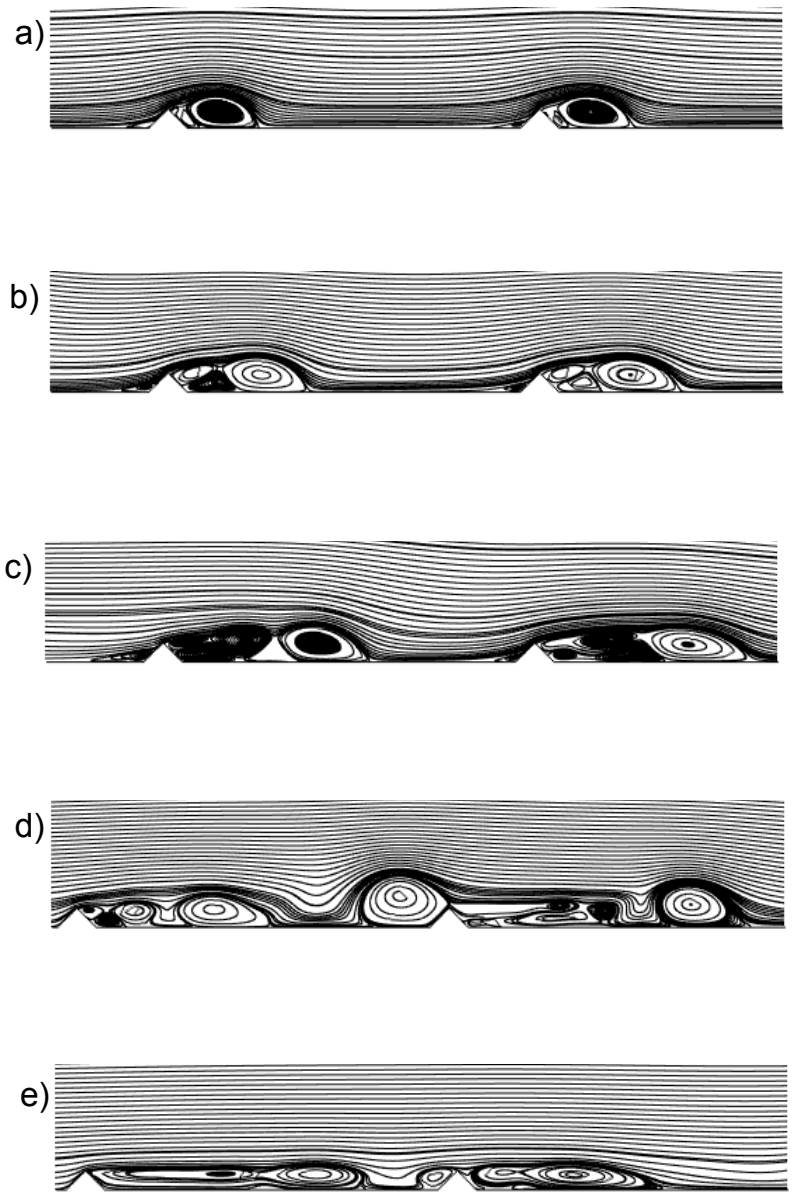


FIGURE C.8: Evolution of velocity streamlines for $w/k = 17$ (triangle): a) t=10.44 s, b) t= 20.59 s, c) t= 40.26, d) t=80.98 s, e) t=200 s.

## C.2 Velocity profile at different x-location

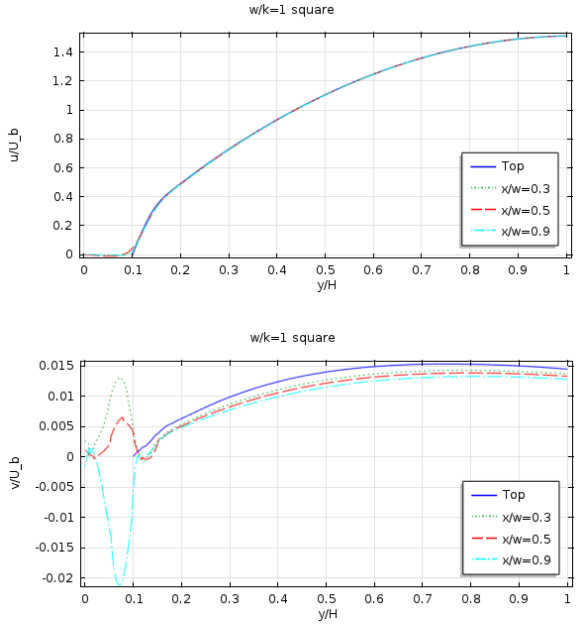


FIGURE C.9: Velocity profile at different x-location for $w/k = 1$ (square): Top(u-velocity), Bottom (v- velocity)

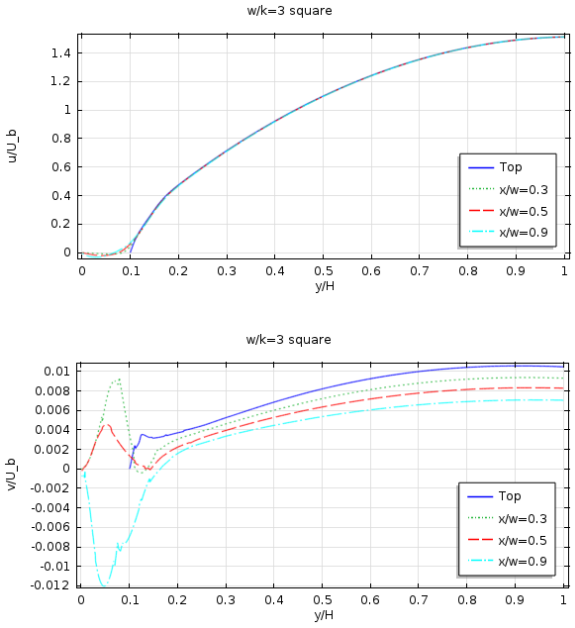


FIGURE C.10: Velocity profile at different x-location for $w/k = 3$ (square): Top(u-velocity), Bottom (v- velocity)

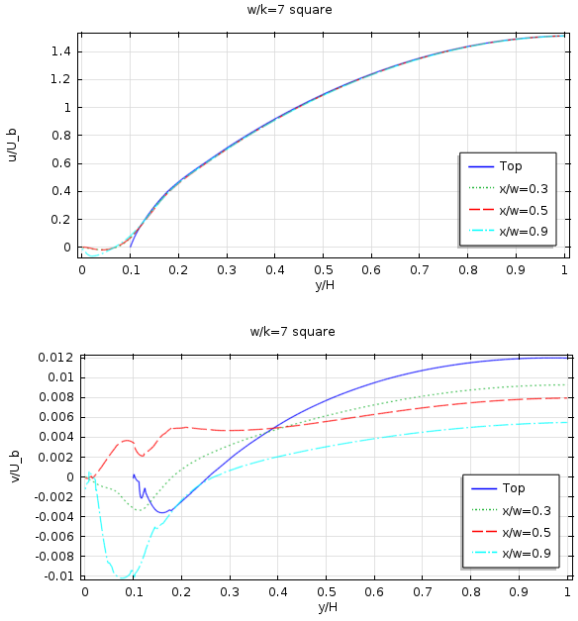


FIGURE C.11: Velocity profile at different x-location for $w/k = 7$ (square): Top(u-velocity), Bottom (v- velocity)

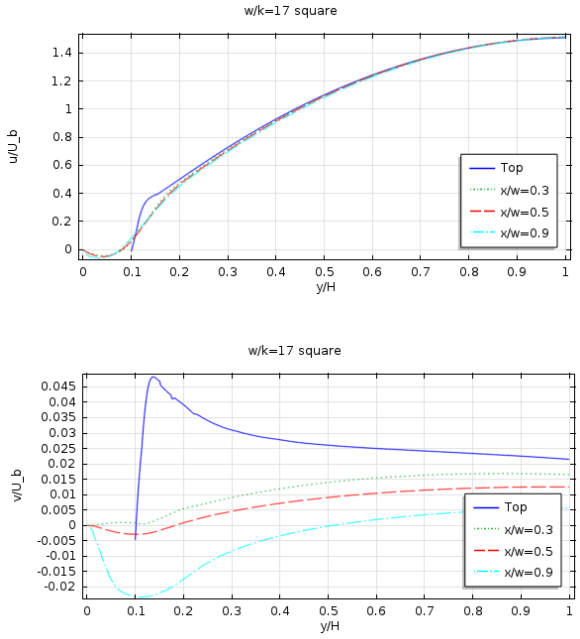


FIGURE C.12: Velocity profile at different x-location for $w/k = 17$ (square): Top(u-velocity), Bottom (v- velocity)

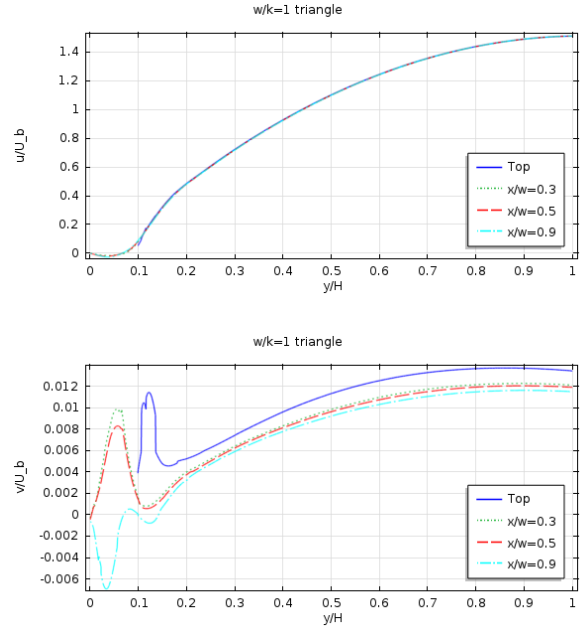


FIGURE C.13: Velocity profile at different x-location for $w/k = 1$ (triangle): Top(u-velocity), Bottom (v- velocity)

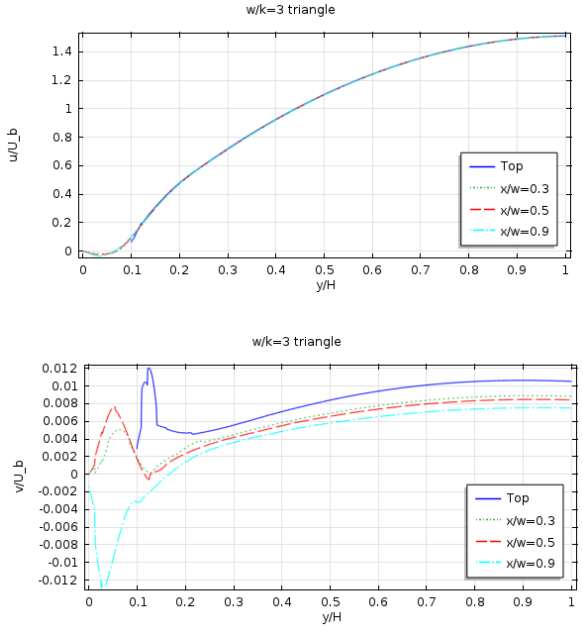


FIGURE C.14: Velocity profile at different x-location for $w/k = 3$ (triangle): Top(u-velocity), Bottom (v- velocity)

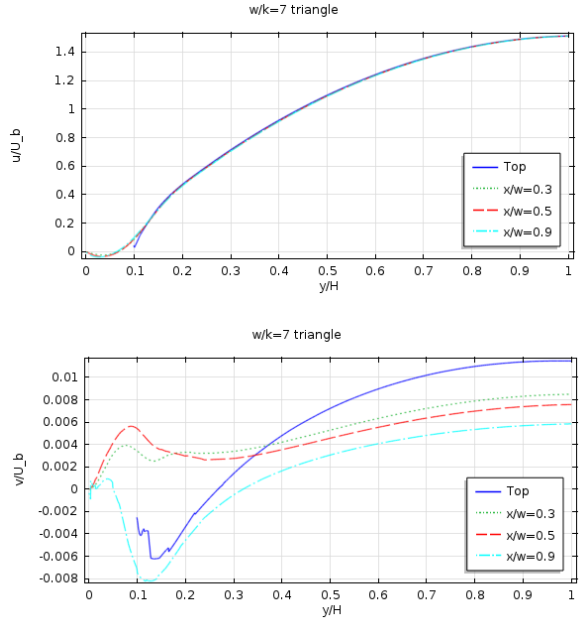


FIGURE C.15: Velocity profile at different x-location for $w/k = 7$ (triangle): Top(u-velocity), Bottom (v- velocity)

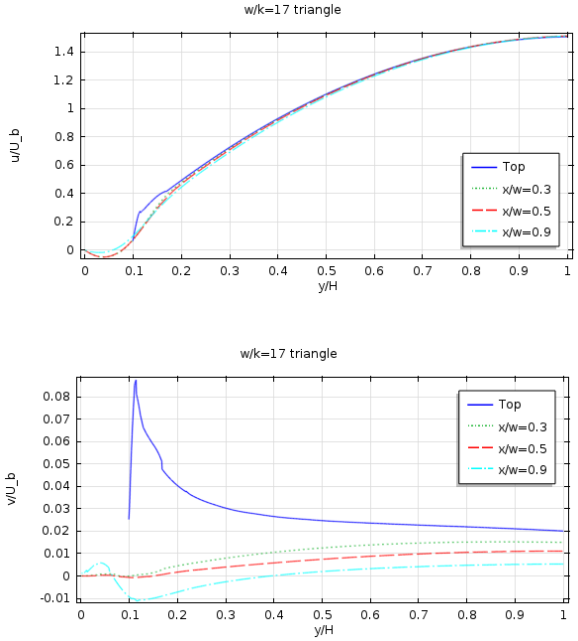


FIGURE C.16: Velocity profile at different x-location for $w/k = 17$ (triangle): Top(u-velocity), Bottom (v- velocity)

## C.3 Friction velocity $u_\tau$ contour plots

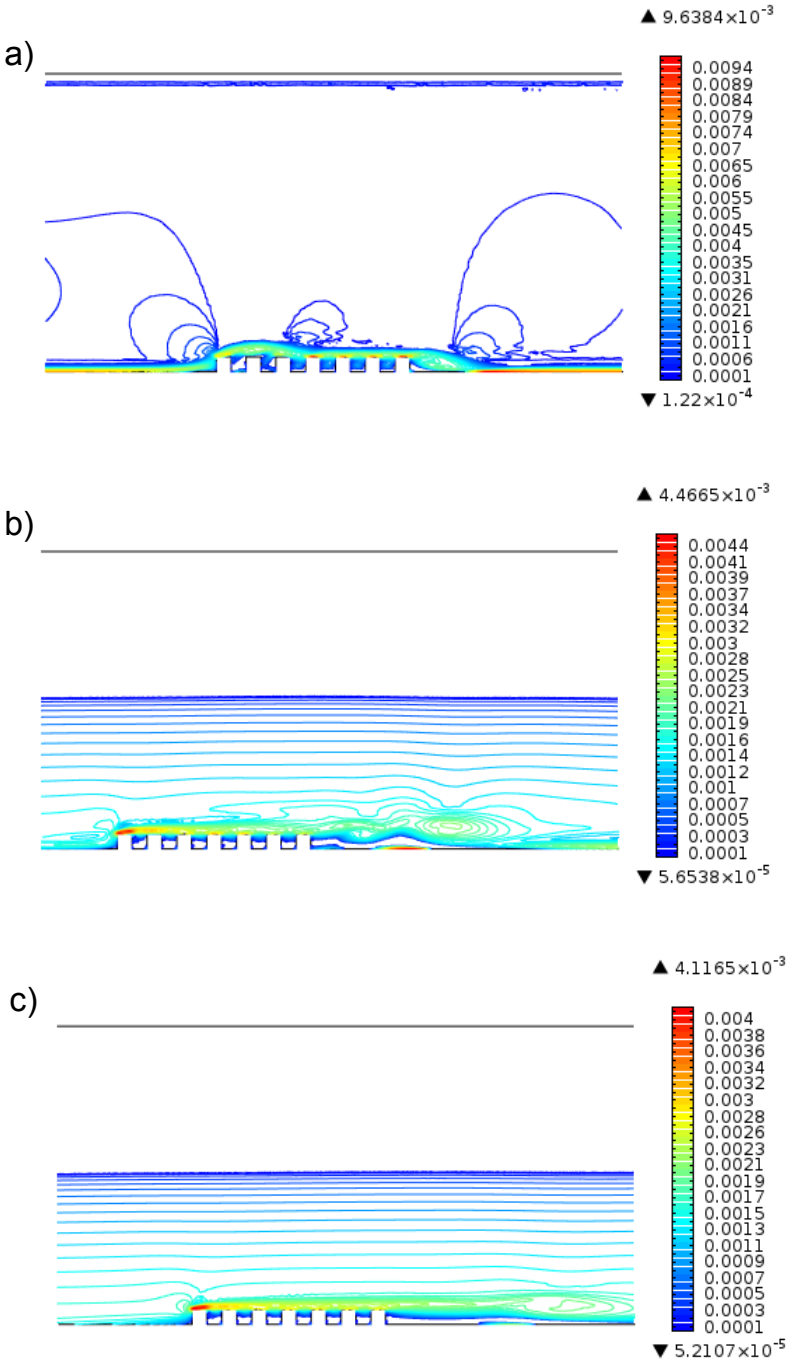


FIGURE C.17: Flow evolution of the friction velocity ($u_\tau$) in [m/s] for $w/k = 1$ (square): a) 10.43 s, b) 102.82 s, c) 200 s

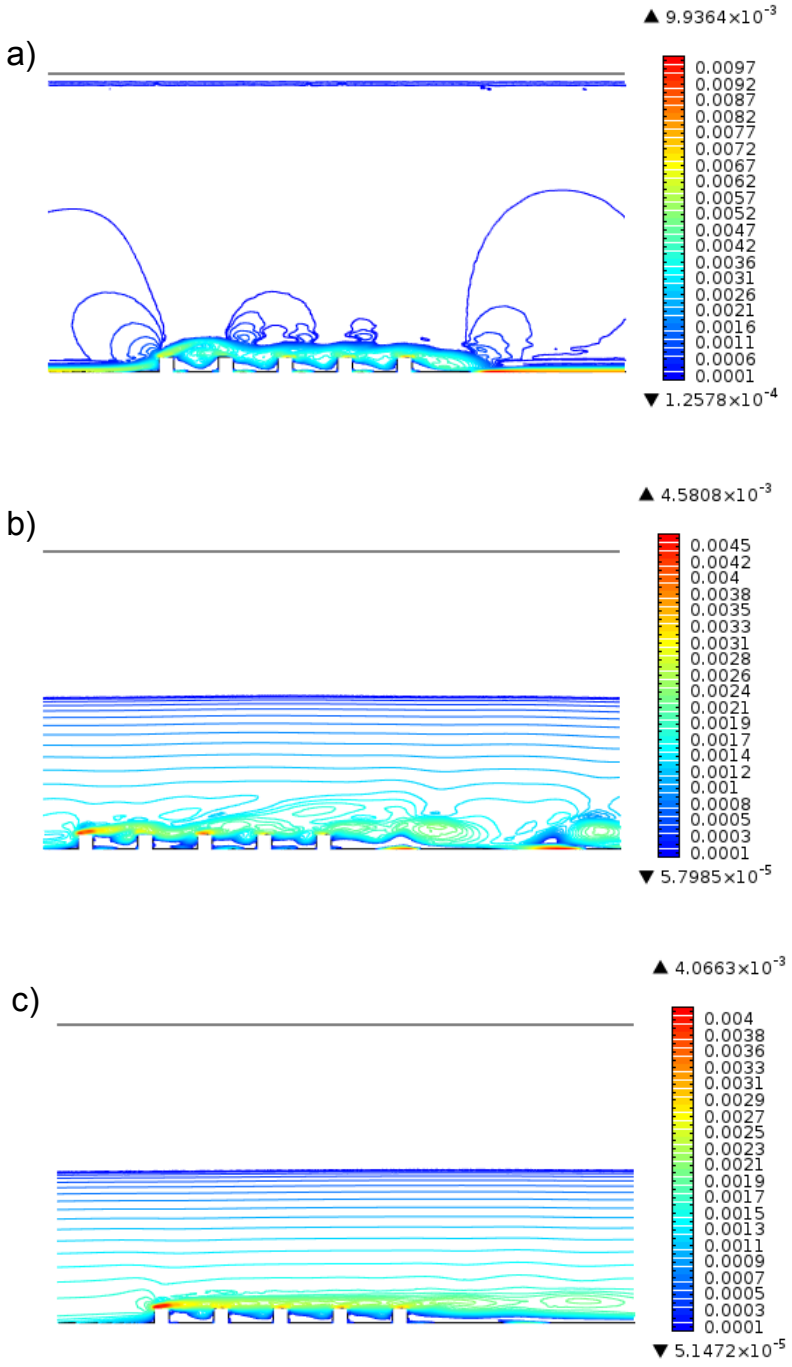


FIGURE C.18: Flow evolution of the friction velocity ($u_\tau$) in [m/s] for $w/k = 3$ (square): a) 10.36 s, b) 101.22 s, c) 200 s

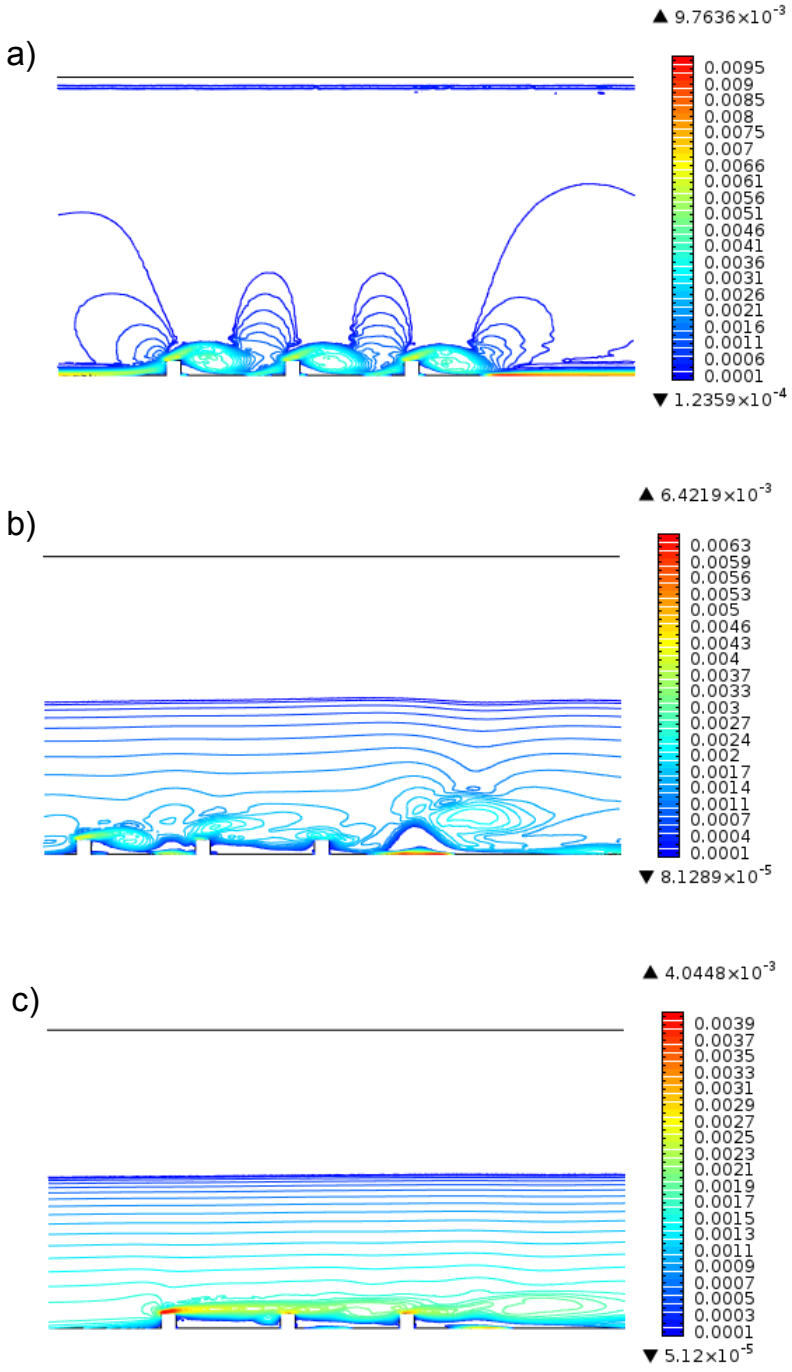


FIGURE C.19: Flow evolution of the friction velocity ($u_\tau$) in [m/s] for $w/k = 7$ (square): a) 10.52 s, b) 100.38 s, c) 200 s

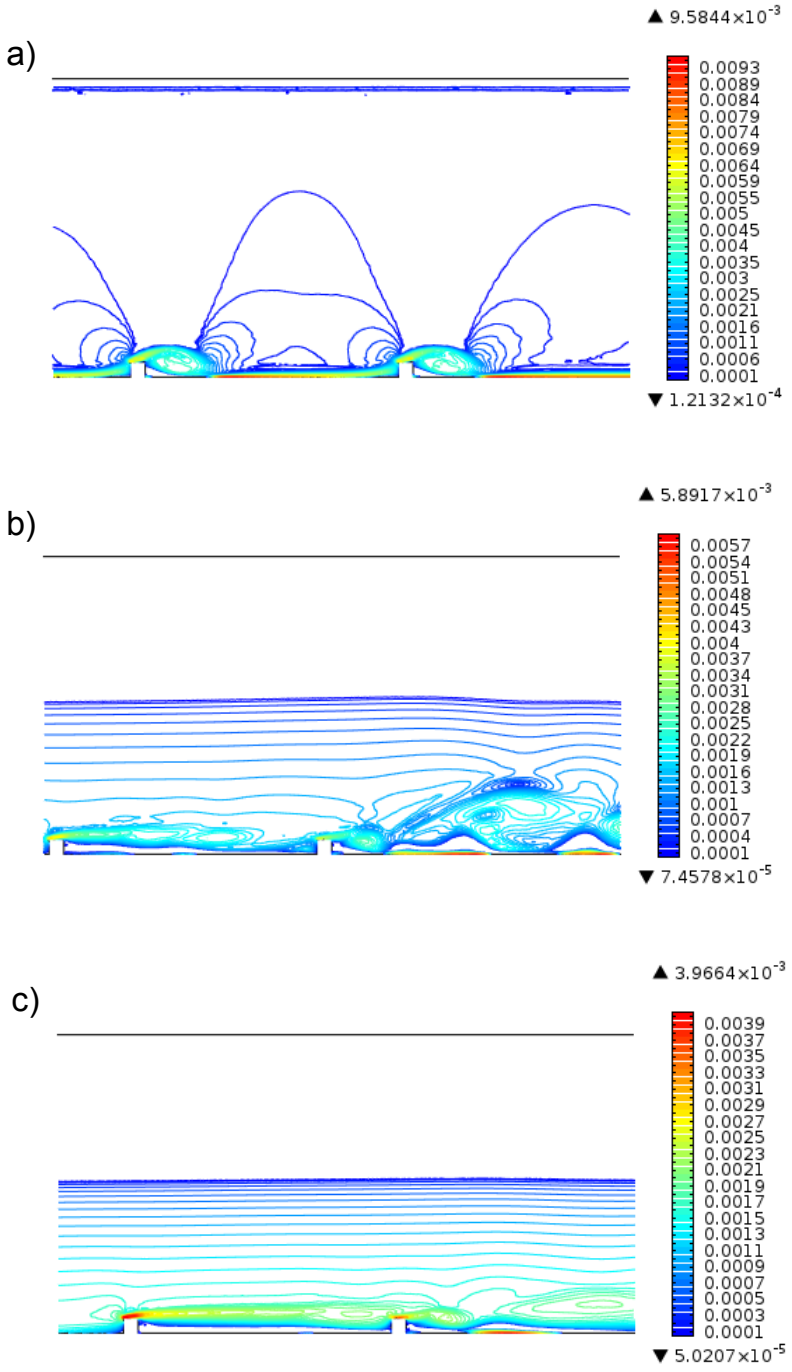


FIGURE C.20: Flow evolution of the friction velocity ($u_\tau$) in [m/s] for $w/k = 17$ (square): a) 10.31 s, b) 100.59 s, c) 200 s

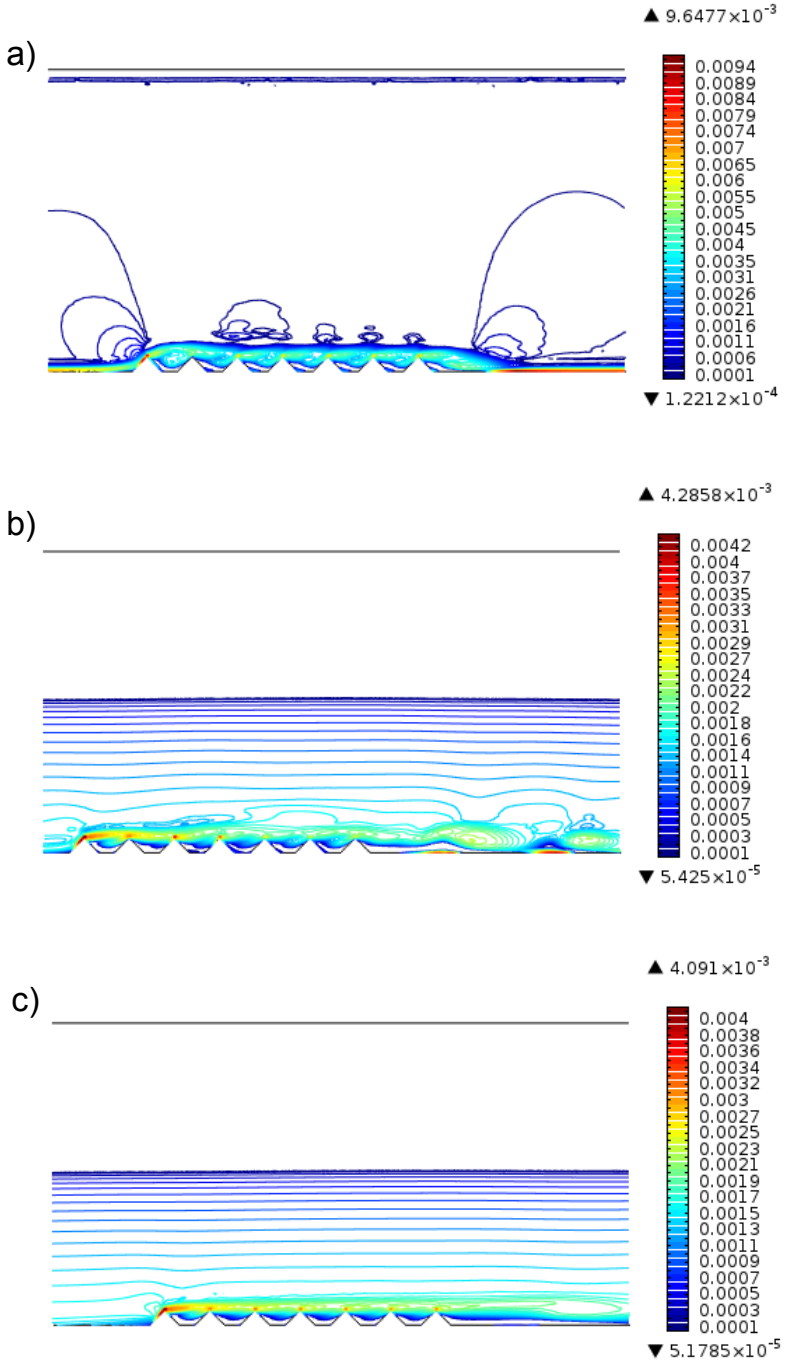


FIGURE C.21: Flow evolution of the friction velocity ($u_\tau$) in [m/s] for $w/k = 1$ (triangle): a) 10.32 s, b) 101.98 s, c) 200 s

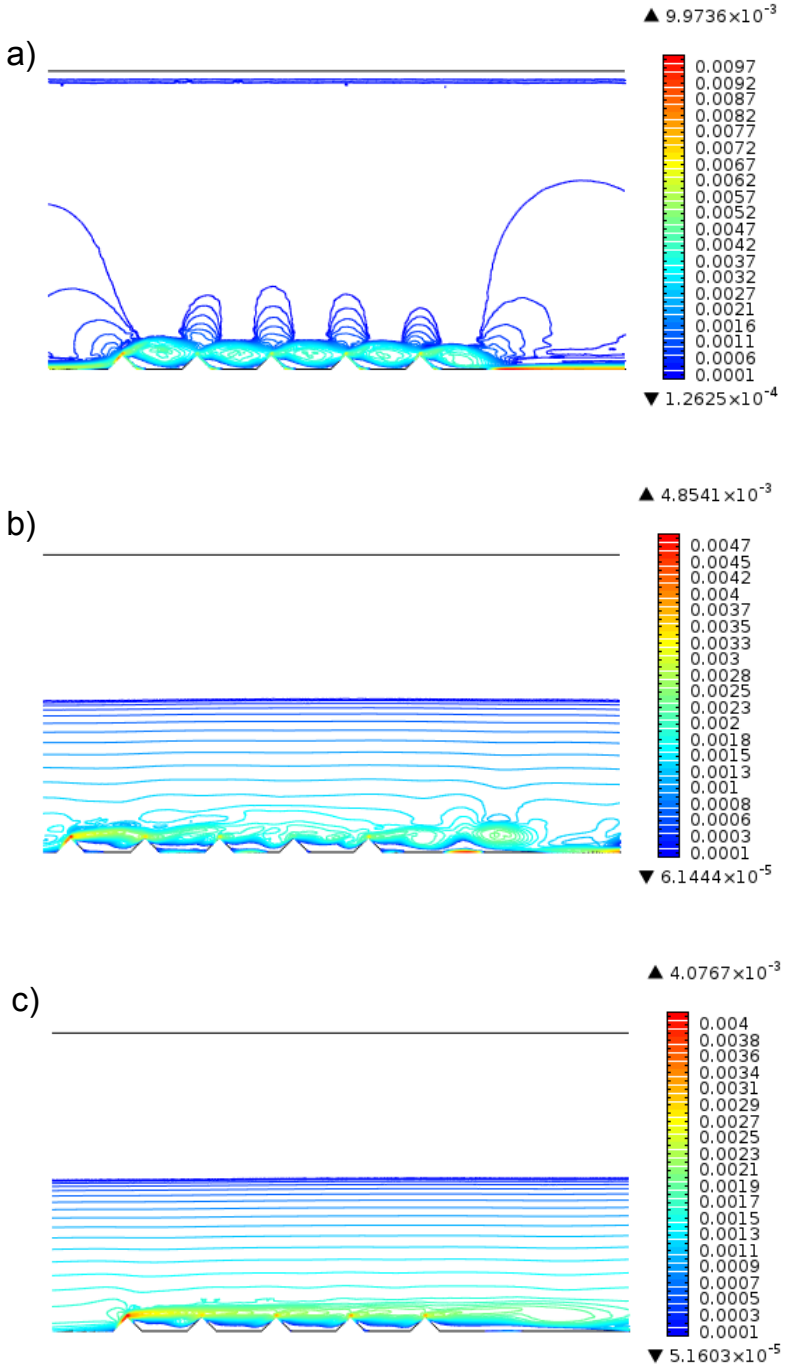


FIGURE C.22: Flow evolution of the friction velocity ($u_\tau$) in [m/s] for $w/k = 3$ (triangle): a) 10.17 s, b) 100.91 s, c) 200 s

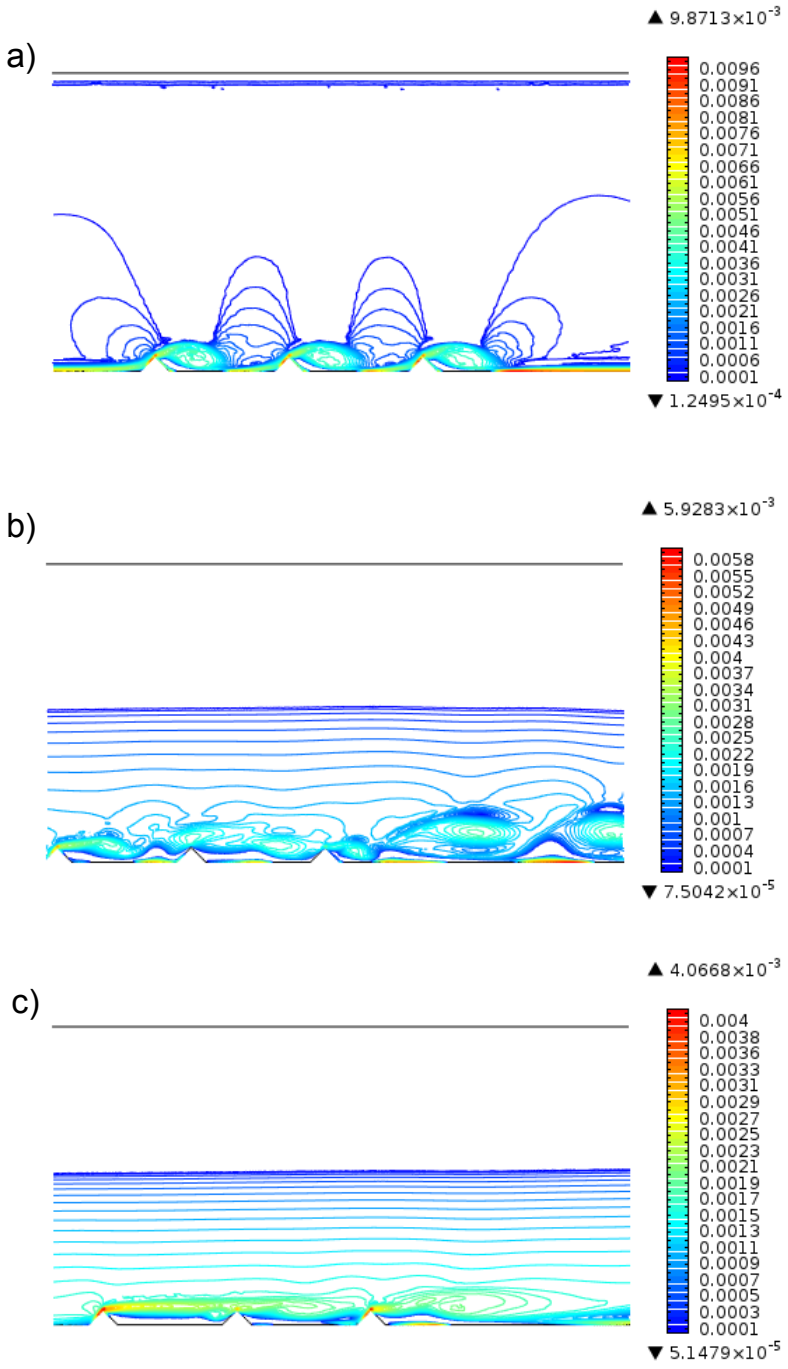


FIGURE C.23: Flow evolution of the friction velocity ($u_\tau$) in [m/s] for $w/k = 7$ (triangle): a) 10.42 s, b) 100.84 s, c) 200 s

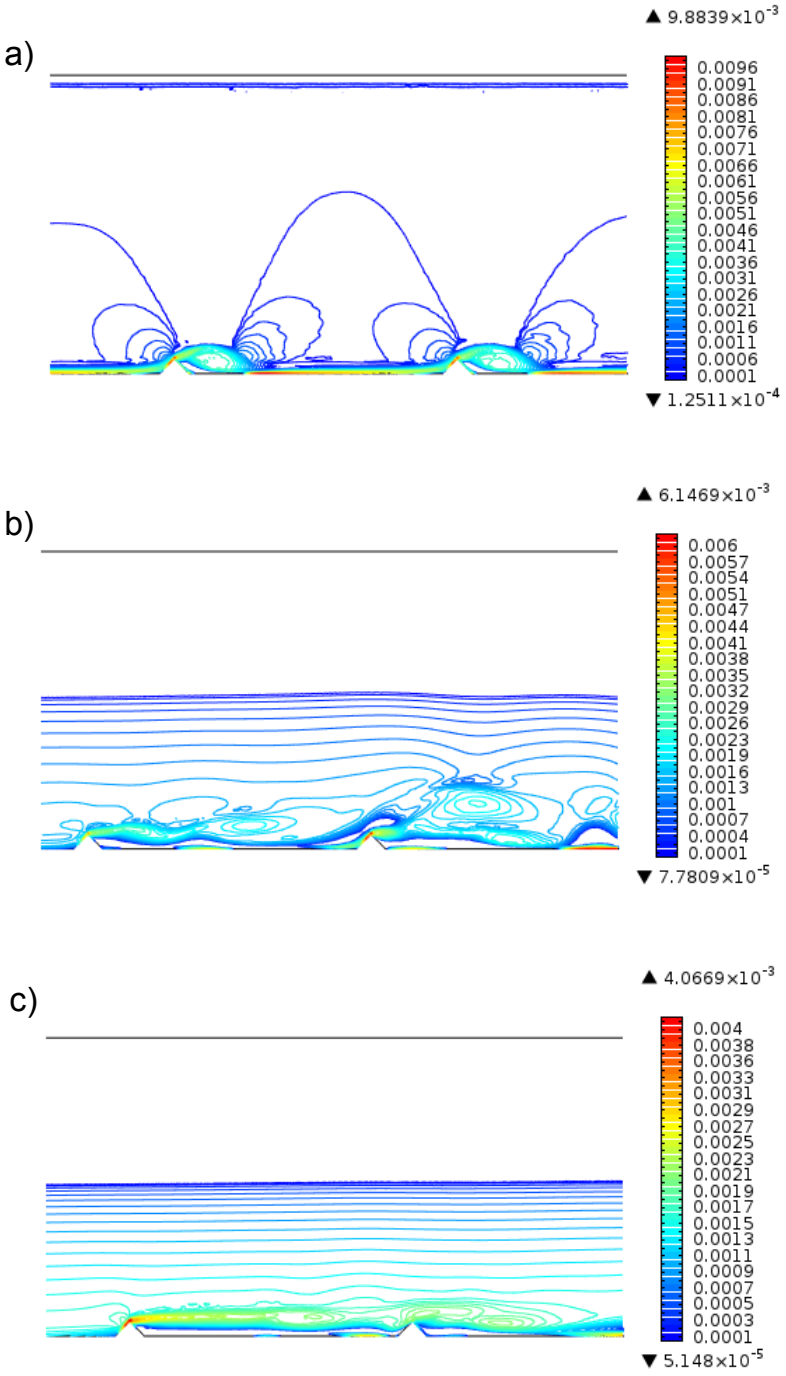


FIGURE C.24: Flow evolution of the friction velocity ($u_\tau$) in [m/s] for $w/k = 17$ (triangle): a) 10.41 s, b) 101.33 s, c) 200 s

## C.4 Pressure gradient $p_x$ contour plots

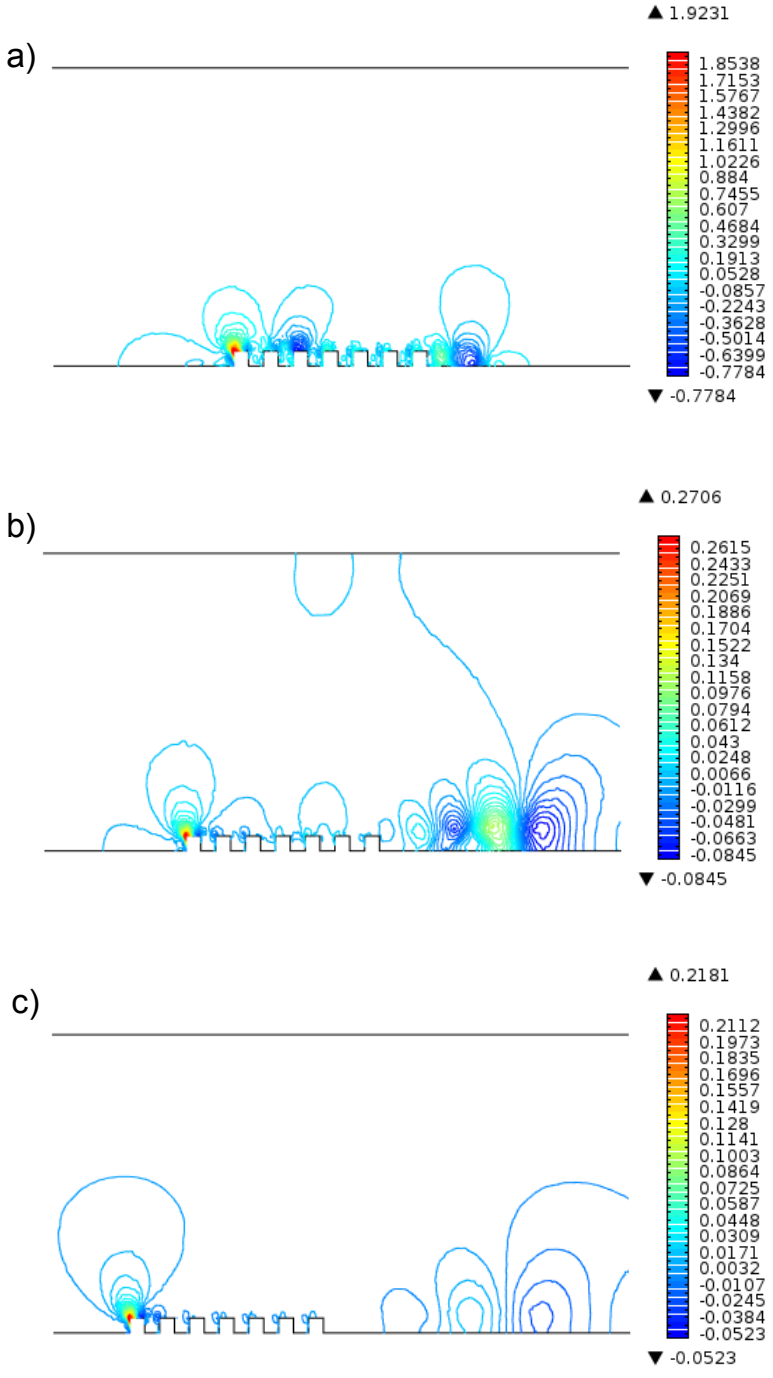


FIGURE C.25: Flow evolution of the pressure gradient ($p_x$) for $w/k = 1$ (square): a) 10.43 s, b) 102.82 s, c) 200 s

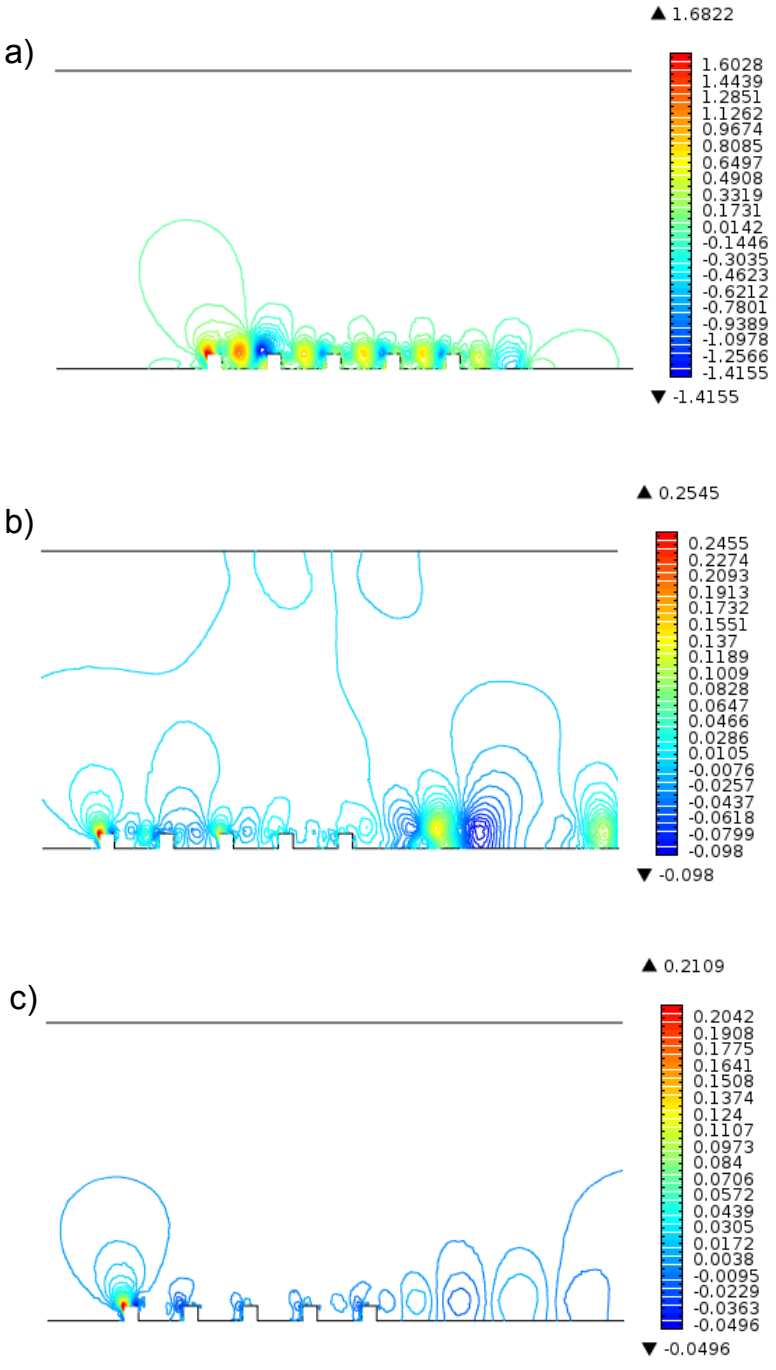


FIGURE C.26: Flow evolution of the the pressure gradient ($p_x$) for $w/k = 3$ (square): a) 10.36 s, b) 101.22 s, c) 200 s

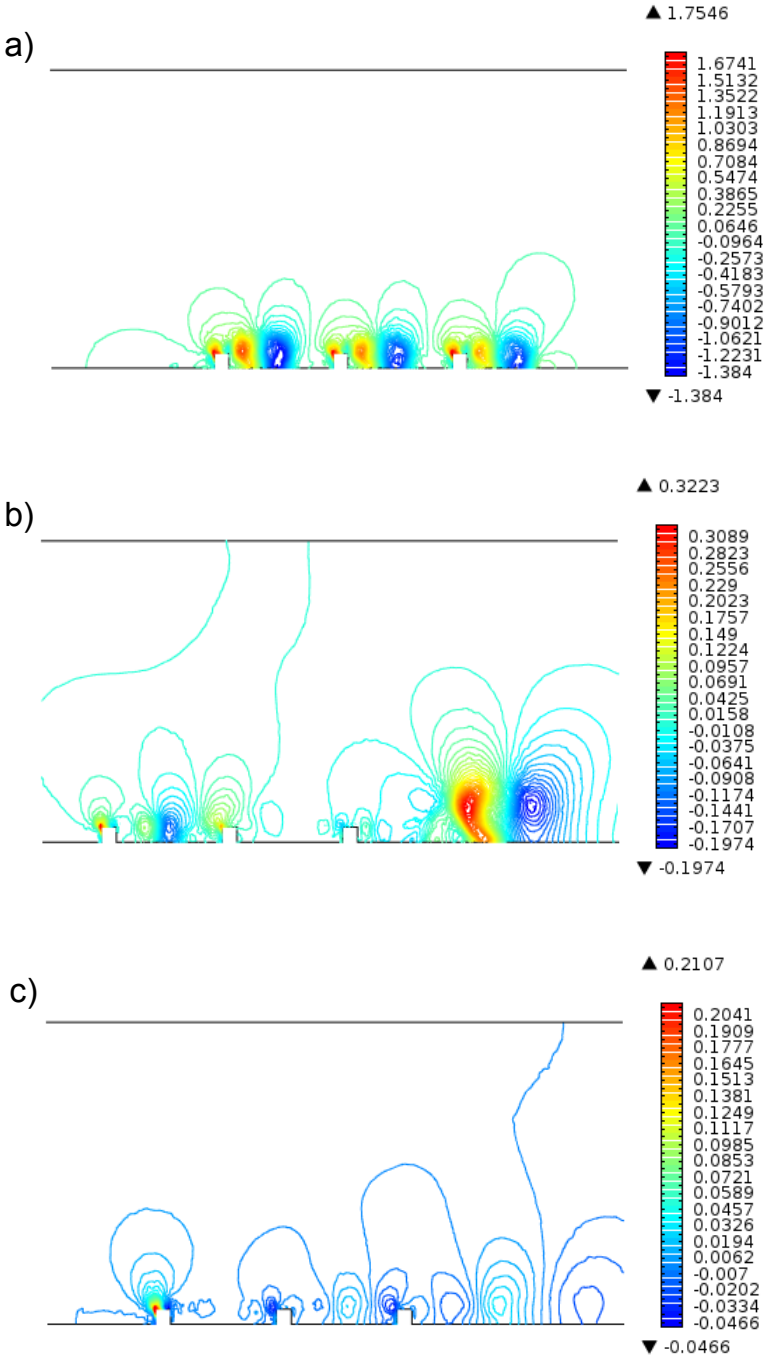


FIGURE C.27: Flow evolution of the pressure gradient ($p_x$) for $w/k = 7$ (square): a) 10.52 s, b) 100.38 s, c) 200 s

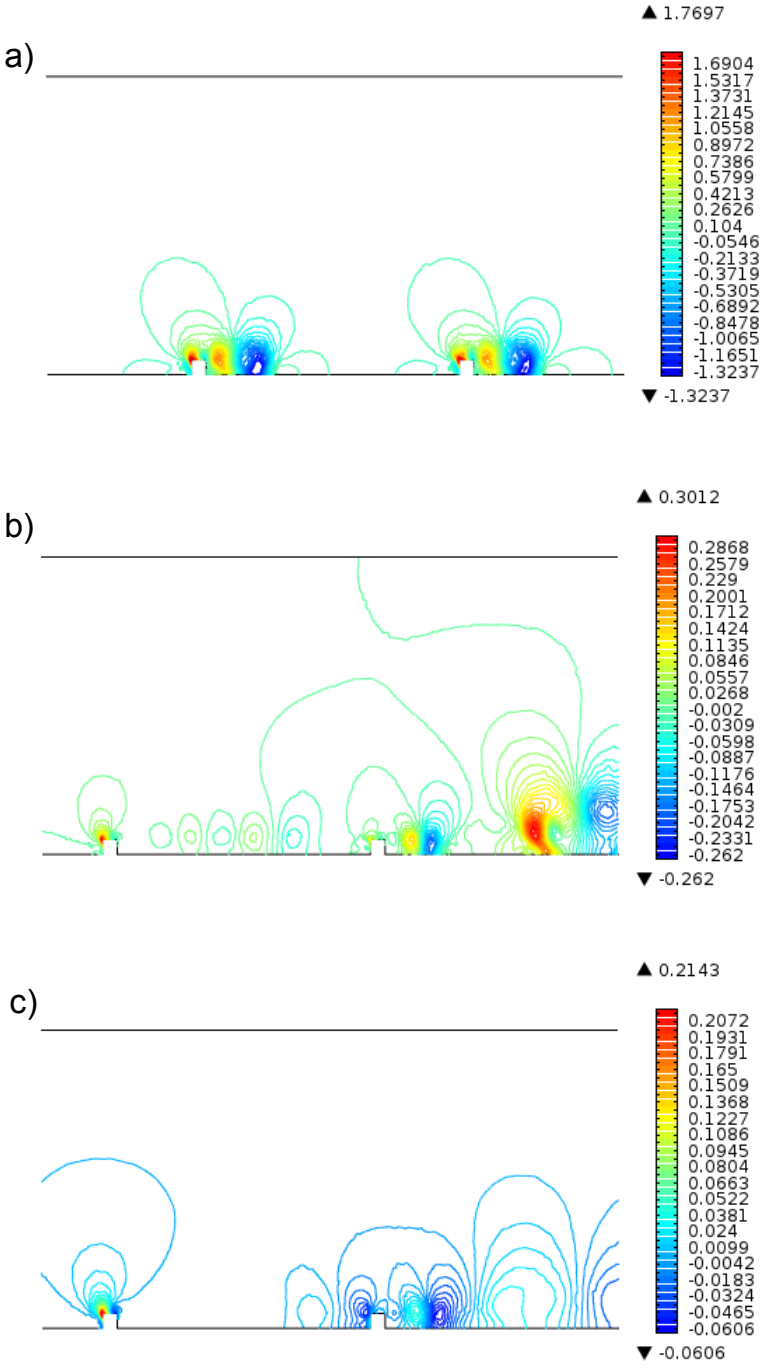


FIGURE C.28: Flow evolution of the pressure gradient ($p_x$) for $w/k = 17$ (square): a) 10.31 s, b) 100.59 s, c) 200 s

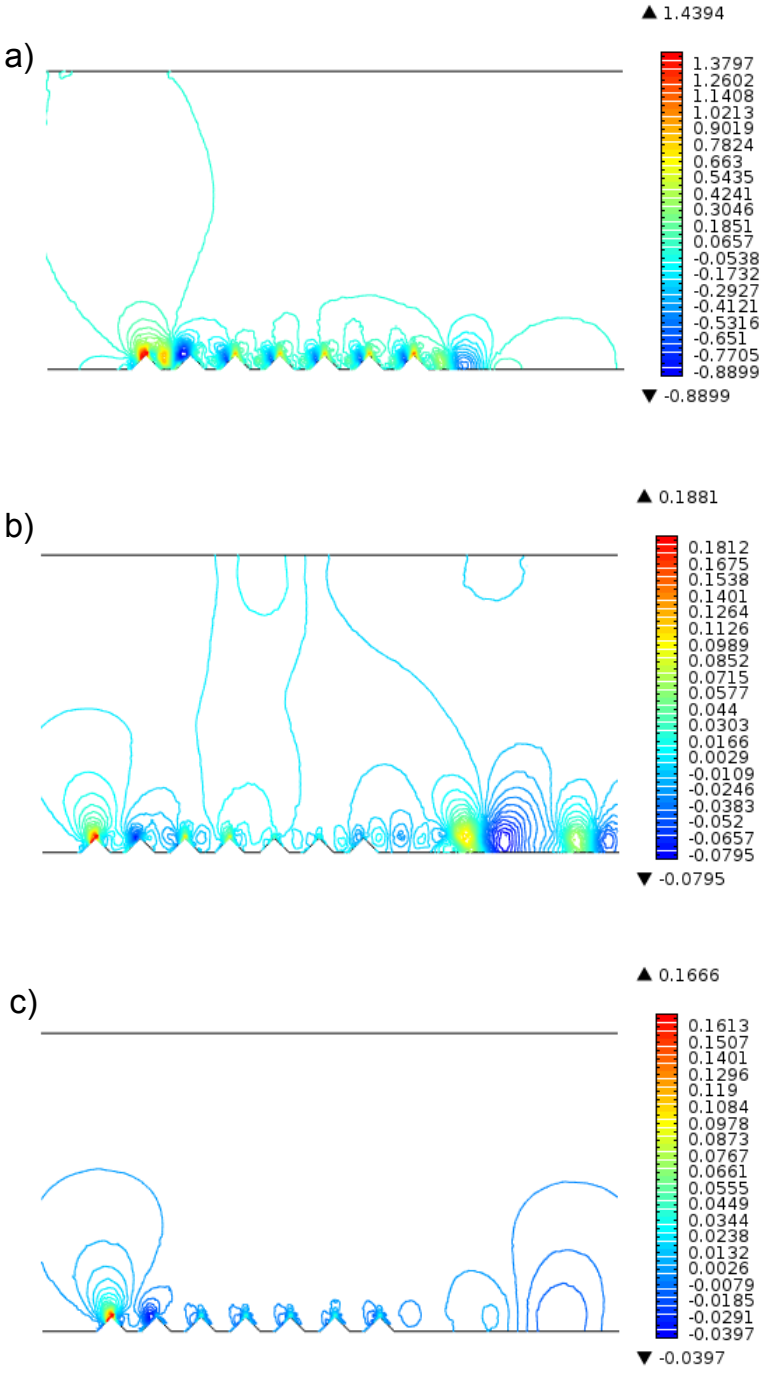


FIGURE C.29: Flow evolution of the pressure gradient ($p_x$) for $w/k = 1$ (triangle): a) 10.32 s, b) 101.98 s, c) 200 s

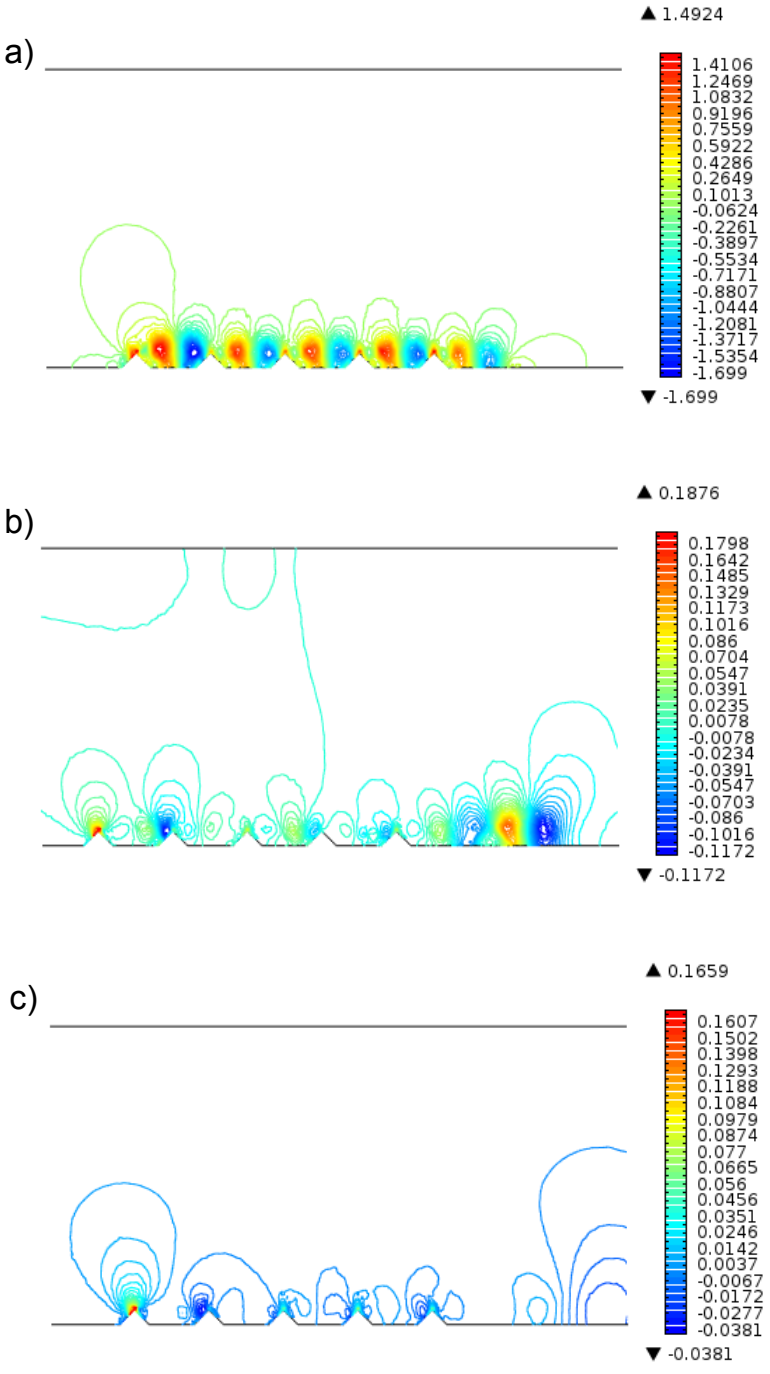


FIGURE C.30: Flow evolution of the pressure gradient ($p_x$) for $w/k = 3$ (triangle): a) 10.17 s, b) 100.91 s, c) 200 s

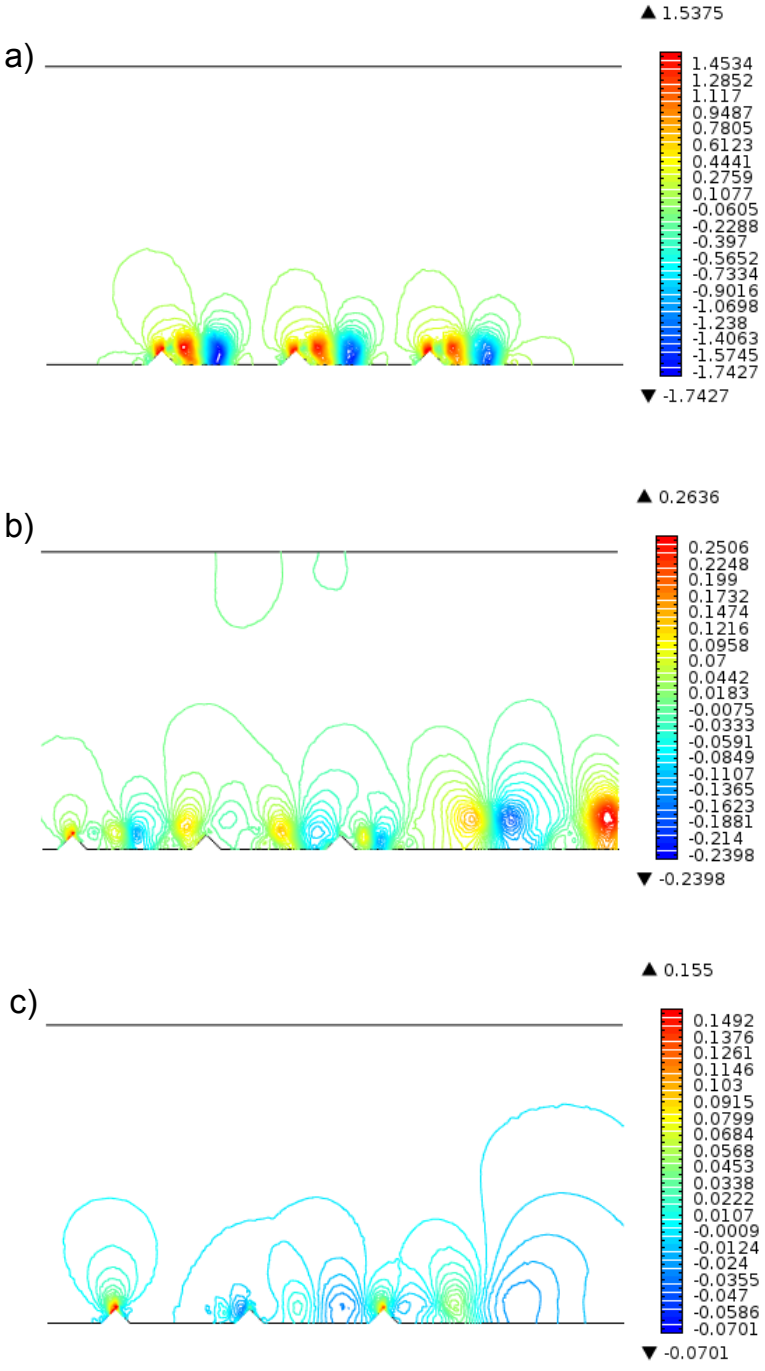


FIGURE C.31: Flow evolution of the pressure gradient ($p_x$) for $w/k = 7$ (triangle): a) 10.42 s, b) 100.84 s, c) 200 s

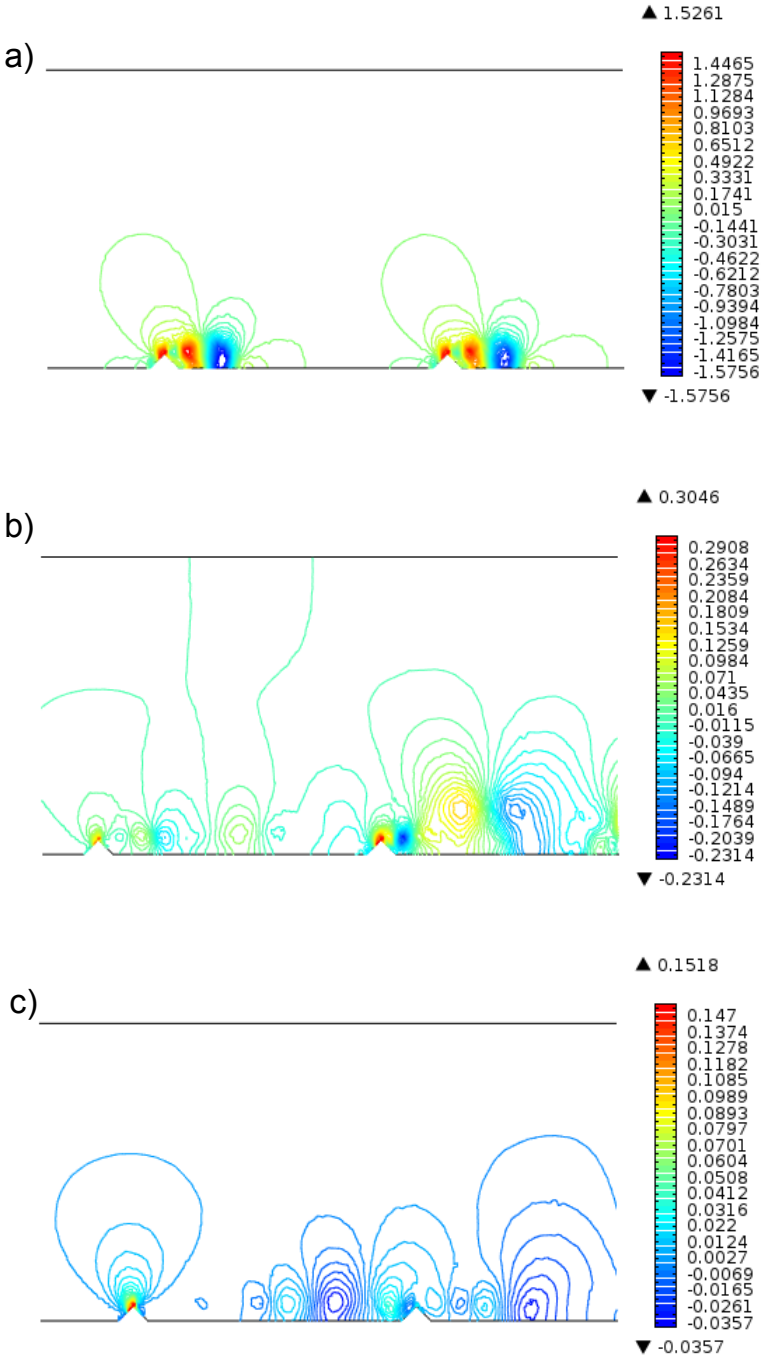


FIGURE C.32: Flow evolution of the pressure gradient ($p_x$) for $w/k = 17$ (triangle): a) 10.41 s, b) 101.33 s, c) 200 s

## C.5 Resistance components line plots

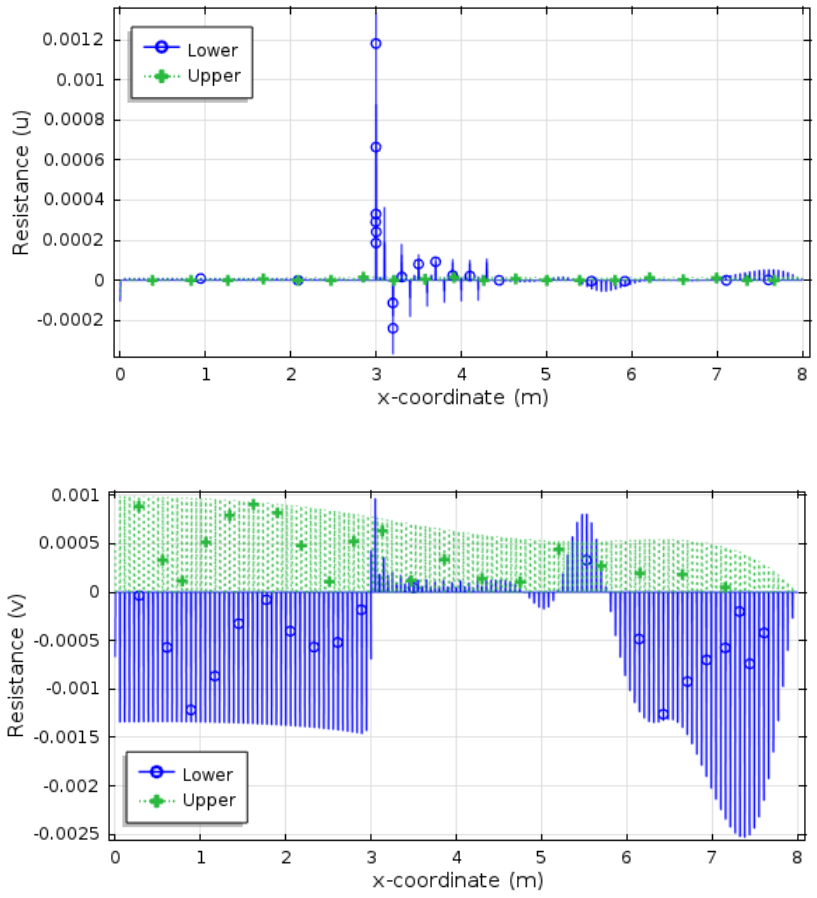


FIGURE C.33: Resistance components balance for w/k = 1 (square); Top (Resistance (u)), Bottom (Resistance (v)).

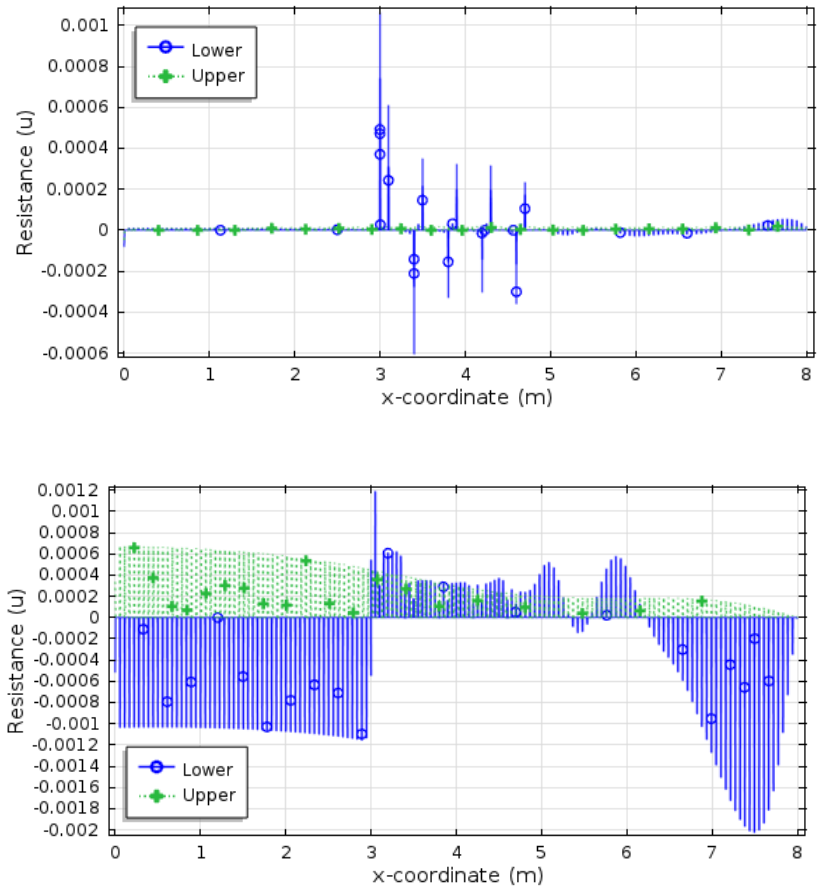


FIGURE C.34: Resistance components balance for w/k = 3 (square); Top (Resistance (u)), Bottom (Resistance (v)).

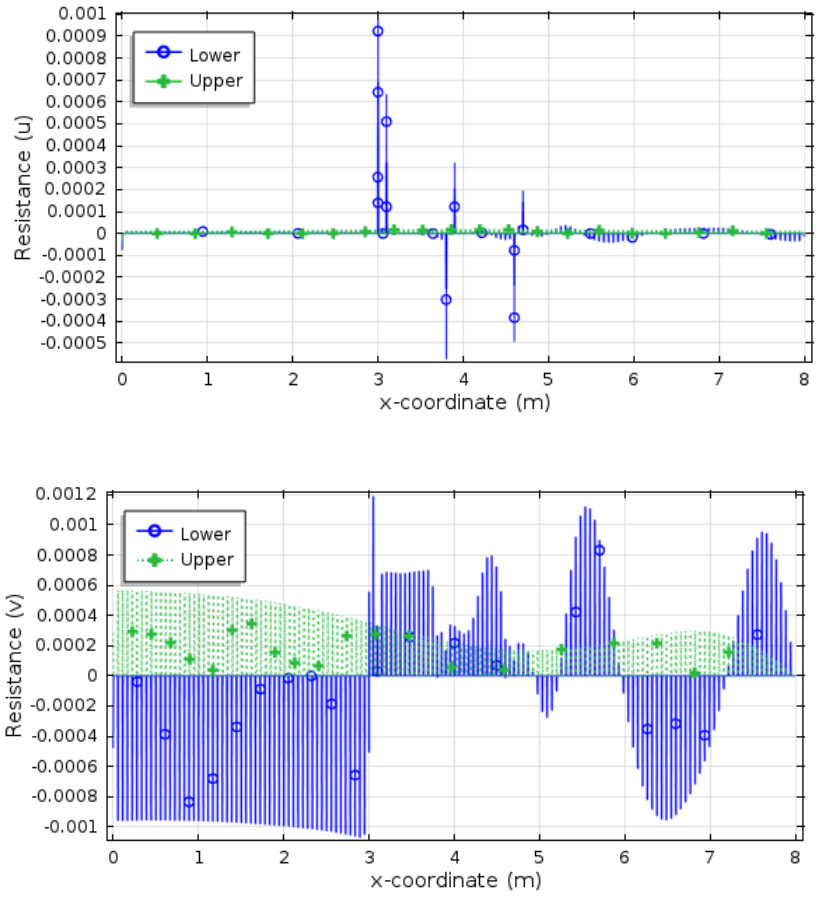


FIGURE C.35: Resistance components balance for w/k = 7 (square); Top (Resistance (u)), Bottom (Resistance (v)).

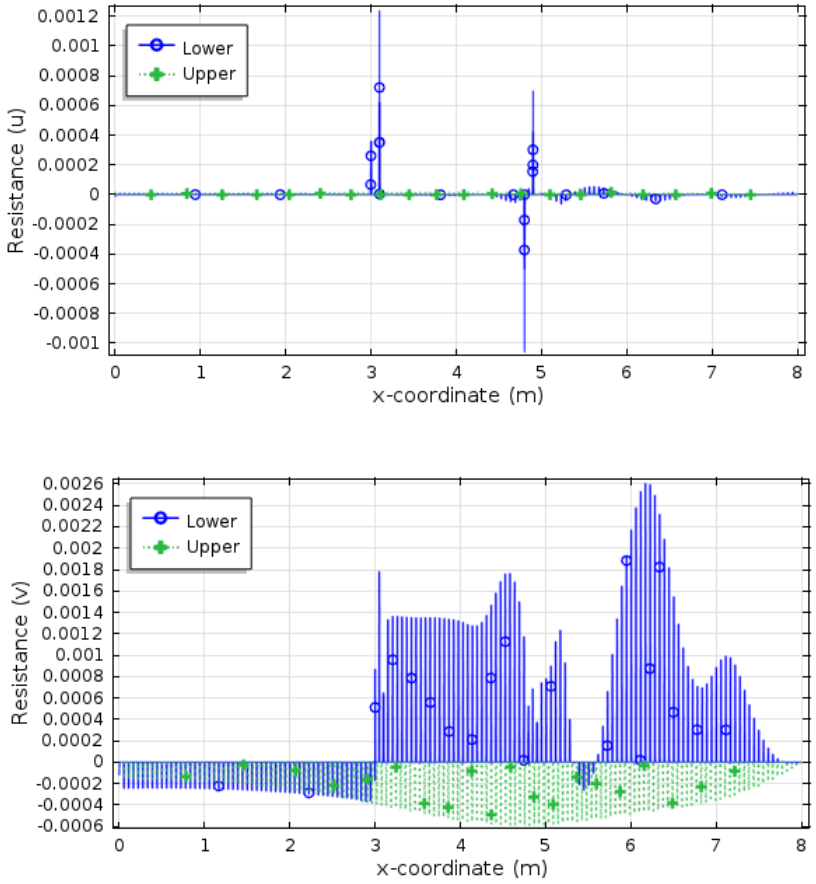


FIGURE C.36: Resistance components balance for w/k = 17 (square); Top (Resistance (u)), Bottom (Resistance (v)).

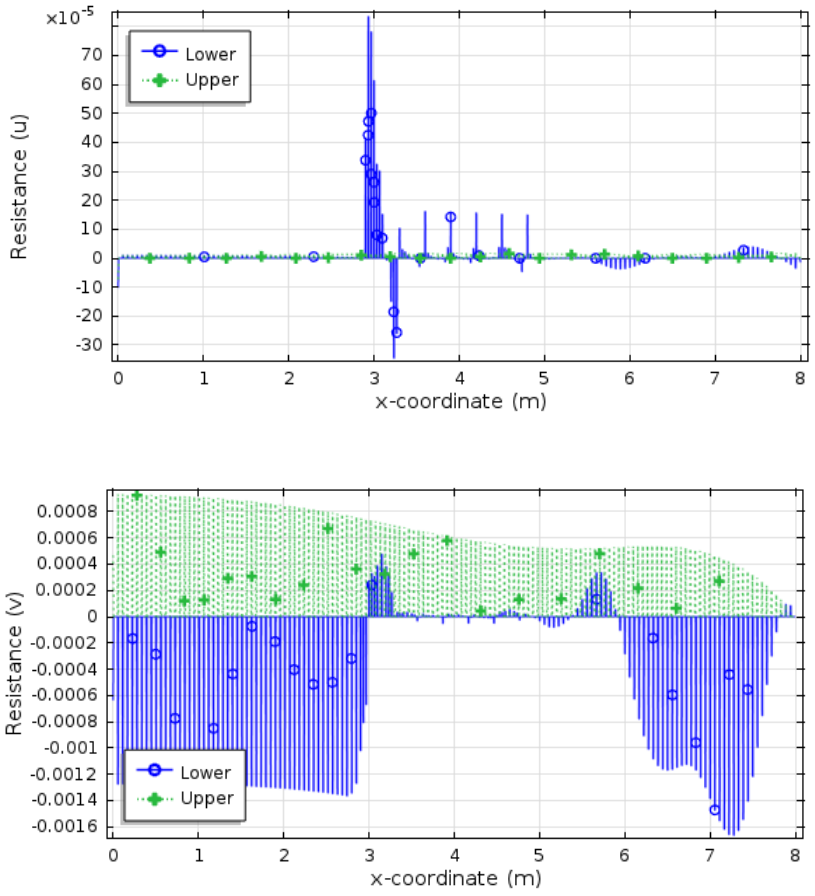


FIGURE C.37: Resistance components balance for w/k = 1 (triangle); Top (Resistance (u)), Bottom (Resistance (v)).

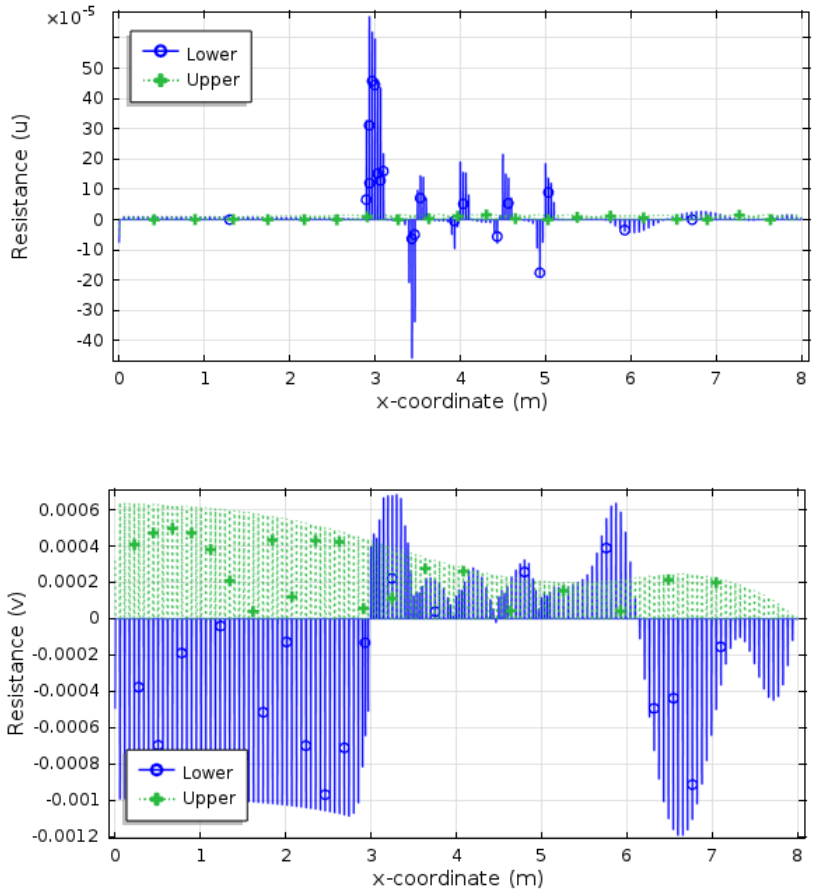


FIGURE C.38: Resistance components balance for w/k = 3 (triangle); Top (Resistance (u)), Bottom (Resistance (v)).

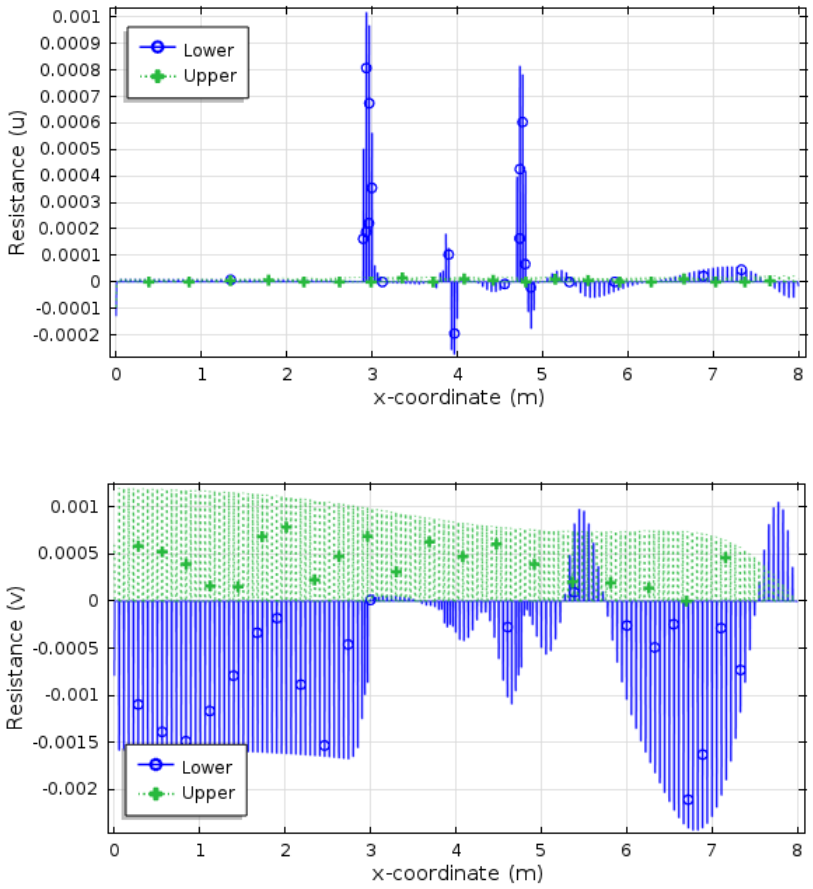


FIGURE C.39: Resistance components balance for w/k = 7 (triangle); Top (Resistance (u)), Bottom (Resistance (v)).

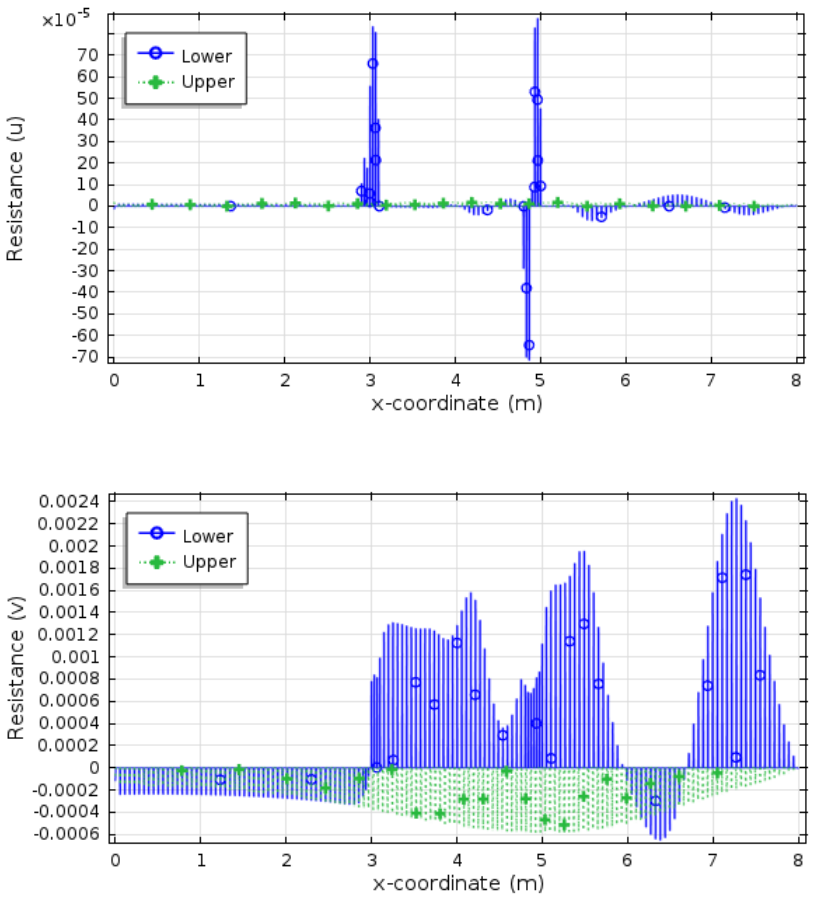


FIGURE C.40: Resistance components balance for w/k = 17 (triangle); Top (Resistance (u)), Bottom (Resistance (v)).

## C.6 Instantaneous velocity contour plots

### C.6.1 Streamwise velocity (u)

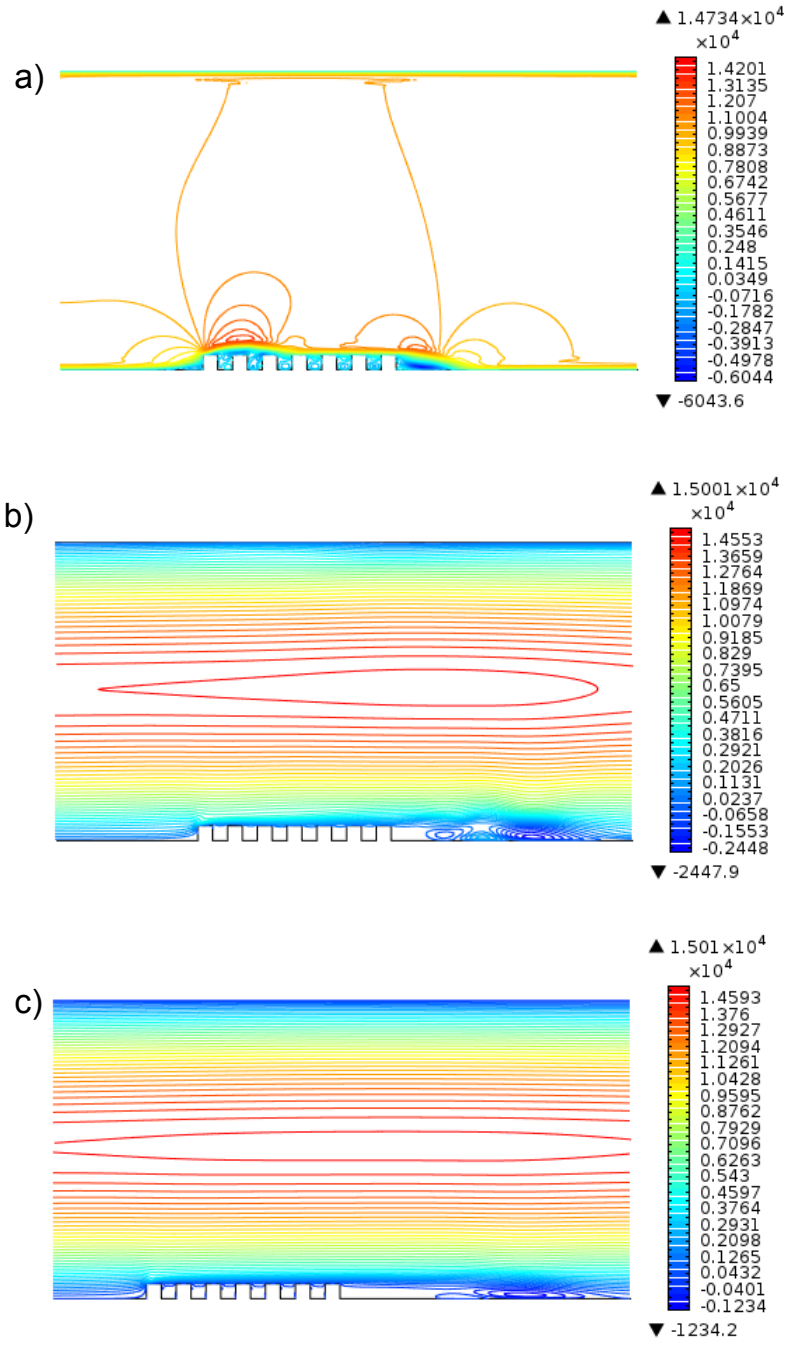


FIGURE C.41: Evolution of the streamwise velocity (u) for $w/k = 1$ (square): a) t = 10.43 s, b) t = 102.82 s, c) t = 200 s.

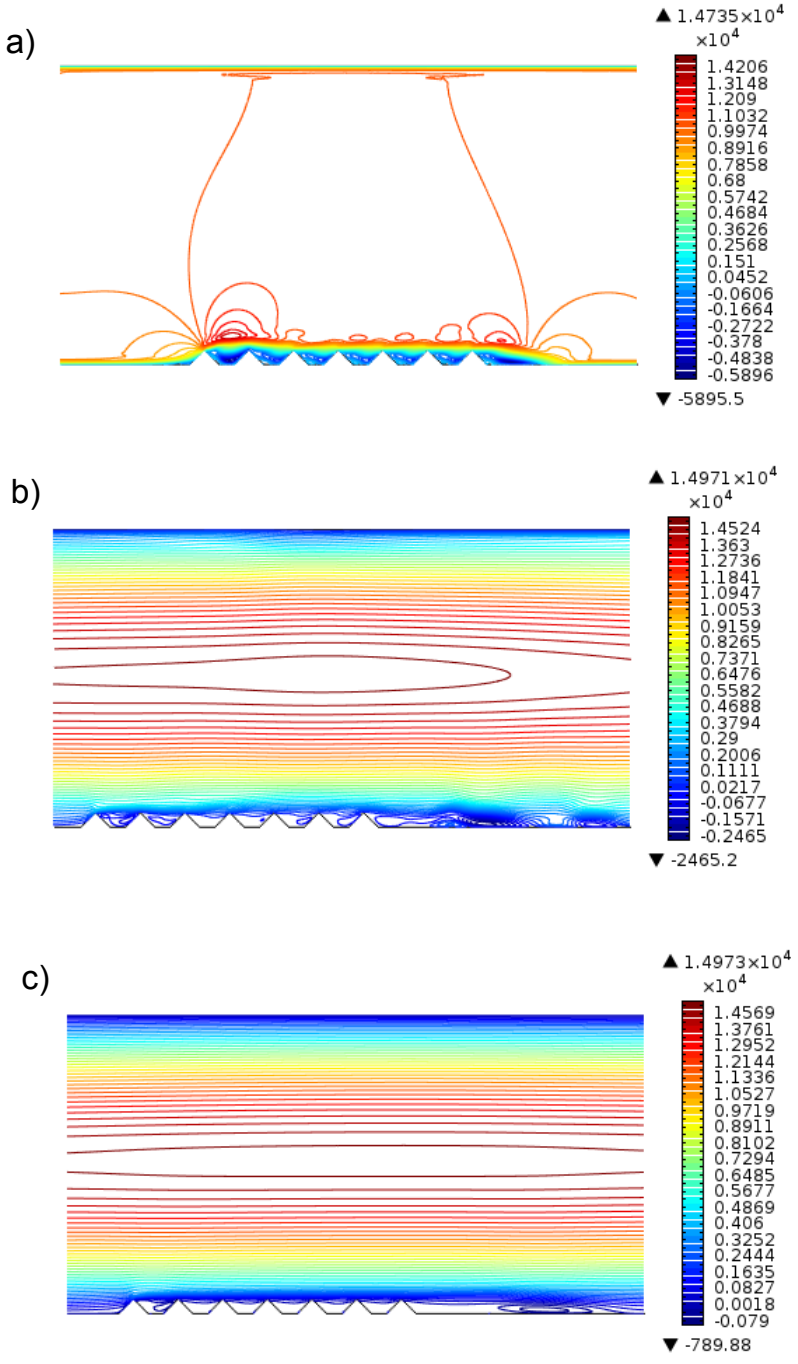


FIGURE C.42: Evolution of the streamwise velocity (u) for $w/k = 1$ (triangle): a) t = 10.32 s, b) t = 101.98 s, c) t = 200 s.

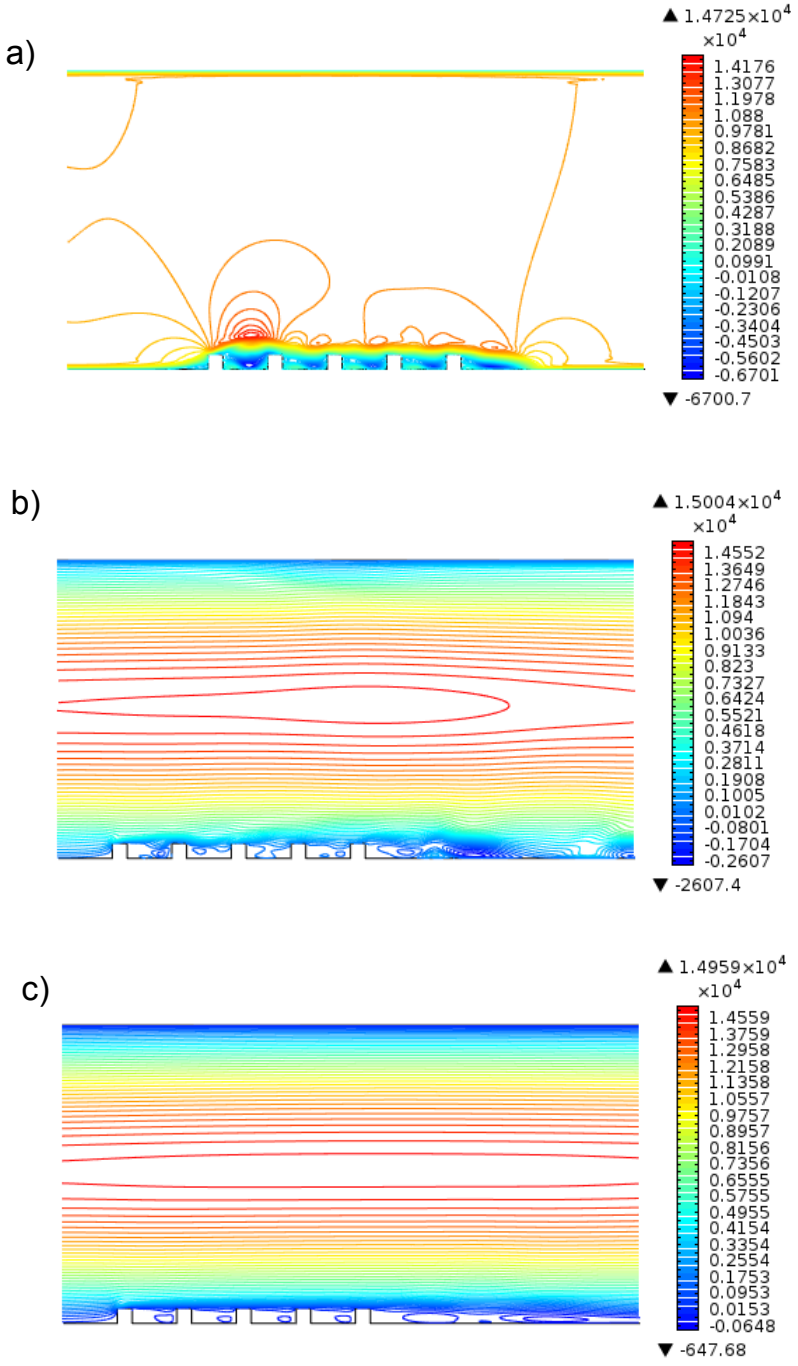


FIGURE C.43: Evolution of the streamwise velocity (u) for $w/k = 3$ (square): a) t = 10.36 s, b) t = 101.22 s, c) t = 200 s.

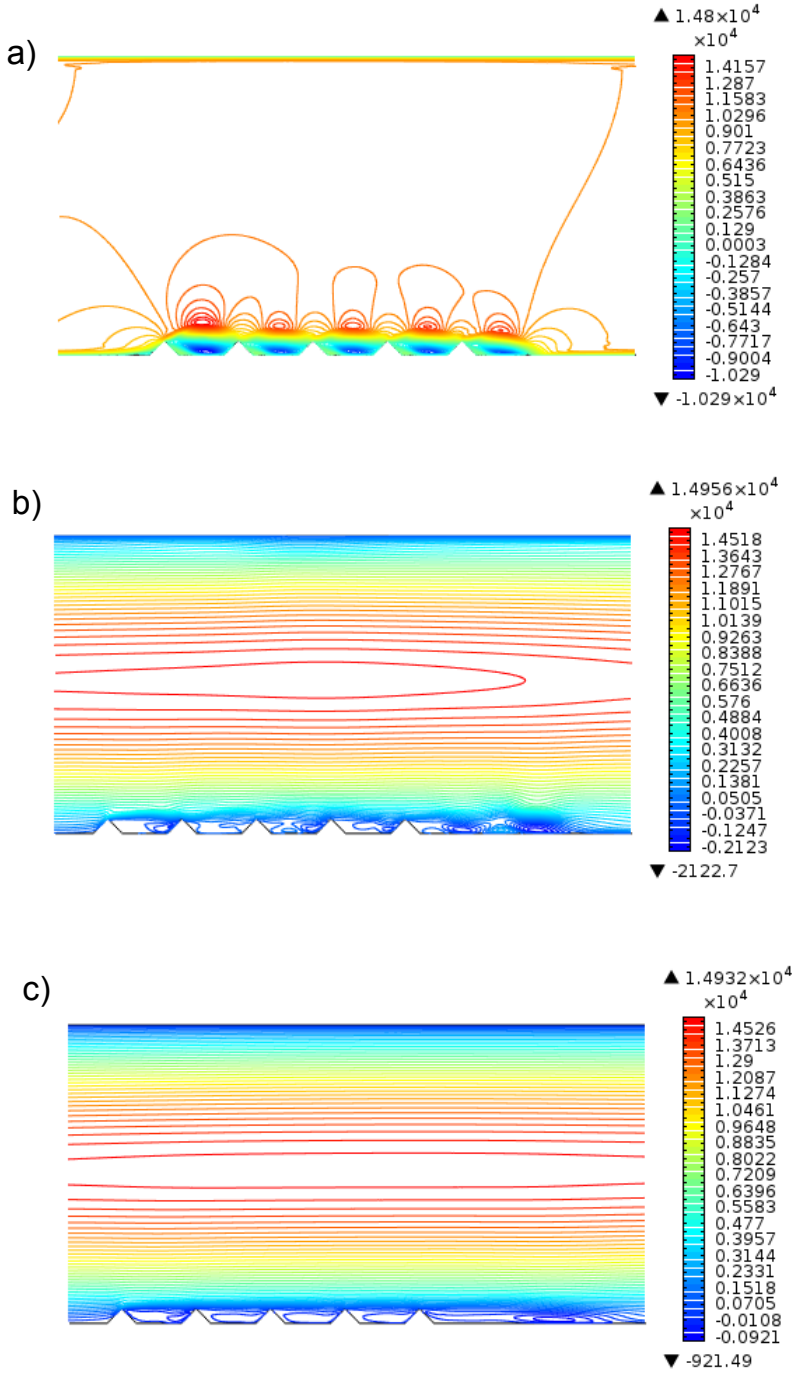


FIGURE C.44: Evolution of the streamwise velocity (u) for $w/k = 3$ (triangle): a) t = 10.17 s, b) t = 100.91 s, c) t = 200 s.

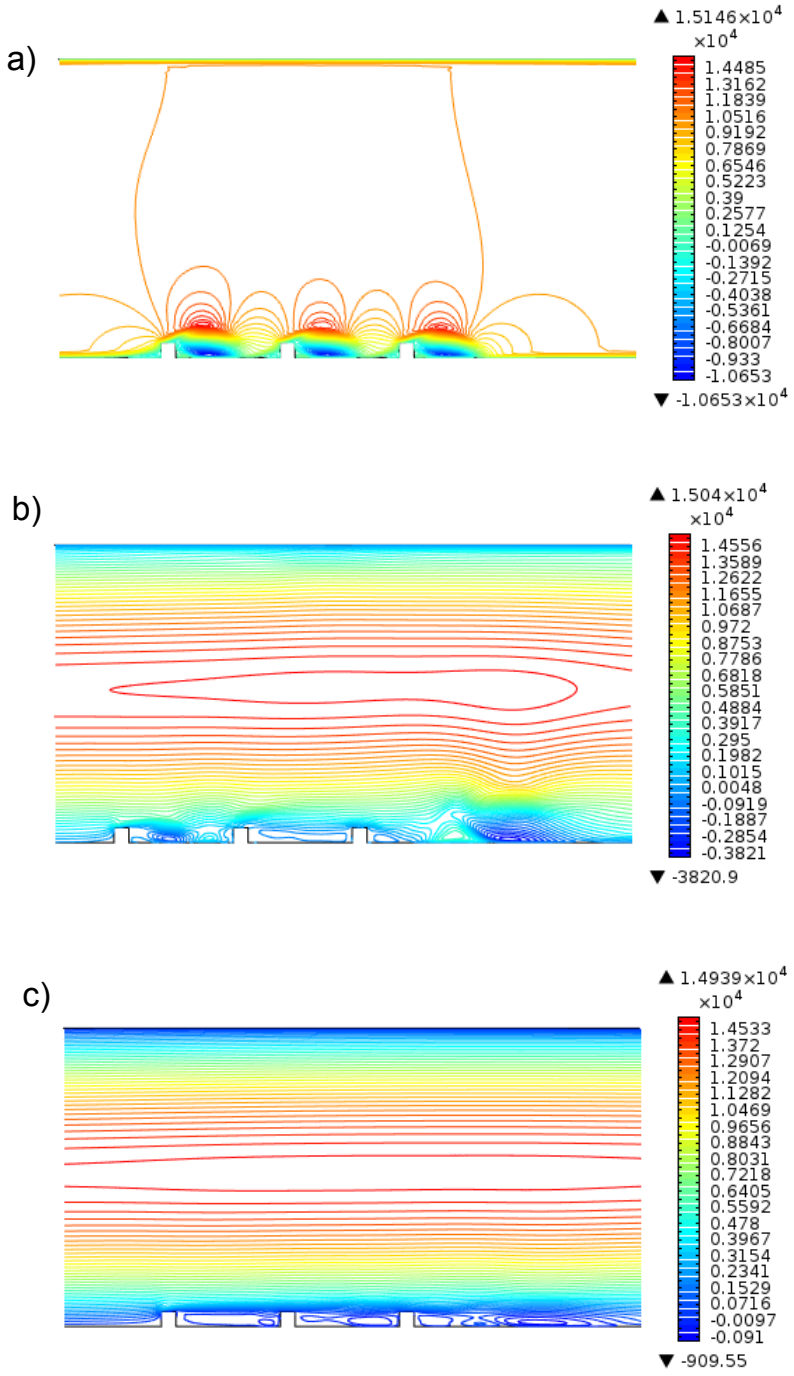


FIGURE C.45: Evolution of the streamwise velocity (u) for $w/k = 7$ (square): a) t = 10.52 s, b) t = 100.38 s, c) t = 200 s.

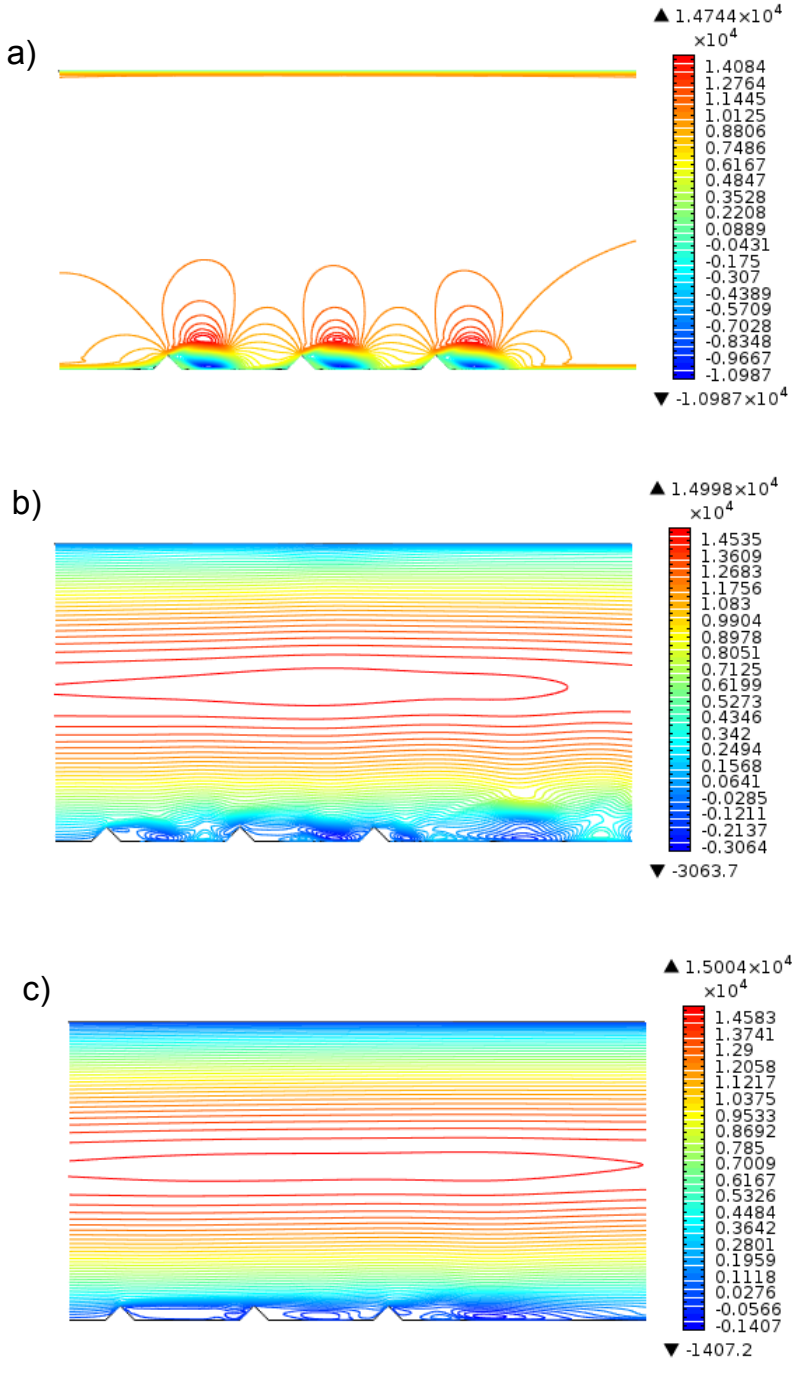


FIGURE C.46: Evolution of the streamwise velocity (u) for $w/k = 7$ (triangle): a) t = 10.42 s, b) t = 100.84 s, c) t = 200 s.

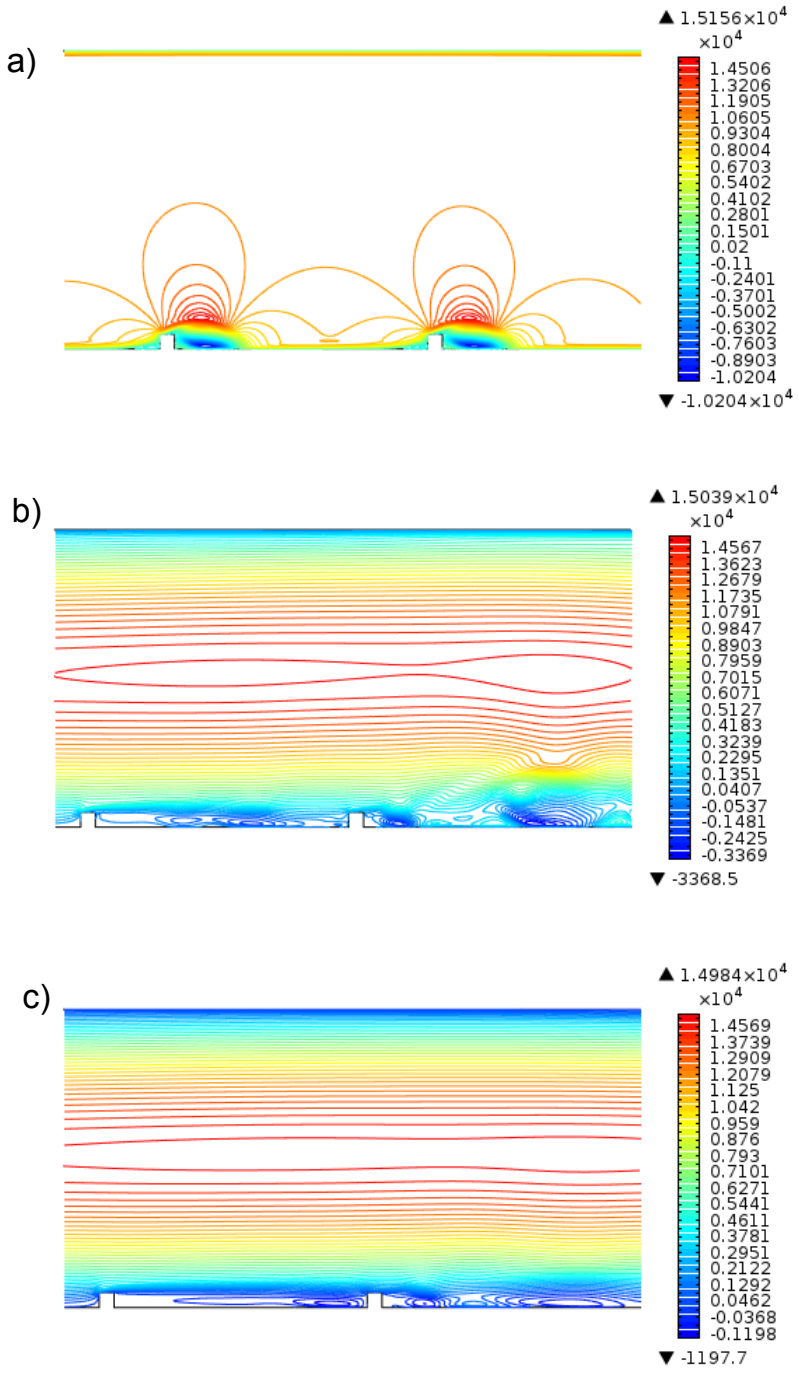


FIGURE C.47: Evolution of the streamwise velocity (u) for $w/k = 17$ (square): a) t = 10.31 s, b) t = 100.59 s, c) t = 200 s.

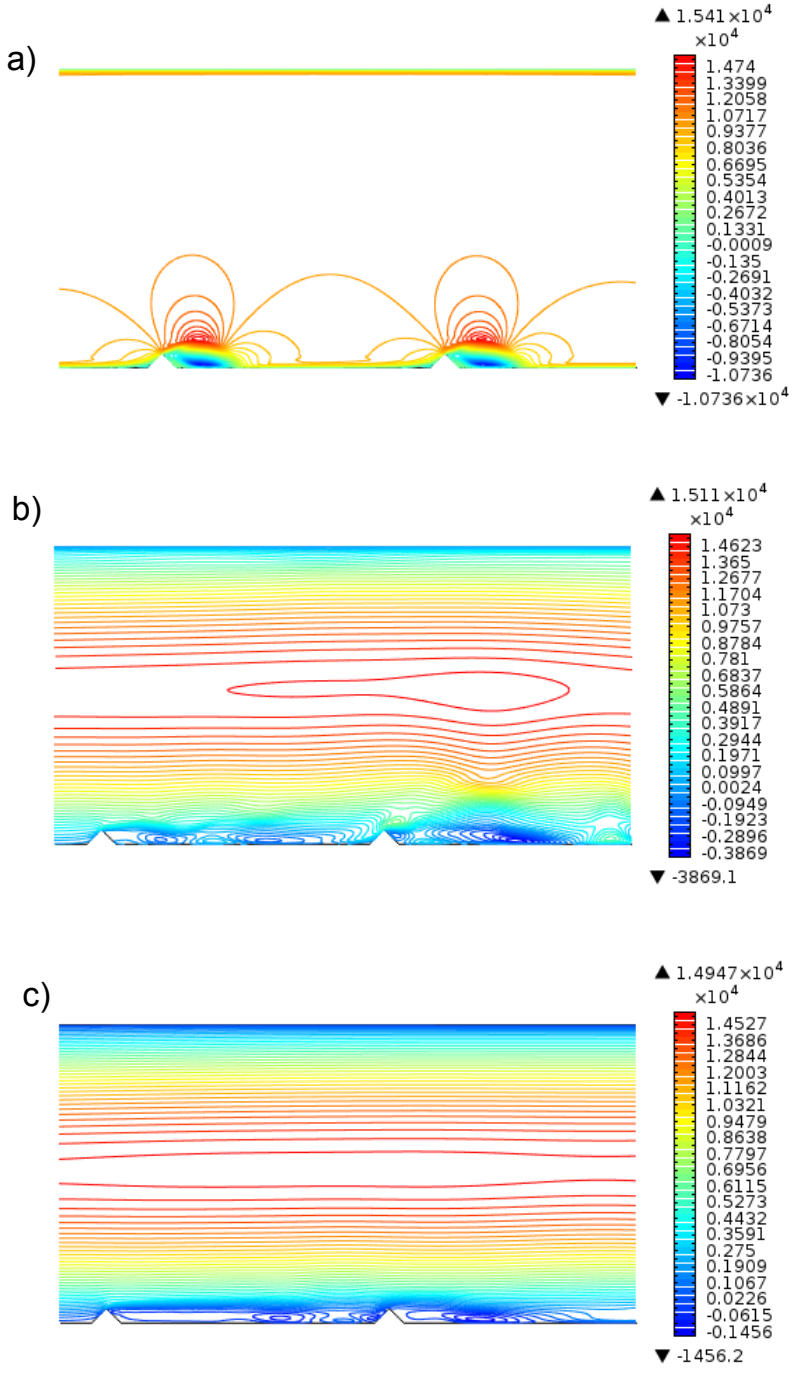


FIGURE C.48: Evolution of the streamwise velocity (u) for $w/k = 17$ (triangle): a) t = 10.41 s, b) t = 101.33 s, c) t = 200 s.

### C.6.2 Spanwise velocity (v)

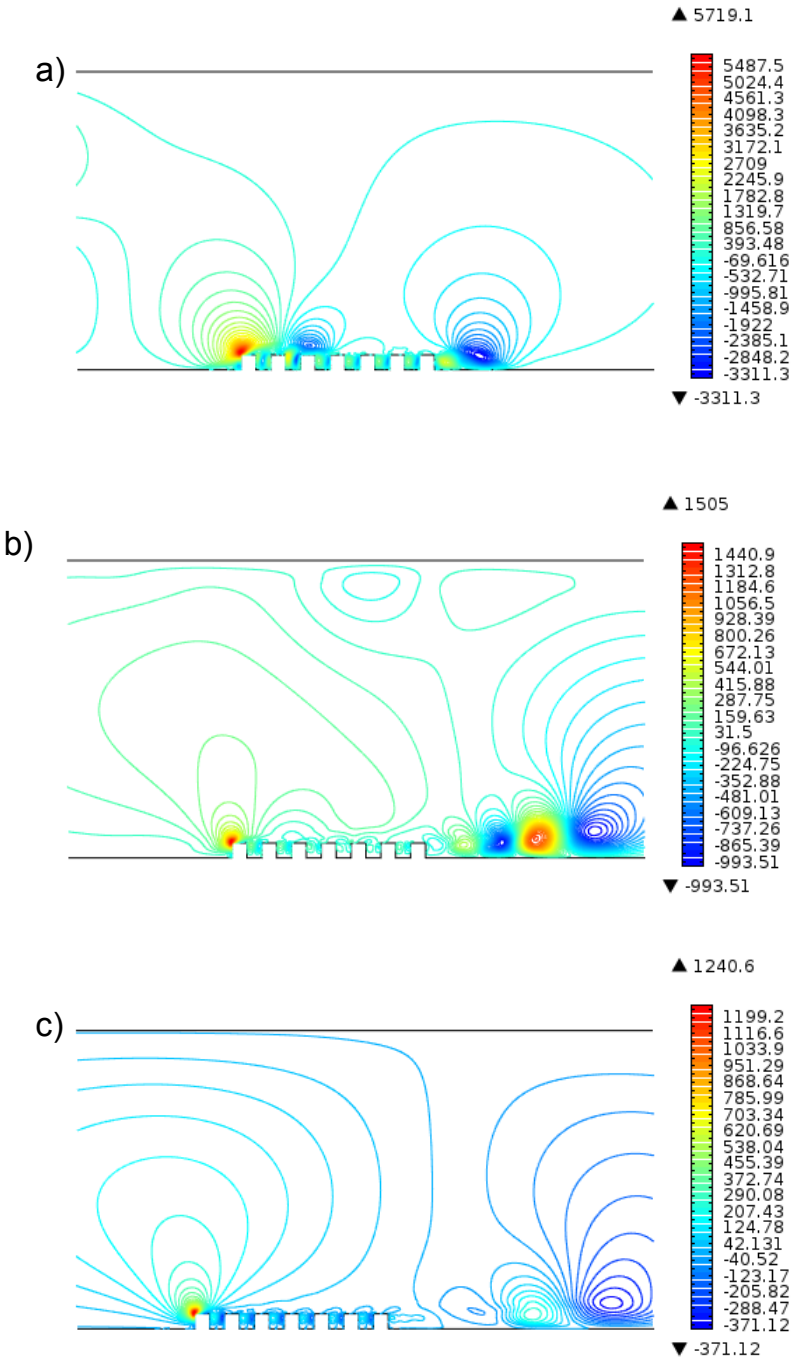


FIGURE C.49: Evolution of the streamwise velocity (u) for $w/k = 1$ (square): a) t = 10.43 s, b) t = 102.82 s, c) t = 200 s.

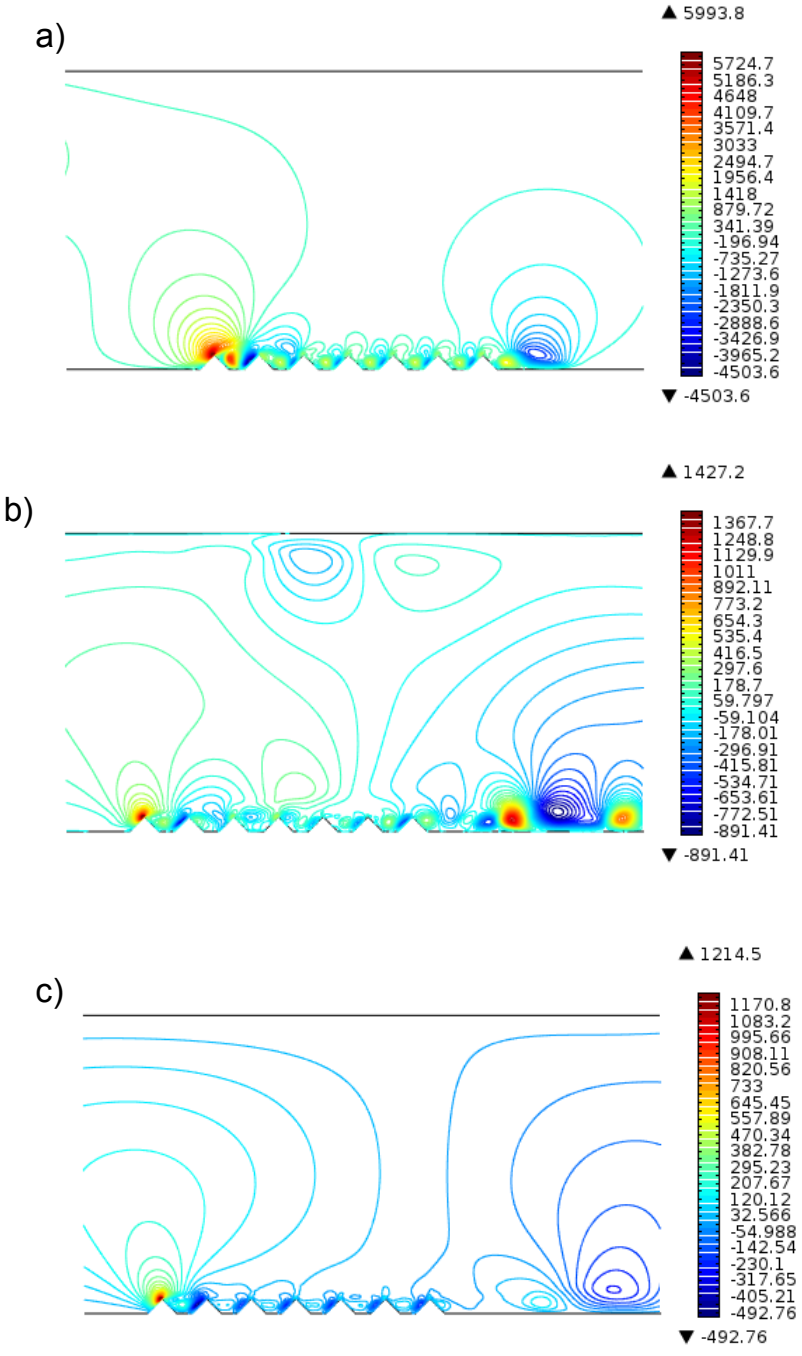


FIGURE C.50: Evolution of the streamwise velocity (u) for $w/k = 1$ (triangle): a) t = 10.32 s, b) t = 101.98 s, c) t = 200 s.

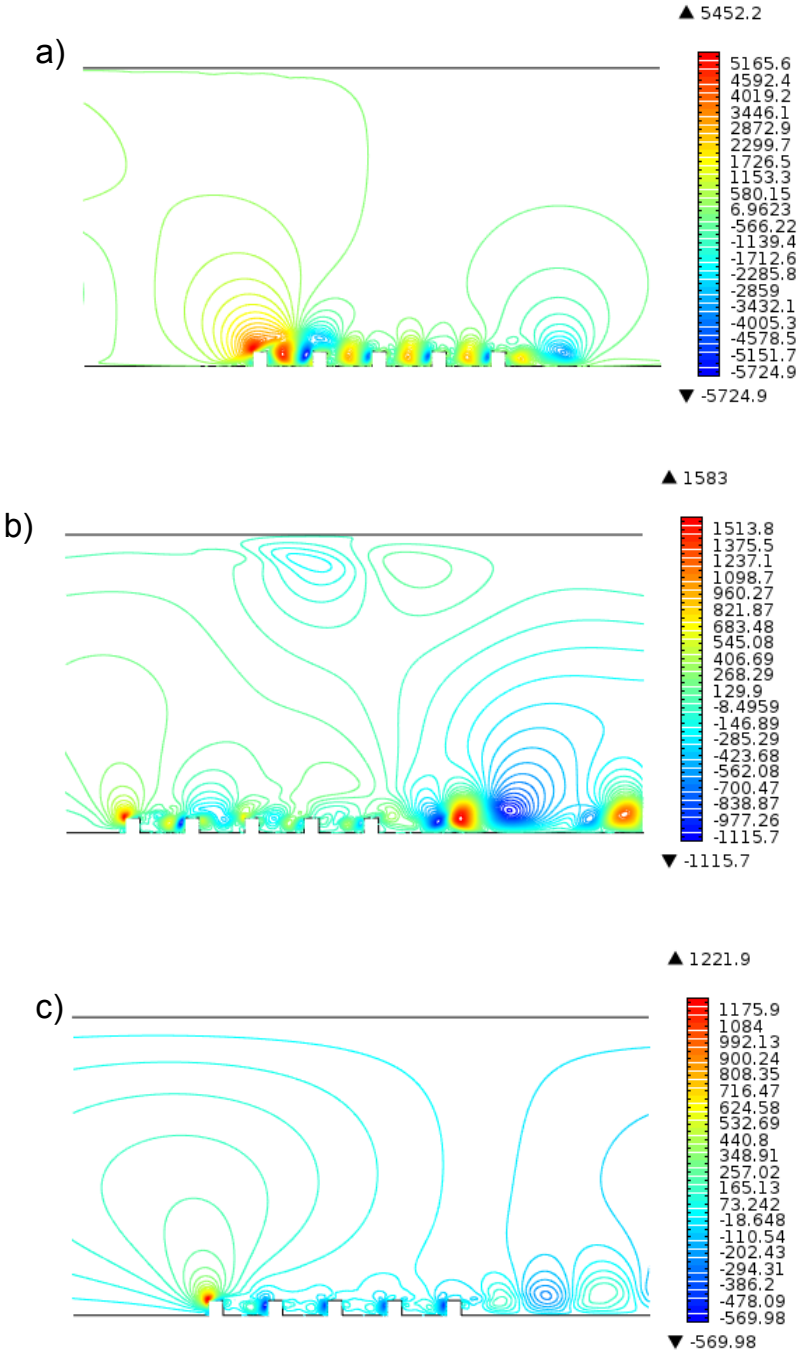


FIGURE C.51: Evolution of the streamwise velocity (u) for $w/k = 3$ (square): a) t = 10.36 s, b) t = 101.22 s, c) t = 200 s.

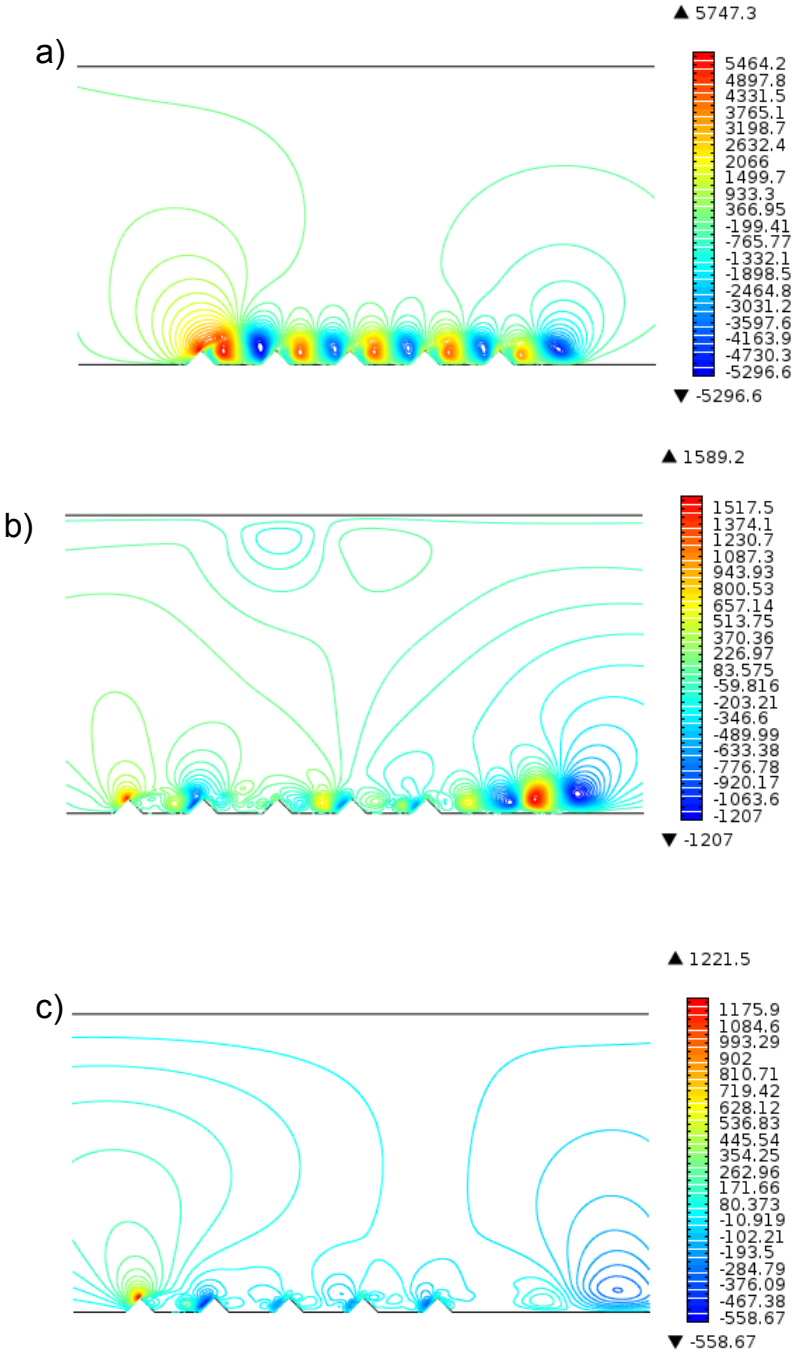


FIGURE C.52: Evolution of the streamwise velocity (u) for $w/k = 3$ (triangle): a) t = 10.17 s, b) t = 100.91 s, c) t = 200 s.

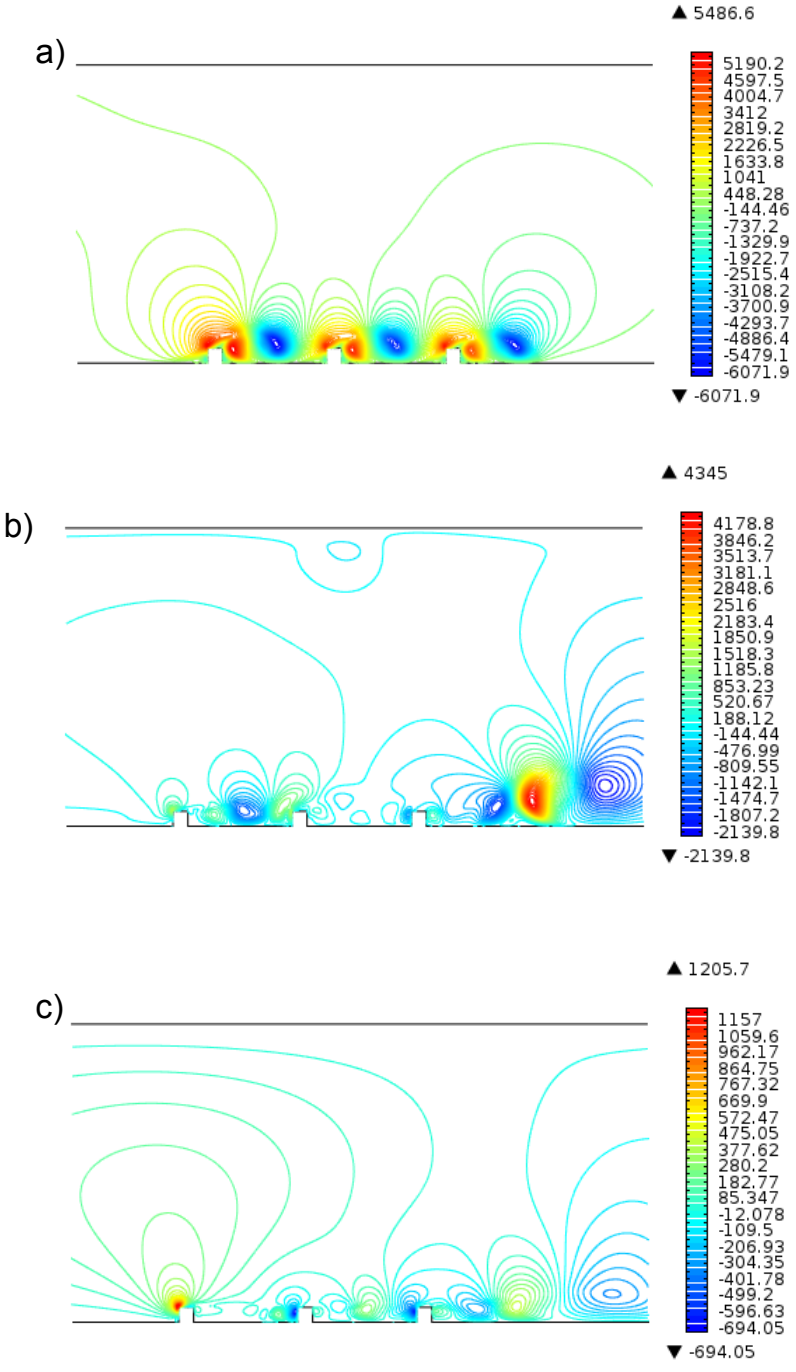


FIGURE C.53: Evolution of the streamwise velocity (u) for $w/k = 7$ (square): a) t = 10.52 s, b) t = 100.38 s, c) t = 200 s.

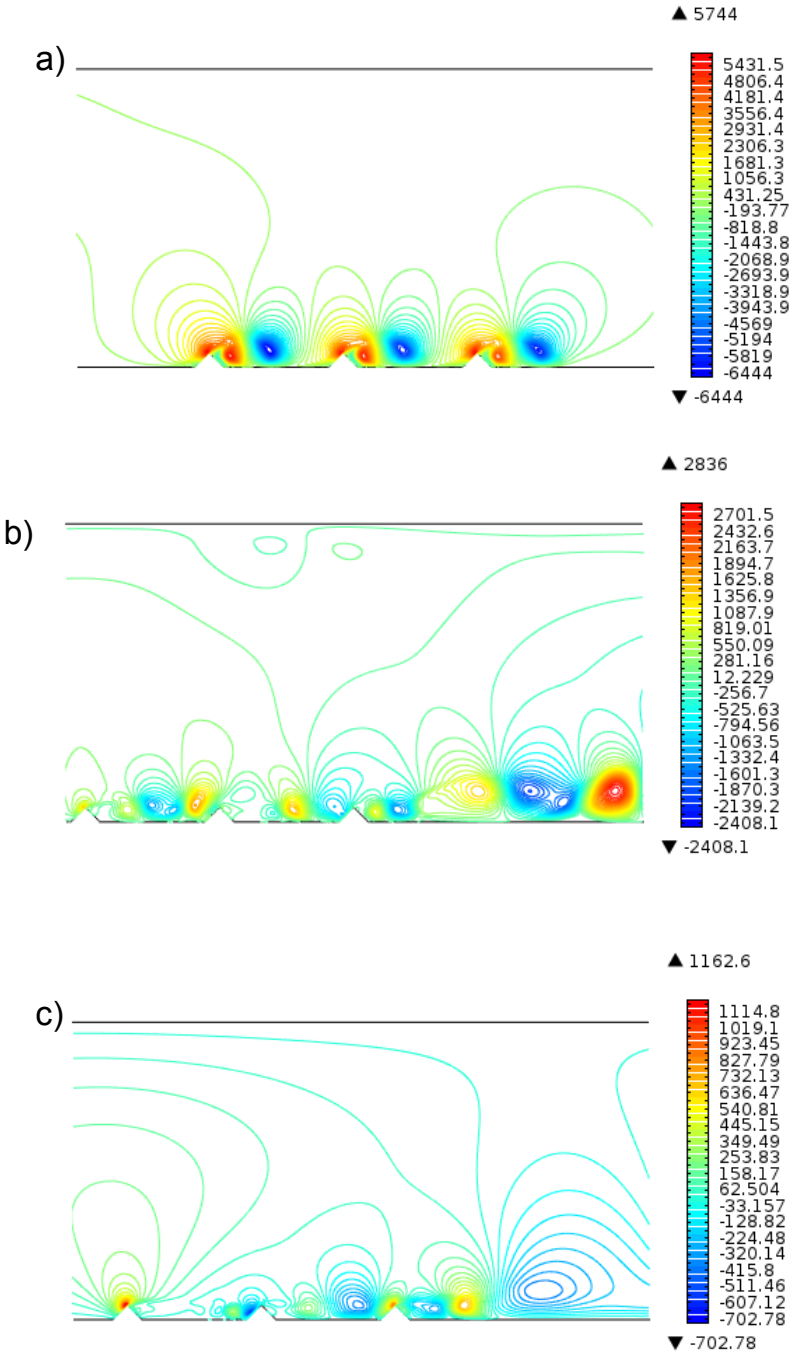


FIGURE C.54: Evolution of the streamwise velocity (u) for $w/k = 7$ (triangle): a) t = 10.42 s, b) t = 100.84 s, c) t = 200 s.

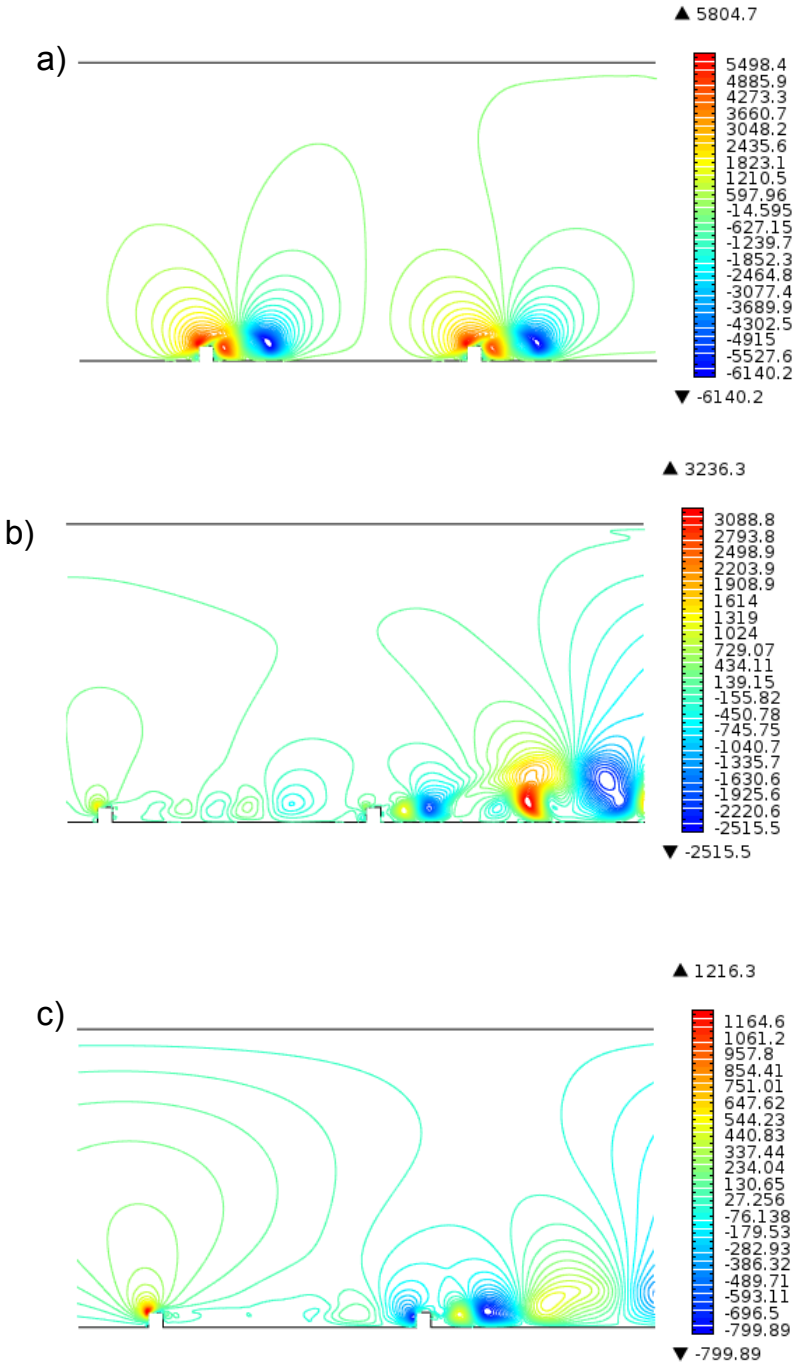


FIGURE C.55: Evolution of the streamwise velocity (u) for $w/k = 17$ (square): a) t = 10.31 s, b) t = 100.59 s, c) t = 200 s.

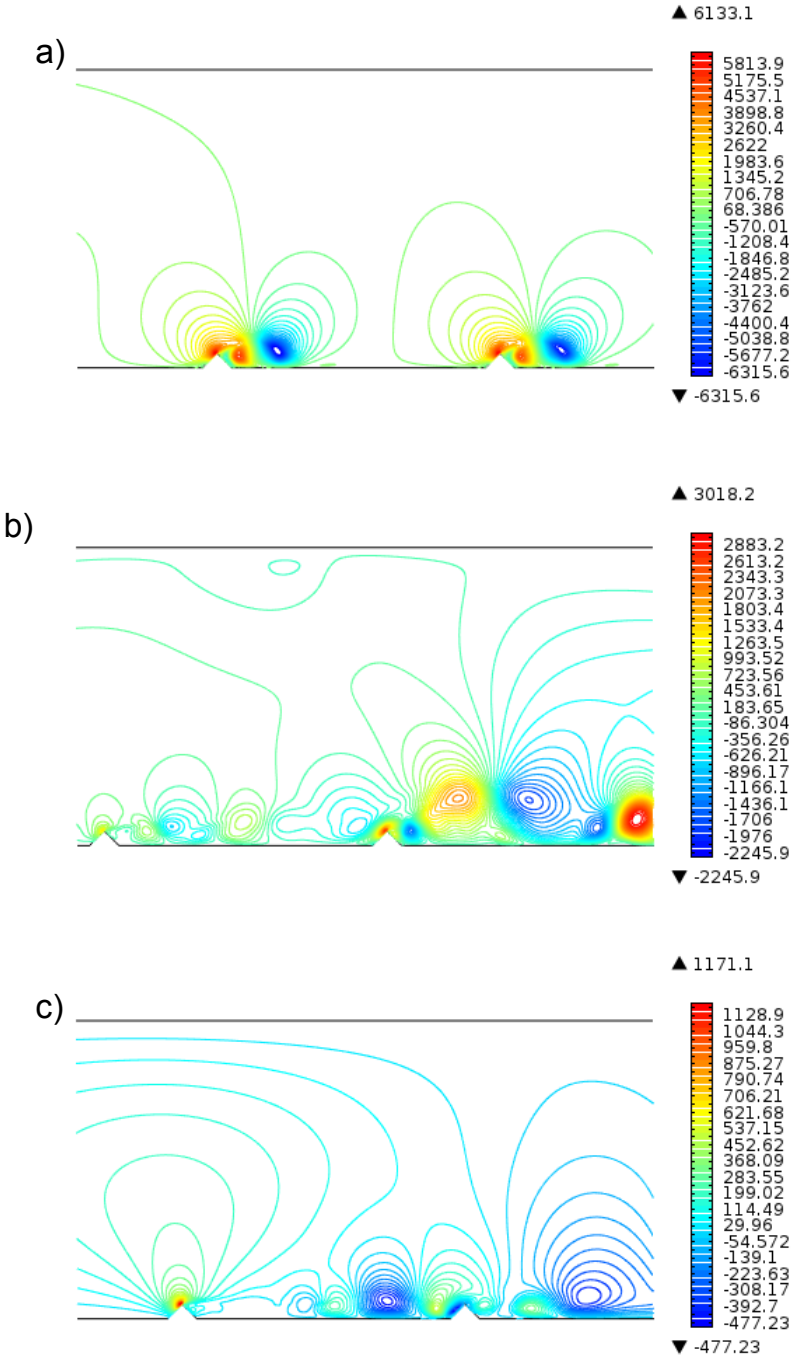


FIGURE C.56: Evolution of the streamwise velocity (u) for $w/k = 17$ (triangle): a) t = 10.41 s, b) t = 101.33 s, c) t = 200 s.

## C.7 $y^+$ contour plots

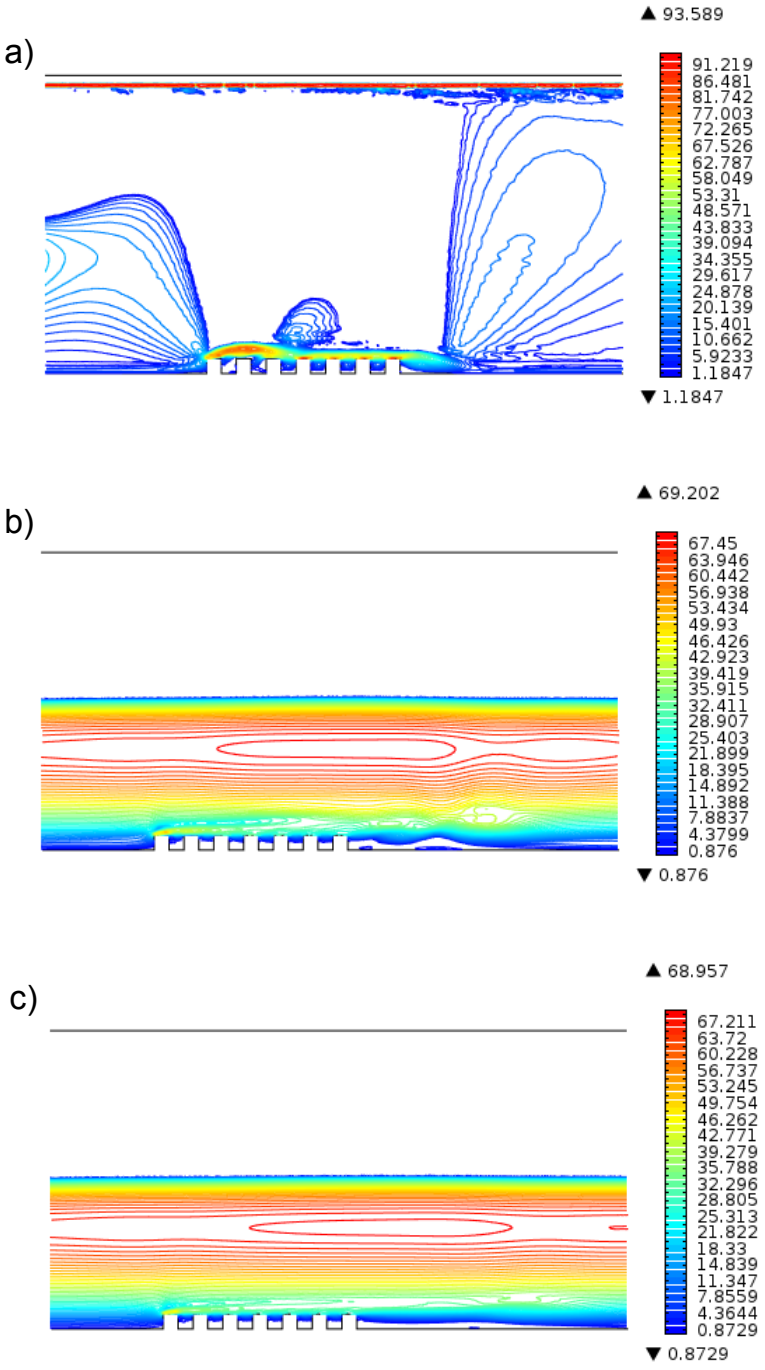


FIGURE C.57: Flow evolution of $y^+$ for $w/k = 1$ (square): a) 10.43 s, b) 102.82 s, c) 200 s

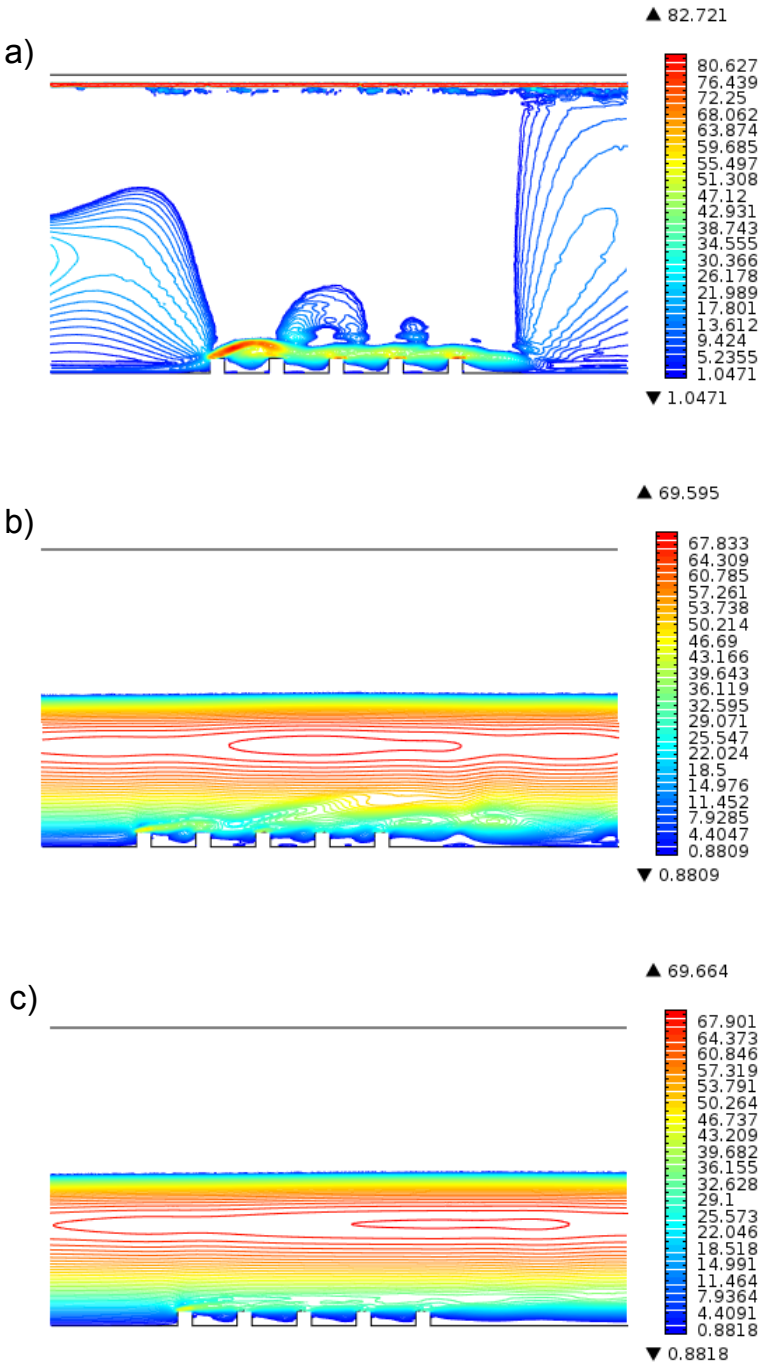


FIGURE C.58: Flow evolution of $y^+$ for $w/k = 3$ (square): a) 10.36 s, b) 101.22 s, c) 200 s

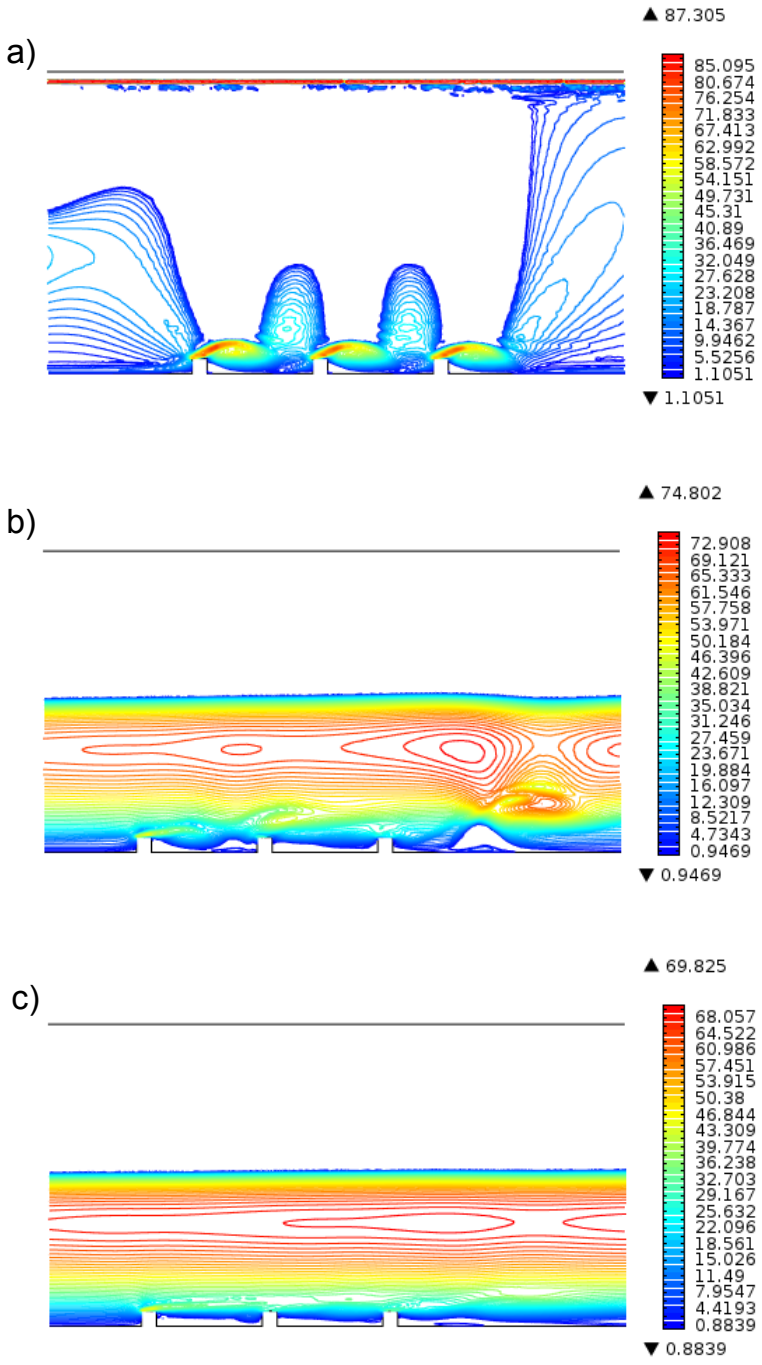


FIGURE C.59: Flow evolution of $y^+$ for $w/k = 7$ (square): a) 10.52 s, b) 100.38 s, c) 200 s

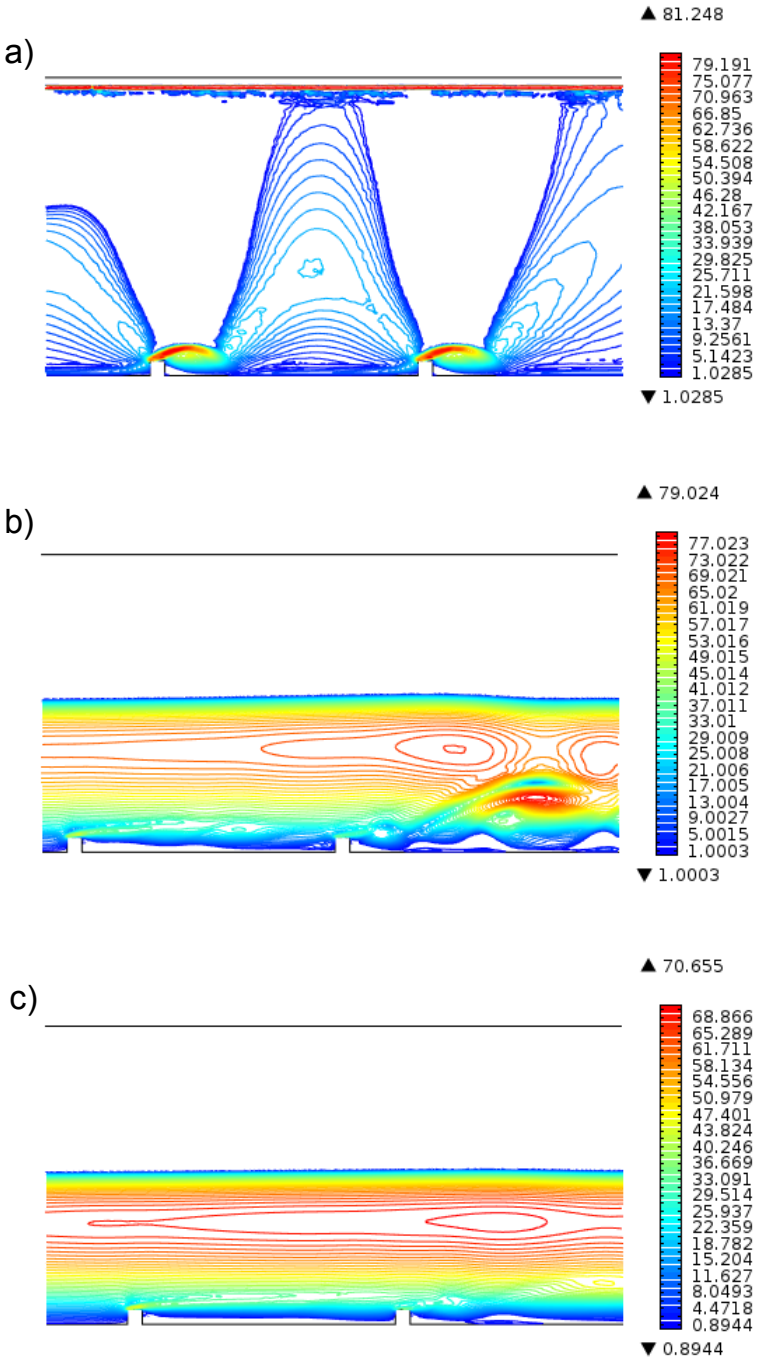


FIGURE C.60: Flow evolution of $y^+$ for $w/k = 17$ (square): a) 10.31 s, b) 100.59 s, c) 200 s

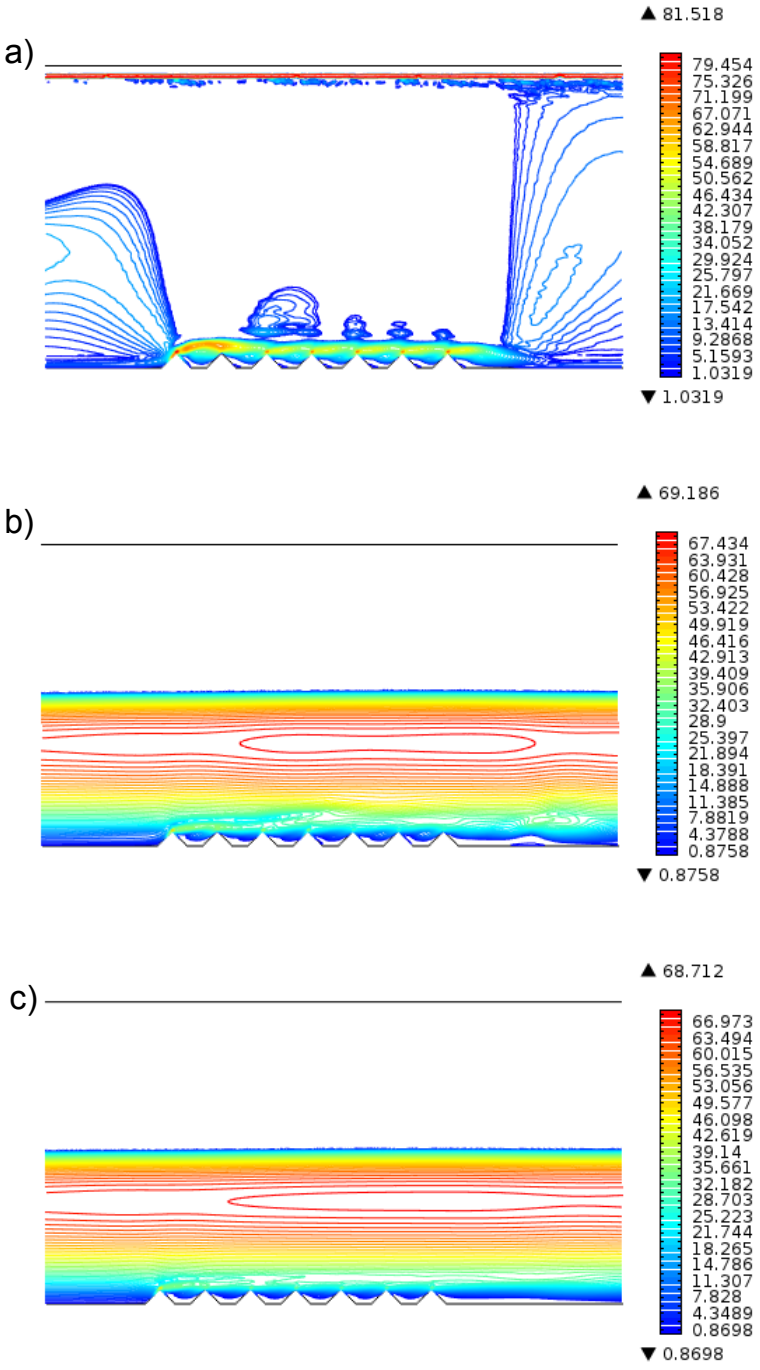


FIGURE C.61: Flow evolution of $y^+$ for $w/k = 1$ (triangle): a) 10.32 s, b) 101.98 s, c) 200 s

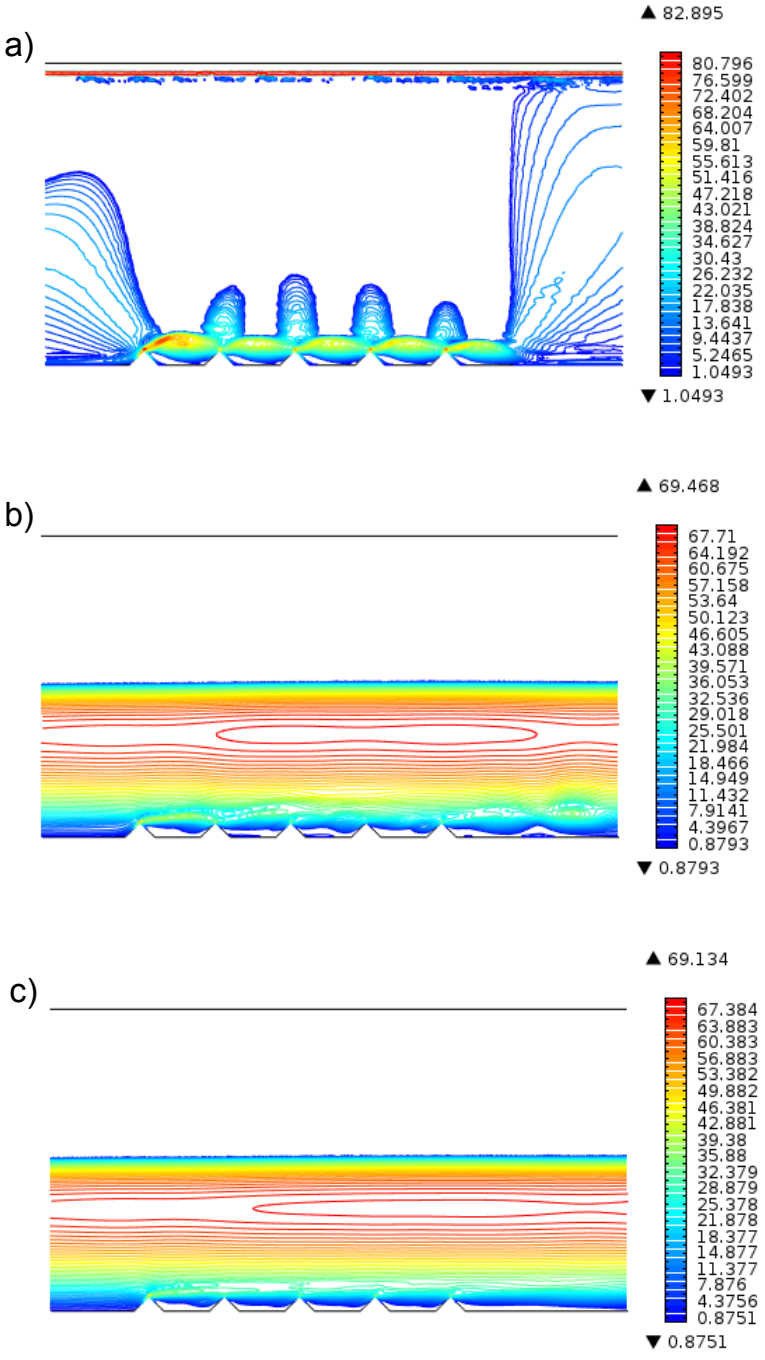


FIGURE C.62: Flow evolution of $y^+$ for $w/k = 3$ (triangle): a) 10.17 s, b) 100.91 s, c) 200 s

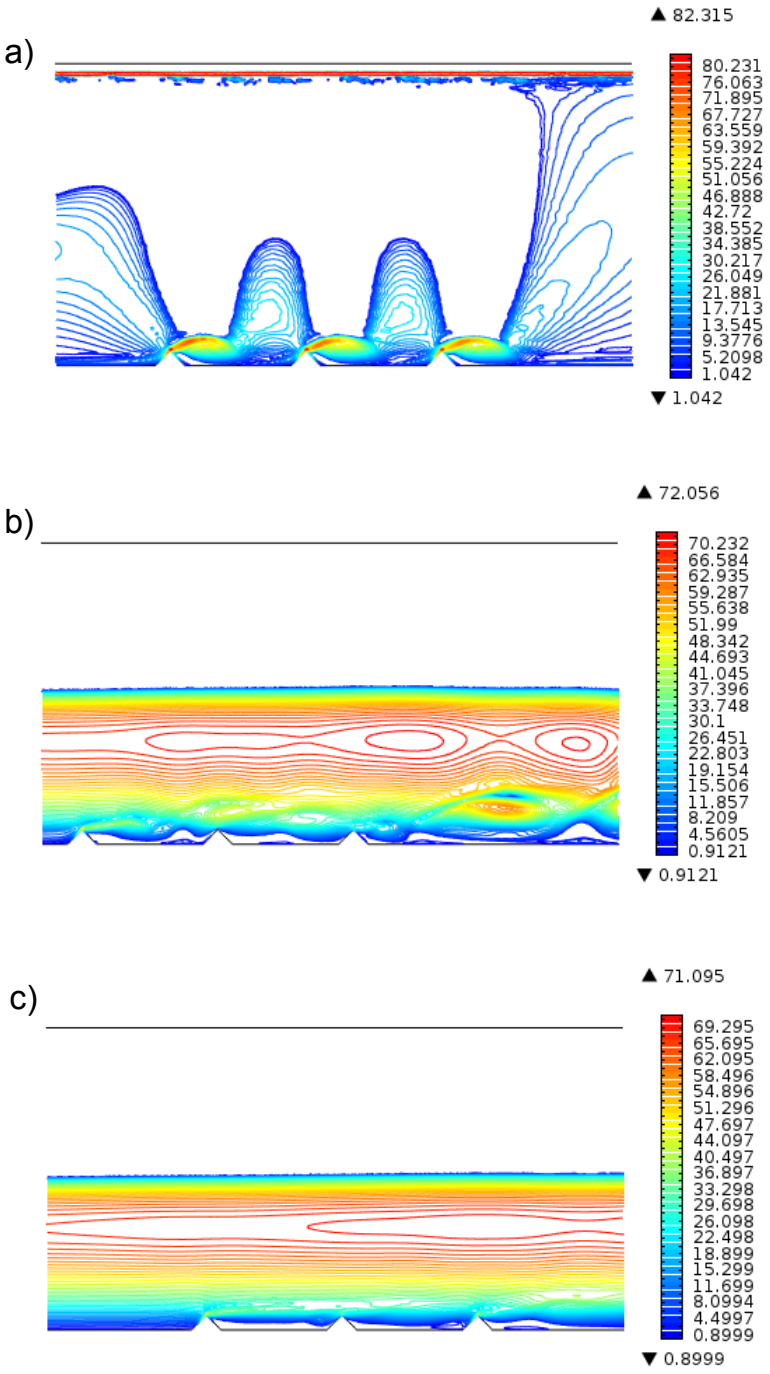


FIGURE C.63: Flow evolution of $y^+$ for $w/k = 7$ (triangle): a) 10.42 s, b) 100.84 s, c) 200 s

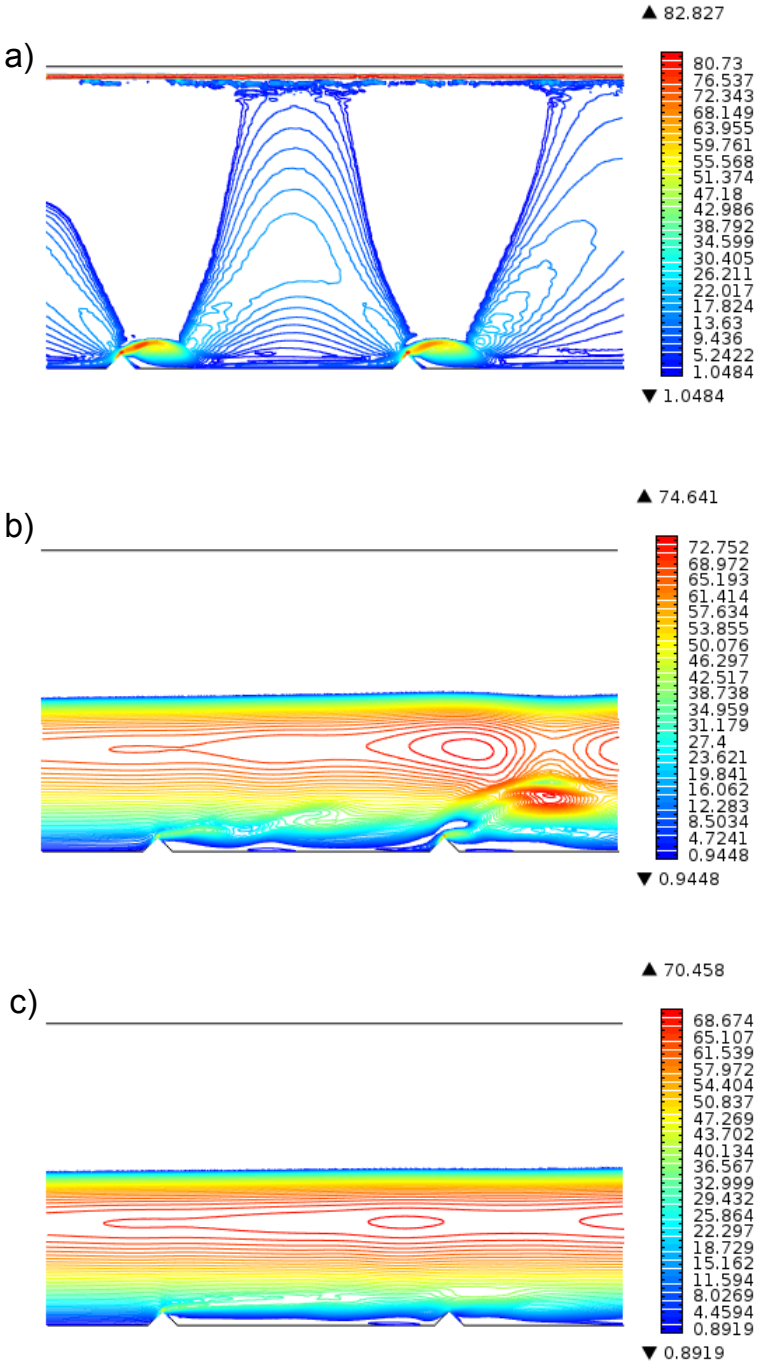


FIGURE C.64: Flow evolution of $y^+$ for $w/k = 17$ (triangle): a) 10.41 s, b) 101.33 s, c) 200 s

## C.8 Falco eddies

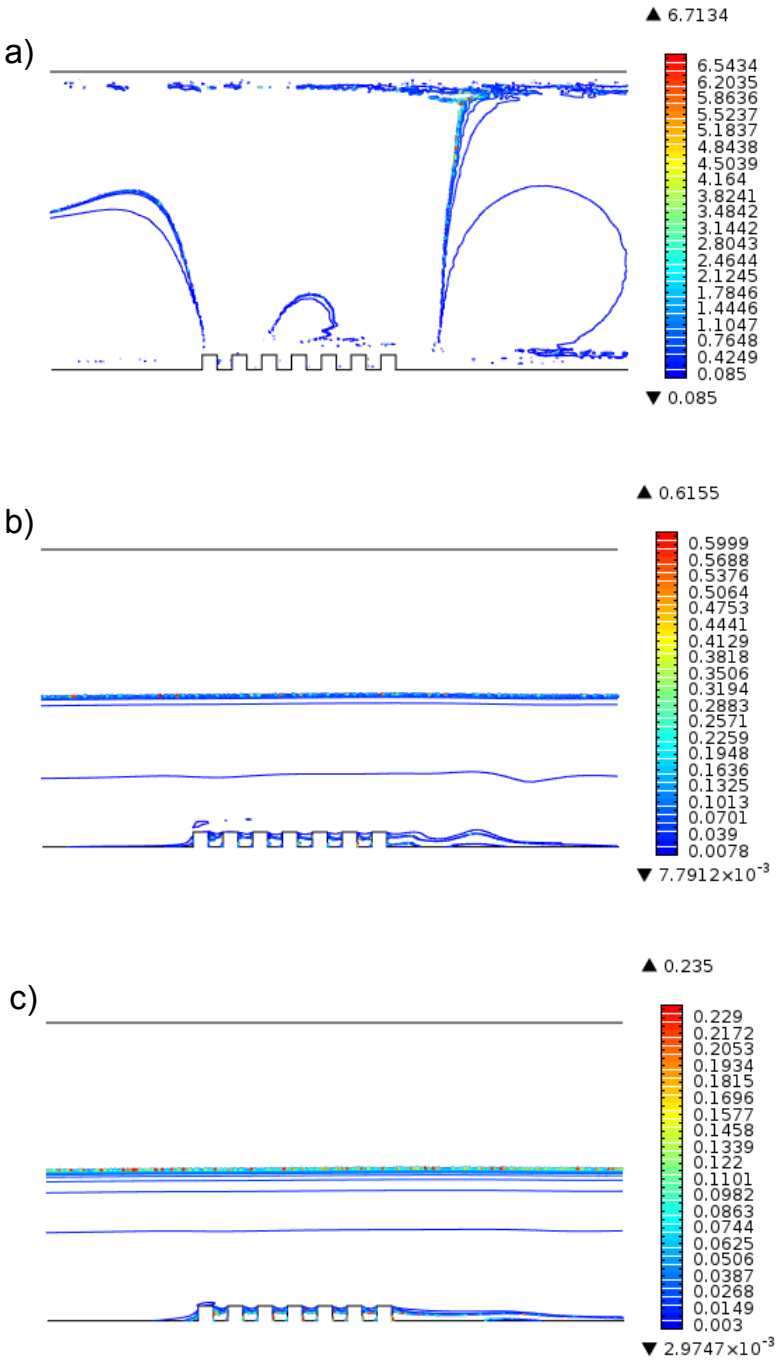


FIGURE C.65: Flow evolution of the Falco eddies for $w/k = 1$ (square): a) 10.43 s, b) 102.82 s, c) 200 s

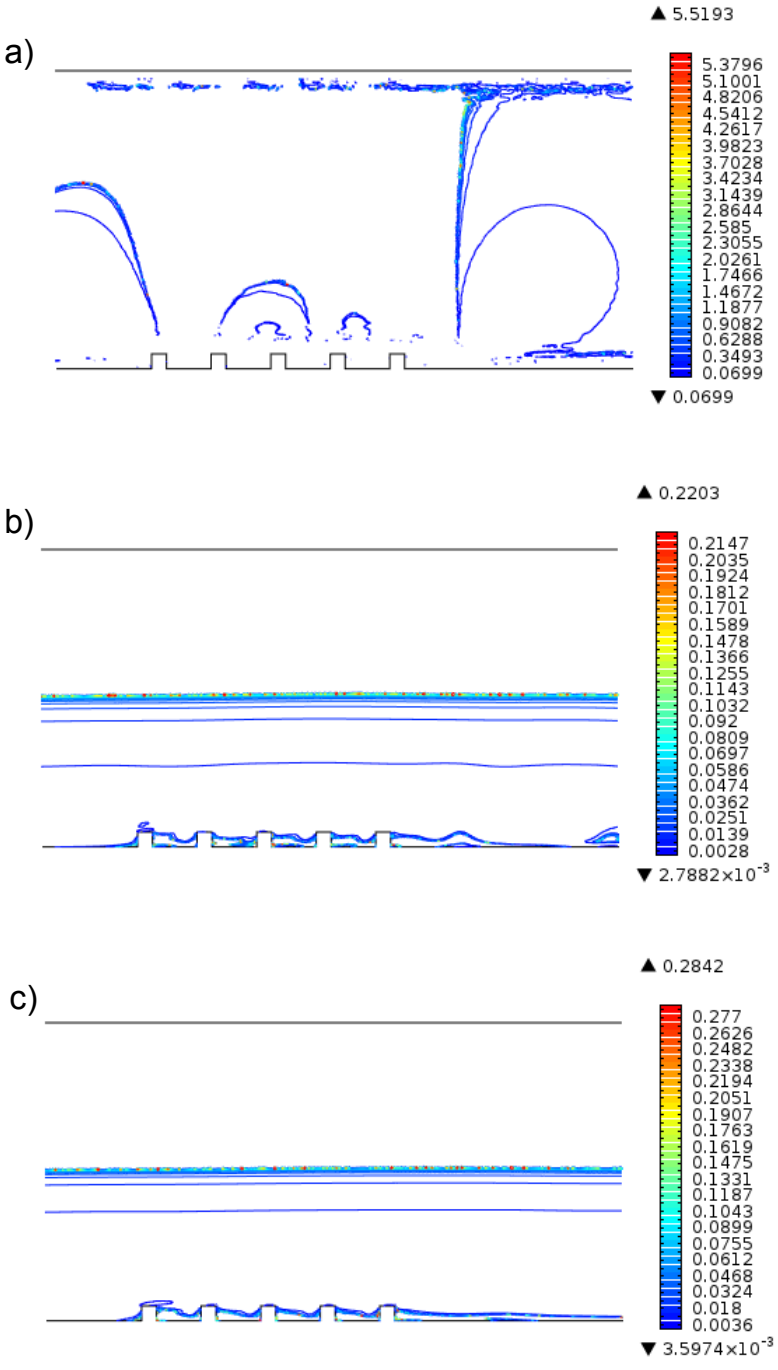


FIGURE C.66: Flow evolution of the Falco eddies for $w/k = 3$ (square): a) 10.36 s, b) 101.22 s, c) 200 s

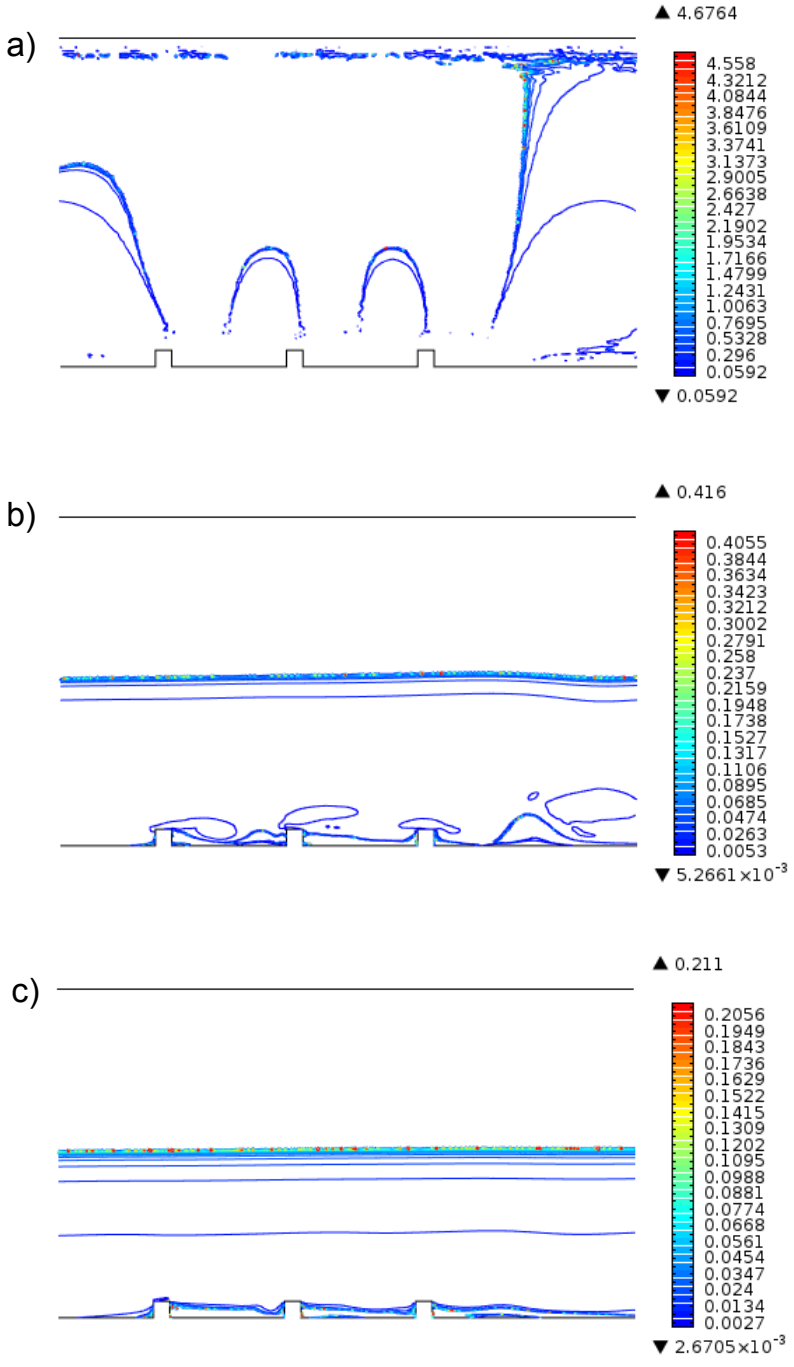


FIGURE C.67: Flow evolution of the Falco eddies for $w/k = 7$ (square): a) 10.52 s, b) 100.38 s, c) 200 s

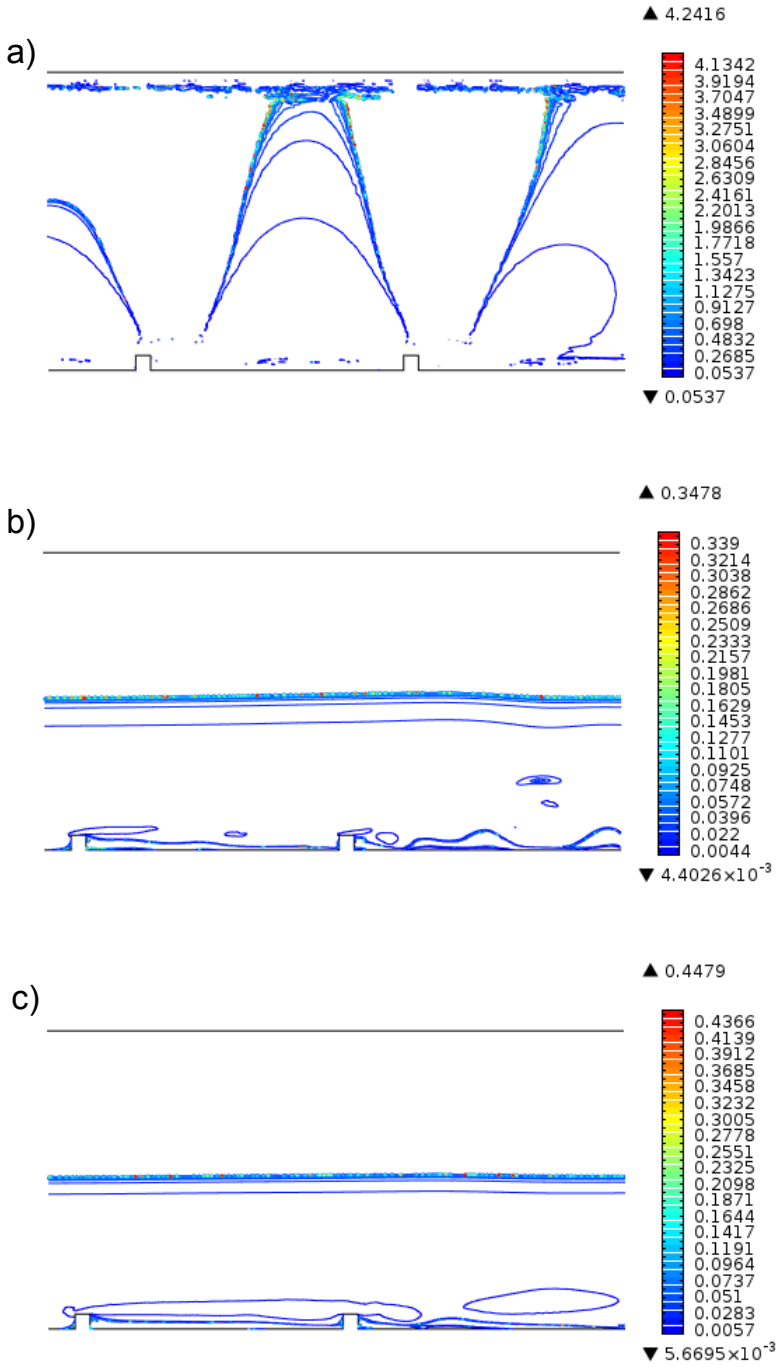


FIGURE C.68: Flow evolution of the Falco eddies for $w/k = 17$ (square): a) 10.31 s, b) 100.59 s, c) 200 s

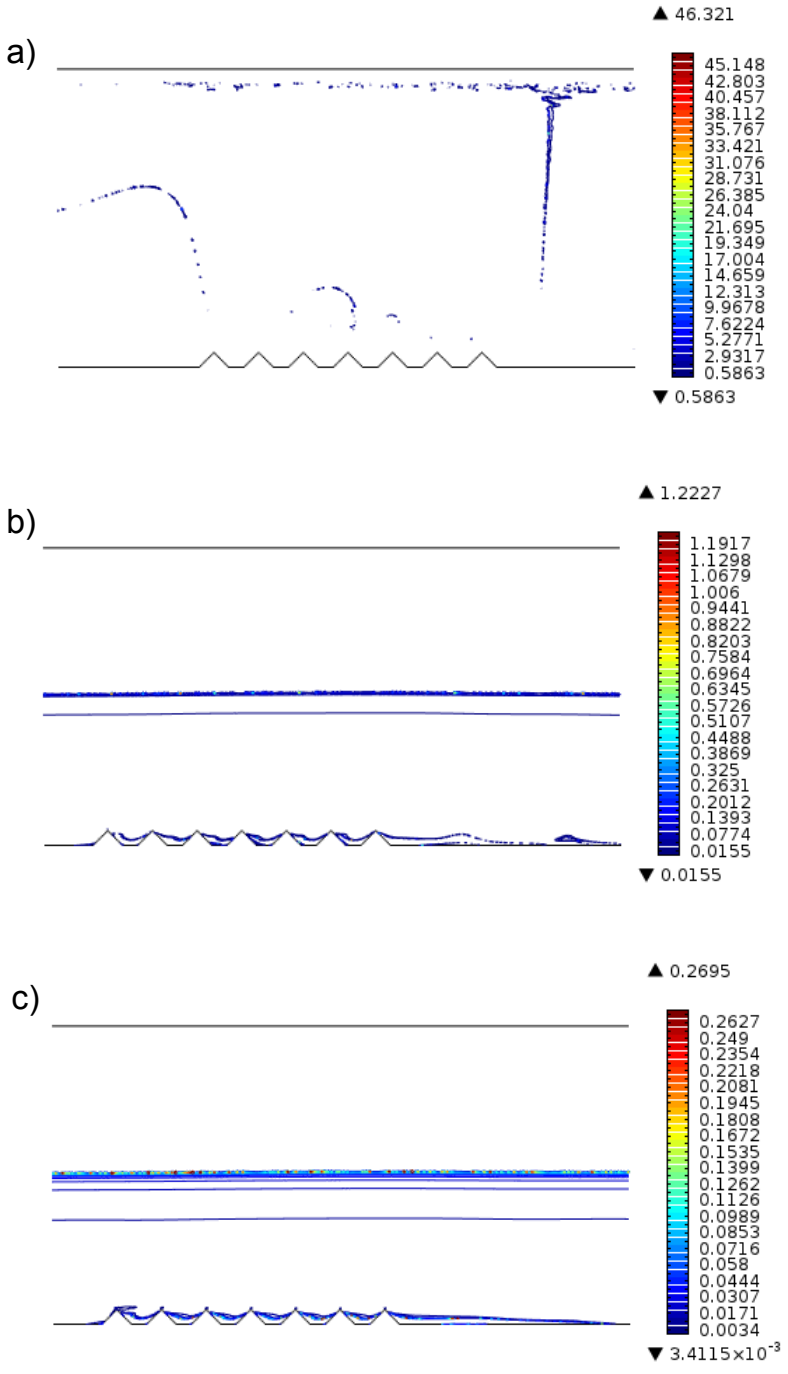


FIGURE C.69: Flow evolution of the Falco eddies for $w/k = 1$ (triangle): a) 10.32 s, b) 101.98 s, c) 200 s

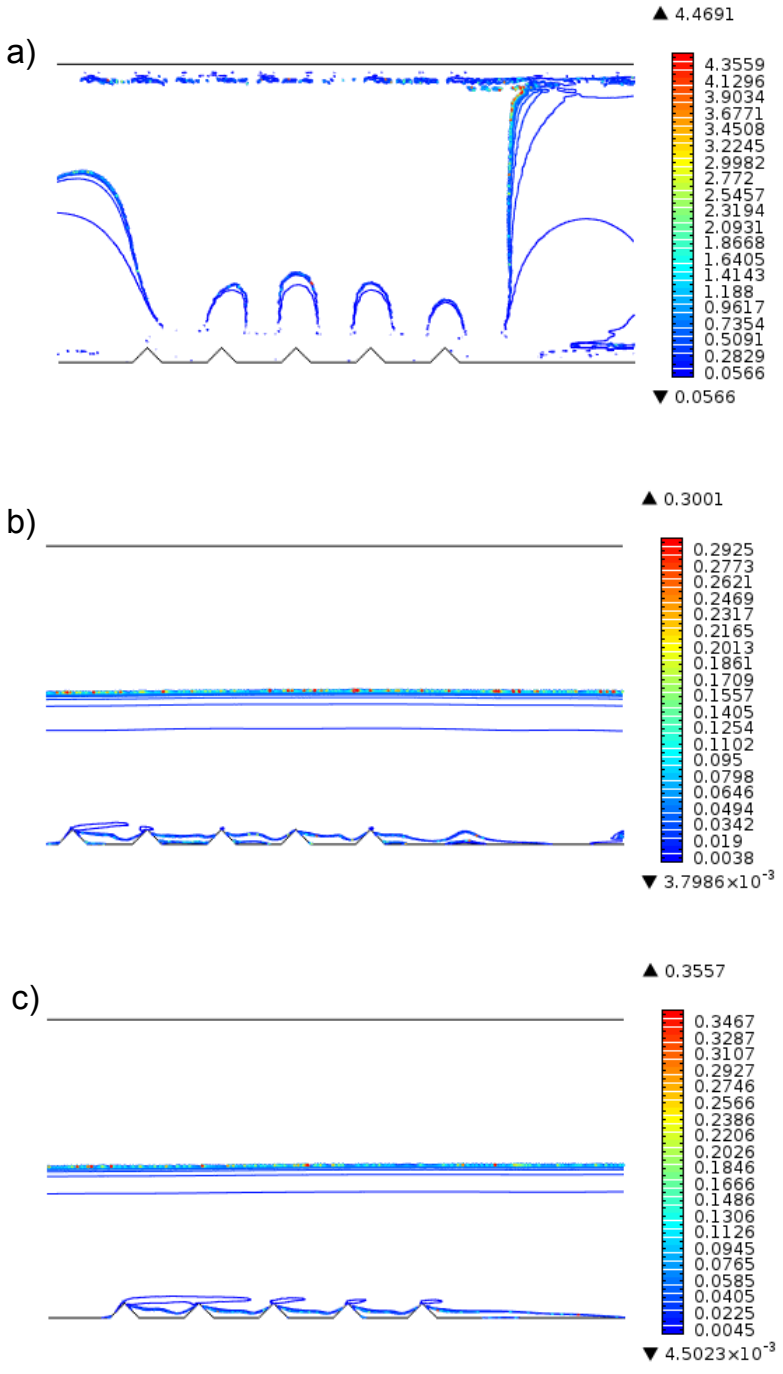


FIGURE C.70: Flow evolution of the Falco eddies for $w/k = 3$ (triangle): a) 10.17 s, b) 100.91 s, c) 200 s

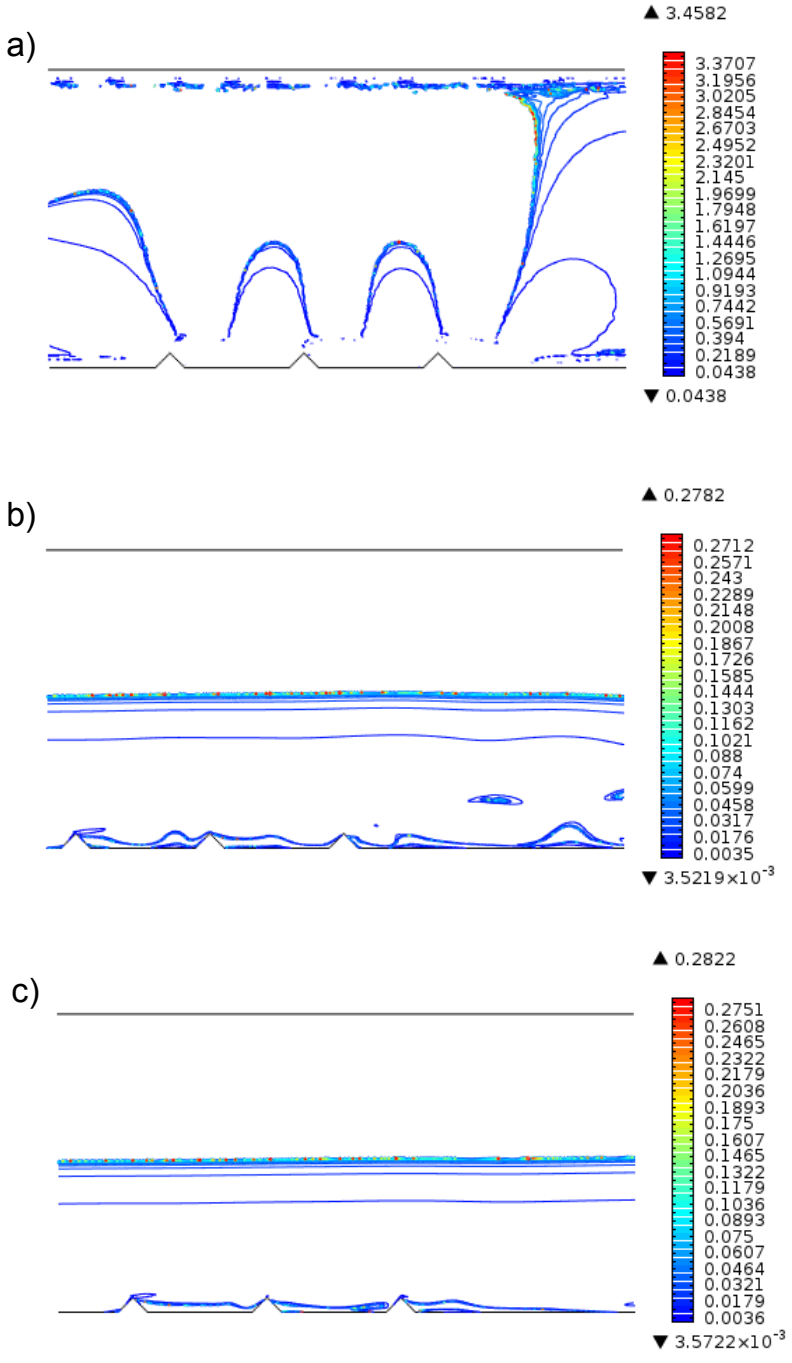


FIGURE C.71: Flow evolution of the Falco eddies for $w/k = 7$ (triangle): a) 10.42 s, b) 100.84 s, c) 200 s

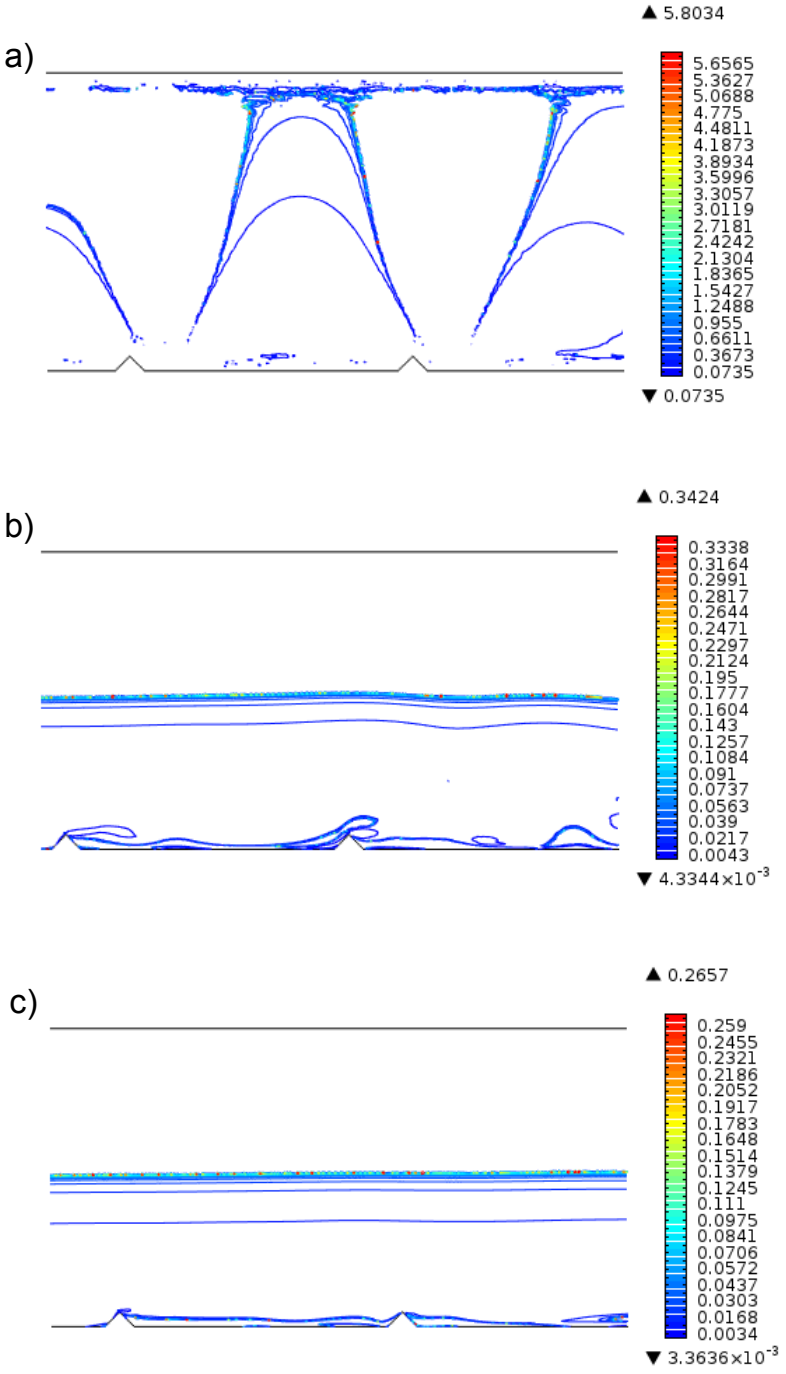


FIGURE C.72: Flow evolution of the Falco eddies for $w/k = 17$ (triangle): a) 10.41 s, b) 101.33 s, c) 200 s

# Appendix D

# conference paper

European Congress on Computational Methods
in Applied Sciences and Engineering (ECCOMAS 2012)
J. Eberhardsteiner et.al. (eds.)
Vienna, Austria, September 10-14, 2012

# UNDERSTANDING THE DRAG REDUCTION PROPERTIES OF THE FLOW OVER *K* AND *D* -TYPE ROUGH SURFACES

**Almajd A. Alhinai** *, **Andrzej F. Nowakowski**

Sheffield Fluid Mechanics Group, Department of Mechanical Engineering, University of Sheffield,
S1 3JD, UK
*e-mail: mep09aa@shef.ac.uk

**Keywords:** Drag Reduction, Roughness Types, CFD

**Abstract.** *Understanding the flow over rough surfaces is an important problem in fluids engineering. Here, we present studies on turbulent flow over various roughness types. The rough surfaces considered in this study were based on the k and d -type behaviour used to classify the different roughness types. Previous results demonstrated that drag reduction can only be achieved using d -type roughness arranged in the streamwise direction. This arrangement is also known as flow over riblets. Obtaining an exact solution for such a problem is very challenging, therefore the problem was solved computationally using the finite element method. The flow simulation cases considered for this study were; laminar, turbulent and fully turbulent. The domain is represented by a channel flow with one sided profield roughness. Simulations were carried out to study the k and d -type behaviour over transverse and streamwise roughness. We were able to identify and benchmark the k and d -type behaviour for the flow over a transverse surface. Some similarities between the transverse and the streamwise roughness were observed in terms of k and d-type behaviour, mainly the production of stable vortices between the roughness elements, but further research is required to fully identify and benchmark the k and d-type behaviour in the flow over streamwise roughness.*

# Bibliography


[1] D. F. Young, B. R. Munson, T. H. Okiishi, and W. W. Huebsch. *A Brief Introduction to Fluid Mechanics (Wiley Custom Select)*. Wiley, 2007. URL http://amazon.com/o/ASIN/0470039620/.

[2] M. Gad el Hak. *Flow Control: Passive, Active, and Reactive Flow Management*. Cambridge University Press, 2007. URL http://amazon.com/o/ASIN/0521036712/.

[3] A. E. Perry, W. H. Schofield, and P. N. Joubert. Rough wall turbulent boundary layers. *Journal of Fluid Mechanics*, 1969. URL http://dx.doi.org/10.1017/S0022112069000619.

[4] A. Segal C. Cuvelier and A. A. van Steenhoven. *Finite Element Methods and Navier-Stokes Equations*. D. Reidel Publishing, 1986.

[5] D. J. Tritton. *Physical Fluid Dynamics*. Oxford University Press, USA, 1988. URL http://amazon.com/o/ASIN/0198544936/.

[6] S. B. Pope. *Turbulent Flows*. Cambridge University Press, 2000. URL http://amazon.com/o/ASIN/0521598869/.

[7] P. Moin J. Kim and R. Moser. Turbulence statistics in fully developed channel flow at low reynolds number. *Journal of Fluid Mechanics*, 1987. URL http://dx.doi.org/10.1017/S0022112087000892.

[8] J. Cui, V.C. Patel., and C. Lin. Large-eddy simulation of turbulent flow in a channel with rib roughness. *International Journal of Heat and Fluid Flow*, 2003. URL http://www.sciencedirect.com/science/article/pii/S0142727X0300002X.

[9] J. H. Lee, H. J. Sung, and P. Krogstad. Direct numerical simulation of the turbulent boundary layer over a cube-roughened wall. *Journal of Fluid Mechanics*, 2011. URL http://dx.doi.org/10.1017/S0022112010005082.

[10] H. Schlichting and K. Gersten. *Boundary-Layer Theory*. Springer, 2000. URL http://amazon.com/o/ASIN/3540662707/.

[11] J. Jimenez. Turbulent flows over rough walls. *Annual Review of Fluid Mechanics*, 2004. URL http://www.annualreviews.org/doi/abs/10.1146/annurev.fluid.36.050802.122103.

[12] J. Piquet. *Turbulent Flows: Models and Physics*. Springer, 2010. URL http://amazon.com/o/ASIN/3642084753/.

[13] A.J. Reynolds. *Turbulent Flows in Engineering*. John Wiley & Sons Ltd, 1974. URL http://amazon.com/o/ASIN/0471717827/.

[14] F. White. *Viscous Fluid Flow (McGraw-Hill Mechanical Engineering)*. McGraw-Hill Science/Engineering/Math, 2005. URL http://amazon.com/o/ASIN/0072402318/.

[15] A. A. R. Townsend. *The Structure of Turbulent Shear Flow (Cambridge Monographs on Mechanics)*. Cambridge University Press, 1980. URL http://amazon.com/o/ASIN/0521298199/.

[16] P. M. Gresho and R. L. Sani. *Incompressible Flow and the Finite Element Method, Volume 1, Advection-Diffusion and Isothermal Laminar Flow*. Wiley, 2000. URL http://amazon.com/o/ASIN/0471492493/.

[17] F. Grinstein, L. Margolin, and W. Rider, editors. *Implicit Large Eddy Simulation: Computing Turbulent Fluid Dynamics*. Cambridge University Press, 2007. URL http://amazon.com/o/ASIN/052186982X/.

[18] W. L. Oberkampf and T. G. Trucano. Verification and validation in computational fluid dynamics. *Progress in Aerospace Sciences*, 2002. URL http://www.sciencedirect.com/science/article/pii/S0376042102000052.

[19] W. L. Oberkampf and C. J. Roy. *Verification and Validation in Scientific Computing*. Cambridge University Press, 2010. URL http://amazon.com/o/ASIN/0521113601/.

[20] L. Djenidi, R. A. Antonia, and F. Anselmet. Lda measurements in a turbulent boundary layer over a d-type rough wall. *Experiments in Fluids*, 1994. URL http://dx.doi.org/10.1007/BF00195431.

[21] P. Krogstad and V. Efros. About turbulence statistics in the outer part of a boundary layer developing over two-dimensional surface roughness. *Physics of Fluids*, 2012. URL http://link.aip.org/link/?PHF/24/075112/1.

[22] S. Leonardi, P. Orlandi, L. Djenidi, and R. Antonia. Guidelines for modeling a 2d rough wall channel flow. *Flow, Turbulence and Combustion*, 2006. URL http://dx.doi.org/10.1007/s10494-006-9036-4.

[23] S. Leonardi, P. Orlandi, and R. A. Antonia. Properties of d- and k-type roughness in a turbulent channel flow. *Physics of Fluids*, 2007. URL http://link.aip.org/link/?PHF/19/125101/1.

[24] M. Amir and I. P. Castro. Turbulence in rough-wall boundary layers: universality issues. *Experiments in Fluids*, 2011. URL http://dx.doi.org/10.1007/s00348-011-1049-7.

[25] K. A. Flack, M. P. Schultz, and T. A. Shapiro. Experimental support for townsend's reynolds number similarity hypothesis on rough walls. *Physics of Fluids*, 2005. URL http://link.aip.org/link/?PHF/17/035102/1.

[26] P. Krogstadt and R.A. Antonia. Surface roughness effects in turbulent boundary layers. *Experiments in Fluids*, 1999. URL http://dx.doi.org/10.1007/s003480050370.

[27] J. H. Lee, S. H. Lee, K. Kim, and H. J. Sung. Structure of the turbulent boundary layer over a rod-roughened wall. *International Journal of Heat and Fluid Flow*, 2009. URL http://www.sciencedirect.com/science/article/pii/S0142727X09001222.

[28] L. D. Landau and E. M. Lifshitz. *Course of Theoretical Physics: Fluid Mechanics*. Butterworth-Heinemann, 2nd edition, 2003.

[29] J.L. Guermond, P. Minev, and Jie Shen. An overview of projection methods for incompressible flows. *Computer Methods in Applied Mechanics and Engineering*, 2006. URL http://www.sciencedirect.com/science/article/pii/S0045782505004640.

[30] *COMSOL Multi-Physics V4.2 User Guide: Ch.12 The Fluid Flow Branch*, 2012. URL http://nf.nci.org.au/facilities/software/COMSOL/4.3/doc/pdf/mph/COMSOLMultiphysicsUsersGuide.pdf.

[31] P. Deuflhard. A modified newton method for the solution of ill-conditioned systems of nonlinear equations with application to multiple shooting. *Numerische Mathematik*, 1974.

[32] J. D. Anderson. *Computational Fluid Dynamics: The Basics with Applications*. McGraw-Hill: Mechanical Engineering Series, 1995.

[33] O. C. Zienkiewicz, R. L. Taylor, and P. Nithiarasu. *The Finite Element Method for Fluid Dynamics Vol.3, Sixth Edition*. Butterworth-Heinemann, 2005. URL http://amazon.com/o/ASIN/0750663227/.

[34] J. Kent, J. Thuburn, and N. Wood. Assessing implicit large eddy simulation for two-dimensional flow. *Quarterly Journal of the Royal Meteorological Society*, 2012. URL http://dx.doi.org/10.1002/qj.925.

[35] A. Brooks and T. Hughes. Streamline upwind/petrov-galerkin formulations for convection dominated flows with particular emphasis on the incompressible navier-stokes equations. *Computer methods in applied mechanics and engineering*, 1982.

[36] J. R. Stewart and T. JR. Hughes. A tutorial in elementary finite element error analysis: A systematic presentation of a priori and a posteriori error estimates. *Computer Methods in Applied Mechanics and Engineering*, 1998. URL http://www.sciencedirect.com/science/article/pii/S0045782597002302.

[37] D. W. Trott and M. K. Gobbert. Conducting finite element convergence studies using COMSOL 4.0. In *Proceedings of the COMSOL Conference 2010, Boston, MA*, 2010. URL http://userpages.umbc.edu/~gobbert/papers/TrottGobbertCOMSOL2010.pdf.

[38] V. C. Patel and M. R. Head. Some observations on skin friction and velocity profiles in fully developed pipe and channel flows. *Journal of Fluid Mechanics*, 1969. URL http://journals.cambridge.org/article_S0022112069000115.

[39] P. R. Spalart. Direct simulation of a turbulent boundary layer up to $re_\theta = 1410$. *Journal of Fluid Mechanics*, 1988. URL http://dx.doi.org/10.1017/S0022112088000345.